UNIVERSITÀ DEGLI STUDI FIRENZE

Tesi di Dottorato in Scienze ed Ingegneria dei Materiali

Ciclo XXXI

Dual pH and Temperature Responsive Magnetic Nanocomposite for Controlled Drug Delivery

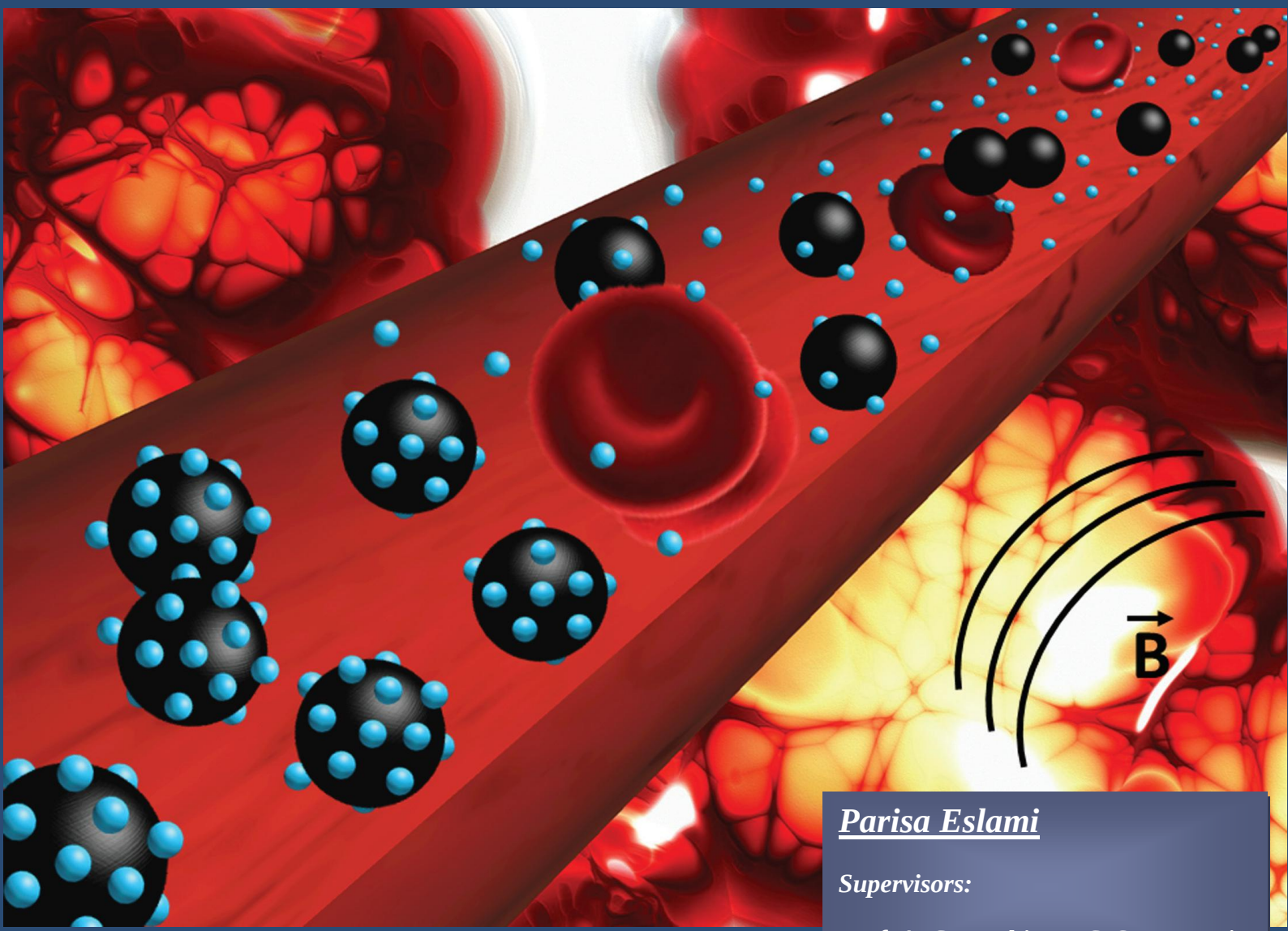

Parisa Eslami

Supervisors:

Prof. A. Caneschi, Dr. C. Sangregorio

UNIVERSITÀ
DEGLI STUDI
FIRENZE

DOTTORATO DI RICERCA IN
INGEGNERIA INDUSTRIALE
(*Indirizzo in SCIENZE ED INGEGNERIA DEI MATERIALI*)

CICLO XXXI

COORDINATORE Prof. De Lucia Maurizio

Dual pH and temperature responsive magnetic nanocomposite for controlled drug delivery

Settore Scientifico Disciplinare CHIM/07

Dottorando
Dott. ssa. Parisa Eslami

_____

Tutori
Prof. Andrea Caneschi

_____

Dott. Claudio Sangregorio

_____

Coordinatore
Prof. De Lucia Maurizio

_____

Anni 2015/2018

DEDICATION

To my grandfather's memory and beloved family for always supporting, helping, and standing by me

"We must have perseverance and above all confidence in ourselves. We must believe that we are gifted for something and that this thing must be attained." — Marie Curie

ACKNOWLEDGEMENTS

First and foremost, I have to express my heartful thanks to my inspiring parents and my brother for their love, endless support, and sacrifices. Their dedicated partnership encouraged me to achieve my goals.

I would like to thank the director of Ce.Ri.Col (Research Center of Colorobbia Consulting S.r.l.), Dr. Giovanni Baldi, for the privilege of starting my research career; he gave me the great opportunity to gain invaluable experience in Materials Science & Nanotechnology. Under his guidance, I was given the freedom to pursue my research in my own way, and I greatly appreciate him for supporting and encouraging me through these years.

I would like to express my deep appreciation to my supervisors, Prof. Andrea Caneschi and Dr. Claudio Sangregorio, for helpful discussions, valuable suggestions, their support during travels for conferences and hard work. I also would like to express extreme gratitude to Prof. Federica Chiellini and Dr. Andrea Morelli, who introduced me to the world of thermoresponsive polymers and broadened my research interests to this scientific field. They are gratefully acknowledged for helpful discussions during my PhD thesis work, interesting collaborations, and pleasant time.

I am also appreciative of all the help from colleagues in our research group at Colorobbia, Dr. Saer Doumett, Dr. Costanza Ravagli, Luca Antonini, Laura Cappiello, Giada Lorenzi, Dr. Riccardo Rapini, Dr. Stefano Fedeli, Valentina Dami, Marco Trassinelli, Lucrezia Ballerini, and Andrea Cioni. In addition, I sincerely thank my friends in University of Florence: Dr. Andrea Guerrini, Dr. Michele Petrecca, Dr. Martin Albino, Dr. Claudia Innocenti, and Donella Rovai that helped me to carry out my thesis successfully.

I am also grateful of the financial support provided by the Colorobbia Consulting S.r.l and National Interuniversity Consortium for Materials Science and Technology (INSTM).

Chapter 1

Chapter 2

Chapter 3

Chapter 4

Chapter 5

Chapter1

Introduction

Magnetic nanoparticles (MNPs) have emerged as promising nanomaterials for their potential use in biomedical applications such as magnetic resonance imaging (MRI) [1–3], cell separation [4,5], magnetic hyperthermia [6–8], and drug delivery [9-11]. Iron oxide MNPs have been greatly investigated for clinical trial due to their good biocompatibility, low toxicity, heat generation ability, and high chemical stability. In fact, MNPs are suitable for hyperthermia cancer treatment as a consequence of their heat generation potential under applying alternating magnetic field. Hyperthermia is known as a treatment where tumours are heated to temperatures between 40 ^{o}C and 45 ^{o}C [12] causing cancer cells to undergo apoptosis [13], while normal tissues are still alive as they are less sensitive to heat [14]. Hyperthermia therapy is also used as an auxiliary method to augment efficiency of standard cancer treatments such as chemotherapy or radiotherapy.

Chemotherapy is a widely used treatment for cancer. However, the major drawback of chemotherapy is the non-specificity of the anticancer drugs, which may cause strong damage of healthy organs and cells during the therapy. Nanocarrier-based drug delivery system is a possible strategy that may improve therapeutic efficacy of chemotherapeutic agents and decreases their side effects in clinical trial. One of the major advantages of using nanoparticles (NPs) as drug carrier, especially MNPs, over conventional chemotherapy is that nanoparticles have possibility of targeting specific locations in the body, allowing the reduction of the chemotherapeutic dose to reach the concentrations needed in the tumour for an effective therapy. In addition, the concentration of drugs at non-targeted sites is reduced, minimizing undesirable side effects of chemotherapy [15].

The advantages provided by the synergistic effect of the combined thermo-chemotherapy by combining highly efficient magnetic hyperthermia with magnetothermally-controlled drug release, make MNPs-based therapeutic agents a really promising candidate for the treatment of cancer; in fact, increased anti-cancer drug accumulation in tumour and thermal enhancement of drug cytotoxicity are among the most important mechanisms behind the synergistic effect of thermo-chemotherapy [16,17]. These are mainly caused by the improved intracellular uptake of drugs due to enhanced cell membrane permeability, inhibition of DNA repair of the chemically induced lethal or sublethal damages, and

acceleration of the cytotoxic chemical reaction. However, controlled drug release is still challenging, and there is an evident need to solve this issue particularly as concerns the control of the release rate. Indeed, the delivery of a drug is often problematic because the concentration of the released drug at the target area is either too low or too high and there is no possibility to control the delivery over time. Although the desirable-controlled drug release is not easily achievable, smart organic-inorganic nanohybrids have been proposed to provide multi-stimuli responsive platforms, which are able to optimize the efficiency of nanocarrier-based drug delivery system by allowing delivery and release of the drug at the right time and concentration by activation through external or internal stimuli such as temperature and pH. Among the many approaches proposed in the literature, particularly appealing method is the possibility to exploit the thermoresponsive drug nanocarriers, composed of a temperature-responsive polymer shell and a MNPs core to promote the effective controlled drug release only by response to an external AMF thanks to the heat generation ability of MNPs. To fulfil this aim the drug nanocarriers should ideally retain their load at body temperature (~ 37 °C), and release the drug within a locally heated tumour at the therapeutic temperature for magnetic hyperthermia (42.5 ^{o}C −46 °C) [18]. In this manner, the localized heat generated by the MNPs under AMF excitation can significantly raise the temperature of the thermoresponsive polymer shell above its critical solution temperature (CST), around which a sudden demixing from aqueous solutions occurs, leading the polymer to exhibit conformational transformation in response to change in temperature for remote-controlled drug release.

pH-responsive polymers can also be exploited for drug delivery applications because of the pH changes between healthy and tumour tissues. The pH in the tumour environment is, in fact, often more acidic than one that in the blood or healthy tissue. Therefore, if pH-sensitive drug delivery systems target the tumour site, they can then release their payload due to the pH difference [19].

The use of polymer sequences owning sensitivity to more than one stimulus such as pH and temperature can have even more advantages over one stimulus responsive polymers for regulating drug release since they can respond to a combination of external stimuli, which provides unique opportunities to advance medicine especially in controlled drug delivery strategies. An interesting example of this approach is represented by double pH- and temperature responsive polymer coated MNPs, which can release drug in a controlled way by exploiting the abnormal acidic pH values (around 4.5–5.5) that are found in tumour

endosome/lysosome microenvironments or either through the hyperthermia of superparamagnetic core of these nanocomposites under exposure of an external AC magnetic field (AMF) that can serve as the "trigger" to control the "on–off" of the thermo-sensitive polymer shell, which is capable of drug release in a controlled manner; thus, pH and temperature variations can simultaneously boost the drug release on tumour tissues, improving the efficacy of the therapy.

The aim of this thesis is the development of a nanoencapsulation technology to produce highly effective smart multifunctional nanocomposites that have potential to be exploited as a multi-functional therapeutic agent for drug delivery and controlled drug release in combination with localized hyperthermia. To accomplish this ambitious goal, the thesis involves synthesis and characterization of smart nanohybrids made up of a superparamagnetic iron oxide core and a dual pH and temperature-responsive poly (N-vinylcaprolactam-*b*-acrylic acid) shell, which are subsequently loaded with an anticancer drug, Doxorubicin. In fact, this dual stimuli-responsive magnetic nanocomposite offers spatial and temporal control over the release of the anticancer drug, which is triggered as a consequence of hyperthermia and tumour acidic pH at desired time without degradation or premature drug release, to enhance the effectiveness of the treatment. Moreover, the evaluation of this novel smart nanocomposite efficacy on selected pathological models *in vitro* is evaluated. To achieve this aim, the *in vitro* drug release of the drug-conjugated Fe_3O_4 MNPs coated with the stimuli responsive polymer is investigated at physiological pH (7.4) and acidic pH (4.5-5.5, similar to the one found in tumour environment) under exposure to AMF at predetermined time interval, and the concentration of released drug is quantified using UV-VIS spectrophotometer. Finally, cytotoxic property of smart nanohybrids after and before drug loading is determined by incubation of magnetic nanohybrids on melanoma cell for 24 h at body temperature since nontoxicity of any material considered for therapeutic application is imperative.

In order to grant for a multifunctional approach, it is essential to obtain MNPs with optimal heating characteristics that allow the clinical trials of hyperthermia technology in a safe manner, while being effective in cancer treatment. That means, MNPs that have potential to generate a large quantity of heat and thus a higher Spesific Absorption Rate (SAR) at their minimum concentration under low magnetic field amplitudes are clinically required. Therefore, engineering MNPs (control their physical and chemical properties using proper synthesis), which satisfy the above criteria, is highly desirable, and several synthetic techniques have been already developed to achieve this aim. Although thermal decomposition

and co-precipitation approaches are the most commonly synthetic methods used for MNPs preparation, we mainly focused on polyol synthetic procedure as this approach offers some advantages including: [20] (i) the high boiling point of polyol allows synthesis to proceed at relatively high temperature, ensuring that well crystallized materials are obtained, (ii) the reducing medium protects the as-prepared metal particles from oxidation as long as they remain in the medium, (iii) the ability of polyol to coordinate metal precursors as well as the particle surface, minimizing coalescence, (iv) the high viscosity of the medium favors a diffusion-controlled regime for particle growth [21], resulting in controlled structures and morphologies, (v) polyol process can be easily scaled up. Indeed, the polyol process was found to be particularly well-suited method as it can yield crystalline materials with a specific flower-like morphology i.e. aggregates of small NPs (10.0 nm or below in diameter) without subsequent thermal treatment, while allowing a fine control on particle size, shape and aggregate size. [20]. Importantly, flower-like MNPs show interesting magnetic behavior with extremely high heating power compared to isolated MNPs [22,23]. For instance, direct aggregation between 5.0 nm nanoparticles of manganese-doped magnetite ($MnFe_2O_4$) to form large spherical clusters of ca. 100.0 nm diameter was found to minimize the effect related to their characteristic magnetic dead layer at the surface. As a consequence, the clustering process provided nanostructures with high saturation magnetization (86 emu g^{-1}) and very large specific absorption rate (SAR), which could be exploited for heat delivery [24].

In the following, pH and temperature responsive poly (N-vinylcaprolactam-*b*-acrylic acid) (PVCL-*b*-PAA) is prepared corresponding to free-radical polymerization by modifying some procedures previously reported in the literature for functionalization the surface of MNPs. In fact, poly N-vinylcaprolactam-based copolymers have been scarcely investigated for surface modification of MNPs, while the most of research being focused on poly isopropylacrylamide (PNIPAM). That is most probably because of the controlled radical polymerization of non-conjugated N-vinylcaprolactam monomers is inherently difficult; however, PVCL seems more promising biocompatible polymer as it has been shown to support higher cell viability and have lower cytotoxicity compared to PNIPAM. Importantly, the nitrogen atom in the caprolactam ring is directly connected to the chain backbone, so hydrolysis of PVCL if it occurs, will not produce a small toxic amide compound as PNIPAM does. This makes PVCL highly useful for biomedical applications including drug delivery and *in vivo* release systems [25]. Despite of the fact that synthesis of PVCL is challenging due to the high reactivity of vinyl monomers, and few works, in fact, have been done on controlled copolymerization of vinyl caprolactam, we selected PVCL-based copolymer as a

smart polymer owing to the high biocompatibility, lower toxicity, and proper thermal sensitivity that PVCL shows respect to PNIPAM. Thanks to the presence of PAA blocks in copolymer backbone, the copolymer can be sensitive to pH as well. Moreover, the thermo-responsive copolymer can be engineered so as to reveal reversible phase transition behavior at temperature above physiological temperature (~ 37 ^{o}C) close to that which can be obtained by magnetic hyperthermia. In our case we perform for the first time surface modification of MNPs by this stimuli responsive PVCL-*b*-PAA polymer using a ''grafting to'' approach.

To our knowledge, there is no previous work describing procedures for directly coating the magnetic nanoparticles using a temperature- and pH-sensitive poly (N-vinylcaprolactam-*b*-acrylic acid) with a simple covalent ''grafting to'' method. Previously published works [26–29], describing polymer-coated MNP, indeed, involve a polymerization step or covalent grafting reaction, which includes: (i) the use of initial reactants (monomers, initiators, catalysts, etc.), (ii) the need of an additional purification step to remove the non-reacted reagents, (iii) longer preparation time and (iv) complex synthesis conditions (vacuum, inert atmosphere, high temperatures, etc.), i.e. a long list of issues, which can be overcome using the procedure developed in this work. In addition, we will show how one of the most challenging issues in drug delivery system, i.e. the long-time stability of colloidal suspension of NPs in aqueous media at physiological pH, can be solved by selecting this smart and biocompatible polymer.

In the following, we will outline how with the proposed coating strategy, highly stable and monodisperse nanosystems with negative surface charge can be achieved, confirming strong adherence of polymer to the surface of the MNPs. Obtained results, in fact, demonstrated that we successfully fabricated nanosized drug delivery systems, which can be utilized as multimodal therapeutic agent in the tumour therapy by exploiting magnetic fluid hyperthermia and controlled drug release under exposure to AMF.

Many magnetic nanoparticles-based drug delivery systems have been developed in the last decade. However, the major bottleneck for their clinical theranostic achievement has been the low drug loading capacity and poor controlled-drug release of the developed magnetic nanoparticles. Nevertheless, our nanocomposite exhibited exceptional drug loading capacity and controlled drug release triggered by the acidic tumour microenvironment in combination with hyperthermia performance. In this regard, pH and temperature responsive

magnetic nanohybrids, which developed in this work as multifunctional nanocarriers, are able to have a dramatic impact in medicine and in the treatment of cancer.

All the experimental work carried out to prepare and investigate this nanosystem is described in this thesis, which is organized as follows:

Chapter 2 introduces drug delivery systems based on MNPs, strategies for their accumulation into cancer cells, and recent advances in cancer therapy. A brief summary of fundamental properties of MNPs and their potential for the combination of hyperthermia and chemotherapy are presented as well. Moreover, unique advantages of a double pH- and thermo-responsive magnetic nanohybrids drug carrier suitable for multi-modal cancer therapy by combining magnetic hyperthermia and controlled drug delivery are summarized. **Chapter 3** mainly focuses on synthesis and characterization of superparamagnetic iron oxide nanoparticles, prepared by polyol method; magnetic property and heat generation ability of MNPs are evaluated in terms of their potential application for hyperthermia performance in clinical trials. In **Chapter 4** synthesis of temperature responsive (co)polymers based-PVCL with well-controlled molecular weights by applying sequential Reversible Addition Fragmentation Chain Transfer (RAFT) polymerization approach is discussed, and subsequently their temperature responsive behavior is evaluated. Development and characterization of a double pH- and thermo-responsive poly (N-vinylcaprolactam-*b*-acrylic acid) are reported as well. **Chapter 5** is devoted to the encapsulation of superparamagnetic iron oxide nanoparticles by dual pH- and temperature responsive polymer to provide smart nanocomposite platform for triggered drug release. The effectiveness of surface modification approach is evaluated by employing some techniques including FT-IR, TEM, TG, and DLS analyses. **Chapter 6** evaluates drug loading potential of stimuli responsive nanocomposite, and doxorubicin (DOX) as an anticancer drug is selected to explore drug delivery properties of this smart nanohybrids. Indeed, doxorubicin is a cationic chemotherapeutic drug with broad-spectrum antitumour activity that can be loaded on PVCL-*b*-PAA coated MNPs through electrostatic interactions. Moreover, the pH and temperature dependent drug release of DOX loaded on smart nanocomposite are assessed in the absence and presence of AFM. Finally, cytotoxicity of functionalized MNPs after and before drug loading is estimated as well.

The final **Chapter** briefly summarizes the main conclusions obtained from the experimental work presented above and provides some hints about future work that needs to be done to address all the open issues to make feasible the application of this product in clinics.

Chapter1

References

1. J. Huang.; X. D. Zhong.; L. Y. Wang.; L. L. Yang.; H. Mao. *Theranostics.* **2012**, *2*, 86.
2. R. Hachani.; M. Lowdell.; M. Birchall.; N. T. K. Thanh. *Nanoscale*. **2013**, *5*, 11362.
3. H. B. Na.; I. C. Song.; T. Hyeon. *Adv. Mater*. **2009**, *21*, 2133.
4. M. Schwalbe.; K. Pachmann.; K. Hoffken.; J. H. Clement. *J. Phys. Condens. Matter*. **2006**, *18*, S2865.
5. H. Y. Xu.; Z. P. Aguilar.; L. Yang.; M. Kuang.; H. W. Duan.; Y. H. Xiong.; H. Wei.; A. Wang. *Biomaterials*. **2011**, *32*, 9758.
6. I. Sharifi.; H. Shokrollahi.; S. Amiri. J. *Magn. Magn. Mater*. **2012**, *324*, 903.
7. I. Hilger. *Int. J. Hyperth*. **2013**, *29*, 828.
8. S. Laurent.; S. Dutz.; U. O. Hafeli.; M. Mahmoudi. *Adv. Colloid Interface Sci*. **2011**, *166*, 8.
9. M. Arruebo.; R. Fernández-Pacheco.; M. R. Ibarra.; J. Santamaría. *Nano Today*. **2007**, *2*, 22.
10. M. Mahmoudi.; S. Sant.; B. Wang.; S. Laurent.; T. Sen. *Adv. Drug Deliv. Rev*. **2011**, *63*, 24.
11. O. Veiseh.; J. W. Gunn.; M. Zhang. *Adv. Drug Deliv. Rev*. **2010**, *62*, 284.
12. A. Chicheł.; J. Skowronek.; M. Kubaszewska.; M. Kanikowski. *Rep. Pract. Oncol. Radiother*. **2007**, *12*, 267.
13. B. V. Harmon.; Y. S. Takano.; C. M. Winterford.; G. C. Gobe. *Int. J. Radiat. Biol*. **1991**, *59*, 489.
14. J. van der Zee. *Ann. Oncol*. **2002**, *13*, 1173.
15. R. Tietze.; J. Zaloga.; H. Unterweger.; S. Lyer.; C. Alexiou. *Biochem. Biophys. Res. Commun.* **2015**, 468, 463.
16. W. Rao.; Z. S. Deng.; J. Liu. *Crit. Rev. Biomed. Eng*. **2010**, *38*, 101.
17. J. P. May.; S. D. Li. *Expert Opin. Drug Deliv*. **2013**, *10*, 511.
18. A. Hervault.; A. E. Dunn.; M. Lim.; S. Maenosono.; N. T. K. Thanh. *Nanoscale*. **2016**, *8*, 12152.
19. S. Mura.; J. Nicolas.; P. Couvreur. *Nat Mater*. **2013**, *12*, 991.

20. F. Fie´vet.; S. Ammar-Merah.; R. Brayner.; J. Y. Piquemal. *Chem. Soc. Rev.* **2018**, *47*, 5187.
21. D. Nguyen. *Nanoscale*. **2013**, *5*, 9455.
22. P. Hugounenq.; M. Levy.; D. Alloyeau.; F. Gazeau. *J. Phys. Chem. C*. **2012**, *116*, 15702.
23. S. Dutz.; M. Kettering.; I. Hilger.; R. Müller.; M. Zeisberger. *Nanotechnology*. **2011**, *22*, 265102.
24. R. Otero-Lorenzo.; E. Fantechi.; C. Sangregorio.; V. Salgueiri. *Chem. Eur. J*. **2016**, *22*, 6666.
25. N. A. Cortez-Lemus.; A. Licea-Claverie. *Prog. Polym. Sci*. **2016**, 53, 1.
26. Z. X. Dong.; H. Wei.; J. Mao.; D. P. Wang.; M. Q. Yang.; X. L. Ji. *Polymer*. **2012**, *53*, 2074.
27. J. W. Park.; K. H. Bae.; C. Kim.; T. G. Park. *Biomacromolecules*. **2011**, *12*, 457.
28. L. Zhou.; C. Gao.; W. J. Xu. *J. Mater. Chem*. **2009**, *19*, 5655.
29. G. Hemery.; E. L. S. Garanger.; A. D. Wong.; E. R. Gillies.; B. Pedrono.; T. Bayle.; D. Jacob.; O. Sandre. *J. Phys. D: Appl. Phys.* **2015**, *48*, 494001.

Chapter 2

Since this thesis is focused on the fabrication and characterization of smart magnetic nanohybrids for magnetic hyperthermia therapy in conjunction with drug delivery, in this chapter the basic concepts relevant to physical behavior of superparamagnetic nanoparticles and, the importance of smart magnetic nanohybrids in nanomedicine are briefly overviewed.

2.1 Superparamagnetic Behavior

Among all types of nanoparticles, biocompatible superparamagnetic iron oxide nanoparticles with proper surface architecture and conjugated targeting ligands/proteins have attracted a great deal of attention for biomedical applications [1]. This is because their unique physical properties, among which superparamagnetism is undoubtedly the most notable one. Superparamagnetism is a form of magnetism that occurs in ferromagnetic or ferrimagnetic materials, when their size is lower than a critical size d_c, which varies between tens to few hundreds of nanometers, depending on the type of materials. The critical size d_c for a spherical particle can be estimated using the following equation (1) [2].

$$d_c = \sqrt[3]{\frac{6\,K_B T}{K}} \qquad (1)$$

where k_B is the Boltzmann constant, T is the temperature, and K is the magnetic anisotropy constant, which is characteristic for each material. Depending on K, the critical size of nanoparticles can be 3–4 nm for very hard magnets and over ca. 130 nm for soft magnets including magnetite (Fe_3O_4) and maghemite (Fe_2O_3) [3].

Superparamagnetic nanoparticles are single-domain particles since the formation of magnetic domains is no longer energetically favoured, so they can be described by one giant magnetic moment, whose value equals the sum of all magnetic moments of the atoms forming the nanoparticles. The superparamagnetic behavior derives from the fact that a magnetic particle with size lower than d_c prefers to be uniformly magnetized along one of its easy axes, the preferred crystallographic axes for the magnetic moment to point along, and the energy required to rotate the magnetization away from the easy direction is called

magnetic anisotropy energy, which is related to the constant K. In a simple model for a non-interacting single domain spherical particle with uniaxial anisotropy in zero magnetic field, the magnetic anisotropy energy, E_a, is given by equation (2) [4].

$$Ea = KVSin^2\theta \qquad (2)$$

Where V is the volume of the particle and θ is the angle between the particle magnetization and the easy magnetization axis of the particle. According to equation (2), the magnetic anisotropy energy decreases when the volume of the particle becomes smaller. When E_a becomes comparable to or lower than the thermal energy ($E_{thermal} = k_BT$) [5], the energy barrier for magnetization reversal can be thermally overcome (Figure 2.1), and the giant magnetic moment associated to the particle becomes free to fluctuate under the effect of $E_{thermal}$, like in a paramagnetic system. For this reason, this phenomenon is called 'superparamagnetism'.

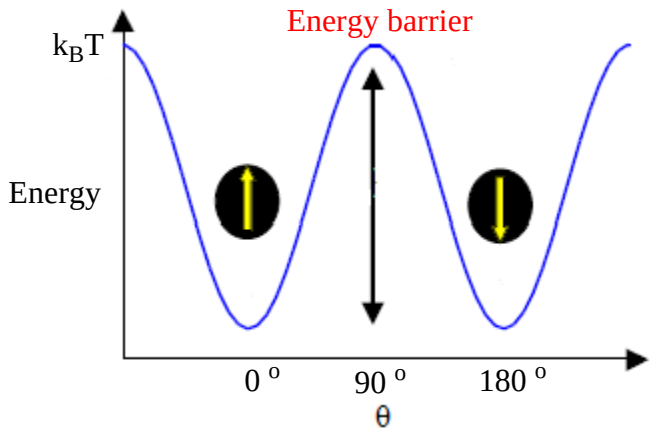

Figure 2.1 Scheme representing the anisotropy energy barrier for magnetization [6]

Superparamagnetism can be thus regarded as a thermally activated regime, which occurs above the so-called blocking temperature (T_B), which is described by the equation (3),

$$T_B = \frac{KV}{K_B Ln\left(\tau_m/\tau_0\right)} \qquad (3)$$

where τ_m is the measurement time, and τ_0 is the attempt time, which is typically approximated as 10^{-9} s for not interacting MNPs. Above T_B, nanoparticles exhibit superparamagnetic behavior, which manifested by rapid and random reversal of their

magnetic moments, resulting in a zero averaged magnetization. Conversely, below T_B the particles are in a blocked regime. That means, the magnetic moment has not the required energy to overcome the energy barrier, and thus magnetic irreversibility occurs (i.e. open hysteresis loop). The value of T_B, associated with the energy barrier, depends on the characteristic measuring time, which can vary widely from 100 to 10^{-8} s, depending on the experimental techniques used [7]. The magnetic behavior observed, indeed, arises from the relative difference between the measuring time of the instrument and the intrinsic relaxation time of the system, i.e. the characteristic time needed for the magnetization reversal, τ :

$$\tau_N = \tau_0 \, exp \, (\frac{KV}{K_B T}) \qquad (4)$$

If the measuring time is greater than the relaxation time, the nanoparticles are in the superparagmagnetic regime. If, conversely, the measuring time is lower than the relaxation time, the nanoparticles are in a "blocked" regime [7], so note that the blocking temperature definition derives from the equality condition of these two characteristic times. Experimentally, the blocking temperature value can be estimated as the temperature of the "maximum" of the zero-field cooled (ZFC) magnetization curves [8]. In the standard experimental procedure of this magnetic characterization, the sample is cooled twice from room temperature to 10 K or lower, first with no applied magnetic field (ZFC) and then with a weak external field (field cooled, FC) Figure 2.2 shows the typical ZFC and FC magnetizations versus temperature curves and the T_B position at the ZFC maximum.

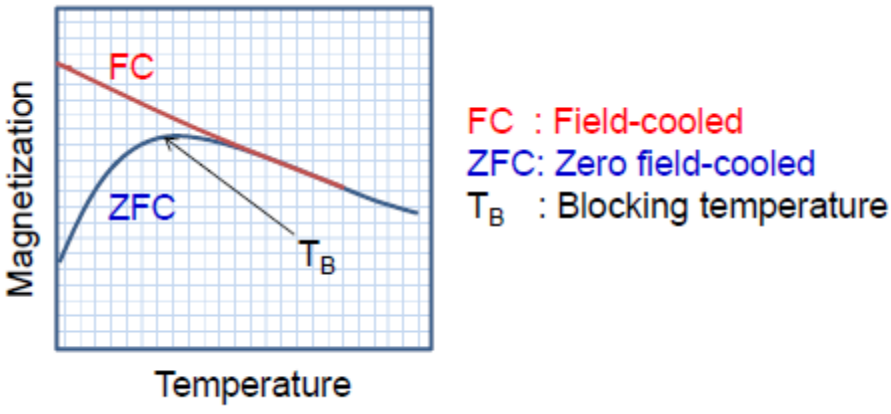

Figure 2.2 Magnetization versus temperature curves measured under ZFC and FC conditions, respectively. The maximum on the ZFC curve is commonly assumed to correspond to the blocking temperature, T_B [9]

As well known, ferromagnetic (or ferrimagnetic) nanoparticles show hysteresis loop with non zero coercivity field (Hc) and remanant magnetization (Mr). In the superparamagnetic regime, instead, Hc and Mr are zero as the magnetic moments of particles align themselves in the same direction as the applied external magnetic field, and revert to a random orientation state (zero magnetization remanence) when the external magnetic field is removed (Figure 2.3) [10]. Therefore, a set of superparamagnetic nanoparticles with large susceptibility $(\frac{M}{H})$ can be easily magnetized to reach saturation, and the initial state can be easily restored by simply removing the external field. On the ground that superparamagnetic nanoparticles can be controlled by an external magnetic field, they are extremely advantageous for biomedical applications [11].

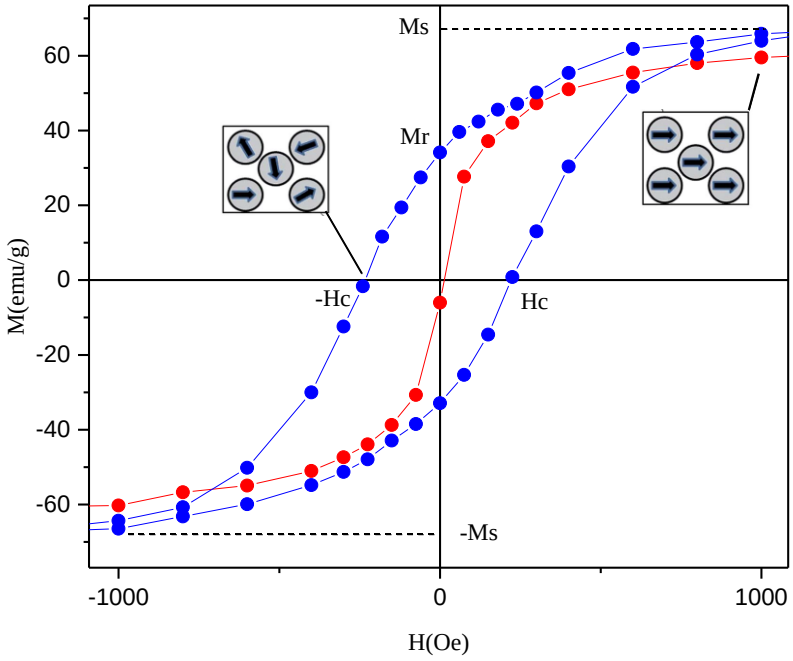

Figure 2.3 The magnetic response characteristic of nanoparticles in a superparamagnetic (red) and blocked (blue) state

2.2. Basic Principles of Application of MNPs as Heat Mediators in Magnetic Hyperthermia

Various models and experimental data have been employed to better understand the heating process in magnetic hyperthermia. In 2002, Rosensweig developed a model to explain the heating of colloidal magnetic fluids subjected to an alternating magnetic field [12]. He assumed that the heat generation was only due to the rotational relaxation of non-interacting single domain MNPs, which their magnetization varies linearly with the applied

magnetic field (linear response theory, LRT). From the LRT model, the expression for the power dissipation (*P*) is given by the following equation [12]

$$P = \mu_0 \mathcal{X}'' f {H_0}^2 \qquad (5)$$

Where μ_0 is the permeability of free space, $\mathcal{X}''$ is the AC magnetic susceptibility, f and H_0 are the frequency and the amplitude of the applied AC magnetic field respectively. Beside, $\mathcal{X}''$ can be expressed as:

$$\mathcal{X}'' = \frac{\omega\tau}{1+(\omega\tau)^2}\mathcal{X}_0 \qquad (6)$$

Where $\omega = 2\pi f$, $\mathcal{X}_0$ is isothermal susceptibility and τ is the effective relaxation time.

Two mechanisms for the effective relaxation time, which is directly dependent on inversion of the magnetic moment, must be considered: Néel relaxation and Brownian relaxation. It is worth noting that the mechanisms of relaxation not only depends on the size of the NPs but also depends on the composition of magnetic materials owing to their specific anisotropy constant, K [13]. Nèel relaxation, which is strongly size-dependent (exponential dependence on the particle's volume), comes from the internal rotation of the magnetic moment over the energy barrier in the same direction of the applied magnetic field with each field oscillation (Figure 2.4, a) [14,15], and the characteristic time τ_N for Néel relaxation is given by equation 4. On the other hand, Brownian relaxation is pertinent to the rigid rotation of the whole particle in a carrier liquid, and so it is absent when the particle cannot freely move (Figure 2.4, b) [14,15].

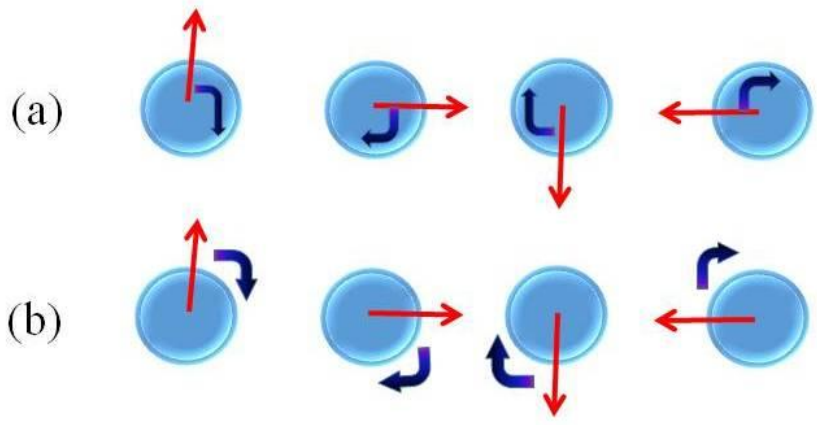

Figure 2.4 a) Néel relaxation: rotation of the magnetization inside the particle, b) Brown relaxation: mechanical rotation of the whole magnetic particle [14,15].

Brownian relaxation time τ_B is expressed by the following equation:

$$\tau_B = \frac{3\eta V_H}{K_B T} \quad (7)$$

Where η is the viscosity of the liquid carrier, V_H is the hydrodynamic volume of the particle. The Brownian relaxation mechanism linearly depends on volume and viscosity [16]. A higher viscosity of the liquid medium will slow down the rotation of the particles. Generally, losses by Néel relaxation prevail for small MNPs, while the Brownian regime dominates for larger MNPs [14,17]. In fact, the Brownian losses are not exclusively found in superparamagnetic MNPs [18].

For hyperthermia applications, it is better to have MNPs relaxing essentially through the Nèel mechanism because when internalized in the cells, a change in the viscosity medium and particle aggregation can happen, and free rotation of the particles can be prevented. As the two relaxation mechanisms take place in parallel, the overall effective relaxation time τ of the particles will be given by the combination of the two magnetic relaxation times [14]:

$$\tau = \frac{\tau_B \tau_N}{\tau_B + \tau_N} \quad (8)$$

2.2.1 Measurement of Magnetic Hyperthermia Efficiency by a Calorimetric Method

The calorimetric approach is the most commonly adapted method for evaluating directly the magnetic hyperthermia efficiency of MNPs. In this method, the temperature increase in the sample is recorded over a period of time as the MNPs are exposed to an AMF field of a proper amplitude and frequency (Figure 2.5).

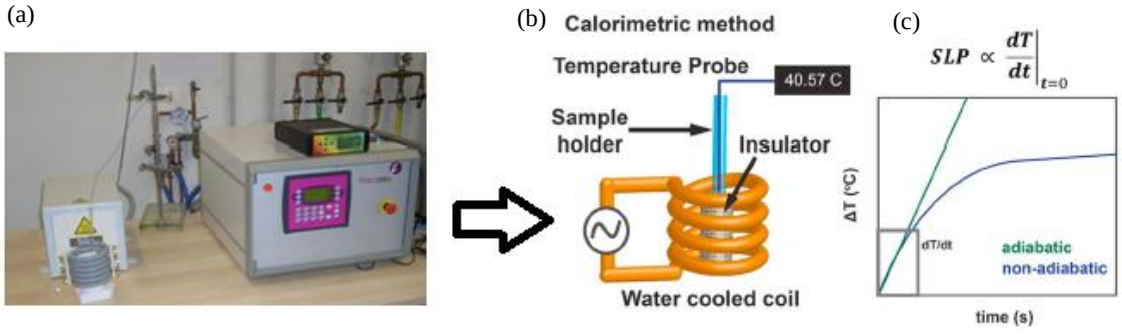

Figure 2.5 (a) Experimental set-up used to evaluate the SAR of suspensions of nanopartciles, (b) scheme of the apparatus, (c) typical experimental temperature kinetics (blue curve), the green curve represents the ideal beahvior for a perfectly adiabatic apparatus, the SAR is estimated from the initial slope of temperature vs. time curve

The main apparatus is made by a magnetic induction heating system consisting of a water cooled coil connected to a high power *rf* generator, while an optical fiber optic is typically used to measure the temperature.

Samples are placed in a thermally insulated container to avoid heat loss to the environment during measurement, and quantification of the power dissipation of magnetic nanoparticles in an AMF is usually done by evaluating the specific absorption rate (SAR), which is the power dissipated by mass unit and is expressed in W g^{-1} (also referred to as Specific Loss Power - SLP) according to the formula:

$$SAR = \frac{m_d\, C_{p,d}}{m_{NP}} \left|\frac{dT}{dt}\right| t = 0 \qquad (9)$$

where m_d and $C_{p,d}$ are the mass and heat capacity of the dispersion medium (4.18 J/g·K for water), respectively, while m_{NP} is the mass of nanoparticles. As the system used is not adiabatic, the time derivative $\left|\frac{dT}{dt}\right|$ of temperature is taken in the initial linear stage of heating (first 30 s).

According to Eq. 9 the SAR value is also proportional to the applied AC magnetic field strength and frequency. Considering the equation of the heat dissipation value, it is clear that SAR values increase with the frequency *f* and the amplitude H of the applied field. However, in order to apply hyperthermia safely to patients and avoid any detrimental effect on healthy tissues due to electromagnetic radiation exposure, the H*f* factor should not exceed a threshold, which was experimentally estimated equal to 5×10^{-9} A m^{-1} s^{-1} [19].

2.2.2 Dependence of Magnetic Hyperthermia Efficiency on Morpho-Structural Properties

The power dissipated during magnetic hyperthermia measurements depends on external parameters such as AC field and magnetic dipolar interaction effects in addition to the intrinsic magnetic properties of the MNPs, which influences their relaxation dynamics (Néel and Brownian). According to the LRT model, the heating efficiency is proportional to the square of the saturation magnetization of the MNP, but it can be maximized also by tuning the MNP size and magnetic anisotropy [12,20]. On the other hand, optimum MNP size and crystalline anisotropy vary, depending on the strength and frequency of the applied AC field. Magnetic dipolar interactions that promote the formation of nano-assemblies organized as nanoclusters or nanochains, can also modify the relaxation behavior of the MNPs. In the

following, the effect of size, shape, and aggregation of nano-assemblies on the heating efficiency of superparamagnetic nanoparticles will be discussed to provide a better understanding on how each of these parameters can be optimized for magnetic fluid hyperthermia applications.

2.2.3 Size Dependence of the Magnetic Hyperthermia Efficiency of Superparamagnetic Nanoparticles

Superparamagnetic NPs are governed by size dependent Néel and Brownian relaxation losses, which in turn directly affect the heat power dissipation process. To separate and understand the contributions of size dependent Néel and Brownian relaxation on the SAR, MNPs can be placed in solvents more viscous than water such as glycerol [21] or gel [22] to inhibit Brownian relaxation. Cobalt ferrite ($CoFe_2O_4$) NPs, for instance, placed in increasing amounts of glycerol showed a sharp change in SAR from 420 to 90 W g^{-1}.

Changing the size of MNPs dramatically alters its response to an applied AC field. That means, magnetization of MNPs decreases with decreasing particle size [23]. Owing to their small size, MNPs exhibit a reduced saturation magnetization due to surface and internal spin canting effects (spin canting or surface magnetic reconstruction is pertinent to different orientation of the surface spins with respect to the bulk ones) [20,21]. Spin canting gives rise to magnetically disordered spin glass-like layers on the surface of MNPs, which is not readily observed in bulk magnetic materials, causing decrease of magnetization [24,25]. Because the SAR value depends on magnetization and the relaxation time, for a given magnetic material, there is an optimum size to enhance hyperthermia effects by Vreeland et al. observed that under an AC excitation field of H = 36.5 kA m^{-1} and f = 341 kHz, the optimum size was around 22 nm, which matches the theoretical prediction of the LRT [12,26]. tuning these both parameters [23]. As an illustration, for superparamagnetic nanoparticles,

2.2.4 Effect of Shape Anisotropy on Magnetic Hyperthermia Efficiency

The heating efficiency of MNPs also depends on the magnetic anisotropy and so it can be enhanced by optimizing the shape anisotropy by developing MNPs with different morphologies. Along this line, MNPs with specific morphology such as nanoflowers have been reported to show higher SAR values compared to spherical MNPs [27]. The increase in the heating efficiency is attributed to the magneto-structural properties of the nanoflowers, which are composed of highly ordered smaller nanocrystals of few nanometers, that do not behave like isolated grains [27]. In addition, the nanoflowers exhibit lower anisotropy due to

coalescence and crystal ordering of the individual grains, while the spherical particles showed higher surface disorder and consequently, higher surface anisotropy.

Superparamagnetic nanoparticles with novel and more complex shapes and structures such as hexagonal nanoplates, brick-like nanostructures, as well as nanoclusters of Mn-Zn-ferrite nanoparticles have also demonstrated enhanced SAR [28,29]. These results show the importance of shape anisotropy in improving the magnetic hyperthermia performance of iron oxide-based nanoparticles.

2.2.5 Magnetic Dipolar Interactions: Effect of Nanochain and Nanocluster Formation on Magnetic Hyperthermia Efficiency

Dipolar interaction effects on heating efficiency in magnetic hyperthermia have been shown to be positive [30,31] or negative [32,33]. It has been demonstrated that the reduction or enhancement in the heating efficiency of MNPs is as a result of the formation of nano-assemblies during hyperthermia measurements. When MNPs exposed to an AC field, they can form linear aggregates of magnetically ordered structures such as chains (Figure 2.6) [34]. Several research groups have pointed out theoretically [35,36] and have shown experimentally [37,38] that chain-like structures can give rise to a strong increase in the heating efficiency of MNPs. [35,37]. This type of assembly leads to an enhancement of the effective anisotropy of the MNPs due to the unidirectional magnetization orientation as a result of the dipolar coupling along the chain [37].

Conversely, negative effects on heating efficiency have been reported upon formation of cluster of MNPs due to an increase in particle concentration [38]. Modification of particle concentration has been employed to vary the strength of dipole-dipole interactions, and the structure of the particle assembly [33,39]. Coral et al. also arrived at the same conclusion, wherein nanoclusters were shown to have lower heating efficiency with increasing cluster size and increasing number of particles in the cluster [33]. Moreover, the negative effects of nanoclustering to the heat dissipated during magnetic hyperthermia have been reported by other groups, which confirms an increase in the intensity of dipolar interactions resulted in a decrease in magnetic susceptibility and a reduction in the SAR value [32,39]. On the other hand, it has been reported in the literature that favorable increase in heating effects were observed with clusters in the form of nanoflowers compared to cluster formed by individual particles [27]. These nanoflowers, in fact, contain single grains that have the same crystal orientation, *i.e.* their anisotropy axes are all aligned, giving it a different magnetic

organization than clusters of individual particles where the anisotropy axes are randomly oriented [27,33,39].

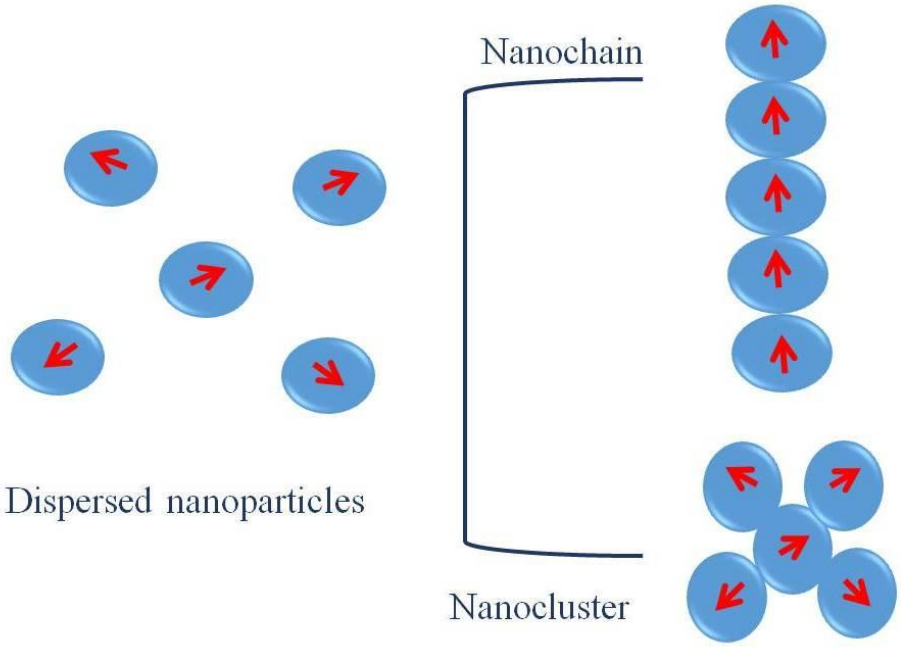

Figure 2.6 Schematic representation of the different nano-assemblies that could form during AC magnetic field excitation

To summarize, magnetic hyperthermia is a promising therapeutic approach, but in order to move this treatment modality to the clinical setting, a better understanding of the behavior of MNPs during hyperthermia measurements is required. As a first step, it is imperative to develop a standardized method of reporting hyperthermia efficiencies, and to establish clinically acceptable AC magnetic field excitation conditions. Another key aspect is the development of optimized and well characterized magnetic iron oxide-based nanoparticles by tuning size, composition, shape, and exchange anisotropy to improve their heating performance as hyperthermia agents. Combining all these parameters is the challenge in the development of MNPs with unprecedented heating efficiencies to enable effective cancer treatment *in vivo* applications.

2.3 Nanomedicine Approach for Cancer Treatments

Cancers are traditionally treated with surgery, radiation, and chemotherapy. Each of these approaches bears the risk of killing normal cells or fatally damaging healthy tissues. Hence, treatment options are limited, and accurate diagnosis and prognosis are difficult in many cases. In addition, although currently used *in vivo* cancer imaging techniques are

capable of identifying anatomical location of tumour and surrounding tissues, their sensitivity is not high enough for detecting abnormalities at the cellular (microscopic) level. This fact seriously limits our ability to perform early cancer diagnosis. Owing to the above-mentioned pharmaceutical, diagnostic, and therapeutic constraints, cancer still remains one of the most challenging problems in modern medicine.

Nanotechnology, an emerging interdisciplinary research field, has the great potential to offer solutions to current limitations in early detection and effective treatment of cancer. Currently, the development of a wide range of nanoscale materials such as biocompatible nanoparticles and nanorobots enable new scientific approaches in prevention, diagnosis, treatment, and monitoring diseases in clinical conditions. These technological innovations of nanotechnology within medicine are referred to as “nanomedicine”. In general, the major areas in which nanomedicine is being developed for treating cancer includes early detection, proteomics, multifunctional therapeutics (hyperthermia and drug delivery), or simultaneous therapeutic and diagnostic functions (theranostics).

2.4 Superparamagnetic Nanoparticles for Biomedical Application

As already mentioned in the previous sections, the properties of nano-sized materials due to their small size and their large surface-to-volume ratio can be strongly different from those of the corresponding bulk materials. In particular, nanoscale particles have attracted much attention as a consequence of their unusual electronic [40], optical [41] and magnetic [42] properties, which are particularly appealing for biomedical applications. Consequently, a broad range of nanocarriers with diverse sizes, architectures, and surface properties has been designed [43,44] including liposomes, polymer nanoparticles, micelles, dendrimers, and inorganic nanoparticles made of iron oxide, quantum dots, gold, or metal oxide frameworks. The dimensions of these systems (< 100 nm) make them ideal candidates for the production of functional nanostructures by nanoengineering of surfaces. The surface functionalization capability, indeed, allows their use in clinical trials for cancer diagnosis or treatment [45].

Iron oxide MNPs show interesting properties such as heat generation ability, high saturation field, extra anisotropy contributions, etc. [46]. Due to these unique properties, iron oxide MNPs have attracted widespread attention in nanomedicine especially for drug delivery. The optimization of iron oxide MNPs for this application continues today with the objectives (i) to reduce the amount of systemic distribution of cytotoxic drugs, thus limiting

the associated side effects, and (ii) to reduce the required dose by a more efficient localized targeting of the drug.

The application of iron oxide MNPs in biology, medical diagnosis (i.e. as magnetic resonance imaging contrast agents (MRI) [47,48], magnetic particle imaging tracers, cell labeling, magnetic separation, bacteria detection [49]), and therapy (e.g. drug and gene delivery [50], specific release of drug [51], hyperthermia [52]) requires iron oxide MNPs to be stable in water at neutral pH and physiological salinity. Such colloidal stability depends on the dimensions of the particles, which should be sufficiently small, so to avoid precipitation. Another important factor is the charge and surface chemistry, which allow stabilization through steric and coulombic repulsions. To control the surface properties of iron oxide MNPs, they can be coated with a biocompatible polymer during or after the synthesis process in order to prevent the formation of large aggregates, changes from the original structure, and biodegradation when exposed to the biological system. The coating acts to shield the magnetic particle from the surrounding environment and can also be functionalized with targeting agent by attaching carboxyl groups, biotin, avidin, carbodiimide, folic acid, and other molecules [53–55]. These molecules then act as attachment points for the coupling of therapeutic drugs, fluorophore for imaging, or target antibodies to the carrier complex (Figure 2.7).

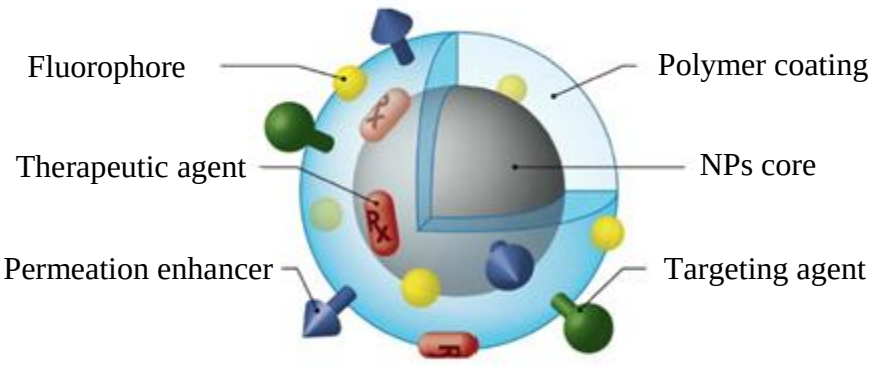

Figure 2.7 Nanoparticle possessing various ligands to enable multifunctionality from a single platform. [56]

The biocompatibility and toxicity of iron oxide MNPs are other important criteria to take into account for their *in vivo* applications. The most important parameters determining biocompatibility and toxicity of NPs contain (i) the nature of the magnetically responsive component (for instance, magnetite, iron, nickel, cobalt, neodimium–iron–boron or samarium–cobalt), and (ii) the final size of the particles including their core and the coatings (shell).

2.5 Magnetic Nanoparticle Stability

One of most promising applications of colloidal superparamagnetic nanoparticles is the use as carriers of drug for site-specific drug delivery to minimize side effect of chemotherapy. Ideally, they could bear on their surface a pharmaceutical drug that could be driven to the target organ and released there. For these applications, the size, surface charge, and colloidal stability of the magnetic nanoparticles are particularly important, and strongly affect both the blood circulation time as well as bioavailability of the particles within the body [57].

2.5.1 Colloidal Stability of Iron Oxide MNPs

The stabilization of MNPs in biological suspension is a critical issue to employ them as drug carriers. The stability of MNPs in suspension is controlled by three principal forces: (a) hydrophobicity–hydrophilicity, (b) magnetic and (c) Van der Waals forces. MNPs tend to aggregate to sub-micron size clusters in suspension due to the magnetic interactions between the nanometric size particles. Moreover, they can also aggregate because of the attractive Van der Waals forces in order to minimize the total surface or interfacial energy. Such aggregation can hamper the efficacy of MNPs in drug delivery (less drug loading) as a result of their low surface area and larger sizes, so surface modification approaches of MNPs can prevent aggregation and can be carried out either during their synthesis or in a post-synthesis process. The ideal molecules used for stabilization of MNPs should be biocompatible and biodegradable polymers or surfactants [58]. As an illustration, one of the most important and widely employed functionalities for the modification of MNPs surfaces is the carboxylic acid group, which can interact with the surface of nanoparticles by coordination processes [59-63]. Phosphonic acid and dopamine also improve MNPs stability over a large range of pH and temperature [64]. In addition, biocompatible polymer such as cysteine-terminated polyethylene glycol (PEG) anchors to the surface of MNPs to provide highly stable ferrofluid for biological applications [65].

2.5.2 Shape, Size, and Size Distribution

The main advantage of using particles of sizes smaller than 100 nm is their higher effective surface areas (larger number of attached ligands), lower sedimentation rates (i.e. high stability in suspension), and improved tissular diffusion. Indeed, particles should be small enough (~100 nm) to escape from the reticuloendothelial system (RES), to remain in

the blood circulation after injection, and to be capable of passing through the capillary systems of organs and tissues avoiding vessel embolism. When the drug-loaded MNPs are injected systemically into the bloodstream, the size, morphology, and surface charge are the three important parameters, which determine their behavior. As a case in point, tissue macrophages (i.e. Kupffer cells in the liver) are highly sensitive to invading micro-organism and MNPs with diameter of 200 nm [66]. The plasma proteins (opsonins) can easily adsorb on the surface of invading MNPs, depending on their sizes and surface charge. Hence, particles with sizes above 200 nm are not suitable due to their uptake by the RES, whereas the NPs between 10 and 100 nm are most effective for drug delivery purposes because they can evade the RES [67].

2.6 Nanoparticle Delivery to the Tumour Site

Magnetic nanoparticles (MNPs) loaded drug must be delivered specifically to the cancer site and should be retained in the tumour in order to reach a sufficient concentration for effective hyperthermia cancer therapy as well as controlled drug release. Three main approaches for the delivery of nanoparticles can be distinguished: direct injection, systematic passive, and active delivery. The direct injection method consists of injecting directly the magnetic fluid into the tumour. In fact, the intratumoural injection is the simplest way to administer the MNPs, and is the most widely used method for *in vivo* studies [68,69]. This technique, moreover, has even already been applied in clinical trials [70,71].

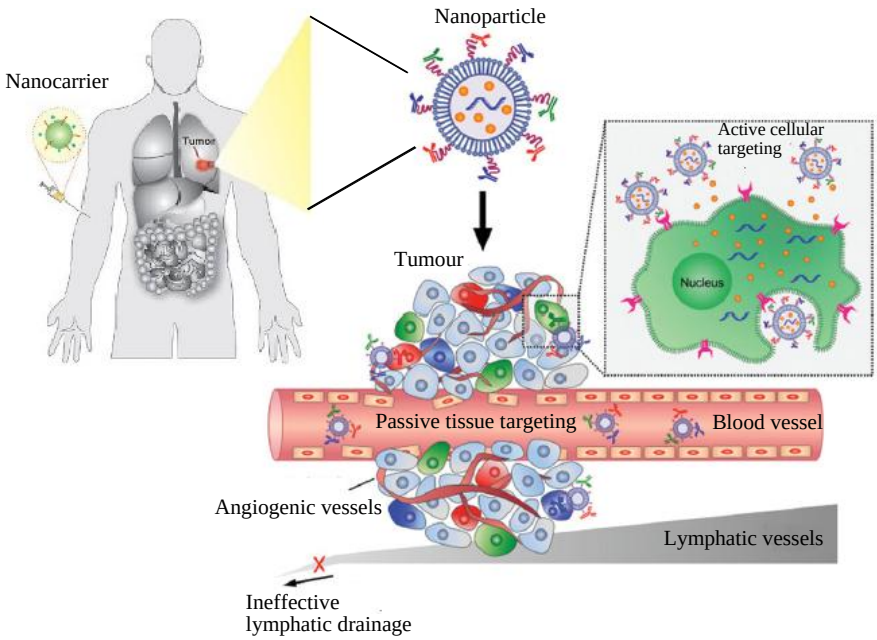

Figure 2.8 Scheme representing active and passive targeting of NPs. Reprinted from Ref [72]

The main advantage of this technique is the ease of achieving a high and localized concentration of MNPs in the tumour. However, direct injection results in a non-homogeneous MNP distribution in the tumour, which makes the complete regression of the tumour more difficult [73].

Passive delivery is achieved by injecting MNPs intravenously. The MNPs will accumulate preferentially in tumour tissue due to the enhanced permeability and retention (EPR) effect [74-76]. The EPR effect rests on the fact that solid tumours exhibit a defective vascular architecture and the lymphatic clearance from the interstitium of tumour tissue is impaired. The former that results in an enhanced vascular permeability, facilitating nutrient and oxygen supply to satisfy the demand of growing tumours, while the latter, resulting in the retention of macromolecules in the tumour. The EPR effect originates from the fact that solid tumours possess a leaky vasculature compared to normal tissues, which facilitates the extravasation of nanoparticles (Figure 2.8). To take advantage of the EPR effect, the nanoparicles should be able to circulate long enough in the blood stream.

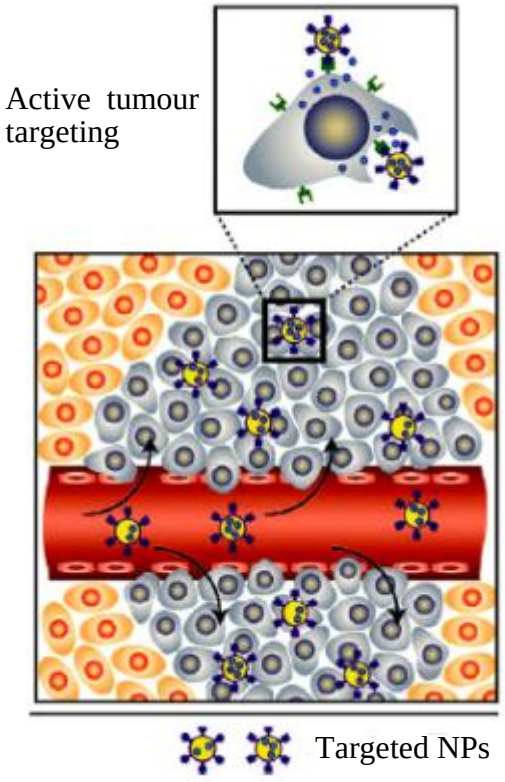

Figure 2.9 Once nanoparticles have extravasated in the target tissue, the presence of targeting ligands (e.g. proteins) on the nanoparticle surface can result in active targeting of nanoparticles to receptors that are present on target cell or tissue resulting in enhanced accumulation and cell uptake through receptor-mediated endocytosis [77]

However, the principal disadvantage of this method is the difficulty to reach high enough concentration of nanoparticles for effective treatment because the amount of nanoparticles injected cannot be further increased in order to avoid non-negligible MNPs toxicity. In order to achieve higher deposition and improve tumour uptake of the nanoparticles, they can be driven magnetically inside the body *via* an external magnetic field and/ or can be functionalized with a targeting ligand for active delivery. Active delivery consists of improving the specificity of the nanoparticles by functionalizing their surface with a targeting moiety that binds to cell receptors. It usually results in a higher nanoparticle accumulation and cellular uptake in the targeted cancer cells (Figure 2.9). Among the most commonly used targeting agents, we can find antibodies [78,79], antibody fragments [80,81], receptor ligands [82,83], peptides [84,85], and aptamers [86,87]. The superiority of targeted MNPs in cancer treatments has already been proven many times [88].

2.7 Magnetic Hyperthermia

During the 19th century, it was observed that high fever can cause tumour regression [84], and scientific study was performed on hyperthermia to treat cervical cancer. The use of hyperthermia as a treatment for cancer was considered more seriously in the 1970s, and controlled clinical trials on induced hyperthermia began to be conducted. It was then discovered that cancer cells have greater sensitivity to hyperthermia as compared to normal cells. Indeed, healthy tissues are able to withstand temperatures of 42 ^{o}C–45 ^{o}C, in contrast to cancer cells, which undergo apoptosis at those temperatures [89,90].

Recently new technology has been developed to provide local hyperthermia using superparamagnetic nanoparticles as heating source, which is called Magnetic Fluid Hyperthermia (MFH). Upon excitation with an AC field, these unique materials can transform part of electromagnetic energy into heat, and the heat generated can raise the temperature up to 45 ^{o}C–48 ^{o}C, which is mortal for cancer cells and pathogenic microbes. This treatment is currently adopted in conjunction with chemotherapy or radiotherapy, as it also renders the cells more sensitive [91]. A high heating potential is crucial for the clinical use of MFH since it would require a smaller amount of MNPs to be administered into the body patient as well as to treat smaller tumours, which are not surgically addressable. The latter, indeed, have a larger dissipation capability and thus require larger amount of heat to be destroyed. Therefore, engineering MNPs (control their physical and chemical properties using proper synthesis approach) to obtain an exceptional SAR value is highly desirable [92].

2.8 Magnetic Nanosystems for Thermo-Chemotherapy

The potential of MFH as a treatment for cancer is clear, but can even be improved by designing MNPs with multiple therapeutic functions, i.e. hyperthermia and drug delivery. The major drawback of chemotherapy is the non-specificity of the drugs, which may strongly damage healthy organs and cells during the treatment. With MNPs, the possibility of targeting to the specific locations in the body allows the lower dosage of chemotherapeutic drug to be administered into the patient to reach to the needed concentrations in the tumour area for an effective therapy. In addition, the concentration of drugs at non-targeted sites is reduced, therefore, minimizing undesirable side effects of chemotherapy[93]. Besides, the synergistic effect of the combined thermo-chemotherapy can strongly enhance the effect of chemotherapy for the same amount of drug available. The enhancement of chemotherapy effects with application of concurrent hyperthermia is called thermo-chemosensitisation. Several mechanisms are involved in this thermal enhancement such as increased antineoplastic drug accumulation in tumours and enhanced drug cytotoxicity (improved intracellular uptake of drugs and increased sensitivity of cells to drugs) [94,95]. The first one is due to the physiological effect of mild hyperthermia on tumour vasculature, including an increased blood flow, perfusion, and blood vessel pore size of the already leaky tumour vasculature. All these factors facilitate drug extravasation in tumour tissues. The mechanisms responsible for the enhanced drug cytotoxicity are not yet fully understood, but several studies have demonstrated that the thermal enhancement of the cytotoxic activity of many anti-cancer agents is maximized at mild hyperthermia temperatures (40.5 ^{o}C–43 ^{o}C) [96]. Increased drug cytotoxicity generally involves improved intracellular uptake of drugs as a result of increased cell membrane permeability, inhibition of DNA repair of the chemically induced lethal or sublethal damage, and acceleration of the cytotoxic chemical reaction in the case of alkylating or platinum-based antineoplastic agents at elevated temperatures [97]. Figure 2.10 summarizes the mechanisms behind the synergistic effect of hyperthermia and chemotherapy.

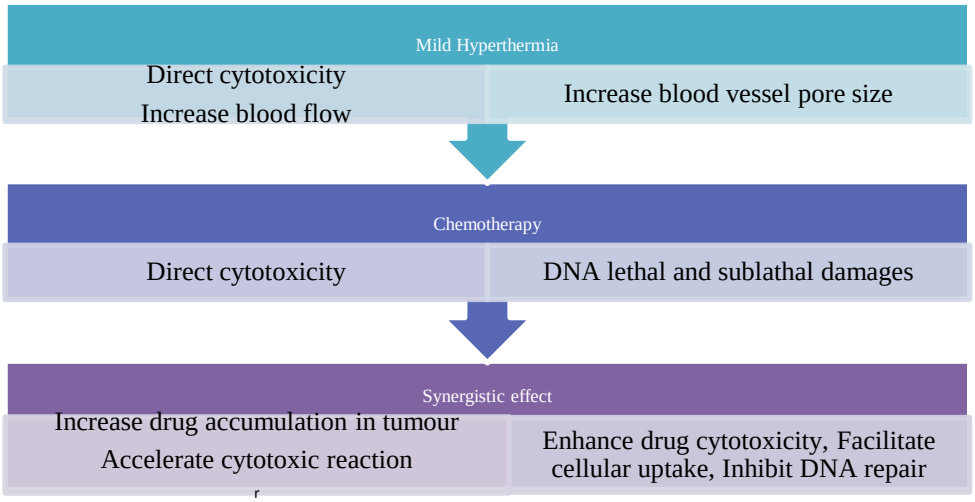

Figure 2.10 Mechanisms responsible for the synergistic effect of the combined thermo-chemotherapy

2.9 Controlled Drug Delivery System

It is known that the drug concentration levels in the blood plasma depend on the quantity of drug released from the carrier. The delivery and release of a drug at target area, in fact, are often problematic since the concentration of the released drug at the target cell is either too low or too high, and is not delivered for the desirable amount of time. In the view of the fact that desirable drug release (that is often characteristic of a zero-order kinetic rate) is not easily achievable, controlled drug release technique has been proposed to solve this problem. The main advantages of the use of controlled drug delivery systems include: (1) sustained constant concentration of therapeutically active compounds in the blood with minimum fluctuations; (2) predictable and reproducible release rates over a long period of time; (3) protection of bioactive compounds having a very short half-life; (4) elimination of side-effects, waste of drug and frequent dosing; (5) optimized therapy in addition to better patient compliance; and (6) solution of the drug stability problem [98]. Hence, smart polymers, responding to external stimuli, represent a very attractive choice of polymer coating for drug delivery to achieve a controlled release of the drug. Using polymers for controlled drug delivery requires complete control over the architecture of the polymer microstructure, especially when synthesizing materials such as multi-stimuli responsive polymers [99].

Temperature-responsive soft materials used in conjunction with localized heating (e.g., *via* hyperthermia) are, therefore, prime candidates for biomedical applications to remotely trigger the release of the drug [100]; in fact, at physiological temperature the drug is

retained in the polymeric matrix, and when the surrounding temperature rises above the LCST, which is the temperature at which polymers undergo a reversible conformational change from a swollen hydrophilic state to a shrunken hydrophobic one, triggers the release of the drug in a temporal control manner. Other stimuli such as pH, glucose, stress or strain, and electromagnetic fields can be combined with thermal stimulus to create a multi-stimuli-responsive system. [101].

2.9.1 pH Responsive Polymer

Different parts of the human body have different pH levels. The saliva and blood are neutral, but the gastric juices inside the stomach are acidic [102, 103]. Specifically, tumours have an acidic environment at around 5.5-6.75, which is below the pH (7.4) of normal tissues [104–107]. When being internalized into the cells, NPs will encounter more acidic endosomes and lysosomes (pH 5.0–5.5) as listed in table 2.1.

Tissue/Cell compartment	pH
Blood	7.4-7.5
Stomach	1.0-3.0
Duodenum	4.8-8.2
Colon	7.0-7.5
Lysosome	4.5-5.0
Golgi complex	6.4
Tumour-Extracellular medium	6.2-7.2

Table 2.1 pH values from several tissues and cell compartments [108]

Based on these pH variations, researchers have developed various pH-responsive nanohybrids, which are constituted by metal nanoparticles core and pH-responsive polymer shell [109–117] to deliver drugs, genes, and proteins to enhance the curative effect in tumour sites and specific organs [118–122]. pH-responsive polymers share the common feature of being polyelectrolytes, which include in their structures weak acidic or basic groups that either accept or release protons in response to a change in the environmental pH. Such an ionic/non-ionic transition, or hydrophobic/hydrophilic characteristic changes of polymeric surfaces, or swelling/deswelling behavior of nanogel (crosslinked polymeric network) allow

to tune their nature (hydrophilicity, self-assembly polyelectrolyte nature), in the aqueous phase (Figure 2.11).

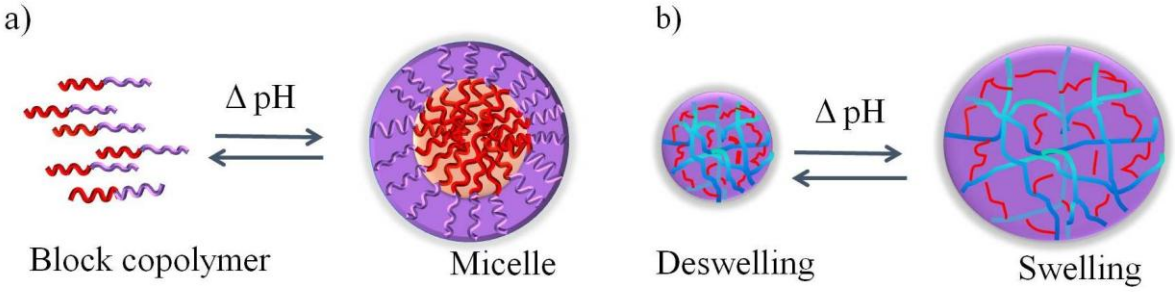

Figure 2.11 pH-responsive polymers with different architectures: (a) unimer–micelle, (b) nanogels or microgels [123]

Two main strategies exist to pH-trigger cargo release: a) the use of polymers (polyacids or polybases) with ionizable groups that undergo conformational and/or solubility changes in response to environmental pH variation (Figure 2.12); as an example, polyhistidine-based micelles could respond to acidic tumour microenvironments by efficient exposure of the transactivating regulatory protein (TAT) sequence (Figure 2.12) [124], which is essential for micelle translocation into the cells. The micelle surface hides TAT during circulation, but exposes it at the slightly acidic tumour extracellular pH, facilitating the internalization process.

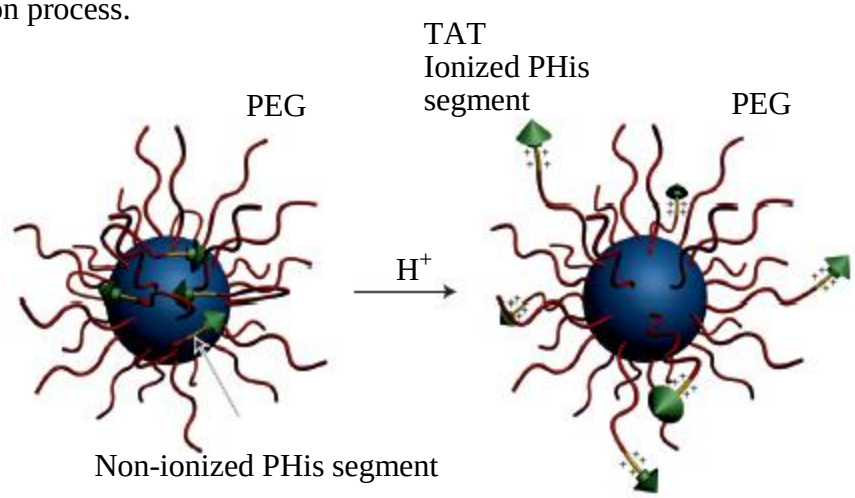

Figure 2.12 pH-sensitive nanocarriers for efficient TAT-peptide exposure. Polyhistidine (PHis)-based micelles responding to acidic tumour microenvironments by an efficient TAT-sequence exposure following ionization of the polyhistidine segments [124]

b) The design of polymeric systems with acid-sensitive bonds, whose cleavage, enables the release of molecules anchored at the polymer backbone, the modification of the charge of the polymer, or the exposure of targeting ligands (Figure 2.13). For instance, TAT-peptide

decorated liposomes comprising an acidic hydrolyzable polyethylene glycol (PEG) shell, allowing improved exposure of the TAT sequence at low pH to enhance cellular uptake of the TATp-containing immunoliposomes as shown in Figure 2.13 [125]. For this purpose, a degradable pH-sensitive hydrazone bond between a long shielding PEG chains was introduced by modifying the structure of PEG. At normal pH, surface TATp moieties are "hidden" by the long PEG chains, while upon the exposure to lowered pH, this multifunctional carrier exposes TATp moieties due to the degradation of the hydrazone bond and removal of the long PEG chains.

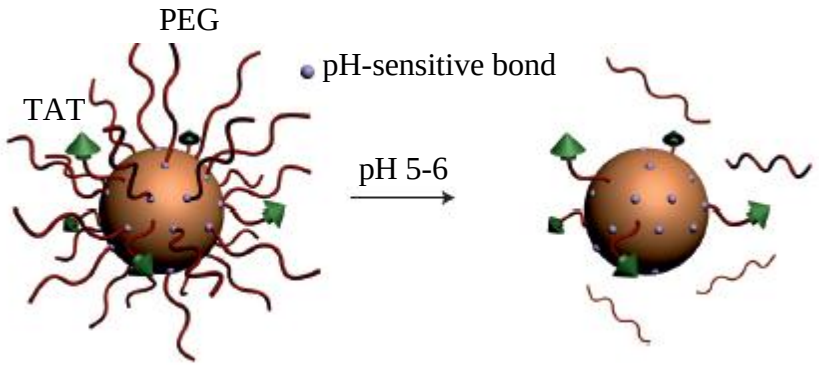

2.13 pH-sensitive nanocarriers for efficient TAT-peptide exposure. TAT-peptide-decorated liposomes comprising a hydrolyzable PEG shell allowing improved exposure of the TAT sequence at low pH [125]

Among pH-responsive polyacids, poly acrylic acid (PAA) has attracted widespread attention [126] as a result of its unique properties. Acrylic acid can be easily polymerized *via* various polymerization techniques and is inexpensive. Importantly, one of the most widely employed functional groups for anchoring ligand to the MNPs surfaces is the carboxylic acid units. PAA surface grafted-MNPs is a favorable candidate to be utilized as a smart nanocomposite for intracellular pH-triggered drug release [127].

2.9.2 Temperature Responsive Polymer

Thermoresponsive polymers exhibit a temperature-dependent phase transition in solution across a critical temperature, which is known as the critical solution temperature (CST). The polymers, which are water soluble below a certain temperature and turn to be phase separated above that temperature, are defined to have a lower critical solution temperature (LCST), whereas the polymers exhibiting the opposite behavior are defined to have an upper critical solution temperature (UCST) (Figure 2.14) [128]. Therefore, a polymer

solution below the LCST is clear and homogeneous solution, while above the LCST appears cloudy as exhibited in Figure 2.15 for this reason, LCST is also referred to as cloud point.

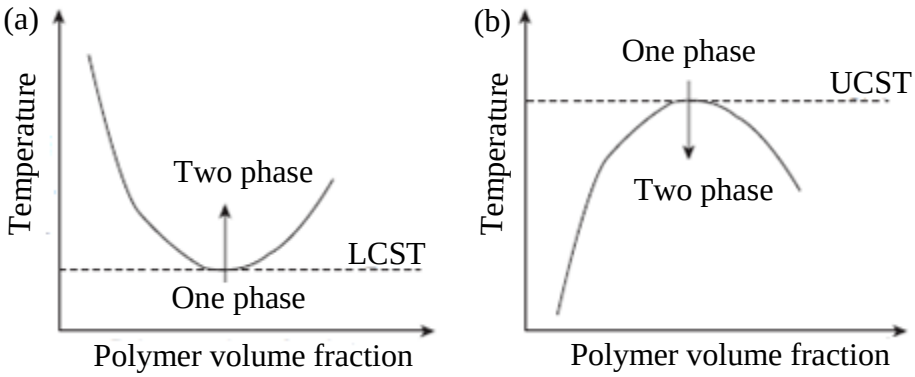

Figure 2.14 Scheme showing phase transition phenomenon. (a) Lower critical solution temperature (LCST) and (b) upper critical solution temperature (UCST) phase transition behaviors of thermo-responsive polymers in solution [129]

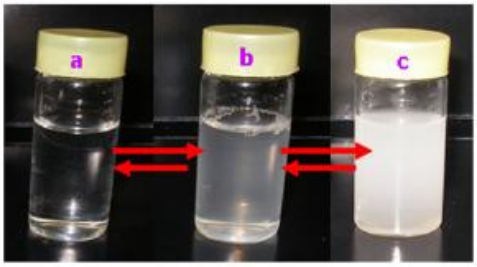

Figure 2.15 LCST transitions (cloud point) of poly (N-vinylcaprolactam) solution at different temperatures: (a) at 25°C, (b) 38 °C and (c) 42 °C

This conformational transition can be described by taking into account the thermodynamics of polymer in solution. For a process to be favored, it is required that the Gibbs free energy (ΔG) ((ΔG) = ΔH−T·ΔS) is negative. Dissolution of polymer in solvent involves a variety of interactions between the polymer and solvent. For polymers showing LCST behavior, Gibbs free energy for the dissolution in water is negative at room temperature, thus they dissolve in water. The water molecules from the solvent form a thin layer surrounding the hydrophilic part of the polymer, and this hydration process gives negative enthalpic contribution to the dissolution process. However, there is formation of a structured arrangement of water molecules around the hydrophobic part of the polymer, where there is formation of extensive hydrogen bonding among the surrounding water molecules, which provides negative value to entropy (ΔS) of the reaction [130]. When

temperature of the aqueous polymer system is increased, entropy (ΔS) of the system increases; indeed, hydrogen bonds break, leading to collapse of the hydration shell formed by the water molecules. The entropic term becomes greater than the enthalpic one, providing positive value of ΔG of the dissolution process. Breakage of hydrogen bonds and loss of hydration shell lead to increased hydrophobic interactions between hydrophobic parts of the same or different polymer molecules [131]. This leads to chain collapse and intermolecular aggregation (Figure 2.16) [132], and thereby separation into two phases, which ultimately leads to suppression in conformation changes of polymer chains [133-136]. Polymers that show UCST behavior, exhibit opposite property.

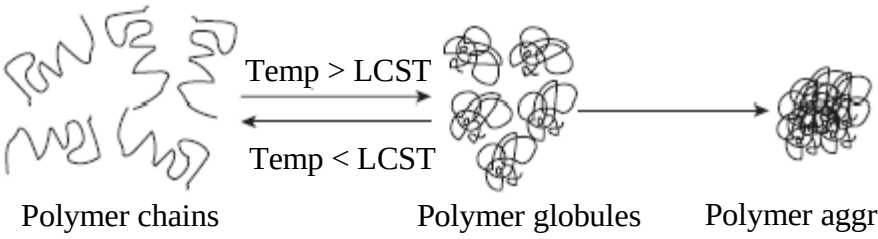

Figure 2.16 Temperature-induced phase transitions in thermo-responsive polymer chains. Extended chains-to-globules-to-aggregate transition is shown [137]

2.9.3 Thermoresponsive Polymers Based on Poly N-vinylcaprolactam

Poly N-vinylcaprolactam (PVCL) is a non-ionic polymer and exhibits LCST behavior in water between 31 ^{o}C-50 ^{o}C [138]. The growing interest in PVCL-based copolymers is driven by its thermoresponsive essence, the hydrophilic/hydrophobic transition temperatures close to the body temperature, as well as its complexation capability [139]. Additionally, PVCL is stable against hydrolysis and is highly biocompatible [140,141], so all these strengths make it an interesting candidate for biomedical applications. In addition, PVCL is a typical polyvinylamide, bearing both hydrophilic amide groups and hydrophobic carbon–carbon backbones. In fact, PVCL has been shown to support high cell viability and low cytotoxicity especially in the hydrophobic state above the LCST [142]. Importantly, the nitrogen atom in the caprolactam ring is directly connected to the chain backbone, so the hydrolysis of PVCL, if it occurs, will not produce a small toxic amide compound [143,144]. Some basic physicochemical properties of N-vinylcaprolactam (NVCL) monomer and PVCL polymer as displayed in Figure 2.17 are listed in table 2.2.

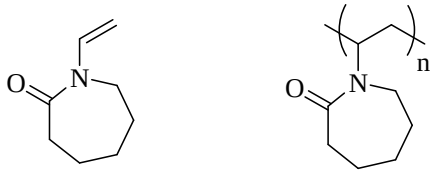

N-vinylcaprolactam Poly (N-vinylcaprolactam)

Figure 2.17 Structure of N-vinylcaprolactam and poly (N-vinylcaprolactam)

Like NVCL monomer, PVCL also shows a good solubility in many organic solvents such as aromatic hydrocarbons, alcohols, ketones, dioxane, chlorinated aromatic, and aliphatic hydrocarbons, etc. The solubility decreases with the increase of molar mass of PVCL. On the other side, PVCL could also dissolve in water at 14 ^{o}C–20 ^{o}C, and high concentrations, e.g., 40 wt %, can be achieved. The lack of popularity among researchers for PVCL compared to other thermoresponsive polymers can be ascribed to the difficulty of polymerizing NVCL in a controlled fashion. The polymerization kinetics of these monomers is very different, and the controlled copolymerization of NVCL with other monomers is more difficult to achieve.

NVCL	NVCL	PVCL	PVCL
T_b (°C)	128 in 22 mm Hg	T g (^{o}C)	147 (dry polymer)-17-38 (aqueous solution)
T_m (°C)	32-36	LCST (^{o}C)	30-45
D (g mL^{-1})	1.029	Tc or Tm (^{o}C)	None
T_f (°C)	101	Good solvents	Aromatic/aliphatic hydrocarbons/ alcohols, dioxane
Solubility (g mL^{-1})	5.0 (aqueous)	Solubility	Depending on molar mass

Table 2.2 Physic-chemical parameters of NVCL monomer and PVCL polymer

T_b : boiling temperature; T_m : melting temperature; d : density; T_f : flash point; T_g : glass transition temperature

Up to now, PVCL-containing materials such as micelles, nanogels, microgels, and core/corona hybrids, which have been explored for cell immobilization, [145] tissue engineering, [146] anticancer drug delivery [147,148], and protein separation, [149] to be cited a few. More specifically, multifunctional PVCL-based micelles, hydrogels, and nanohybrids are now developed and investigated for biomedical applications, notably for drug delivery system as demonstrated in Figure 2.18.

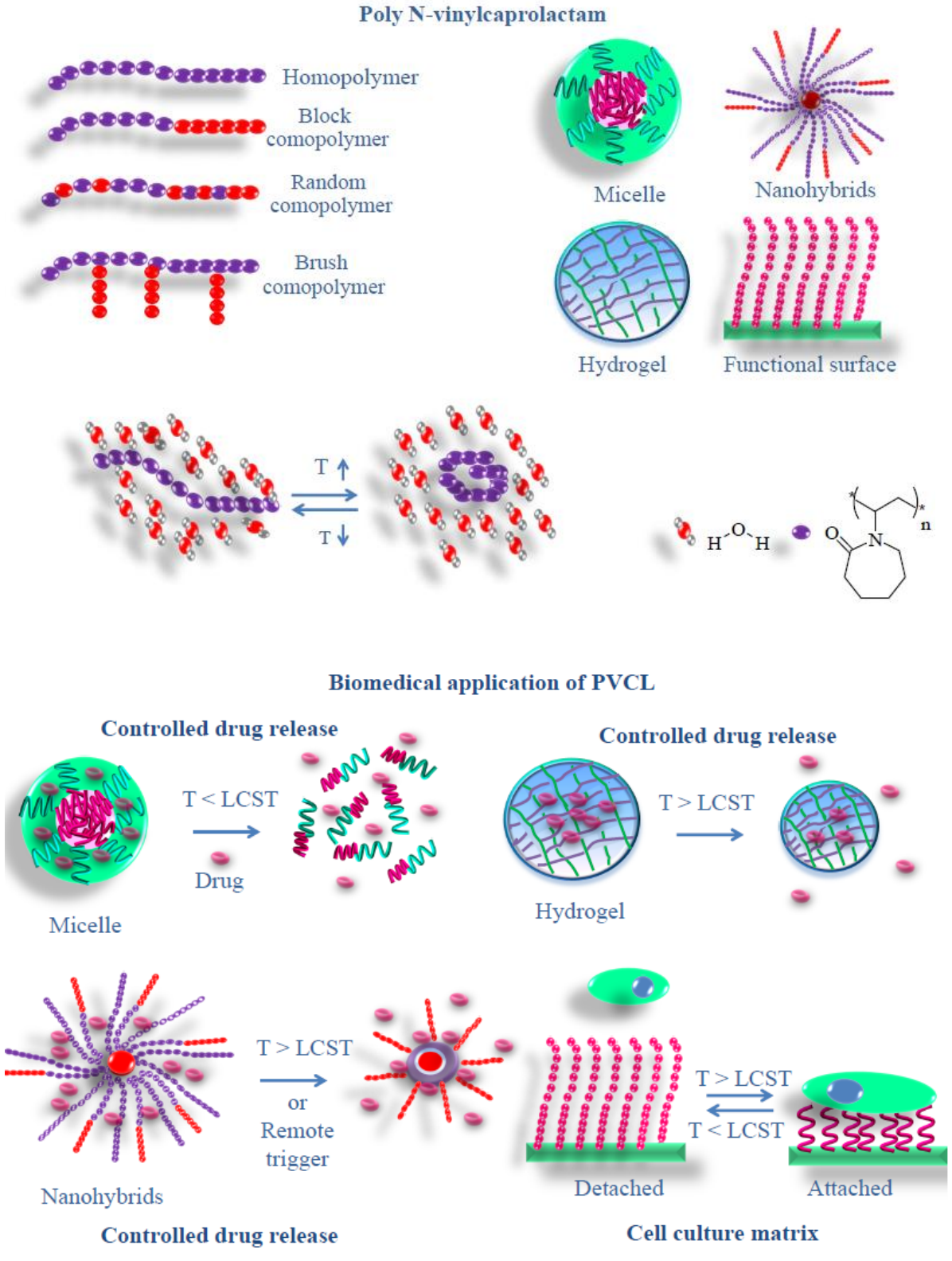

Figure 2.18 Thermo-induced global-coil transition of poly (N-vinylcaprolactam) (PVCL), well-defined PVCL-based homopolymer, block copolymer, random copolymer, and brush copolymer *via* controlled radical polymerization, as well as their corresponding topological self-assembly structures, like micelles, hydrogels, organic/inorganic nanohybrids, functional surface *via* surface-initiated polymerization; and potential biomedical applications such as controlled drug release and cell culture matrix

2.10 Multistimuli-Responsive Drug Delivery

Sensitivity to more than one stimulus can further improve drug delivery efficiency [150]. One of the biggest advantages of an ideal stimuli-responsive drug delivery system is the precise control of drug release in response to exogenous or endogenous stimuli such as temperature and pH [151]. In the past year, polymers with unique sensitivity are mostly used for the construction of dual pH and temperature-responsive drug delivery nanocarriers. In general, to obtain a temperature and pH sensitive polymer, it is only necessary to integrate temperature sensitive monomers (as an example, N-vinylcaprolactam) with pH sensitive monomers (for example, acrylic acid) [152-154]. Combination of pH and temperature sensitivity in polymeric backbone, indeed, offers a way to control the polymer phase behavior [155]. That is to say, the presence of pH-responsive segments modifies the hydrophilicity/hydrophobicity balance in polymeric structure, leading to LCST changes at desired temperature range. For instance, the LCST of copolymers increases over physiological temperature by increasing acrylic acid comonomer contents at all pH ranges due to its high hydrophilicity [156].

Recently, integration of iron oxide superparamagnetic nanoparticles (Fe_3O_4) and smart cross-linked polymers such as poly (N-vinylcaprolactam-*b*-acrylic acid) nanogel into a composite/hybrid core-shell system resulted in a smart platform, responding to both temperature and pH [157]. This double pH- and thermo-responsive magnetic nanocarrier is suitable for multi-modal cancer therapy, by combining magnetic hyperthermia and controlled drug delivery. Indeed, by tuning the LCST of polymeric shell in the hyperthermia range (41 ^{o}C-48 ^{o}C), the drug will be retained by nanocarrier at physiological temperature, and remotely released under magnetic hyperthermia performance and tumour acidic pH [158].

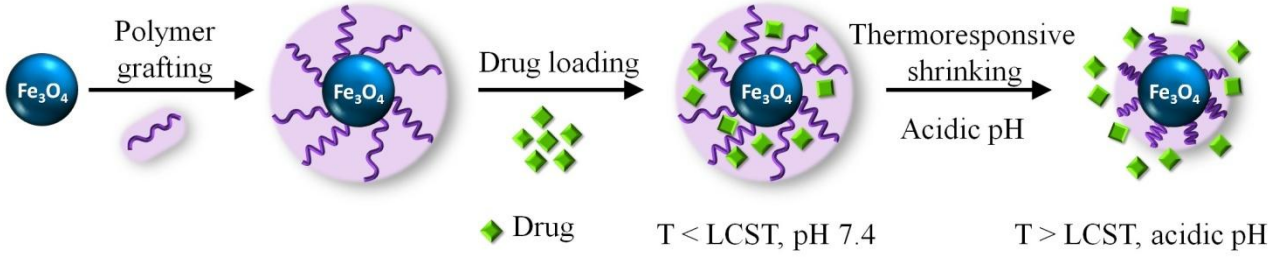

Figure 2.19 Smart magnetic nanocomposites-loaded drug provides advanced features for dual pH and thermo-responsive behavior, which offers spatial and temporal control over the release of drug

The objective of this thesis moves in this complex scenario and is schematized in Figure 2.19. In fact, our work reports fabrication and characterization of a smart nanocomposite composed of a superparamagnetic core and dual pH-temperature sensitive shell containing an anticancer drug (doxorubicin) for multimodality cancer therapy corresponding to this mechanism: (i) the magnetic core produces heat in response to harmless AC magnetic field enhancing temperature up to 45 ^{o}C (above LCST of polymer), (ii) heat generated is simultaneously conducted from core to the thermoresponsive polymer shell, which shrinks and triggers the fast release of the drug. The increase of the temperature up to 45 ^{o}C, and the pH decreasing from 6 to 4 (due to the acidic pH of cancer cell) boost the release of drug with controlled rate and concentration [159].

Chapter2

References

1. M. Mahmoudi.; B. Wang.; S. Laurent.; T. Sen. *Adv. Drug Deliv. Rev.* **2011**, *63*, 24.
2. S. Martel. *J Nanopart Res*. **2015**, *17*, 75.
3. R. Skomski.; J. M. D. Coey. Permanent Magnetism, Institute of Physics Publishing, Bristol and Philadelphia, **1999**.
4. E. C. Stoner.; E. P. Wohlfarth. *Phil Trans R Soc A*. **1948**, *240*, 599.
5. K. M. Krishnan. *IEEE Trans Magn*. **2010**, *46*, 2523.
6. L. Kafrouni.; O. Savadogo. *Prog Biomater*. **2016**, *5*, 147.
7. M. Knobel.; W. C. Nunes.; L. M Socolovsky.; E. Biasi.; J. M. Vargas.; J. C. J. Denardin. *Nanosci. Nanotech.* **2008**, *8*, 2836.
8. M. F. Hansen.; S. Morup. *J. Magn. Magn. Mater*. **1999**, *203*, 214.
9. A. G. Kolhatkar.; A. C. Jamison.; D. Litvinov.; R. C. Willson.; T. R. Lee. *Int. J. Mol. Sci*. **2013**, *14*, 15977.
10. V. V. Mody.; A. Singh.; B. Wesley. *Eur J Nanomed*. **2013**, *5*, 11.
11. a) J. W. M. Bulte.; T. Douglas.; B. Witwer.; S. C. Zhang.; E. Strable.; B. K. Lewis.; H. Zywicke.; B. Miller.; P. Van Gelderen.; B. M. Moskowitz.; I. D. Duncan.; J. A. Frank,. *Nat. Biotechnol.* **2001**, *19*, 1141, b) E. H. Dunlop.; W. A. Feiler.; M. J. Mattione.; *Biotechnol. Adv.* **1984**, *2*, 63.
12. R. E. Rosensweig. *J. Magn. Magn. Mater*. **2002**, *252*, 370.
13. J. P. Fortin.; F. Gazeau.; C. Wilhelm. *Eur. Biophys. J*. **2008**, *37*, 223.
14. M. Suto.; Y. Hirota.; H. Mamiya.; A. Fujita.; R. Kasuya.; K. Tohji.; B. Jeyadevan. *J. Magn. Magn. Mater*. **2009**, *321*, 1493.
15. R. Kotitz.; W. Weitschies.; L. Trahms.; W. Semmler. *J. Magn. Magn. Mater*. **1999**, *201*, 102.
16. R. Kotitz.; P. C. Fannin.; L. Trahms. *J. Magn. Magn. Mater*. **1995**, *149*, 42.
17. M. Levy.; C. Wilhelm.; J. M. Siaugue.; O. Horner.; J. C. Bacri.; F. Gazeau. *J. Phys.: Condens. Matter*. **2008**, *20*, 204133.
18. a) R. Hergt.; S. Dutz.; R. M¨uller.; M. Zeisberger. J. *Phys.:Condens. Matter*. **2006**, *18*, S2919, b) A. Hervaultab.; N. T. K. Thanh. *Nanoscale*. **2014**, *6*, 11553.
19. R. Hergt.; S. Dutz. *J. Magn. Magn. Mater*. **2007**, *311*, 187.

20. D. Yoo.; J.H. Lee.; T.H. Shin.; J. Cheo. *Acc. Chem. Res*. **2011**, *44*, 863.
21. J. P. Fortin.; C. Wilhelm.; J. Servais.; C. Ménager.; J.C. Bacri.; F. Gazeau. *J. Am. Chem. Soc*. **2007**, *129*, 2628.
22. M. Avolio.; A. Guerrini.; F. Brero.; C. Innocenti.; C. Sangregorio.; A. Lascialfari. *J. Magn. Magn. Mater.* DOI: /10.1016/j.jmmm.2018.09.111.
23. Y. W. Jun.; Y. M. Huh.; J. S. Choi.; J. H. Lee.; H. T. Song.; S. Kim.; S. Yoon.; K. S. Kim.; J. S. Shin.; J. S. Suh.; J. Cheon. *J. Am. Chem. Soc*. **2005**, *127*, 5732.
24. M. P. Morales.; C. J. Serna.; F. Bødker.; S. Mørup. *J. Phys. Condens. Matter*.**1999**, *9* 5461.
25. M. P. Morales.; S. Veintemillas-Verdaguer.; M.I. Montero.; C.J. Serna.; A. Roig.; L. Casas.; B. Martínez.; F. Sandiumenge. *Chem. Mater*. **1999**, *11*, 3058.
26. E. C. Vreeland.; J. Watt.; G. B. Schober.; B. G. Hance.; M. J. Austin.; A. D. Price.; B. D. Fellows.; T. C. Monson.; N. S. Hudak.; L. Maldonado-Camargo.; A. C. Bohorquez.; C. Rinaldi.; D. L. Huber. *Chem. Mater*. **2015**, *27*, 6059.
27. P. Hugounenq.; M. Levy.; D. Alloyeau.; L. Lartigue.; R. Bazzi. *J. Phys. Chem. C*. **2012**, *116*, 15702.
28. M. Ikenberry.; K. L. Hohn.; V. Chikan.; D. L. Troyer.; S. H. Bossmann. *J. Mater. Chem. B*. **2015**, *3*, 4647.
29. M. Worden.; M. A. Bruckman.; M. H. Kim.; N. F. Steinmetz.; T. Hegmann. *J. Mater. Chem. B*. **2015**, *3*, 6877.
30. E. Alphandéry.; I. Chebbi.; F. Guyot.; M. Durand-Dubief. *Int. J. Hyperth*. **2013**, *29*, 801.
31. P. de la Presa.; Y. Luengo.; V. Velasco.; M. P. Morales.; A. Hernando. *J. Phys. Chem. C*. **2015**, *119*,11022.
32. M. E. Materia.; P. Guardia.; A. Sathya.; M. Pernia Leal.; T. Pellegrino. *Langmuir*. **2015**, *31*, 808.
33. D. F. Coral.; P.M. Zélis.; M. Marciello.; M. Del Puerto.; A. Craievich.; M. B. F. Van Raap. *Langmuir*. **2016**, *32*, 1201.
34. S. L. Saville.; B. Qi.; J. Baker.; R. Stone.; O. Thompson Mefford. *J. Colloid Interface Sci*. **2014**, *424*, 141.
35. B. Mehdaoui.; R. P. Tan.; A. Meffre.; J. Carrey.; S. Lachaize.; M. Respaud. *Phys. Rev. B Condens. Matter Mater. Phys*. **2013**, *87*, 1.
36. R. Fu.;Y. Y. Yan.; C. Roberts. *AIP Adv*. **2015**, *5*, 127232.

37. D. Serantes.; K. Simeonidis.; M. Angelakeris.; O. Chubykalo-Fesenko.; C. Martinez-Boubeta. *J. Phys. Chem. C*. **2014**, *118*, 5927.
38. C. Martinez-Boubeta.; K. Simeonidis.; A. Makridis.; M. Angelakeris.; D. Serantes.; D. Baldomir. *Sci. Rep*. **2013**, *3*, 1652.
39. J. G. Ovejero.; D. Cabrera.; J. Carrey.; G. Salas.; F. J. Teran. *Phys. Chem. Chem. Phys*. **2016**, *18*, 10954.
40. P. Poizot.; S. Laruelle.; S. Grugeon.; L. Dupont.; J. M. Tarascon. *Nature.* **2000**, *407*, 496.
41. A. Tari.; R. W. Chantrell.; S.W. Charles.; J. Popplewell. *Physica B & C*. **1979**, *97*, 57.
42. M. Mahmoudi.; A. Simchi.; M. Imani.; P. Stroeve.; A. Sohrabi. *Thin Solid Films.* **2010**, *518*, 4281.
43. L. Gros.; H. Ringsdorf.; H. Schupp. *Angew Chem Int Ed Engl*. **1981**, *20*, 305.
44. Z. Chen. *Trends Mol Med.* **2010**, *16*, 594.
45. R. Langer. *Nature*. **1998**, *392*, 5.
46. R. H. Kodama. *J. Magn. Magn. Mater*. **1999**, *200*, 359.
47. J. Estelrich.; M. J. Sánchez-Martín.; M. A. Busquets. *Int J Nanomedicine*. **2015**, *10*, 1727.
48. M. A. Fortin. Magnetic Nanoparticles Used as Contrast Agents in MRI: Relaxometric Characterisation. In: Kumar C. (eds) Magnetic Characterization Techniques for Nanomaterials. Springer, Berlin, Heidelberg, **2016**, pp 511-555.
49. H. Liang.; X. B. Zhang.; Y. Lv.; L. Gong.; R. Wang.; X. Zhu.; R. Yang.; W. Tan. *Acc. Chem. Res*. **2014**, *47*, 1891.
50. R. Hudson. *RSC Adv*. **2016**, *6*, 4262.
51. A. S. Perera.; S. Zhang.; S. Homer-Vanniasinkam.; M. O. Coppens.; M. Edirisinghe. *ACS Appl. Mater. Interfaces*. **2018**, *10*, 15524.
52. A. K. Hauser.; M. I. Mitov.; E. F. Daley.; R. C. McGarry.; K. W. Anderson.; J. Z. Hilt. *Biomaterials.* **2016**, *105*, 127.
53. L. Li.; F. Gao.; W. Jiang.; X. Wu.; Y. Cai. *Drug Deliv*. **2016**, *23*, 1726.
54. R. P. Chauhan.; G. Singh.; S. Singh.; N. Bag.; R. Mathur. *Cancer Nano*. **2011**, *2*, 111.
55. J. Kudr.; Y. Haddad.; L. Richtera.; Z. Heger.; O. Zitka. *Nanomaterials*. **2017**, *7*, 243.
56. L. Eun-Kyung.; J. Eunji.; L. Kwangyeol.; H. Seungjoo.; H. Yong-Min. *Pharmaceutics.* **2013**, *5*, 294.

57. A. A. Belanova.; N. Gavalas.; Y. M. Makarenko.; P.V. Zolotukhin. *Oncol Res Treat*. **2018**, *41*, 139.
58. A. M. Budgin.; Y. A. Kabachii.; Z. B. Shifrina.; L. M. Bronstein. *Langmuir*. **2012**, *28*, 4142.
59. T. A. Heimer.; S. T. D. Arcangelis.; F. Farad.; J. M. Stipala.; G. J. Meyer. *Inorg. Chem.* **1996**, *35*, 5319.
60. Y. T. Tao. *J. Am. Chem. Soc.* **1993**, *115*, 4350.
61. G. Kataby.; M. Lojocarie.; R. Prozarov.; A. Gedanken. *Langmuir*. **1999**, *15*, 1703.
62. P. G. Hoertz.; R. A. Carlisl.; G. J. Meyer.; D. Wang.; E. Galoppini. *Nano Lett.* **2003**, *3*, 325.
63. J. Ge.; Y. Hu.; M. Biasini.; C. Dong.; J. Guo.; W. P. Beyermann.; Y. Yin. *Chem. Eur. J.* **2007**, *13*, 7153.
64. a) Y. Sahoo.; *Langmuir.* **2001**, *17*, 7907, b) K. Gharbi.; F. Salles.; P. Mathieu.; C. Amiens.; D. Ciuculescu-Pradines. *New J. Chem.* **2017**, *41*, 11898, c) L. Wang. *J. Am. Chem. Soc.* ***2006***, *128*, 13358.
65. G. Huang. *J. Mater. Chem.* **2009**, *19*, 6367.
66. S. M. Moghimi.; A. C. Hunter.; J. C. Murray. *Pharmacol Rev*. **2001**, *53*, 283.
67. A. K. Gupta.; M. Gupta. *Biomaterials*. **2005**, *26*, 3995.
68. Y. Zhai.; H. Xie.; H. C. Gu. *Int. J. Hyperth*. **2009**, *25*, 65.
69. A. Ito.; K. Tanaka.; H. Honda.; S. Abe.; H. Yamaguchi.; T. Kobayashi. *J. Biosci. Bioeng*. **2003**, *96*, 364.
70. K. Maier-Hauff.; R. Rothe.; R. Scholz.; U. Gneveckow.; P. Wust.; B. Thiesen.; A. Feussner.; A. von Deimling.; N. Waldoefner.; R. Felix.; A. Jordan. *J. Neurooncol*. **2007**, *81*, 53.
71. M. Johannsen.; U. Gneveckow.; L. Eckelt.; A. Feussner.; N. Waldofner.; R. Scholz.; S. Deger.; P. Wust.; S. A. Loening.; A. Jordan. *Int. J. Hyperth*. **2005**, *21*, 637.
72. M. Seleci.; D. Ag Seleci.; R. Joncyzk.; F. Stahl. *BioNanoMat.* **2016**, *17*, 33.
73. H. S. Huang.; J. F. Hainfeld. *Int. J. Nanomed*. **2013**, *8*, 2521.
74. H. Kobayashi.; R. Watanabe.; P. L. Choyke. *Theranostics*. **2014**, *4*, 81.
75. S. Acharya.; S. K. Sahoo. *Adv. Drug Deliv. Rev*. **2011**, *63*, 170.
76. H. Maeda.; H. Nakamura.; J. Fang. *Adv. Drug Deliv. Rev*. **2013**, *65*, 71.
77. M. Mahmoudi.; S. Sant.; B. Wang.; S. Laurent.; T. Sen. *Adv. Drug Deliv. Rev.* **2011**, *63*, 24.

78. H. Xu.; Z. P. Aguilar.; L. Yang.; A. Wang. *Biomaterials.* **2011**, *32*, 9758.
79. C. C. Yang.; S. Y. Yang.; C. S. Ho.; J. F. Chang.; B. H. Liu.; K. W. Huang. *J. Nanobiotechnol*. **2014**, *12*, 44.
80. D. A. Richards.; A. Maruani.; V. Chudasama. *Chem. Sci*. **2017**, *8*, 63.
81. D. A. Richards. *Drug Discov. Today Technol*. **2018**, *in press*, doi.org/10.1016/j.ddtec.2018.10.005.
82. J. J. Lee.; M. Hashimoto.; A. H. Know.; D. S. Kohane. *Nano Lett.* **2014**, *14*, 1.
83. M. Kumar.; G. Singh.; V. Arora.; S. Mewar.; U. Sharma.; N. R. Jagannathan.; S. Sapra.; A. K. Dinda.; S. Kharbanda.; H. Singh. *Int. J. Nanomed*. **2012**, *7*, 3503.
84. F. Y. Kuo.; W. L. Lin.; Y. C. Chen. *Nanoscale*. **2016**, *8*, 9217.
85. L. Y. Jie.; L. L. Cai.; L. J. Wang.; X. Y. Ying.; R. S. Yu.; M. M. Zhang.; Y. Z. Du. *Int. J. Nanomed*. **2012**, *7*, 3981.
86. S. Niazi.; X. Wang.; I. Pasha.; I. M. Khan.; S. Zhao.; Z. Wang. *Talanta*. **2018**, *186*, 97.
87. Z. Xiao.; O. C. Farokhzad. *ACS Nano*. **2012**, *6*, 3670.
88. M. J.Williams.; S. A.Corr. *Frontiers of Nanoscience*. **2013**, *5*, 29.
89. R. Cavaliere.; E. C. Ciocatto.; B. C. Giovanella.; C. Heidelberger.; A. Rossi-Fanelli. *Cancer*. **1967**, *20*, 1351.
90. R. T. Gordon.; J. R. Hines.; D. Gordon. *Med. Hypotheses*. **1979**, *5*, 83.
91. I. Hilger.; K. Fruhauf.; W. Andra.; R. Hiergeist.; R. Hergt.; W. A. Kaiser. *Acad. Radiol.* **2002**, *9*, 198.
92. a) I . Sharifi.; H. Shokrollahi.; S. Amiri. *J. Magn. Magn. Mater*. **2012**, *324*, 903, b) X. L. Liu.; H. M. Fan.; J. B. Yi.; Y. Yang.; E. S. G. Choo.; J. M. Xue.; D. D. Fan.; J. Ding. *J. Mater. Chem*. **2012**, *22*, 8235.
93. M. Arruebo.; R. Fern´andez-Pacheco.; M. R. Ibarra.; J. Santamarı´a. *Nano Today*, **2007**, *2*, 22.
94. J. P. May.; S. D. Li. *Expert Opin. Drug Deliv*. **2013**, *10*, 511.
95. W. Rao.; Z. S. Deng.; J. Liu. *CRC Crit. Rev. Bioeng*. **2010**, *38*, 101.
96. M. Urano.; M. Kuroda.; Y. Nishimura. *Int. J. Hyperth*. **1999**, *15*, 79.
97. R. D. Issels. *Eur. J. Cancer*. **2008**, *44*, 2546.
98. S. F. Medeirosa.; A. M. Santosa.; H. Fessi.; A. Elaissari. *Int J Pharm*. **2011**, *403*, 139.
99. M. Wei.; Y. Gao.; X. Li.; M. J. Serpe. *Polym. Chem*. **2017**, *8*, 127.
100. E. S. Gil.; S. M. Hudson. *Prog. Polym. Sci*. **2004**, *29*, 1173.

101. L. Wu.; L. Chen.; F. Liu.; X. Qi.; Y. Ge.; S. Shen. *Colloids Surf. B Biointerfaces*. **2017**, *152*, 440.
102. D. Schmaljohann. *Adv Drug Deliv. Rev*. **2006**, *58*, 1655.
103. C. Park.; J. Lim.; M. Yun.; C. Kim. *Angew Chem Int Edit*. **2008**, *47*, 2959.
104. E. S. Lee.; Z. G. Gao.; Y. H. Bae. *J Control Release*. **2008**, *132*, 164.
105. G. R. Martin.; R. K. Jain. *Cancer Res*. **1994**, *54*, 5670.
106. K. Engin.; D. B. Leeper.; J. R. Cater.; A. J. Thistlethwaite.; J. D. Mcfarlane. *Int J Hyperth*. **1995**, *11*, 211.
107. R. Van Sluis.; Z. M. Bhujwalla.; N. Raghunand.; P. Ballesteros.; J. Alvarez.; S. Cerdan.; R. J. Gillies. *Magnet Reson Med*. **1999**, *41*, 743.
108. P. Bawa.; V. Pillay.; Y. E. Choonara.; L.C. Toit. *Biomed. Mater*. **2009**, *4*, 1.
109. E. Y. Yan.; Y. Ding.; C. J. Chen.; R. T. Li.; Y. Hu.; X. Q. Jiang. *Chem Commun*. **2009**, *19*, 2718.
110. B. S. Kim.; H. Lee.; Y. H. Min.; Z. Poon.; P. T. Hammond. *Chem Commun*. **2009**, *28*, 4194.
111. H. Q. Yin.; Y. H. Bae. *Eur J Pharm and Biopharm*. **2009**, *71*, 223.
112. D. X. Lu.; X. T. Wen.; J. Liang.; Z. W. Gu.; X. D. Zhang.; Y. J. Fan. *J Biomed Mater Res Part B*. **2009**, *89B*, 177.
113. V. A. Sethuraman.; M. C. Lee.; Y. H. Bae. A. *Pharm Res*. **2008**, *25*, 657.
114. J. V. M. Weaver.; R. T. Williams.; B. J. L. Royles.; S. P. Rannard. *Soft Matter*. **2008**, *4*, 985.
115. E. S. Lee.; K. T. Oh.; D. Kim.; Y. S. Youn.; Y. H. Bae. *J Control Release*. **2007**, *123*, 19.
116. Y. Hu.; T. Litwin.; A. R. Nagaraja.; B. Kwong.; J. Katz.; N. Watson.; D. J. Irvine. *Nano Letters*. **2007**, *7*, 3056.
117. J. Jung.; I. H. Lee.; E. Lee.; J. Park.; S. Jon. *Biomacromolecules*. **2007**, *8*, 3401.
118. S. Ganta.; H. Devalapally.; A. Shahiwala.; M. Amiji. *J Control Release*. **2008**, *126*, 187.
119. X. Y. Yang.; L.T. Chen.; B. Huang.; F. Bai.; X. L. Yang. *Polymer*. **2009**, *50*, 3556.
120. B. Jeong.; A. Gutowska. *Trends Biotechnol*. **2002**, *20*, 305.
121. C. P. Leamon.; J. A. Reddy. *Adv Drug Deliv. Rev*. **2004**, *56*, 1127.
122. N. Nishiyama.; Y. Bae.; K. Miyata.; S. Fukushima.; K. Kataoka. *Drug Discov Today: Technol*. **2005**, *2*, 21.
123. G. Kocak.; C. Tuncer.; V. Bütün. *Polym. Chem*. **2017**, *8*, 144.

124. E. S. Lee. *J. Control. Release.* **2008**, *129*, 228.
125. E. Koren.; A. Apte.; A. Jani.; V. P. Torchilin. *J. Control. Release.* **2012**, *160*, 264.
126. A. E. Felber.; M. H. Dufresne.; J. C. Leroux. *Adv. Drug Deliv. Rev*. **2012**, *64*, 979.
127. L. Yang Yang.; D. Hai Quing.; W. Kang.; Z. Xian Zheng. *Sci China Chem.* **2010**, *53*, 447.
128. B. Jeong.; S. W. Kim.; Y. H. Bae. *Adv. Drug Deliv. Rev.* **2002**. *54*, 37.
129. M. A. Ward.; T. K. Georgiou. *Polymers.* **2011**, *3*, 1215.
130. R. A. Horne.; J. P. Almeida.; A. F. Day.; N. T. Yu. *J Colloid Interface Sci*. **1971**, *35*, 77.
131. J. Zhang. Switchable and Responsive Surfaces and Materials for Biomedical Applications. 1st Edition, **2015**, part one, pp 4.
132. a) C. Boutris.; E. G. Chatzi.; C. Kiparissides. *Polymer*. **1997**, *38*, 2567, b) S. Fujishige.; K. Kubota.; I. Ando. *J Phys Chem*. **1989**, *93*, 3311.
133. J. B. Cheon.;Y. I. Jeong.; C. S. Cho. .*Polymer*. 1999, *40*, 2041.
134. I. Idziak.; D. Avoce.; D. Lessard.; D. Gravel.; X. X. Zhu. *Macromolecules*. **1999**, *32*, 1260.
135. H. G. Schild. *Prog Polym Sci*. **1992**, *17*, 163.
136. F. Zeng.; Z. Tong.; H. Q. Feng. *Polymer*. **1997**, *38*, 5539.
137. Z. Zhang. Switchable and Responsive Surfaces and Materials for Biomedical Applications, ISBN 978-0-85709-713-2, chapter 1, **2015**.
138. P. Arvidsson.; A. E. Ivanov.; I. Y. Galaev.; B. Mattiasson. *J. Chromatogr. B*: *Biomed. Appl*. **2001**, *753*, 279.
139. a) D. C. Wan.; Q. Zhou.; H. T. Pu.; G. J. Yang. *J. Polym. Sci. Polym. Chem.* **2008**, *46*, 3756, b) J. Spevacek.; J. Dybal.; L. Starovoytova.; A. Zhigunova.; Z. Sedlakova. *Soft Matter.* **2012**, *8*, 6110.
140. L. Liu.; C. Detrembleur.; M. C. De Pauw-Gillet.; S. Mornet.; E. Duguet.; C. Jerome. *Polym. Chem.* **2014**, *5*, 799.
141. a) H. Vihola.; A. Laukkanen.; L. Valtola.; H. Tenhu.; J. Hirvonen. *Biomaterials. 2005*, *26*, 3055, b) J. Liu.; C. Detrembleur.; M. Hurtgen.; A. Debuigne.; M. C. De Pauw-Gillet.; S. Mornet.; E. Duguet.; C. Jerome. *Polym. Chem.* **2014**, *5*, 77.
142. H. Vihola.; A. Laukkanen.; L. Valtola.; H. Tenhu.; J. Hirvonen. *Biomaterials*. **2005**, *26*, 3055.
143. J. Ramos.; A. Imaz.; J. Forcada. *Polym. Chem*. **2012**, *3*, 852.

144. J. Li.; B. Wang.; Y. Wang. *Int. J. Pharmacol*. **2006**, *2*, 513.
145. E. A. Markvicheva.; S. V. Kuptsova.; T. Yu.; A. A. Vikhorv.; T. N. Dugina.; R. Kumar.; L. D. Rumsh. *Appl. Biochem. Biotechnol*. **2000**, *88*, 145.
146. A. Srivastava.; A. Kumar. *J. Mater. Sci. Mater. Med.* **2010**, *21*, 2937.
147. J. Ramos.; A. Imaz.; J. Forcada. *Polym. Chem.* **2012**, *3*, 852.
148. A. Imaz.; J. Forcada. *J. Polym. Sci. Polym. Chem.* **2010**, *48*, 1173.
149. Y. Q. Ling.; H. L. Nie.; C. Brandford-White.; G. R. Williams.; L. M. Zhu. *Colloid. Surf. B Biointerfaces.* **2012**, *94*, 281.
150. X. Fu.; L. Hosta-Rigau.; R. Chandrawati.; J. Cui. *Chem*. **2018**, *4*, 1.
151. M. Karimi.; A. Ghasemi.; P. Sahandi Zangabad.; R. Rahighi.; M. R. Hamblin. *Chem. Soc. Rev*. **2016**, *45*, 1457.
152. W. Sun.; S. Thies.; A. Pich.; X. Shi. *ACS Appl. Mater. Interfaces*. **2017**, *9*, 3411.
153. S. Tan.; Z. Lu.; J. Zhao.; J. Zhang. *Polym. Chem*. **2016**, *7*, 4106.
154. X. Jiang.; G. Lu.; C. Feng.; Y. Li.; X. Huang. *Polym. Chem*. **2013**, *4*, 3876.
155. I. Dimitrov.; B. Trzebicza.; A. H. E. Müller.; A. Dworak.; C. B. Tsvetanov. *Prog. Polym. Sci*. **2007**, *32*, 1275.
156. A. Khan. *Mat. Lett*. **2008**, *62*, 898.
157. S. F.Medeiros.; P. F. M. Oliveria.; A. M. Santos. *Mater. Lett*. **2016**, *175*, 296.
158. a) M. A. Ward.; T. K. Georgiou. *Polymers*. **2011**, *3*, 1215, b) T. Y. Liu.; S. H. Hu.; D. M. Liu.; S. Y. Chen.; I. W. Chen. *Nano Today*. **2009**, *4*, 52, c) S. Mura.; J. Nicolas.; P. Couvreur. *Nat Mater*. **2013**, *12*, 991.
159. A. Hervault.; A. E. Dunn.; M. Lim.; D. Mott.; S. Maenosono.; N. T. Thanh. *Nanoscale*. **2016**, *8*, 12152.

Chapter 3

Synthesis and Characterization of Magnetic Nanoparticles for Biomedical Application

Magnetic iron oxide nanoparticles have been the subject of great interest in recent years due to their various potentials in biological applications such as MRI [1-3], cell tracking [4,5] hyperthermia [6], and drug delivery [7,8]. Currently iron oxide nanoparticles as magnetite (Fe_3O_4) and maghemite (Fe_2O_3) with their remarkable magnetic properties are the most frequently investigated nanomaterials in biological systems owing to their biocompatibility, non-toxicity, and non-immunogenicity [9]. In almost all applications the preparation method of the nanomaterials represents one of the most important tasks as it will determine the particle size, shape, size distribution, surface chemistry of the particles, and consequently their magnetic properties. Therefore, the production of such nanoparticles should be directed towards the achievement of a material, which is suitable for therapeutic and/or diagnostic applications. In general, the effectiveness of the therapeutic magnetic nanoparticles (MNPs) requires:

(a) High magnetic susceptibility and high saturation magnetization [10]
(b) Tailored surface chemistry for specific biomedical applications [11]
(c) An average hydrodynamic size of 10–100 nm with the proper coating and ζ-potential values below -30 or above +30 mV [12]

(d) Capability to incorporate chemotherapeutic drugs

Despite of the many attempts to develop processes and techniques, which are able to yield monodisperse nanoparticles to satisfy these criteria [13], their preparation is still challenging.

To accomplish the objective of this thesis, MNPs that have high heating potential even at their low concentrations under AC excitation, must be prepared [14] because extremely huge SAR implies smaller amount of NPs to be required for injection into the patient for clinical trials. Regarding to the fact that using proper synthesis approach can control physical and chemical properties of NPs to obtain a desirable SAR value, we mainly focused on polyol method to fulfil this goal. Indeed, bottom-up liquid-phase techniques such as polyol process are very attractive synthetic approach as they are versatile, and allow for a

fine control of the structure, chemical nature, and morphology of the particles [15], herein we present and discuss the synthesis of iron oxide magnetic nanoparticles, prepared according to this technique, together with their extended chemical and physical characterizations including evaluation of size distribution, morphology, magnetic property, and heat dissipation ability.

3.1 Iron oxides Crystallographic Structure (Fe_3O_4)

Magnetite contains both Fe^{2+} and Fe^{3+} ions, within a spinel crystal structure. The spinels are a class of minerals of general formulation $A^{2+}\ B_2^{3+}\ O_4^{2-}$ with the oxide anions arranged in a face center cubic (fcc) crystal structure and the metal cations occupying interstitial sites. These interstitial sites are of two types: tetrahedral, T_d, and octahedral, O_h as shown in Figure 3.1. The spinel structure was named for the mineral $MgAl_2O_4$, in which the trivalent aluminum cations occupy the 16 Oh sites, and the 8 Td sites are occupied by the divalent magnesium cations [16,17].

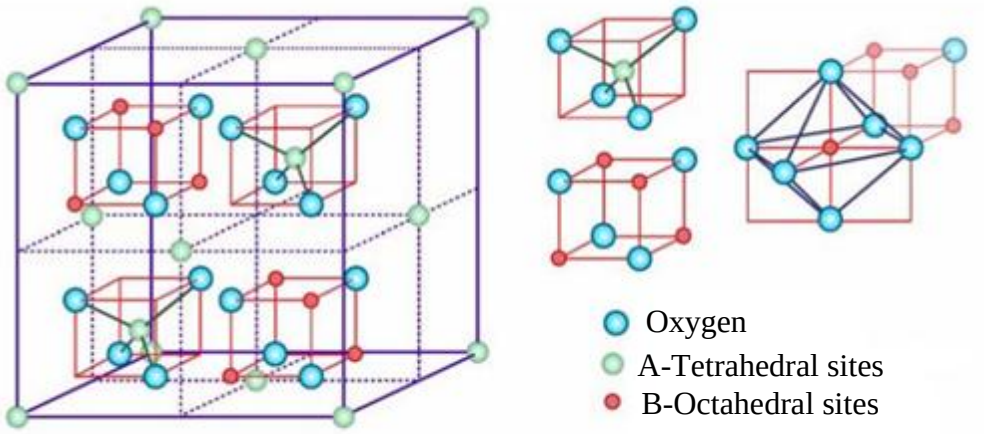

Figure 3.1 Basic spinel structure illustrating the octahedral and tetrahedral sites relative to the position of oxygen [18]

Spinel phases are called normal or inverse according to the arrangement of cations in the cavities. If Oh sites are solely occupied by trivalent atoms, and the Td sites are occupied by the divalent atoms, it is called normal spinel structure as displayed in Figure 3.2; conversely, in inverse spinel structure trivalent ions are equally distributed among Td and Oh sites, while divalent ions are placed in Oh cavities.

In stoichiometric magnetite Fe^{II}/Fe^{III} = 1/2, the divalent irons can be partly or fully replaced by other divalent ions such as Co, Mn, Zn, etc. The general formula for ferrites can then be expressed as $(M_{1-i}Fe_i)[M_iFe_{2-i}]O_4$, where round parentheses and brackets denote Td and Oh sites, respectively, M the divalent metal ion and *i* is the inversion degree, which

varies between 1 (totally inverted spinel) and 0 (normal spinel). The nature of the divalent metal cation and the magnetic ordering in the crystal lattice influence the magnetic hyperthermia property of ferrite nanoparticles. For instance, spherical ($Zn_{0.4}Fe_{0.6}$) Fe_2O_4 nanoparticles were demonstrated to have higher magnetization, and heat generation ability twice larger compared to the undoped Fe_3O_4 nanoparticles of similar size (438.6 and 189.6 W g^{-1}, respectively) [19].

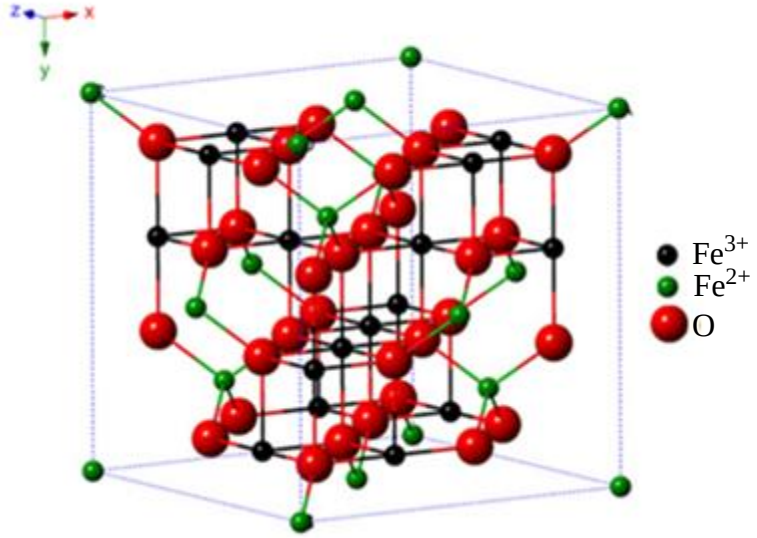

Crystal structure of magnetic nanoparticles

Figure 3.2 Structure of magnetite [20]

3.2 Preparation of Magnetic Nanoparticles

The preparation of iron oxide nanoparticles was described by Khallafalla [21] and Massart [22] in 1980 for the first time. After that, especially during the last decade, many publications have been describing efficient synthetic routes to prepare shape/size controlled, highly stable, monodisperse, and biocompatible iron oxide nanoparticles.

The co-precipitation synthesis is a very simple method for the preparation of MNPs, which is largely used. It is based on the precipitation from aqueous solution containing Fe^{2+} and Fe^{3+} salts by addition of a base (usually ammonia or NaOH). Magnetic phase and particle size can be tuned by variation of iron salts, Fe^{2+}/Fe^{3+} ratio, temperature, pH, and the type of base used [23].

The thermal decomposition of organometallic compounds in boiling organic solvents is another promising way for MNPs preparation, and the resulting particles show a very

narrow size distribution. Usually, iron carbonyls or iron acetylacetonates are used as precursors and oleic acid or fatty acids serve as surfactants. By variation of the proportion of precursors to the starting agents (surfactants and solvents), the size and morphology of the resulting particles can be controlled [24].

Micro-emulsion synthesis is a two-phase method for the production of nearly monodisperse MNPs. For this purpose, a water-in-oil microemulsion is prepared by dispersion of nanosized water droplets (10.0–50.0 nm) in an oil phase, stabilized by surfactant molecules at the water/oil interface [25].

Hydrothermal synthesis is commonly used to prepare MNPs under specific conditions. In fact, hydrothermal synthesis performed in aqueous media at temperatures above 200 ^{o}C, and usually achieved in autoclaves at pressures above 2000 psi. This route exploits the ability of water to hydrolyze and dehydrate metal salts at high temperatures. Due to the low solubility of the obtained metal oxide particles in water at such temperatures [26,27] a precipitation takes place, and particle size in addition to morphology can be controlled by variation of concentration, temperature, and autoclaving time.

The polyol synthesis bases on the oxidative alkaline hydrolysis of Fe^{2+} and Fe^{3+} salts in a polyol mixture (e.g., poly-ethylene glycol (PEG)/diethylene glycol or N-methyldiethanolamine) is a promising approach for MNPs preparation. Size and structure of the resulting MNPs can be tuned either by modifying the reaction conditions or changing the solvent [28]. Despite of the fact that the obtained particles are not always monodisperse, the technique is appealing for magnetic hyperthermia therapy since under certain reaction conditions, “flower-shaped MNPs” can be synthesized. [28] As discussed in the previous chapter, particles with this shape, show excellent heating performance for hyperthermia [29].

Moreover, the polyol method offers other advantages that motivated us to use this method for MNPs synthesis including:

i) Due to the polarity of the polyols ($\varepsilon > 30$), inorganic compounds/salts are often well soluble in polyol mixture [30].

ii) Because nucleation and growth of particles can be performed at temperatures up to the boiling point of the polyol (e.g., glycol: 197 °C, diethylene glycol: 246 °C, tetraethylene glycol: 314 °C) [30], well-crystallized materials can be obtained [31-33].

iii) The chelation of the solid nuclei by the polyol is simultaneous to its formation, which limits the particle growth, and prevents agglomeration of particles [32,34].

iv) As the polyols are normally low-weight molecules, they may act as weak stabilizers, which can be removed from the particle surface under certain experimental conditions [32]. Consequently, solvent exchange as well as controlled precipitation of nanomaterials are possible by this approach.

v) In principle, the synthesis is easy to perform, and suited for a preparation of larger quantities of ferrofluid.

Particle size and shape can be controlled through temperature, amount of metal precursors, and the application of an external magnetic field (often used during the synthesis of ferromagnetic metals). For instance, if the temperature is increased, the size of the particle normally decreases as more nuclei are formed in a shorter nucleation time, allowing the intermediate oxide phase to diffuse more rapidly [35]. When the ratio of metal precursor to polyol is increased, the particle size increases due to the fact that the number of nuclei formed during the short nucleation step at a certain temperature is independent of the amount of metal salt introduced in the system. If the number of particles is constant, but more metal is available, the mean particle size will increase [35]. Moreover, the polyol-mediated method employs relatively mild conditions, and starting materials are much less toxic than those used in other preparation techniques.

As it will be shown, in this thesis we adapted the polyol synthesis at high temperature condition, which allowed us to obtain MNPs with good magnetic properties and controlled morphology.

3.3 Synthesis and Characterization of Fe_3O_4-68 by Polyol Method

The nanoparticles were prepared following a procedure previously published [36], and patented by Colorobbia Italia S.p.A. [37]. In a typical synthesis stoichiometric quantities of $Fe(CH_3COO)_3$ and $FeCl_2$ were solubilized in diethylene glycol (DEG) for 1 h at 150 °C, and kept heating at 170 °C for 19 h. After this time, dark brown stable suspensions were obtained (Figure 3.3). For further growth of average size of MNPs, and to obtain a flower-like structure, synthesis was repeated using the NPs formed in the first step as seeds for 5 h at 170 °C. Details of the synthesis of MNPs are given in the experimental part, Appendix A.2).

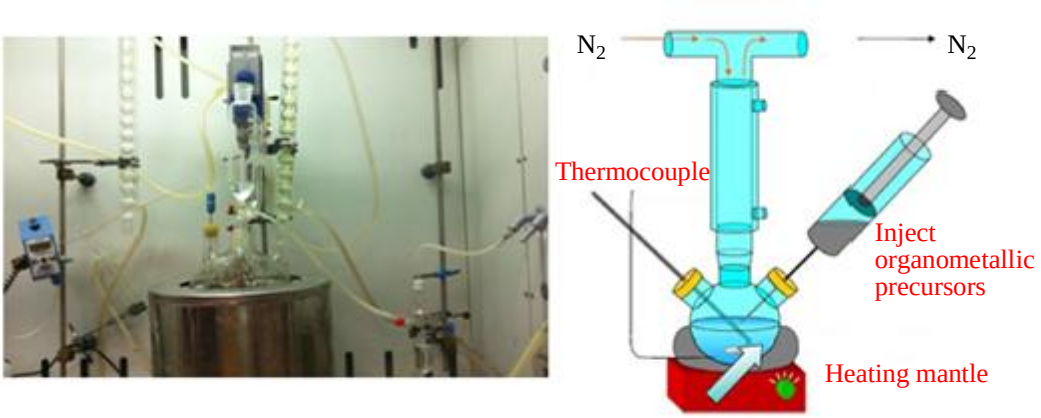

Figure 3.3 Image (left) and scheme (right) of the experimental apparatus used for the synthesis of Fe_3O_4-68 MNPs by the polyol method

The obtained nanoparticles (sample Fe_3O_4-68) are ready to be employed for further modifications without any need of purification procedure. Crystalline phase, morphology, and size distribution of the MNPs were evaluated by XRD, TEM, and DLS analyses.

In order to verify the formation of crystalline iron oxide magnetic nanoparticles, Powder X-Ray Diffraction (XRD) pattern was recorded for the Fe_3O_4-68 sample. As shown in Figure 3.4, all diffraction patterns show the formation of a single crystallographic phase, which can be indexed as the cubic structure of Fe_3O_4 spinel ferrite. The average crystallite size was estimated by the well-known *Scherrer* equation as well. According to this law, once instrument broadening has been taken into account, the crystallite size <D> can be easily calculated from the full width at half maximum peak intensity according to this formula:

$$< D > vol = \frac{K\lambda}{B\ COS\theta}$$

where θ is the diffraction angle, λ is the wavelength of the incident X-ray beam, *B* is the line broadening at half the maximum intensity (FWHM) after subtracting the instrumental line broadening in radians, and *K*, which called *Scherrer constant*, is a dimensionless unit cell geometry dependent constant that has a typical value between 0.85 and 0.99; however, for spinel ferrites *K* can be taken as 0.89.

By using the 5 main diffraction peaks, the average crystallite size of magnetite was determined 14.0 nm. Moreover, the lattice parameter was found 0.840 nm in accordance with the value expected for magnetite, suggesting oxidation of Fe^{2+} ions did not take place.

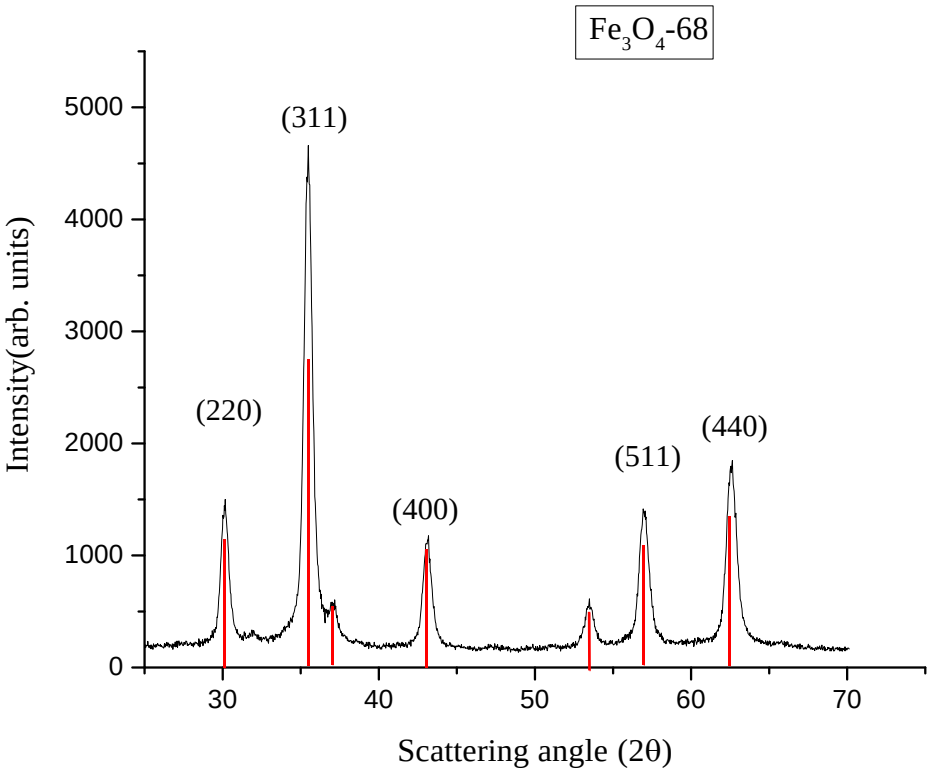

Figure 3.4 Powder X-ray diffraction pattern of Fe_3O_4-68. Evaluation of the particle size by using the Scherrer formula gave an average diameter of 14.0 nm.

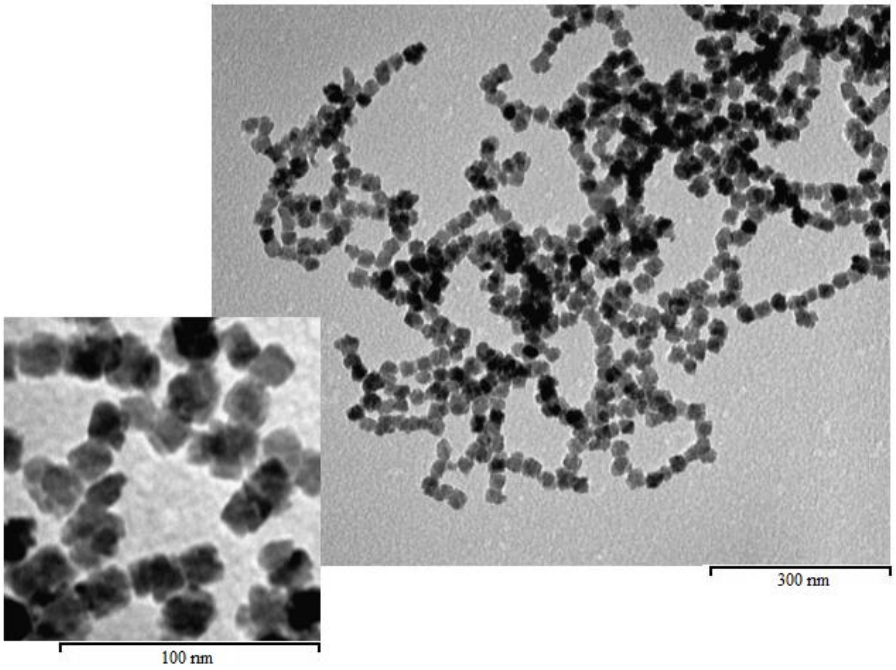

Figure 3.5 TEM image of Fe_3O_4-68 prepared by polyol method

In Figure 3.5 a typical TEM micrograph of the dispersion of Fe_3O_4-68 in ethanol deposited over a 200 mesh carbon-coated copper grids, is shown. The sample consists of a dispersion of almost flower-like nanoparticles with a narrow size distribution. The average diameter obtained from a statistical analysis over 500 nanoparticles gave a mean diameter of 18.0 nm. The measured value is larger than that obtained from XRD measurements as, indeed, expected for a flower like nanosystem.

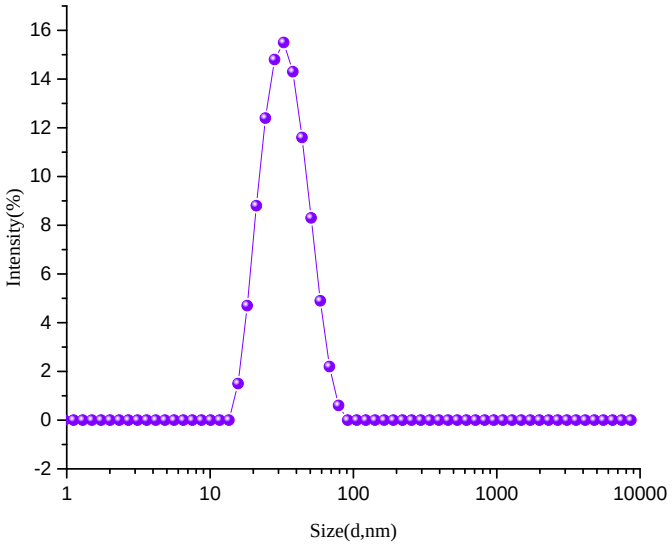

Figure 3.6 Size distribution of Fe_3O_4-68 dispersed in DEG

The average particle size was evaluated by DLS measurement corresponding to three independent runs (almost 15 measurements each run). DLS measurement demonstrated that Fe_3O_4-68 MNPs have uniform size with average particle size of 32.0 nm and PDI ~ 0.124 as shown in Figure 3.6. Although the particle size is slightly larger than that determined by TEM analysis, which points out the presence of small aggregates in the suspensions, this phenomenon does not have any effect on the stability of the NPs suspension. Moreover, ICP-AES analysis indicated a mean concentration of magnetic nanoparticles (Fe_3O_4-68) dispersed in DEG was about 1.33 wt % respect to the Fe_3O_4.

In next step, magnetization measurements of Fe_3O_4-68 nanoparticles were performed using a superconducting quantum interference device (SQUID) magnetometer with a helium flow, and measurements were carried out on pressed powder of sample.

3.4 Magnetic Measurement of Fe_3O_4-68 by SQUID

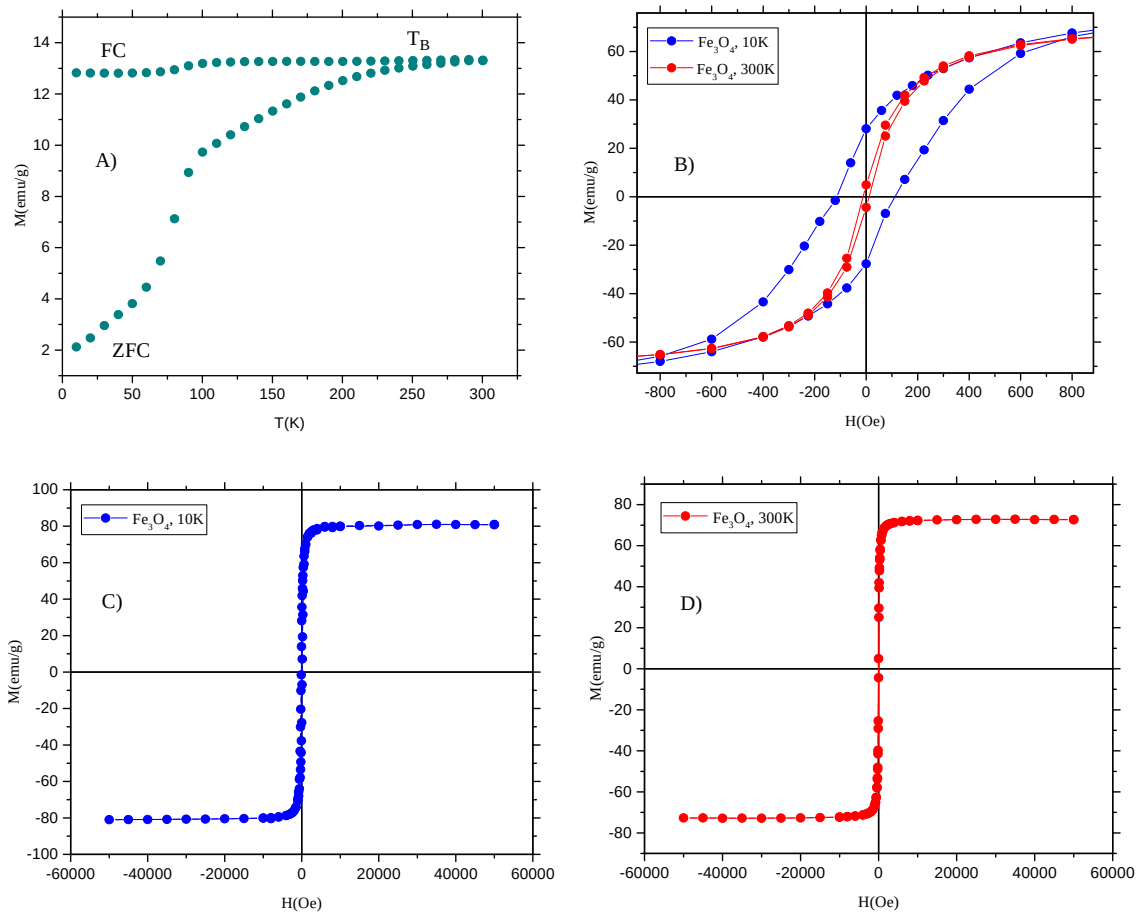

Figure 3.7 Magnetization vs. temperature curves recorded after ZFC-FC procedures (A) hysteresis cycles recorded at 10 K (B,C) and room temperature (B,D) for Fe_3O_4-68

The magnetic properties of powders were measured, and results are summarized in table 3.1.

Sample	Ms (emu g^{-1}) 10K	Ms (emu g^{-1}) 300k	Hc Oe	Mr (emu g^{-1}) 10K	T_B K	Size, TEM nm
Fe_3O_4-68	80	75	115	29	250	18.0

Table 3.1 magnetic properties of Fe_3O_4-68

The zero-field-cooled (ZFC) and field-cooled (FC) curves were measured in a magnetic field of 50 Oe in the temperature range of 10 – 300 K. As shown in Figure (3.7, A) the ZFC curve of Fe_3O_4-68 nanoparticles shows a broad maximum around 300 K, which suggested blocking of the nanoparticles occurs close to room temperature. At low

temperature the magnetic moment aligns along the energetically favorable axis, and cannot align with the field due to the anisotropy energy barrier. The net magnetization is low because of the random axis orientation of nanoparticles. As the temperature increases, thermal fluctuations switch the magnetic moment of nanoparticles to the direction of the applied field, leading to a growing magnetization. At room temperature the thermal energy equals the anisotropy energy barrier, and randomizes the magnetic moment. Thus, the nanoparticles appear almost superparamagnetic behavior, as requested for the magnetic fluid hyperthermia application. The feature observed in both the ZFC and FC curve at around 100 K can be attributed to the Verway transition. This is a first order structural phase transition unique of magnetite (for bulk Fe_3O_4 occurs at 125 K) [38] connected to charge ordering. The transition is known to shift to lower temperature, and eventually to disappear upon oxidation of Fe^{2+} ions and size reduction [39]. The presence of this transition is, thus, a solid confirmation that our particles consist of high crystalline magnetite nanocrystals.

Figure (3.7, B) shows the hysteresis loops of Fe_3O_4-68 nanoparticles at 10 K and 300 K. At 10 K, the hysteresis loop indicates a typical ferromagnetic behavior with coercivity (H_c) of 115 Oe and remanence (M_r) of 29 emu g^{-1} as displayed in Figure (3.7, C). Consistent with the ZFC-FC measurements, the nanocrystals are superparamagnetic at 300 K, and the hysteresis loop shows neither remanence nor coercivity (Figure 3.7, D). Furthermore, as seen in Figure (3.7, C, D) the saturation magnetization (M_s) of Fe_3O_4-68 nanoparticles at 10 K and 300 K are 80 emu g^{-1} and 75 emu g^{-1}, respectively. Since the SAR value is dependent on the magnetization, the high magnetization saturation observed here should result in enhanced hyperthermia effects [40].

3.5 Magnetic Heating Capacity of Fe_3O_4-68

The heating efficiency of Fe_3O_4-68 with average particle size of 18.0 nm was measured by calorimetric method, i.e. by measuring the temperature increase in the sample over a period of time under application of an AMF field with a particular amplitude and frequency. A fiber optic temperature probe was used to measure sample temperature as well. For SAR measurement, 300 µL Fe_3O_4-68 dispersed in DEG, containing 1.33 wt % Fe_3O_4 was exposed to an alternating magnetic field generated by inductive coils at a fixed frequency (f ~ 340 kHz) and amplitude (H ~ 21 kA m^{-1}) for 3 min. The temperature of the ferrofluid was

measured as a function of time, and the slope of the heating profiles was used to calculate the SAR according to the formula:

$$SAR = \frac{m_d\, C_{p,d}}{m_{NP}} \left|\frac{dT}{dt}\right| t = 0$$

Where m_d and $C_{p,d}$ are the mass and heat capacity of the dispersion medium, while m_{NP} is the mass of nanoparticles. The Fe_3O_4-68 raised the solution temperature to 40 °C within 10 seconds, and up to 140 °C during 150 min as displayed in Figure 3.8.

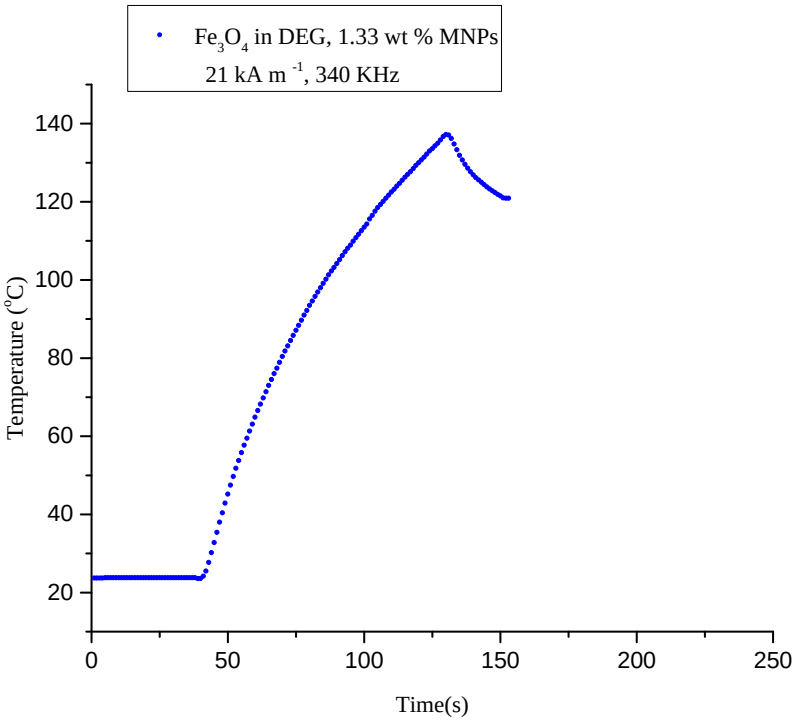

Figure 3.8 Temperature evolution of a suspension containing the Fe_3O_4-68 dispersed in DEG (1.33 wt % MNPs) under application of an AMF (H = 21 kA m^{-1}, *f* = 340 kHz)

Sample	Fe	Fe_3O_4	(dT/dt)t=0	H kA m^{-1}	*f* kHz	$SAR_{(Fe)}$ W g^{-1}	$SAR_{(Fe3O4)}$ W g^{-1}
Fe_3O_4-68	0.0033 g	0.00456g	2.401	21	340	613.0	444.0

Table 3.2 SAR value of ferrofluid containing Fe_3O_4-68 dispersed in DEG (13.0 mg mL^{-1}) under AMF (*f* ~ 340 kHz, H ~ 21 kA m^{-1})

According to the table 3.2 the Fe_3O_4-68 flower-like nanostructure showed significantly high SAR of 613.0 W g^{-1} $_{(Fe)}$, (444.0 W g^{-1} $_{(Fe3O4)}$). These values are considerably higher than

those commonly observed for spherical magnetite MNPs with similar volume (SAR ~ < 50.0 W g^{-1} under applying same magnetic field) [41, 28]. This effect can be ascribed to the morphology of Fe_3O_4-68 nanoparticles as already discussed in chapter 2; indeed, nanoflowers are composed of highly ordered nanocrystals that do not behave like isolated grains [28], and they exhibit lower anisotropy due to coalescence and crystal ordering of the individual grains. Conversely, spherical particles display higher surface disorder, and consequently higher surface anisotropy, which all these factors together make the former NPs to behave as more efficient heat mediators for magnetic fluid hyperthermia.

As discussed in the previous chapter, the SAR value is also proportional to the applied AMF magnetic field strength and frequency. In order to evaluate the influence of frequency and amplitude of the applied AMF on heat dissipation ability of Fe_3O_4-68, the SAR value of the same ferrofluid was measured by calorimetric method under applying AMF with lower *f* (183 kHz) and H (17 kA m^{-1}) for 3 min, which are more suited for clinical application, and results are reported in table 3.3.

Sample	Fe	Fe_3O_4	(dT/dt)t=0	H kA m^{-1}	*f* kHz	$SAR_{(Fe)}$ W g^{-1}	$SAR_{(Fe3O4)}$ W g^{-1}
Fe_3O_4-68	0.011 g	0.0153 g	1.38	17	183	357.0	258.0

Table 3.3 SAR value of ferrofluid containing Fe_3O_4-68 dispersed in DEG (13.0 mg mL^{-1}) under AMF (*f* ~ 183 kHz, H ~ 17 kA m^{-1})

Temperature variation versus time is shown in Figure 3.9. Temperature of solution was raised to 40 ^{o}C within 14 seconds, and increased up to 187 ^{o}C during 170 min. In order to estimate reproducibility of the method, measurement was performed two times and average SAR value was calculated, obtaining SAR = 357.0 W $g^{-1}_{(Fe)}$, (258.0 W $g^{-1}_{(Fe3O4)}$).

The capability of heat dissipation of MNPs was still very high under milder condition (weaker magnetic field), demonstrating once again the selected morphology of nanoparticles is particularly suited for this kind of application. A high heating potential, in fact, implies lower time of residence of nanoparticles in the human body, and also lower dosages to be administered to the patient. Therefore, these nanoparticles are promising candidate for *in vivo* hyperthermia therapy.

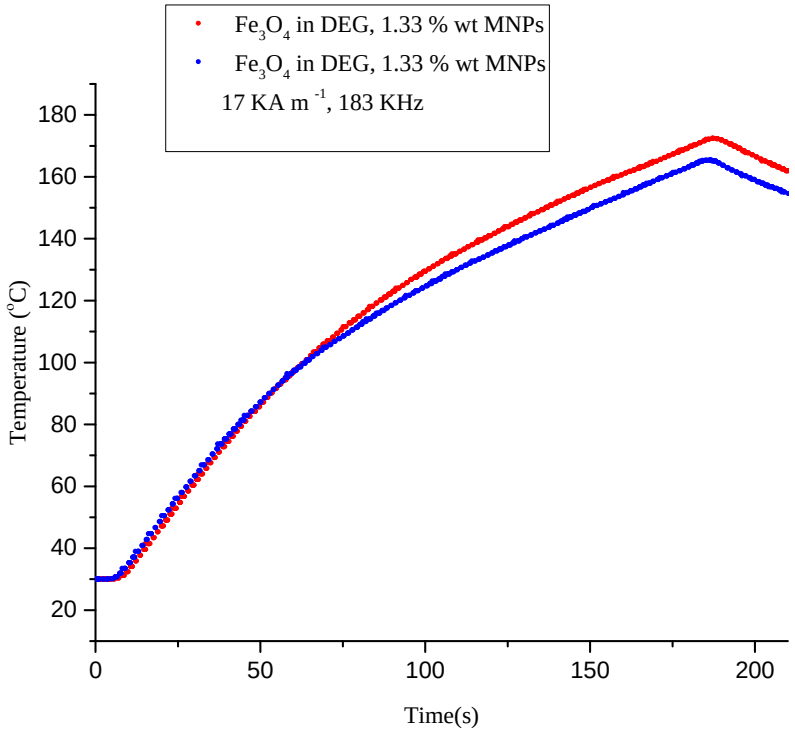

Figure 3.9 Temperature evolution of a suspension containing the Fe_3O_4-68 MNPs dispersed in DEG (1.33 wt % MNPs) under application of an AMF

As discussed before, single-domain NPs can dissipate heat through two mechanisms, Néel relaxation or Brownian relaxation. In order to figure out which mechanism mainly contributes to heat release, the SAR measurements were repeated after dispersing the MNPs in media with different viscosity, water and agar. To this aim, first, surface modification of DEG coated Fe_3O_4-68 nanoparticles was performed by polyacrylic acid (PAA) encapsulation, to prepare stable aqueous suspension. This was realized by precipitating Fe_3O_4-68 nanoparticles from DEG suspension, washing 3 times with ethanol/acetone to completely remove DEG, and then mixing the precipitate to an aqueous solution of PAA under sonication. Finally, MNPs were separated *via* magnetic decantation, washed, and re-dispersed in distilled water (the surface modification procedure is fully discussed in Appendix A.9.1). DLS analysis of the obtained water dispersed NPs indicated that the PAA coating was carried out successfully since MNPs were found to preserve the high monodispersity (PDI ~ 0.154), and have average particle size of 39.0 nm.

Sample	kA m^{-1} Field intensity	kHz Frequency	W g^{-1} SAR/Fe	W g^{-1} SAR/Fe_3O_4
0.091 wt % Fe_3O_4 in water	17	183	250.0	176.0
0.091 wt % Fe_3O_4, 0.25 wt % Gel	17	183	148.0	107.0
0.091 wt % Fe_3O_4, 0.5 wt % Gel	17	183	148.0	107.0
0.091 wt % Fe_3O_4, 1.0 wt % Gel	17	183	120.0	87.0
0.091 wt % Fe_3O_4, 2.0 wt % Gel	17	183	104.0	76.0
0.091 wt % Fe_3O_4, 3.0 wt % Gel	17	183	98.0	71.0
0.091 wt % Fe_3O_4, 4.0 wt % Gel	17	183	84.0	60.0
0.091 wt % Fe_3O_4, 5.0 wt % Gel	17	183	87.0	63.0

Table 3.4 Hyperthermia efficiency of MNPs (~18.0 nm) dispersed in water and agarose gel

Besides, the zeta potential value of -42 mV confirmed the presence of carboxylic acid on the surface of Fe_3O_4-68. Afterward, samples contain Fe_3O_4-68/PAA (0.091 wt % Fe_3O_4 as determined by ICP analysis) were dispersed in agar media with different weight percentage ranging from 0.25 wt % to 5.0 wt % to provide media with diverse viscosity. All samples were subjected to AMF with frequency 183 kHz and amplitude 17 kA m^{-1} for 5 min. The obtained SAR values are reported in table 3.4.

It appears that SAR of PAA coated Fe_3O_4-68 decreases when viscosity of media increases, reaching an almost constant value of ca. 85.0 W $g^{-1}_{(Fe)}$ when the MNPs are completely blocked. This value corresponds to the heat released by just Néel relaxation mechanism since this relaxation will be presumably the only one operating once the MNPs will be internalized in tumour cells, so this is the value, which should be actually considered to evaluate the hyperthermic efficiency of our nanoparticles. Although the SAR obtained in agar at 5.0 wt % is considerably smaller than that measured on water dispersion, it is still very high if compared to that of other magnetite suspensions measured under the same viscosity conditions. We can, therefore, conclude that our particles are extremely appealing for application as heat mediators for magnetic fluid hyperthermia.

To summarize, superparamagnetic nanoparticles of magnetite (Fe_3O_4) were successfully synthesized using the polyol method. Crystal size, morphology, and size distribution of Fe_3O_4-68 NPs were controlled by XRD, TEM, and DLS analyses. XRD

patterns exhibited crystalline phase of magnetite with spinel structure, and TEM images indicated a well-defined and uniform crystalline flower-like structure of magnetite with average particle size ~ 18.0 nm, while DLS confirmed stable suspensions of NPs was obtained. The magnetic behavior of Fe_3O_4-68 and the heating efficiency in an alternating magnetic field were studied, and the iron oxide nanoparticles revealed a high heating power and saturation magnetization at low dosage as a result of their size and specific morphology, which resulted from the polyol method adopted. We can, thus, conclude that this technique fulfilled our goal to provide MNPs with high SAR value, that have potential to be employed at low concentration as an effective therapeutic agent for clinical treatment.

Chapter3

References

1. K. Niemirowicz.; K. Markiewicz.; A. Wilczewska.; H. Car. *Adv Med Sci.* **2012**, 1-12.
2. J. W. M. Bulte.; D. L. Kraitchman. *NMR in Biomedicine*. **2004**, *17*, 484.
3. R. Hachani.; M. Lowdell.; M. Birchall.; N. T. K. Thanh. *Nanoscale*. **2013**, *5*, 11362.
4. K. Andreas.; R. Georgieva.; M. Ladwig.; S. Mueller.; M. Notter.; M. Sittinger.; J. Ringe. *Biomaterials.* **2012**, *33*, 4515.
5. H. Markides.; R. Morris.; S. Roberts.; J. El Haj. *J Tissue Eng Regen Med*. **2017**, *11*, 2333.
6. C. Blanco-Andujar.; D. Ortega.; P. Southern.; Q. A. Pankhurst.; N. T. K. Thanh. *Nanoscale*. **2015**, *7*, 1768.
7. F. Xiong.; S. Huang.; N. Gu. *Drug Dev. Ind. Pharm*. **2018**, *44*, 697.
8. R. Tietze.; J. Zaloga.; H. Unterweger. *Biochem. Biophys. Res. Commun*. **2015**, *468*, 463.
9. S. F. Medeirosa.; A.M. Santosa.; H. Fessi.; A. Elaissari. *Int J Pharm*. **2011**, *403*, 139.
10. A. Jordan.; R. Scholz.; K. Maier-Hauff.; M. Johannsen.; P. Wust.; J. Nadobny.; H. Schirra.; H. Schmidt.; R. Felix. *J Magn Magn Mater*. **2001**, 225, 118.
11. S. M. Moghimi.; A.C.H. Hunter.; J.C. Murray. *Pharm Rev*. **2001**, 53, 283.
12. K. El-Boubbou. *Nanomedicine*. **2018**, *13*, 953.
13. F. Fie´vet.; S. Ammar-Merah.; R. Brayne.; G. Viaub. *Chem. Soc. Rev.* **2018**, *47*, 5187.
14. A. Jordan.; P. Wust.; H. Fahling.; R. Felix. *Int. J. Hyperth*. **1993**, *9*, 51.
15. B. L. Cushing.; V. L. Kolesnichenko.; C. J. O'Connor. *Chem. Rev*. **2004**, *104*, 3893.
16. B. D. Cullity.; C. D. Graham. Introduction to Magnetic Materials; 2 ed.; John Wiley & Sons: Hoboken, New Jersey, **2009**.
17. R. M. Cornell.; U. Schwertmann. The Iron Oxides: Structure, Properties, Reactions, Occurrences and Uses. Weinheim: Wiley-VCH; **2003**.
18. Z. Ristanović.; A. Kalezić-Glišović.; N. Mitrović. *Sci Sinter*. **2015**, *47*, 3.
19. L. M. Bauer.; S.F. Situ.; M. A. Griswold.; A. C. S. Samia. *Nanoscale*. **2016**, *8*, 12162.
20. A) W. Wu.; Z. Wu.; T. Yu.; C. Jiang.; W.S. Kim. *Sci. Technol. Adv. Mater*. **2015**, *16*, 023501.
21. S. E. Khalafalla.; G. W. Reimers. Preparation. *IEEE Trans. Magn*. **1980**, *16*, 178.

22. R. Massart. *C. R. Seances Acad. Sci. Ser. C*. **1980**, *291*, 1.
23. M. Mahdavi.; M. B. Ahmad.; F. Namvar. *Molecules.* **2013**, *18*, 7533.
24. J. Park.; E. Lee.; N. M. Hwang.; M.S. Kang.; S. C. Kim.; J. H. Park. *Angew. Chem. Int. Ed*. **2005**, *44*, 2872.
25. C. Okoli.; M. Sanchez-Dominguez.; M. Boutonnet.; S. Jaras.; G.R. Kuttuva. *Langmuir.* **2012**, *28*, 8479.
26. Y. L. Hao.; A. S. Teja. *J. Mater. Res*. **2003**, *18*, 415.
27. Y. D. Lv.; H. Wang.; X.F. Wang.; J.B. Bai. *J. Cryst. Growth.* **2009**, *311*, 3445.
28. P. Hugounenq.; M. Levy.; D. Alloyeau.; L. Lartigue.; E. Dubois.; F. Gazeau. *J. Phys. Chem. C.* **2012**, *C116*, 15702.
29. S. Dutz.; M. Kettering.; I. Hilger.; R. Müller.; M. Zeisberger. *Nanotechnology.* **2011**, *22*. (265102), (7pp).
30. D. R. Lide (Ed.). Handbook of Chemistry and Physics, vol. 84, CRC Press, Boca Raton, FL, **2003**.
31. P. Toneguzzo.; G. Viau.; O. Acher.; F. Fievet-Vincent.; F. Fievet. *Adv. Mater*. **1998**, *10*, 1032.
32. C. Feldmann.; H. O. Jungk. *Angew. Chem. Int. Ed.* **2001**, *40*, 359.
33. C. Feldmann. *Adv. Funct. Mater.* **2003**, *13*, 101.
34. C. Feldmann. *Z. Anorg. Allg. Chem*. **2004**, *630*, I-IV.
35. F. Fievet.; J. P. Lagier.; M. Figlarz. *MRS Bull*. **1989**, 29.
36. A. Lascialfari.; G. Lorenzi.; F. Orsini.; C. Ravagli.; G.Baldi.; C. Sangregorio. *Dalton Trans*. **2013**, *42*, 10282.
37. G. Baldi.; F. Innocenti; M. Bitossi. WO/073922, **2011**.
38. Z. Lodziana. *Phys. Rev. Lett*. **2007**, *99*, 206402.
39. a) O. Ozdemir.; D. J. Dunlop. *Geophys. Res. Lett*. **1993**, *20*, 1671, b) S. P. Schewaminger.; D. Bauer.; F. E. Wagner.; S. Berensmeier. *Cryst Eng Comm*. **2017**, *19*, 246.
40. R. E. Rosensweig. *J. Magn. Magn. Mater*. **2002**, *252*, 370.
41. I. Morales.; R. Costo.; N. Mille.; G. B. da Silva.; J. Carrey.; P. de la Presa. *Nanomaterials*. **2018**, *8*, 970.

Chapter 4

Synthesis and Characterization of Poly (N-vinylcaprolactam)-Based (Co)polymers

In this chapter we report the synthesis and characterization of thermoresponsive homopolymer poly (N-vinylcaprolactam) (PVCL) and smart copolymers-based PVCL such as poly (N-vinylcaprolactam-*b*-vinylpyrrolidone) (PVCL-*b*-PVPON) and dual pH and temperature responsive poly (N-vinylcaprolactam-*b*-acrylic acid) (PVCL-*b*-PAA) by Reversible Addition-Fragmentation Chain Transfer (RAFT) polymerization and free radical polymerization methods respectively with the purpose of designing and developing a suitable and novel drug delivery system, which is composed of the stimuli responsive (co)polymers shell and magnetic nanoparticles core.

4.1. Living Polymerization

A living polymerization is strictly a chain propagation reaction that, after full monomer conversion, is still capable of propagation *via* addition of further monomer [1]. In an ideal case this occurs in polymerization reactions without any chain transfer and termination [2,3]. Furthermore, the rate of initiation should be fast compared to the rate of propagation, which results in the synthesis of polymer chains with an overall similar degree of polymerization [4].

The main living polymerization techniques are:

- Living anionic polymerization
- Living cationic polymerization
- Living ring-opening metathesis polymerization
- Living free radical polymerization
- Living chain-growth polycondensations

In this thesis we mainly focused our research activity on living radical polymerization to prepare poly N-vinylcaprolactam (PVCL) and (PVCL)-based copolymers containing PVCL-*b*-PVPON and PVCL-*b*-PAA as demonstrated in Figure 4.1, which will be then used to realize smart magnetic nanohybrids.

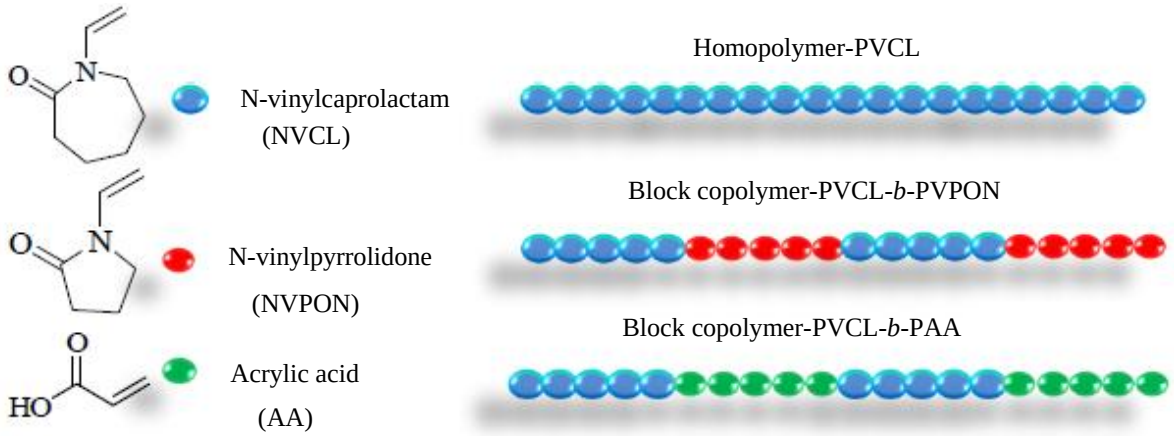

Figure 4.1 Representative schemes of the homopolymer and PVCL-based copolymers

4.2. Free Radical Polymerization

Free-radical polymerization is a method of polymerization by which a polymer forms through the successive addition of free-radical building blocks. Free radicals can be created by involving separate initiator molecules. Following its generation, the initiating free radical adds nonradical monomer units to grow the polymer chain.

4.3. Synthesis of Well-Defined PVCL-Based (Co)polymers by Controlled Radical Polymerization

N-vinyl caprolactam (NVCL) belongs to the family of un-conjugated monomers, and can be polymerized up to high molar mass by a conventional free radical polymerization process by using 2,2′-Azobis (2-methylpropionitrile) (AIBN) for instance as the free radical initiator in the bulk at 65 ^{o}C [5,6]. However, this process leads to highly polydisperse polymer, and does not allow accessing to more complex structures such as block copolymers. During the past decade, Controlled Radical Polymerization (CRP) techniques have been widely developed to give access to (co)polymers with precise molecular weight, low dispersity, and well-defined architectures that are specifically designed to fit the targeted applications. That is to say, a large spectrum of (co)polymers can be prepared by a well

controlled polymerization method with virtually any desired distribution of monomer units along the polymer backbone, or within any specific segment in a copolymer, called well-defined (co)polymer [7-9]. The most useful CRP strategies to prepare well-defined (co)polymers consist of Nitroxide-Mediated Polymerization (NMP) [10], Atom Transfer Radical Polymerization (ATRP) [11], Single-Electron Transfer polymerization (SET) [12], Reversible Addition–Fragmentation Chain Transfer polymerization (RAFT) [13], and Organometallic Mediated Radical Polymerization (OMRP) [14]. Up to now, a great variety of thermoresponsive macromolecules have been synthesized using CRP strategies [15,16]. However, CRP of un-conjugated monomers, such as NVCL, is not an easy task, since the highly active radical species derived from those monomers might result in significant retardation and/or completed inhibition of the polymerization [17,18]. Moreover, it is difficult to find a suitable reagent or catalyst, which induces the fast interconversion between the highly active radical and the dormant species. That is why even though PVCL has a long history, information on the precise synthesis of PVCL *via* CRP is relatively scarce. Since then, ATRP [19,20], OMRP [14,21] and RAFT [22-26] techniques were successively used to provide more sophisticated NVCL-based materials, and opened new doors in the precise design of thermoresponsive polymers for biomedical applications. In this section, the RAFT technique, used for controlling the NVCL polymerization, is discussed, and the preparation of advanced PVCL structures is highlighted.

4.4. RAFT Polymerization and Macromolecular Design via the Interchange of Xanthates (MADIX) of NVCL

Because NVCL is an un-conjugated vinyl monomer that leads to highly reactive growing radicals, the choice of the RAFT/Macromolecular Design *via* the Interchange of Xanthates (MADIX) controlling agent is of prime importance for the reactivation of the dormant PVCL chain and successful control over the polymerization [27]. RAFT/MADIX is based on a degenerative transfer mechanism due to the presence of a chain transfer agent (CTA) with the general structure RSC(=S)Z. The CTA is typically a thiocarbonyl thio compound featuring two substituents that are usually abbreviated as R- and Z-group. These two substituents, R (radical leaving group) and Z (stabilizing group) have a profound influence on the reactivity of the CTA and on the RAFT process [28], so their appropriate choice is a key point for a RAFT polymerization. Various thiocarbonylthio compounds showed to be effective for this purpose including aromatic and aliphatic dithioesters (a),

trithiocarbonates (b), dithiocarbamates (c), and xanthates (d-f) [29] as displayed in Figure 4.2.

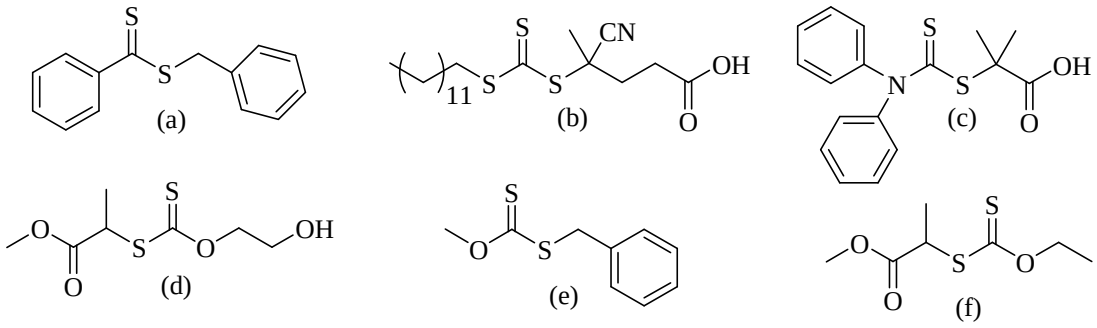

Figure 4.2 Structures of chain transfer agents used for RAFT polymerization

The mechanism of the RAFT process is depicted in Figure 4.3. The RAFT process can be divided into five distinct reaction sequences: (I) Initiation, (II) pre-equilibrium, (III) reinitiation, (IV) main-equilibrium, and (V) termination. The initiation occurs *via* the formation of primary radicals, I, that form during the decay of a radical initiator, I_2, with the rate coefficient k_{de}. The formed radicals react with monomers to form short oligomeric chains $P^{\bullet}m$ with the rate coefficient k_{ini} until a radical reacts with a CTA molecule in pre-equilibrium step. The initiator derived chain ($P^{\bullet}m$), adds to a CTA molecule with the rate constant $k_{add.}$ Subsequently the thiocarbonyl centered radical, undergoes *β*-fragmentation with the rate coefficient k_{β}, which leads to the formation of a free radical ($R^{\bullet}$) and a thiocarbonyl thio capped chain.

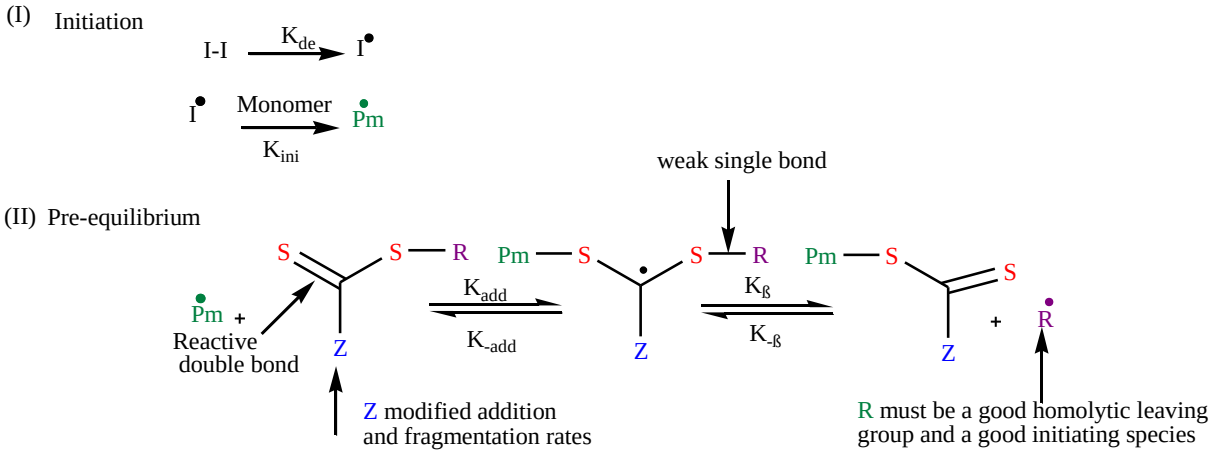

(III) Reinitiation

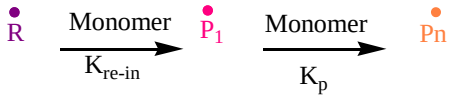

(IV) Main-equilibrium

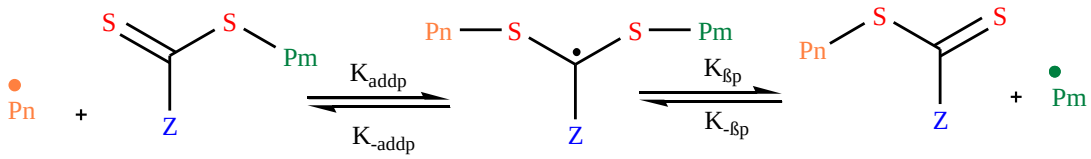

(V) Termination

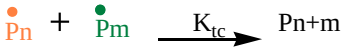

Figure 4.3 Mechanism of RAFT polymerization

As depicted in Figure 4.3 the formed $R^{\bullet}$ radical should reinitiate the polymerization effectively with rate constant $k_{re\text{-}in}$ to provide macroradical $P^{\bullet}_1$. Whenever a fragmentation takes place, the macroradical can add new monomers with the propagation rate constant k_p. Afterward, the main equilibrium starts when CTA molecules-chain end adds macroradical $p^{\bullet}n$ again with rate coefficient k_{addP}, and subsequently β-fragmentation with the rate coefficient $k_{\beta p}$ takes place. Finally, termination reactions occur intrinsically by free radical polymerization, or radical recombination with k_{tc}.

The RAFT process is the most useful controlled radical polymerization technique involving a large variety of monomers to synthesize well-defined water-soluble (co)polymers [30]. This technique is especially attractive as it is compatible with almost all common vinyl monomers, and it can be performed under mild reaction conditions. Additionally, chain-end transformation of prepared polymer after RAFT polymerization is comparably simple, which qualifies this technique for further polymer functionalization [31,32]; therefore, newly developed RAFT polymerization method allows to prepare NVCL-based materials with tunable size (from nm to μm), with a large variety of structures (e.g., hydrogels, micelles, core/coronahybrids), and surface functionality that can be used for the accommodation of cargo molecules. Furthermore, as RAFT polymerization is free from possibly toxic metal

catalysts, it is well suited for synthesis of polymers, in particular smart polymers, which are appealing for medical applications.

Smart polymers or stimuli-responsive polymers have been widely investigated as a building block to realize therapeutic agent for smart drug delivery since they can undergo relatively large physiochemical changes in response to external and internal stimuli, such as variation in temperature, pH, or ionic strength [33]. On the ground that some disease microenvironments manifest themselves with a remarkable change in some specific physiological factors such as temperature, the potential *in vivo* application of temperature-sensitive polymers is significantly evidenced. In fact, thermoresponsive polymers in aqueous medium exhibit a critical temperature, around which a sudden change in the solvated state occurs. Polymers, which undergo a hydration/dehydration transition in aqueous medium upon heating, possess a so-called lower critical solution temperature (LCST) [34]. As shown schematically in Figure 4.4, thermoresponsive polymer can show a coil–globule transition in water at temperature above LCST, or reversible conformational change from a swollen hydrophilic state to a shrunken hydrophobic one, resulting in a volume decrease due to expelling of the aqueous content from its chains. So the polymer solution above the LCST is cloudy, whereas below the LCST appears as a clear and homogeneous solution. .

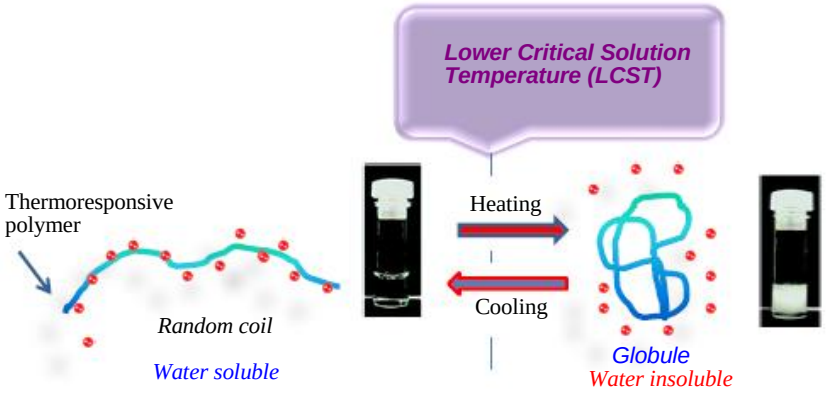

Figure 4.4 Hydration/dehydration behavior of thermoresponsive polymer upon heating

Importantly, the thermo-induced hydration/dehydration transition of this type of polymers can be utilized to trigger the drug release just by response to the temperature variation. For smart drug release using heat as a trigger, the smart drug carriers, which is usually made up of magnetic nanoparticles core and thermoresponsive polymer shell, should ideally retain their load at body temperature (~ 37 °C), and release the drug within a locally heated tumour at the therapeutic temperature for hyperthermia 41 ^{o}C−48 °C. That is to say, the smart

nanocarrier loaded with anti-cancer drug, is injected into the bloodstream, and targeted to the tumour using an external magnetic field gradient, or by chemical targeting. When an alternating magnetic field is applied after localization, the iron oxide magnetic cores of the composite particles generate heat, raising the temperature of the tumour and resulting in hyperthermia. At the same time, the heat generated is conducted from the core to the surrounding polymer and temperature increase of the polymer shell above the LCST, triggers the release of the drug [35]. To satisfy this requirement, thermoresponsive macromolecules should possess LCST slightly above the physiological temperature 38 °C–48 °C. Based on the type of polymer, LCST can be tuned *via* shifting the hydration/dehydration balance, basically by well-controlled RAFT polymerizing technique with another comonomer as well as by varying concentration, pH, and length of polymeric chain.

Thermoresponsive poly (N-vinylcaprolactam) with its unique properties attracted our attention for development of novel drug nanocarriers, complying with main objectives of this thesis. As a case in point, PVCL is a water soluble and temperature-responsive polymer with the LCST range of 31 ^{o}C–50 ^{o}C [36]. LCST value of PVCL varies with the polymer chain length and concentration corresponding to "classical" Flory-Huggins thermoresponsive behavior in water (Type I); that means, LCST of PVCL decreases with increasing polymer chain length and/ or concentration. [37]. Consequently, this unique feature allows modulating the LCST of a PVCL-based thermoresponsive system by controlling the molecular weight, without using any comonomer. Moreover, PVCL has been shown to support high cell viability and low cytotoxicity especially in the hydrophobic state above the LCST [38]. Importantly, the nitrogen atom in the caprolactam ring is directly connected to the chain backbone, so the hydrolysis of PVCL, if it occurs, will not produce a small toxic amide compound [39]. These merits make PVCL highly useful for biomedical applications such as controlled drug delivery and *in vivo* drug release [40].

In spite of the fact that synthesis and properties of PVCL and PVCL-based (co)polymers have been rarely investigated due to the synthetic challenges associated with high reactivity of vinyl monomers, we synthesized PVCL, poly (N-vinylcaprolctam-*b*-N-vinylpyrrolidone) PVCL-*b*-PVPON, and poly (N-vinylcaprolactam-*b*-acrylic acid) PVCL-*b*-PAA in order to prepare novel nontoxic, biocompatible double-hydrophilic block copolymers with temperature-induced amphiphilicity near to 45 ^{o}C. Furthermore, poly acrylic acid (PAA) and poly (N-vinylpyrrolidone) (PVPON), whose monomer unit structure is

similar to PVCL, are both water soluble polymers, and broadly used for surface decoration of nanoparticles in biomedical field because of their hydrophilicity and biocompatibility [41]. Moreover, the structural similarity of those monomers gives a unique opportunity for fine tuning of temperature-induced transitions and copolymer assembly.

Surface modification of magnetic nanoparticles with this type of (co)polymers, consequently, leads to the preparation of stimuli responsive interfaces, which reveal thermoresponsive behavior in response to small changes of environmental temperature, which is aim of this thesis. Besides, PAA units in copolymer backbone with a high binding capacity and a high density of reactive functional groups, providing a strong linkage between the iron oxide and biomolecules, making it very attractive in nanomedicine [41].

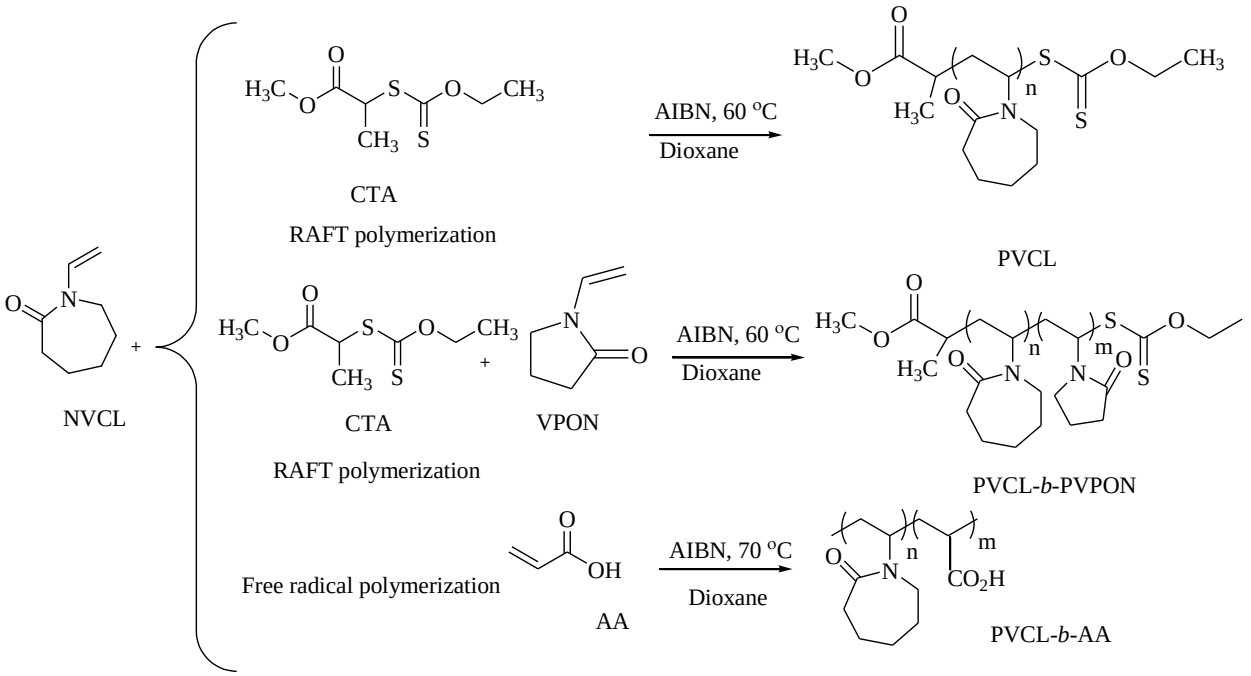

Scheme 4.1 Synthesis of PVCL, PVCL-*b*-PVPON, and PVCL-*b*-PAA *via* RAFT and free radical (co)polymerization

In this work, we followed E. Kharlampieva's [42] and Jean-Daniel Marty's procedures [43] for the synthesis of temperature-responsive (PVCL) and (PVCL-*b*-PVPON) diblock copolymers with well-controlled molecular weights by applying sequential RAFT polymerization using a dithiocarbamate as the chain transfer agent (CTA) [44], and (PVCL-*b*-AA) was also synthesized by using free radical polymerization approach as shown

in Scheme 4.1. Diblock copolymers were synthesized and successfully characterized using ^{1}HNMR, Gel Permeation Chromatography (GPC), Dynamic Light Scattering (DLS), Transmission Electron Microscopy (TEM), UV spectroscopy, and Fourier Transform Infrared spectroscopy (FTIR).

4.5. RAFT Polymerization of PVCL and Characterization

RAFT CTA was prepared according to the literature [45] by reaction between methyl-2-bromopropionate and O-ethyl xanthic acid potassium salt in methanol as displayed in Scheme 4.2. Structure of final product was assigned by ^{1}HNMR (400 MHz, $CDCl_3$) to determine the molecular formula of an obtained compound. The synthesis pathway and spectrum of CTA are reported with more details in materials and method sections, Appendix A.3.

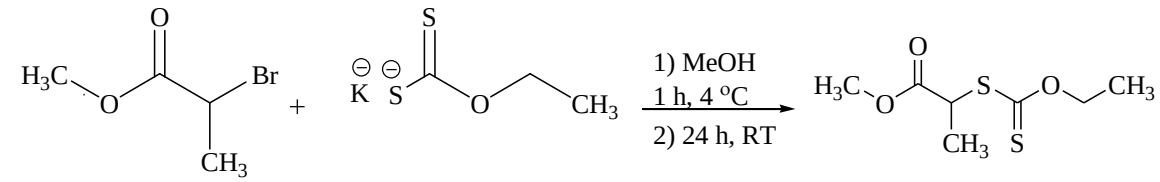

Methyl-2-Bromopropionate | Potassium Ethyl Xanthogenate | Chain Transfer Agent (CTA)

Scheme 4.2 Synthesis of Chain Transfer Agent

RAFT polymerization of vinylcaprolactam was performed according to the literature [43] by mixing NVCL, CTA, and AIBN as initiator in dioxane (Scheme 4.3). Moreover, ^{1}HNMR analysis of polymer was conducted in order to access the structure of PVCL [46]. The synthesis approach in addition to ^{1}HNMR spectrum are fully described in materials and method sections, Appendix A.4, Figure A.1.

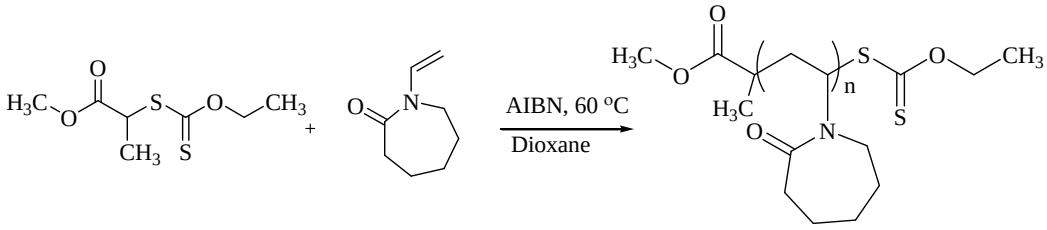

Scheme 4.3 RAFT Polymerization of NVCL

The degree of polymerization (DP), or number of repeating units of PVCL, *n*, was determined from its ^{1}HNMR spectrum by comparing the relative proton peak intensity of a known moiety (typically an end-group(s) with a known number of protons) to that of the repeating chain unit of interest, according to the formula [47]:

$$nx = \frac{ax\ my\ ny}{ay\ mx}$$

Where ax (ay) are the area or intensity of the ^{1}HNMR peak of moiety *x* and *y*, nx (ny) are the number of repeating units and mx (my) are the number of protons. Consequently, the number average molecular weight (M_n) can be calculated by substituting for *n* in the equation:

$$M_n = nM_0 + M_e$$

M_0 is the molecular weight of one repeating unit, and M_e is the combined molecular weight of the end-groups.

To calculate the number of repeating units (*n*) in the PVCL chain, the peak areas of CH_3O-(OMe, δ 3.18) and H_{a-} (H_a−NCH−of the α position, δ 4.39) were obtained from the ^{1}HNMR spectrum (Appendix A.4, Figure A.1), and appropriately substituted into the equation, obtaining *n*=72.

The M_n of PVCL was then estimated by the summation of the atomic masses of the constituent atoms

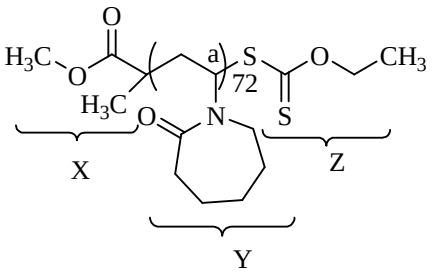

M_n=X+(Yx72)+Z

M_n=10216 g mol $^{-1}$

Molecular weight distribution of the produced polymer was determined by gel permeation chromatography as shown in Figure 4.5 coupled with Waters 410 Differential Refractometer and A Plgel guard column and two PLgel Mixed D 5 μm columns. The eluent employed was THF at a flow rate of 1.0 mL min^{-1}. Polystyrene standards were used for calibration as well.

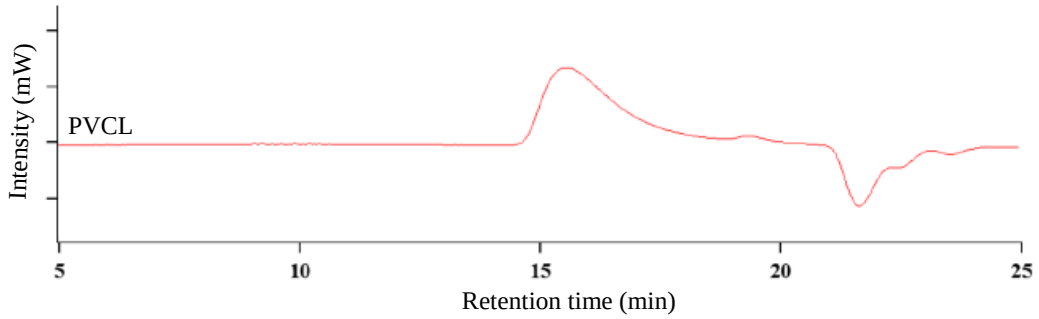

Figure 4.5 GPC curve of PVCL (M_n ~ 10857 g mol^{-1})

Number-average molecular weight (M_n), weight average molecular weight (M_w), and polydispersity index (M_w/M_n) of PVCL were determined by GPC analysis, and results were 10857 g mol^{-1}, 12160 g mol^{-1}, and 1.12 respectively. In fact, M_n obtained by GPC is in good agreement with one obtained by ^{1}HNMR analysis (M_n ~ 10216g mol^{-1}). These results demonstrate that the RAFT polymerization of PVCL provided a polymer with well controlled *Mw* since the molecular weight distribution was relatively narrow with M_w/M_n 1.12, as evidenced by the GPC results.

The FTIR analysis of the synthesized polymer was performed to confirm the desired product was obtained promisingly. FTIR spectrum of sample was in good agreement with published results [43], and confirmed that polymer was successfully achieved by RAFT polymerization. (FTIR spectrum is reported and discussed in materials and method section, Appendix A.4, Figure A.2).

The mean particle size and particle size distribution of the aqueous solution of PVCL were determined by Dynamic Light Scattering (DLS) measurement on 2.0 mL of sample with concentration of 1.0 mg mL^{-1}. DLS of the polymer solution showed narrow size distribution (PDI, 0.294) with the intensity-average hydrodynamic diameter of 59.0 nm, obtained from three independent runs (15 measurements, Figure 4.6).

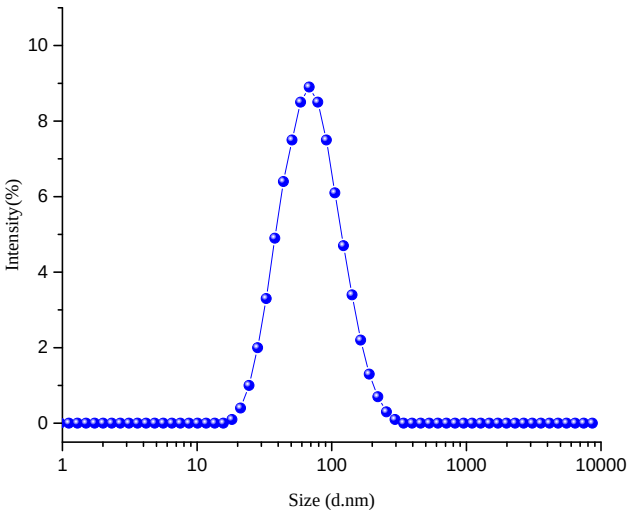

Figure 4.6 Statistics intensity distribution of size for a PVCL nanosphere aqueous solution

The TEM analysis of the polymer structure in aqueous solution was performed to investigate morphology of macromolecular chains. The TEM image, reported in Figure 4.7, shows spherical structure in solution with average diameter ranging from 52.0 to 132.0 nm as obtained from a statistical analysis over 50 nanoparticles, performed by platform software (Olympus).The polymer size results are in good agreement with the average hydrodynamic diameter of 59.0 nm obtained by the DLS.

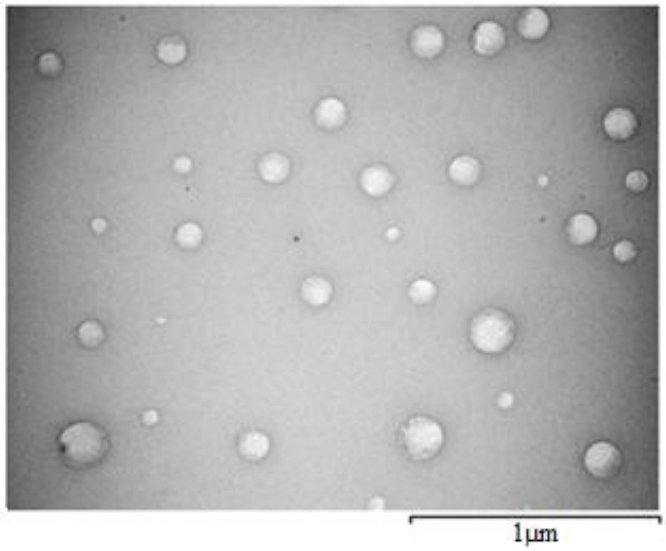

Figure 4.7 TEM images obtained from 1.0 mg mL^{-1} aqueous solution of PVCL nanosphere

Turbidity and DLS measurements were carried out to illustrate the phase transition behavior of the smart polymer in aqueous solutions. For this purpose, the LCST of aqueous solution of PVCL at different concentrations from 0.25 mg mL^{-1} to 2.0 mg mL^{-1} was determined using a UV–Vis spectrophotometer equipped with a temperature controller, and the measurements were performed by monitoring change in transmittance as a function of temperature at 500 nm wavelength. The LCST value was taken as the inflection point of the transmittance curve versus temperature during heating cycle.

As mentioned before in aqueous solution, PVCL exhibits phase transition behavior in the range from 31 ^{o}C to 50 ^{o}C depending on molecular weight and polymer concentration. In fact, LCST could be shifted towards lower value with increasing concentration (Flory–Huggins change phase behavior, (type I). As a result, LCST could be easily modulated in order to be applicable for effectively controlled drug delivery *in vivo* application.

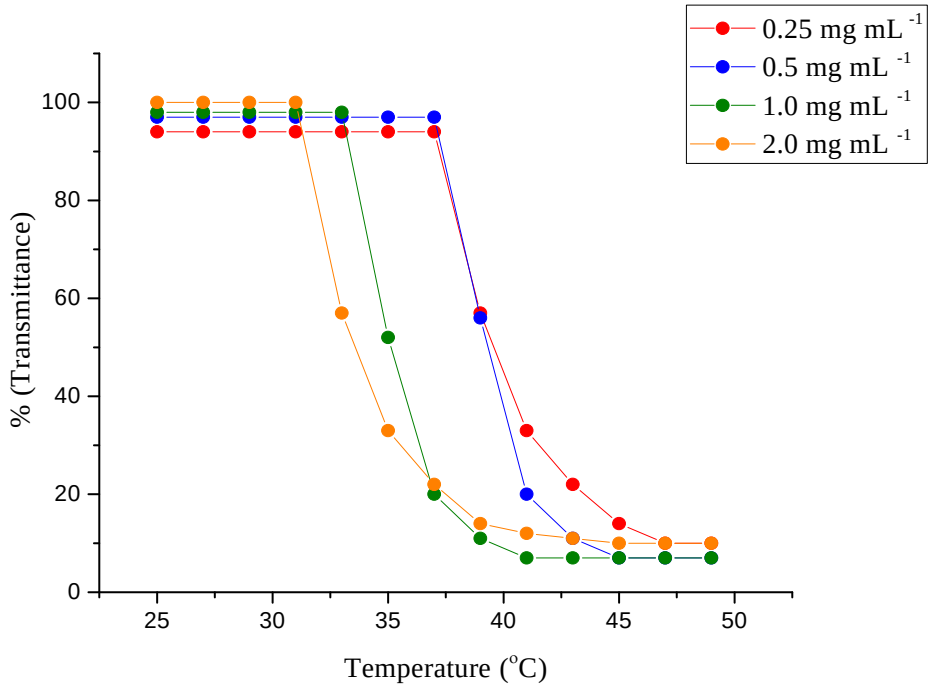

Figure 4.8 Turbidimetric analysis of aqueous solution of PVCL at different concentrations

The type I phase-change behavior of PVCL is well evidenced by data reported in Figure 4.8. The LCST of homopolymer PVCL, indeed, decreased to lower temperature when concentration increased (33 ^{o}C and 35 ^{o}C at 2.0 mg $mL^{-1}$and 1.0 mg mL^{-1} compared to

39 °C and 40 °C at 0.5 mg mL^{-1} and 0.25 mg mL^{-1} respectively). These results confirm that by varying the concentration of PVCL aqueous solution, the LCST of a given polymer can be simply tuned to obtain desired value.

DLS analysis was performed to evaluate the size distribution of polymer solution above and below LCST. According to the Figure 4.9, DLS results reveal the hydrodynamic size of PVCL solution is highly temperature dependent. That means, the hydrodynamic size at the critical temperature is much larger than that one at temperature below LCST, and then begins decreasing with further raising the temperature by 5–10 °C. The onset of temperature at which the abrupt size increase occurred was considered as the LCST value.

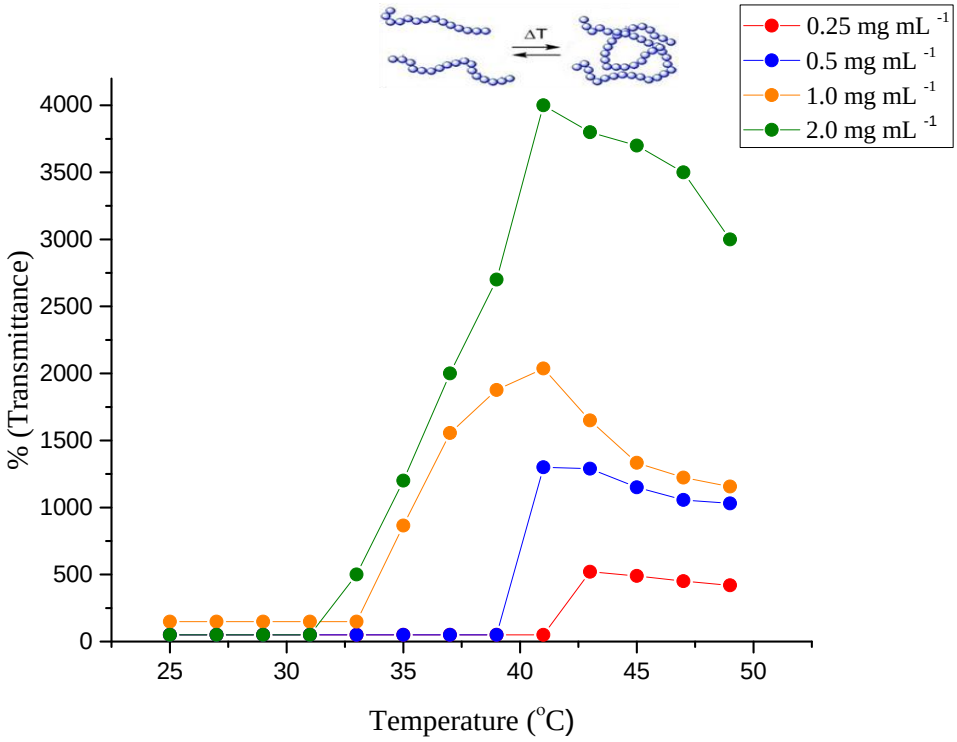

Figure 4.9 Hydrodynamic sizes of aqueous PVCL solution with various concentrations as a function of temperature

For instance, 2.0 mg mL^{-1} aqueous solution of PVCL gave a low hydrodynamic size around 50.0-60.0 nm at 25 °C (below LCST); however, this size value highly increased from 31 °C upon the increase of temperature. The hydrodynamic size of the PVCL was found to be 4000 nm at 39 °C, and began to decrease slightly to 3800 nm, with further raising the temperature to 40 °C. Thus, 31 °C is considered as LCST of polymer. The same trend was

observed also for less concentrated PVCL although the total size variation decreased by decreasing the concentration of polymeric solution.

LCST values of PVCL solutions with various concentrations, measuring by two different techniques, are compared and presented in table 4.1.

Concentration mg mL^{-1}	LCST (^{o}C)-UV	LCST (^{o}C)-DLS
2.0	33	31
1.0	35	33
0.5	39	39
0.25	40	43

Table 4.1 LCST value of PVCL by DLS measurement and UV spectroscopy

According to the data reported in table 4.1, the LCST values obtained from DLS analysis are in good agreement with those obtained from the turbidimetric studies, and demonstrate that the LCST can be well controlled, and increased from 31 ^{o}C to 43 ^{o}C, when the concentration of PVCL solution is decreased from 2.0 to 0.25 mg mL^{-1} respectively.

As seen from DLS data, hydrodynamic size of polymer abruptly increases when the temperature is raised above LCST. This phenomenon is relevant to the formation of large aggregates that occurs as a consequence of gradual dehydration of PVCL after heating above the LCST. That is to say, at temperature ~ LCST polymer-bounded water molecules are released to the solvent as the polymer chains collapse, generating mesoglobules, (i.e. uniform spherical aggregates stable in solution), which are also stabilized against further aggregation *via* hydrophilic surface. Then, upon increasing temperature, this structure can further expel water molecules progressively, leading to the formation of aggregates of increasing size as displayed in Figure 4.10. With the further increase in temperature, larger aggregates dissociate into smaller polymer structure as a result of the crowding effect, i.e. when the configurational entropy of macromolecular chains decreases in a crowded environment due to excluded volume effects, the formation of much smaller structures is favoured, as indeed observed by DLS measurements.

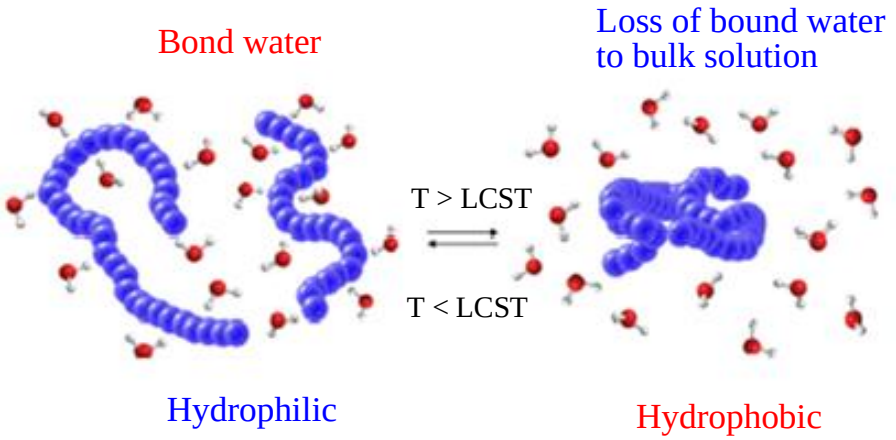

Figure 4.10 Hydrophilic/hydrophobic transition of polymer solution above LCST leading to the size variation [48]

4.6. RAFT Polymerization and Characterization of PVCL-b-PVPON

Since the primary objective of this thesis is to fabricate thermoresponsive magnetic nanohybrids for hyperthermia cancer treatment with thermal response in the 41 ^{o}C−48 °C range, it is essential to design polymer with phase transition temperature above physiological temperature up to hyperthermia range. The LCST of PVCL can be modulated by controlling the molecular weight of polymer segments, and thus by adding another comonomer in the polymer backbone. To this aim poly (N-vinylcaprolactam-*b*-N-vinypyrrolidone), (PVCL-*b*-PVPON) was prepared, and then systematically investigated.

PVCL-*b*-PVPON was synthesized by RAFT polymerization according to the same procedure described previously in section 4.5 [44] (the synthesis procedure is described with more details in Appendix A, section A.5). NVCL, N-vinylpyrrolidone (NVPON), CTA, and AIBN as initiator were mixed in dioxane and kept under stirring for 24 h at 60 ^{o}C as exhibited in Scheme 4.4. ^{1}HNMR and GPC were also employed to check the molecular structure and *Mw* of prepared copolymer respectively.

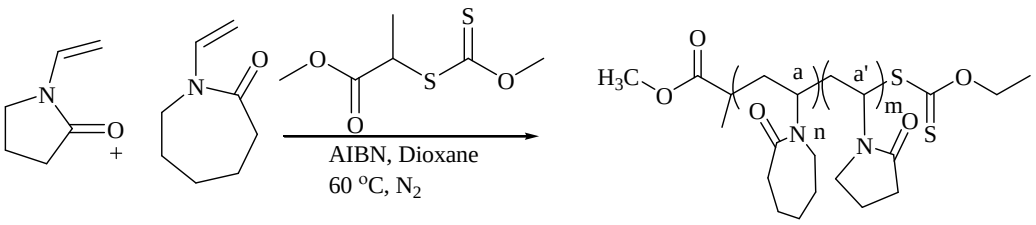

Scheme 4.4 RAFT polymerization of block copolymer PVCL-*b*-PVPON

The degree of polymerization (DP) of a PVCL-*b*-PVPON was determined from ^{1}HNMR spectrum shown in materials and method section (Appendix A.5, Figure A.3) by using the same formula reported in section 4.5. For this purpose, the peak areas of CH_3O- (OMe, δ 3.54), H_{a-} (H_a–NCH–of the *α* position of caprolactam ring, δ 4.38), and of H_a' (H_a'–NCH–of the *α* position of pyrrolidone ring, δ 3.69), were used, and the number average molecular weight (M_n) was calculated by substituting for *n* and *m* in the formula:

$$M_n = nM_0 + mM_1 + M_e$$

Where *n* and *m* are the number of repeating units of PVCL and PVPON blocks, respectively. M_0 is the molecular weight of PVCL repeating unit, M_1 is molecular weight of PVPON block, and M_e is the combined molecular weight of the end-groups. By calculation of nx and mx the M_n of copolymer was estimated by the summation of the atomic masses of the constituent atoms:

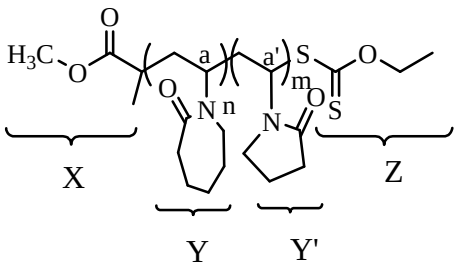

Mn=X+(133xY)+(26xY')+Z

Mn= 21610.21 g mol $^{-1}$

Gel permeation chromatography analysis was carried out to determine molecular weight distribution of the PVCL-*b*-PVPON by following the same procedure mentioned in section 4.5, and result is displayed in Figure 4.11. THF was employed as eluent at a flow rate of 1.0 mL min^{-1}. Polystyrene standards were used for calibration as well.

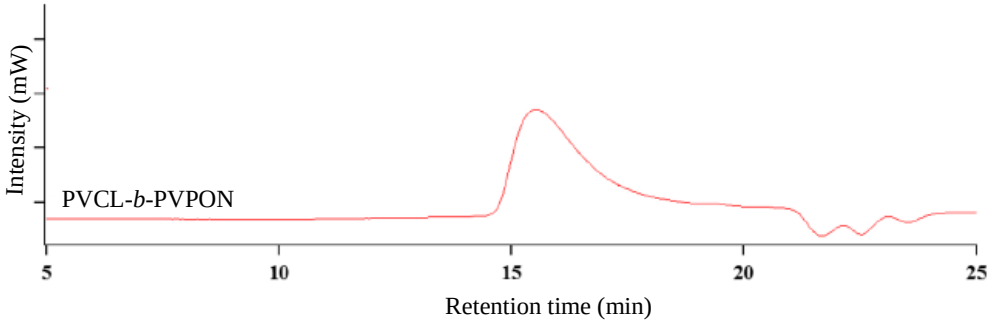

Figure 4.11 GPC curve of PVCL-*b*-PVPON (M_n ~ 20857 g mol^{-1})

Number-average molecular weight (M_n), weight average molecular weight (M_w), and polydispersity index (M_w/M_n) of PVCL-*b*-PVPON obtained by GPC analysis were 20857 g mol^{-1}, 19460 g mol^{-1}, and 1.08 respectively. M_n estimated by GPC analysis is in accordance with M_n obtained by ^{1}HNMR analysis. These results reveal that the PVCL-*b*-PVPON obtained by RAFT copolymerization has a narrow molecular weight distribution with M_w/M_n value 1.08 as evidenced by the GPC results.

FTIR spectrum, which is reported in Appendix A.5, Figure A.4 demonstrated that copolymer was successfully prepared, and the polymerization proceeded correctly.

Dynamic Light Scattering (DLS) measurement was performed through three independent runs (15 measurements) to determine mean particle size and particle size distribution of PVCL-*b*-PVPON aqueous solution on 2.0 mL of sample with concentration of 1.0 mg mL^{-1}. The obtained result shows that the copolymer has an average hydrodynamic diameter of 86 nm with narrow size distribution (PDI, 0.187), as shown in Figure 4.12.

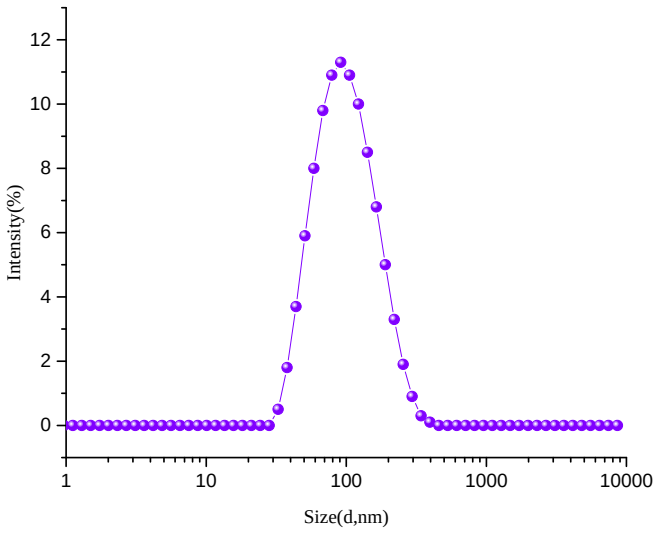

Figure 4.12 Size distribution of PVCL-*b*-PVPON

In order to investigate morphology of macromolecular chains, TEM analysis of the copolymer structure in aqueous solution was performed. The TEM image in Figure 4.13 demonstrates PVCL-*b*-PVPON has spherical shape with the average diameter ranging from 20.0 to 89.0 nm as obtained from a statistical analysis over 80 nanoparticles, performed by platform software (Olympus). The copolymer size is in good agreement with the average hydrodynamic obtained by the DLS.

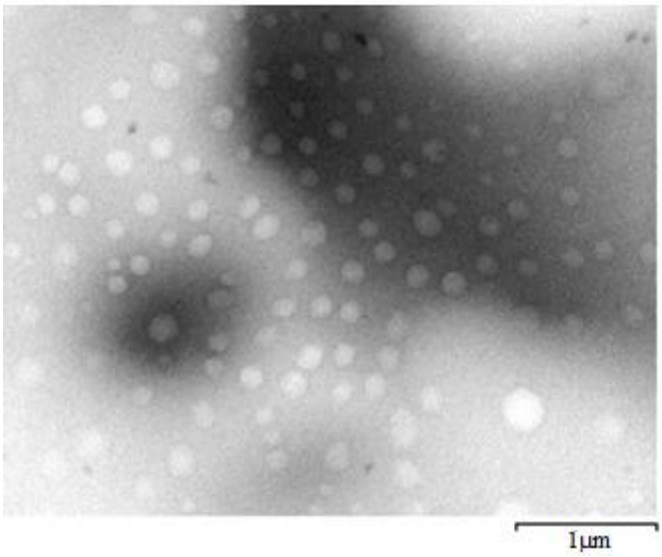

Figure 4.13 TEM images of PVCL-*b*-PVPON aggregates in water

Turbidity, dynamic ^{1}HNMR, and DLS measurements were carried out to determine the critical temperature of copolymer in aqueous solutions.

As mentioned previously, the presence of the hydrophilic component in the thermosensitive polymer with a certain LCST value (denoted as cloud points, Tc) is known to shift the temperature at which the collapse of the hydrophobic backbone occurs to higher values [49,50]. The effect of the hydrophilic PVPON block on the LCST values was studied using turbidimetry measurements performed with a UV–Vis spectrophotometer equipped with a temperature controller. The measurements were carried out by monitoring change in transmittance as a function of temperature at 500 nm wavelength, and results are plotted in Figure 4.14. The cloud point was taken as the inflection point of the transmittance curve versus temperature during heating cycle.

Corresponding to this technique, the diblock copolymer solutions were slowly heated from 25 ^{o}C to 51 ^{o}C. When the solution temperature reached the cloud point of PVCL-*b*-PVPON, the copolymer solution became turbid, and became clear again when the solution was cooled to T < Tc, demonstrating the transition is reversible. Moreover, the cloud point values of the diblock copolymers were compared with those of PVCL at the same concentration, and results are summarized in table 4.2.

Figure 4.14 shows that the transmittance of PVCL-*b*-PVPON with different concentration ranges between 0.25 mg mL^{-1} to 2.0 mg mL^{-1} started decreasing at a higher temperature than PVCL with same concentration reported in table 4.2.

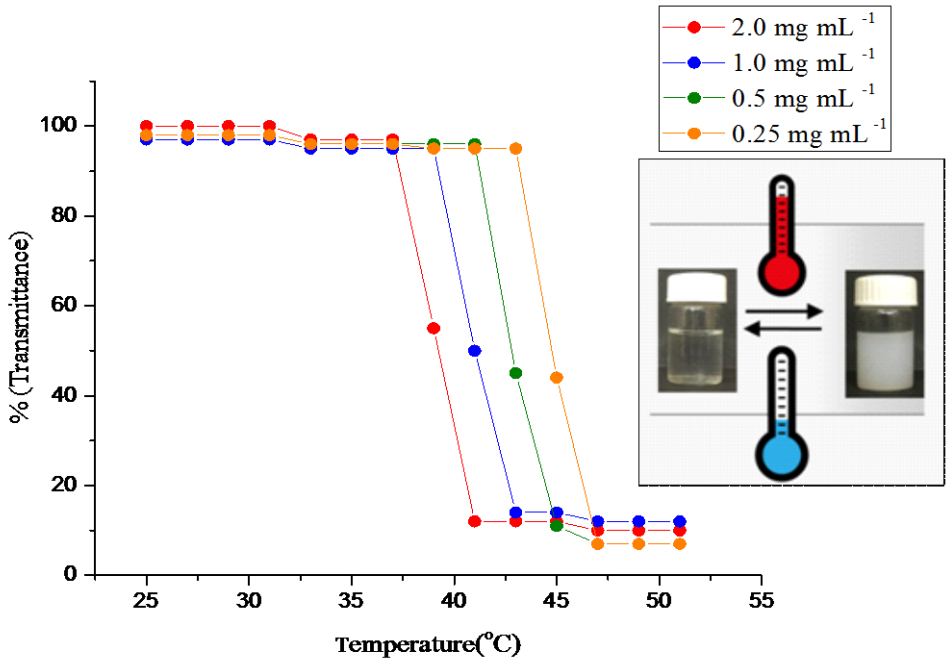

Figure 4.14 Plot of transmission vs. temperature for the PVCL-*b*-PVPON copolymer aqueous solutions with different concentrations from (2.0 mg mL^{-1} to 0.25 mg mL^{-1}) under gradual heating (2 $^{o}C\ min^{-1}$)

In fact, the presence of hydrophilic PVPON component shifted the LCST value of the diblock copolymer of about 6-9 ^{o}C in comparison with PVCL homopolymer due to the augmentation of hydrogen-bonding capabilities of the constituent monomer units. Consequently, the LCST of a given copolymer can be ‘‘tuned’’ as desired by variation in hydrophilic comonomer (NVPON) content and concentration of polymeric solution owing to the phase transition behavior type I of PVCL segment, as discussed in section 4.5.

Concentration of PVCL (mg mL^{-1})	LCST (^{o}C)	Concentration of PVCL-*b*-PVPON (mg mL^{-1})	LCST (^{o}C)
2.0	33	2	39
1.0	35	1	42
0.5	39	0.5	44
0.25	40	0.25	46

Table 4.2 LCST of PVCL-*b*-PVPON in comparison with PVCL

Nowadays, proton nuclear magnetic resonance (^{1}HNMR) spectroscopy method is widely used for investigation of the changes in the chain structure and dynamics during temperature-induced phase separation in polymer solutions and hydrogels [51]. The coil-globule transition leads to a pronounced decrease of the integral intensity of the polymer groups in the NMR spectra, indicating the formation of more compact structures. It allows estimation of the phase transition temperature (determined as an onset temperature of the collapse) and the fraction of mobile component in polymer network.

In the following, the temperature-induced collapse of PVCL segment in PVCL-*b*-PVPON diblock copolymer was investigated by ^{1}HNMR spectroscopy. Figure 4.15 displays ^{1}HNMR spectroscopy results for PVCL-*b*-PVPON in deuterium oxide at 25 ^{o}C and 45 ^{o}C with the concentration of 1.0 mg mL^{-1}. At the lower temperature, the diblock copolymer is molecularly dissolved in water and all peaks from PVCL and PVPON segments are present in the spectrum (Figure 4.15 (a)). The structures of PVCL and PVPON are similar with peaks in the region 1-3.5 ppm (Figure 4.15 (a)). The resonance band at 4.4 ppm (25 ^{o}C) is due to the proton (H_X) in α-position of PVCL carbonyl group. The peaks of the proton (H_Y) at α-position of PVPON carbonyl group are in the range of 3.5–4.0 ppm. However, increasing temperature to 45 ^{o}C causes the collapse of PVCL blocks and self-assembly of the PVCL-*b*-PVPON copolymer chains as evidenced by the attenuated peaks from PVCL block, which are present between 4 and 5.5 ppm, whereas the peaks from PVPON (3.5–4.0 ppm) segment, which are still soluble at this temperature, are observed in the spectrum (Figure. 4.15 (b)). Noticeably at 45 ^{o}C, the PVCL resonance peak intensity is significantly lowered than one at 25 ^{o}C because of the highly restricted motions of the PVCL segments due to the PVCL collapse. Thus, dynamic ^{1}HNMR results confirmed that aqueous polymer solution at concentration of 1.0 mg mL^{-1} has LCST over 40 ^{o}C in accordance with turbidity results.

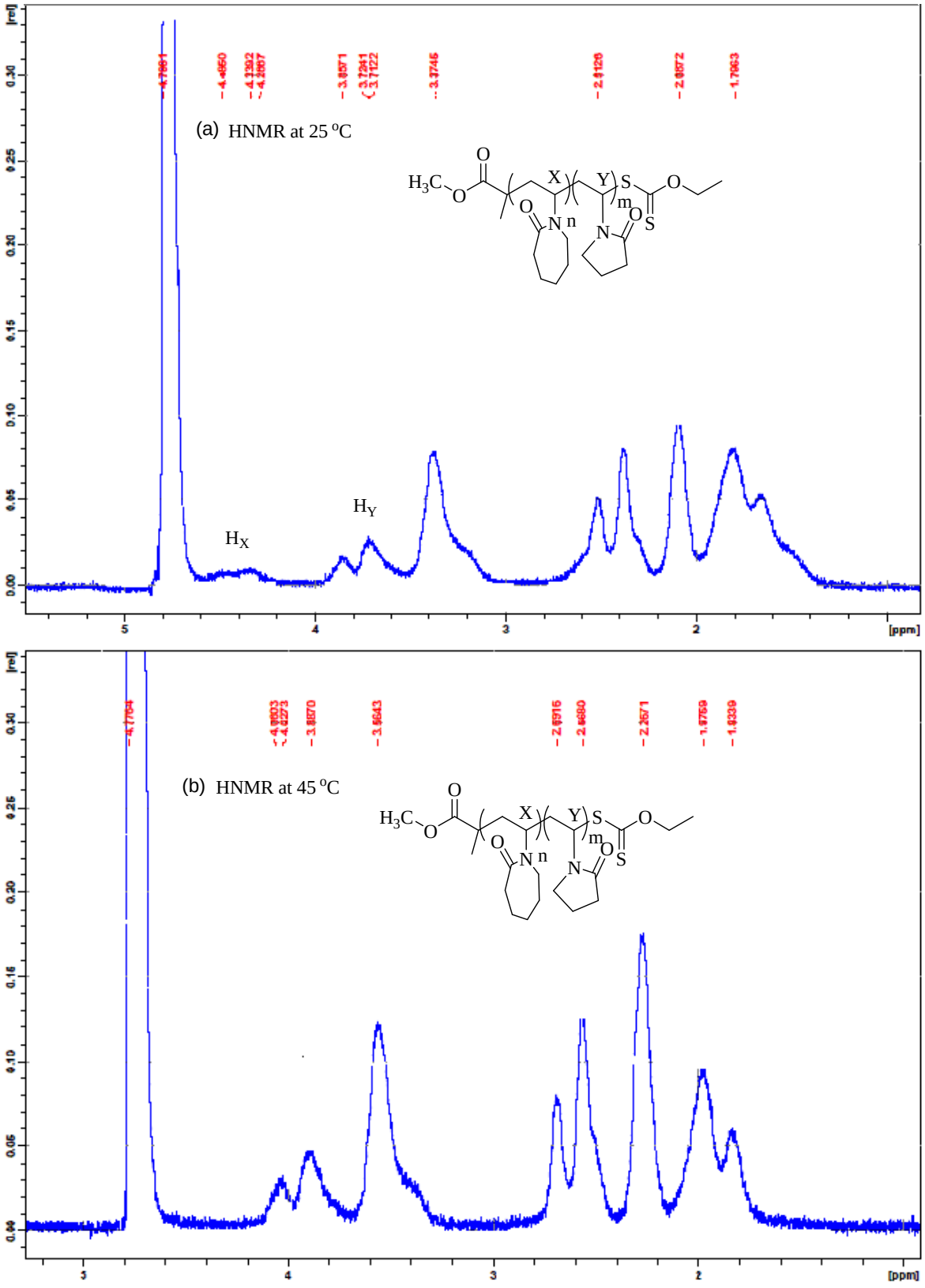

Figure 4.15 ^{1}HNMR spectra of PVCL-*b*-PVPON in D_2O (1.0 mg mL^{-1}) at 25 °C (a) and 45 °C (b)

For further investigation on temperature-triggered self-assembly of PVCL-*b*-PVPON diblock copolymer in water, DLS analysis was performed, and evolution of hydrodynamic sizes of PVCL-*b*-PVPON diblock copolymers as a function of temperature is plotted in Figure 4.16.

The hydrodynamic size (diameter) of the aqueous copolymers solution with different concentrations was around 80.0 nm below 40 ^{o}C (below LCST). However, at the temperatures close to the LCST, the size increased to 230.0 nm and 1714.0 nm for the lowest (0.25 mg mL^{-1}) and highest (2.0 mg mL^{-1}) concentrations respectively. This phenomenon has been observed earlier for PVCL homopolymer shown in Figure 4.9, and was explained by the occurrence of large micelle aggregates.

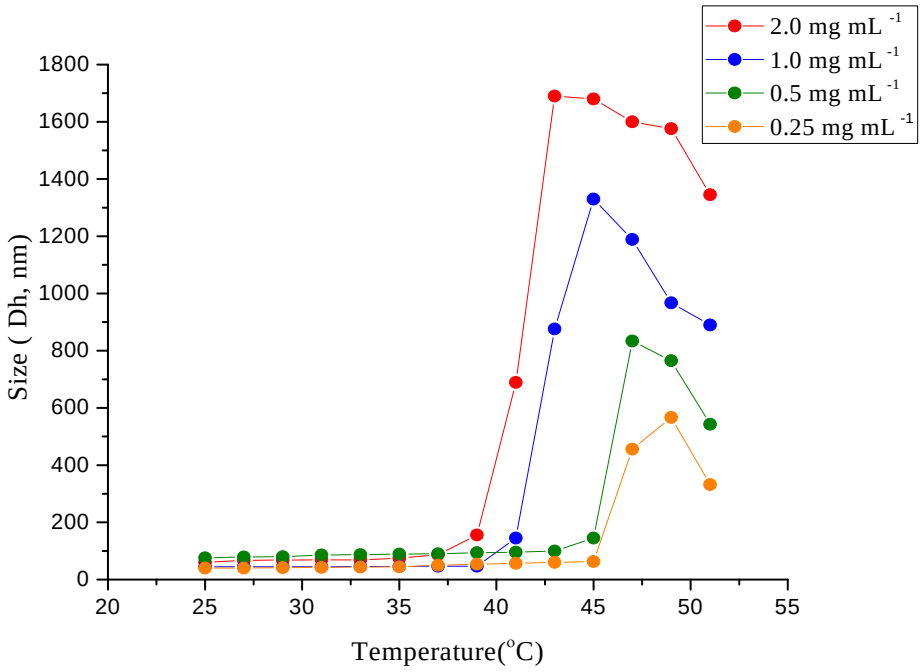

Figure 4.16 Temperature size dependence of PVCL-*b*-PVPON in aqueous solution

In fact, at temperature above LCST, hydrophilic structure of copolymer changed to hydrophobic, which caused clouding of the solution due to the hydrophobic interactions between the polymer chains followed by their aggregation. At the temperature above LCST, indeed, the formation of water-polymer hydrogen bonds becomes less favorable relatively to polymer-polymer interactions, so that monomer units of polymer first interact with their nearest neighbors on the same macromolecule, and then they associate with surrounding polymeric chains [52]. Polymer-polymer hydrophobic interactions are faster in a highly

concentrated solution, leading to the formation of bigger aggregates, and subsequently to the abrupt size increase; therefore, the evolution of hydrodynamic size of copolymer upon heating is extremely high, and is larger for more polymer concentrated solution. As an illustration, polymer solution with concentration of 2.0 mg mL^{-1} showed size variation from 80.0 nm to 1714.0 nm, while polymer solution with 0.25 mg mL^{-1} revealed a less marked size variation from 80.0 nm to 230.0 nm.

LCST of aqueous copolymer solution with different concentrations, measured by DLS and UV analyses, are compared and reported in table 4.3. As seen, the LCST values are in accordance with those obtained from the turbidimetric studies, and confirm Flory–Huggins change phase behavior.

Concentration mg mL^{-1}	LCST-UV (°C)	LCST-DLS (°C)
2.0	39	38
1.0	42	42
0.5	44	45
0.25	46	45

Table 4.3 LCST of PVCL-*b*-PVPON by DLS and UV

4.7 Synthesis of Poly (N-vinylcaprolactam)-b-poly (Acrylic acid)

One of the fundamental prerequisite to employ nanoparticles for clinical diagnosis and treatment purpose is that a stable colloidal solution can be formed without any significant agglomeration over a desired time period. A range of different functionalities and approaches can be used to attain colloidal stability. For many applications in medicine, a polymer coating on the magnetic nanoparticles is preferred over simple functionalization with small organic compounds since polymer stabilizers offer several advantages: (i) they are more effective in generating steric effect, (ii) they provide abundant binding sites and (iii) less prone to dissociation. A polymer coating, indeed, can provide colloidal stability in water through steric stabilization, or through charged groups (often $-COO^{-}$), and can provide surface functionality along with the encapsulation of a therapeutic agent.

In order to encapsulate magnetic nanoparticles with smart polymer, poly N-vinylcaprolactam-*b*-poly acrylic acid was prepared. In fact, the presence of carboxylic acid blocks in the structure of smart copolymer not only allows the anchoring of the polymer

around the nanoparticles but also it yields stable nanoparticles in biological fluid. Furthermore, the incorporation of acrylic acid monomer units into polymer backbones has been investigated for therapeutic use [53] on account of their ability to swell reversibly upon pH variation, and to adhere to biological surfaces when partially protonated.

A first attempt of preparing the diblock copolymer by RAFT polymerization [43] similar to PVCL-*b*-PVPON synthesis procedure, failed. This could result from the fact that controlled radical polymerization of N-vinylcaprolactam as an unconjugated monomer is a big challenge due to the highly reactive growing vinyl radical [54]. To overcome this problem, PVCL-*b*-PAA was synthesized by free radical polymerization method according to slightly modified procedure from literature [55], so as to improve the length of PAA blocks.

The PVCL-*b*-PAA copolymers were synthesized by free radical copolymerization of NVCL with AA in the presence of AIBN as an initiator in three different solvents including DMF (sampler AA_1), dioxane (sample AA_2), and isopropanol (sample AA_3) as shown in Scheme 4.5. ^{1}HNMR and GPC were carried out to consider structures and molecular weights of these three block copolymers.

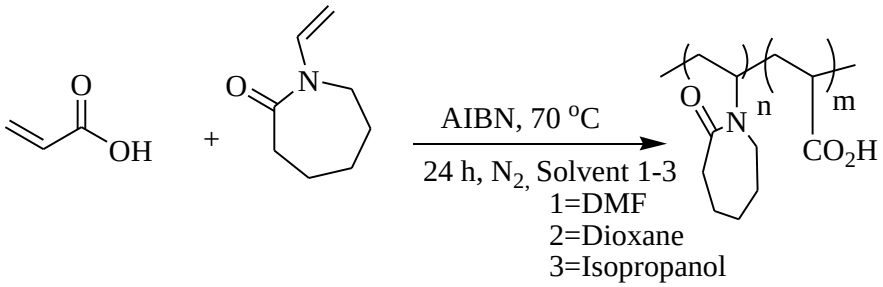

Scheme 4.5 Free radical copolymerization of PVCL-*b*-PAA

The full description of synthetic procedure and ^{1}HNMR assignment are reported in Appendix A.6, Figure A.5 respectively. Significantly, ^{1}HNMR spectra were identical for the three copolymers, indicating solvent did not have any influence on the polymer structure. Besides, FTIR spectroscopy and titration methods were performed to consider the structure of PVCL-AA copolymers. IR measurements also confirmed the PVCL-*b*-PAA copolymers backbone as indicated in Appendix A.6, Figure A.6, and similarly, obtained results from FTIR measurement for all three copolymers were equal as expected. For titration method, the copolymers (200 mg) were dissolved in an excess of 0.1 M sodium hydroxide (NaOH, 10.0 mL) to deprotonate the carboxylic groups. The excess of NaOH was titrated with 0.1 M hydrochloric acid. The amount of the acidic comonomer units was calculated

from the amount of NaOH required to deprotonate the carboxylic acid groups. The copolymer compositions and the content of acrylic acid in their structures, which was almost 0.002 mol g^{-1} for all copolymers, are summarized in table 4.4.

The molecular weight distribution of the copolymers was determined by gel permeation chromatography as exhibited in Figure 4.17 coupled with Waters 410 Differential Refractometer and two Ultrahydrogel TM linear 6–13 μm columns. The eluent employed was water (HPLC grade) at a flow rate of 1.0 mL min^{-1}. Polyethylene oxide standards were used for calibration, and the results of the GPC analyses are tabulated in table 4.4.

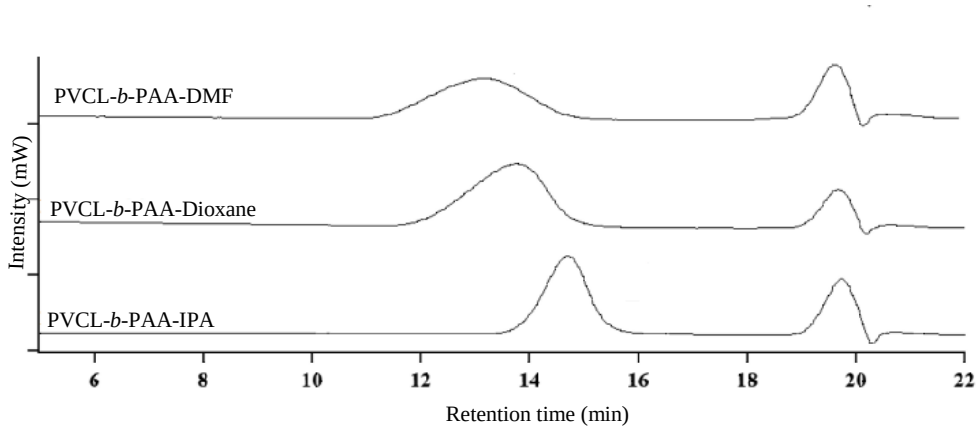

Figure 4.17 Molecular weight distribution of PVCL-*b*-PAA prepared in various solvents

Although a detailed study of the copolymerization behavior of AA and NVCL as a function of solvent was not within the scope of this thesis, the data in table 4.4 demonstrated clear differences in the molecular weight (between 102580 and 378510 g mol^{-1}) as well as polydispersity between these three samples.

Copolymers	Solvent	AA (mol g^{-1})	M_n (g mol^{-1})	PDI
PVCL-*b*-AA_1	DMF	0.00261	378510	1.70
PVCL-*b*-AA_2	Dioxane	0.00202	271890	1.48
PVCL-*b*-AA_3	Isopropanol	0.001934	102580	1.16

Table 4.4 Reaction parameters of PVCL-*b*-PAA

According to Kirsh *et al*, in the copolymerization of AA with similar vinyl monomers such as *N*-vinylpyrrolidone (NVPON) and N- vinylcaprolactam (NVCL), the reactivity of AA in polar environment (eg DMF) is much higher than that of NVPON and NVCL [55], which justifies the higher M_n with broad molecular weight distribution of the copolymer prepared in DMF. By making use of aprotic non polar solvent such as dioxane, the copolymerization parameter of NVCL increases, while that of AA decreases, leading to a medium M_n and medium molecular weight distribution. For the isopropanol, the reactivity of both AA and NVCL are almost equal, leading to a copolymer with low M_n and narrow molecular weight distribution. Consequently, M_w of copolymer could be tuned in accordance with the type of solvent selected for polymerization.

The combination of acrylic acid (AA) as a pH sensitive monomer and temperature-responsive segment in a block copolymer leads to a system that responds to both pH and temperature stimuli (Figure 4.18). As reported previously, LCST of temperature-responsive copolymers is usually affected by a lot of factors including the block length, molecular weight distribution, chemical composition, nature of the comonomer, and polymer concentration. It is worth noting that for dual pH-temperature sensitive copolymers, pH has a great influence on LCST value as well. Therefore, LCST of temperature-sensitive polymer is expected to be altered by the attachment of acrylic acid chains, and it is expected to be raised if the acrylic acid block is hydrophilic, and lowered if it is hydrophobic. In some cases, LCST behavior can even be lost if the length of the acrylic acid block is too large [57].

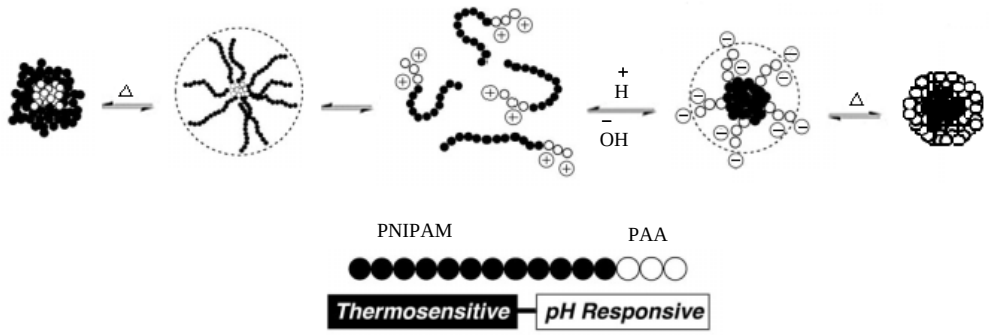

Figure 4.18 Dual pH-temperature responsive behaviour of PNIPAM-*b*-PAA [58]

As an illustration, Figure 4.18 describes the double pH-temperature responsive behavior of poly (N-isopropylacrylamide-*b*-acrylic acid) (PNIPAM-*b*-PAA) in aqueous solution. Clearly the solubility of the PAA blocks in aqueous solutions depends on the pH of the medium. That means, the lower is the pH, the more carboxylate groups of the PAA blocks are protonated

and the less soluble this block becomes in aqueous media. At pH ~ 8.5 and higher pH, virtually all carboxylate groups are deprotonated, and the PAA segment is readily soluble in water. At pH between 7-8, and temperature above LCST, PNIPAM segment is insoluble in aqueous solution, and it is assumed that it forms the core of a micelle with PAA forming the corona [58]. At pH 4.5-5, when the temperature is raised above LCST, the formation of large aggregates occurs due to increasing insolubility of both protonated PAA corona and PNIPAM micellar core. These observations demonstrate diblock copolymer containing temperature- and pH-responsive segments self-assembled in water in response to both temperature and pH changes as clearly obvious in Figure 4.18.

In order to assess pH responsive property of PVCL-*b*-PAA in aqueous solution, zeta potential as a function of pH was measured, and results are reported in Figure 4.19.

pH responsive property of 1.0 mg mL^{-1} PVCL-*b*-PAA in buffer phosphate 10 mM was determined by zeta potential measurements as a function of pH as exhibited in Figure 4.19 by using Zetasizernano series instrument. An equilibration time of 3 min was allowed before each measurement, and at least five replicate measurements were made for each sample. Figure 4.19 indicates that zeta potential of solution decreases from 0 to -30 mV by increasing pH. That is to say, PVCL and PAA are both water soluble (pH = 7) at room temperature in contrast to the PVCL-*b*-PAA copolymers. The lack of water solubility of the copolymer is attributed to complex formation by hydrogen bonding between the amide bonds of PVCL and carboxylic groups in the protonated form. Therefore, the pH-responsive polymer precipitated out of water below pH ~ 5 because of protonation of the carboxylic groups of the polymer (zeta potential near to 0), while they were water soluble above pH ~ 5 because of deprotonation of the acidic groups (zeta potential ~ -25 mV). Subsequently, the higher pH values of the solutions (pH > 8) lead to the ionic dissociation of the carboxylic acid and therefore to less interactions between the AA and NVCL units of the PVCL-*b*-PAA copolymers. Consequently, these results clearly indicated a pH-dependent behavior of copolymer and evidenced PVCL-*b*-PAA can be exploited to control the delivery of drugs in specific organs or intracellular compartments (endosomes or lysosomes), which in principle allow for tailored drug release with excellent spatial, temporal and dosage control when subtle environmental changes are associated with pathological situations such as cancer or inflammation.

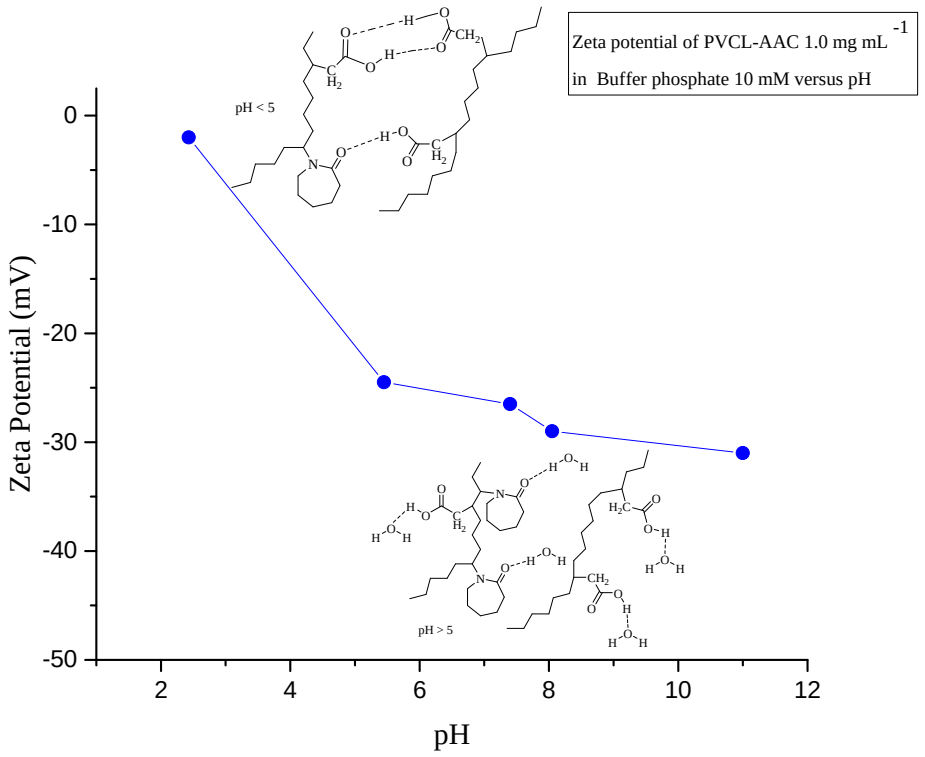

Figure 4.19 Zeta potential of PVCL-*b*-AAC in buffer phosphate 10 mM with various pH values

The influence of pH on the LCST of PVCL-*b*-PAA was investigated on 1.0 mg mL^{-1} buffered aqueous solutions of copolymers (phosphate buffer 10 mM) with pH values ranging from 5.5 to 8.5 by a UV spectrophotometer equipped with a thermostatic bath. The heating rate was 5 ^{o}C min^{-1} and before each measurement, the sample was left to thermalize at the desired temperature for 10 min. The obtained data are reported in table 4.5, and the turbidimetric curves of PVCL-*b*-PAA are shown in Figure 4.20.

Sample	*Mn* (g mol^{-1})	LCST (°C), pH 5.5	LCST (°C), pH 7.4	LCST (°C), pH 8.5
AA_1	378510	35	35	40
AA_2	271890	40	45	50
AA_3	102580	35	40	45

Table 4.5 LCST of PVCL-*b*-PAA_1, PVCL-*b*-PAA_2, and PVCL-*b*-PAA_3 in buffer phosphate 10 mM, pH 5.5-8.5

Table 4.5 demonstrates the presence of acid groups in polymeric backbone allows control of LCST by means of pH. At pH ~ 8.5 deprotonation of the carboxylic acid groups occurs, leading to increase hydrophilicity of copolymer, and subsequent enhance of LCST; on the

other hand, in acidic pH (5-5.5) LCST shifts to lower values as a result of protonation of acidic group.

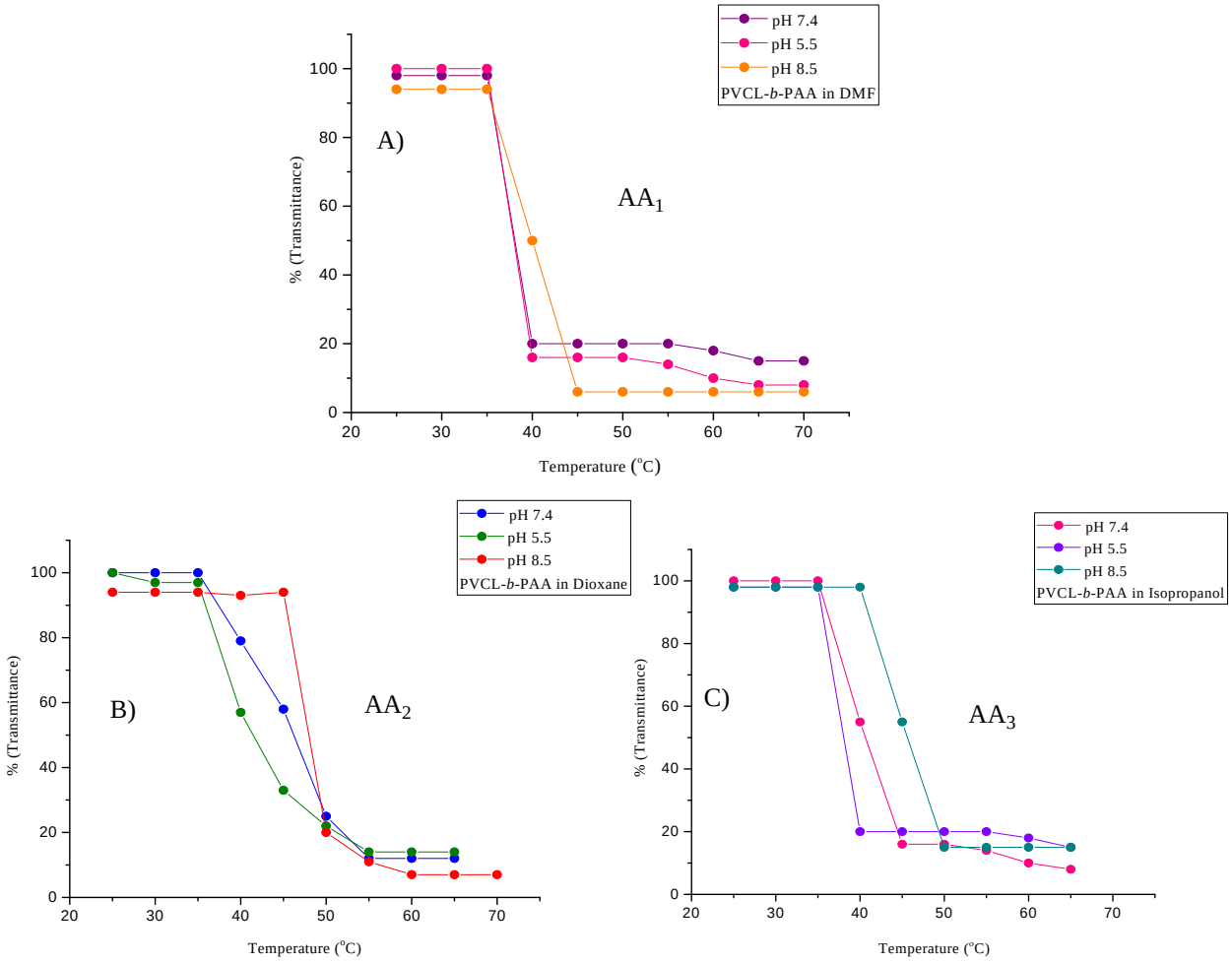

Figure 4.20 Transmission vs temperature curves for the PVCL-*b*-PAA copolymers in buffer phosphate 10 mM (1.0 mg mL^{-1}) at different pH. AA_1 prepared in DMF (A), AA_2 prepared in Dioxane (B), AA_3 prepared in Isopropanol (C)

According to transmission versus temperature curves displayed in Figure 4.20, in all cases the transmission sharply reduced when the temperature was raised above the LCST of copolymers. This behavior can be explained considering that at T > LCST copolymer can form micellar structures with PVCL core and a PAA corona, in consequence of pH and temperature responsive behavior of copolymer in aqueous media [58].

Owing to the fact that the main purpose of this thesis is hyperthermia drug release at temperature above physiological body temperature (~ 37 ^{o}C), PVCL-*b*-PAA_2 is the best candidate to fulfil this goal, in that its LCST is above 37 ^{o}C even at acidic pH (tumours pH). Hence, in the following we mainly focused on the characterization of this copolymer.

Particle size and particle size distribution of aqueous solution of PVCL-*b*-PAA_2 on 2.0 mL of sample with concentration of 1.0 mg mL^{-1} was determined by Dynamic Light Scattering (DLS). Corresponding to the measurement, the copolymer has narrow size distribution (PDI, 0.8) with the intensity-average hydrodynamic diameter of 68.0 nm as exhibited in Figure 4.21.

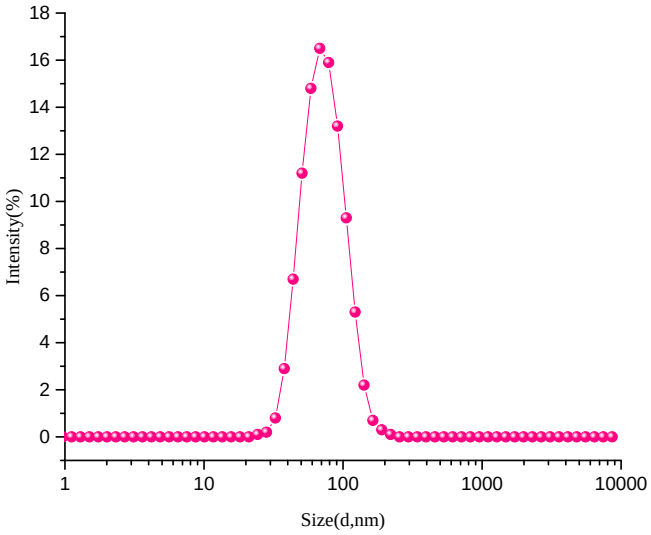

Figure 4.21 Size distribution of PVCL-*b*-PAA_2

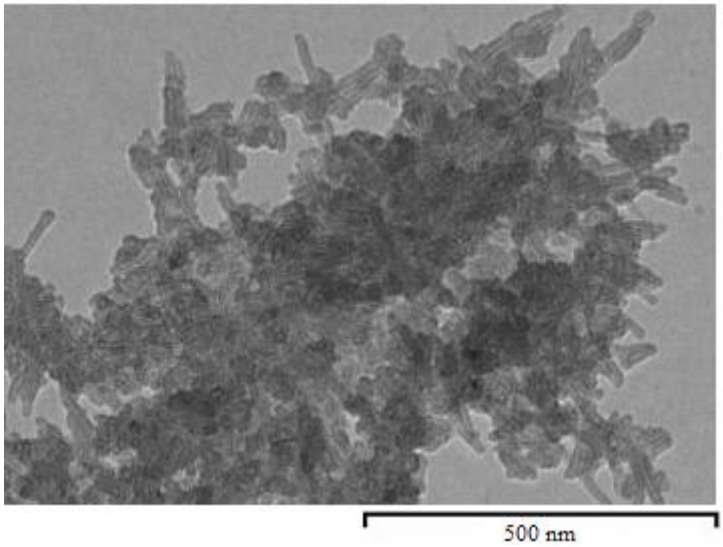

Figure 4.22 TEM image of PVCL-*b*-PAA_2

Morphology of PVCL-*b*-PAA_2 was considered by transmission electron microscopy, and TEM image shows the presence of short chain polymer structure with length of

15.0-65.0 nm, which is in good agreement with the hydrodynamic diameter obtained by DLS characterization. A representative example of polymer morphology is reported in Figure 4.22.

Micelle formation of PVCL-*b*-PAA_2 in aqueous solution at elevated temperature above LCST was evaluated by dynamic ^{1}HNMR and DLS analyses.

In this step, ^{1}HNMR spectroscopy as an experimental technique was employed to study the temperature-induced collapse of PVCL segment (micelle formation) in PVCL-*b*-PAA_2 diblock copolymer as displayed in Figure 4.23.

Figure 4.23 shows the ^{1}HNMR spectra of PVCL-*b*-PAA_2 in deuterium oxide with concentration of 1.0 mg mL^{-1} at 25 ^{o}C (T < LCST) and 48 ^{o}C (T > LCST). At the lower temperature, the diblock copolymer is molecularly dissolved in water by addition of NaOD 0.1M, and all peaks associated with PVCL and PAA segments are present in the ^{1}HNMR spectrum as shown in Figure (4.23, a). On the other hand, increasing temperature to 48 ^{o}C causes the collapse of PVCL blocks and self-assembly of the PVCL-*b*-PAA_2 copolymer chains (micelle formation) as evidenced by the pronounced decrease of the peak intensity of PVCL block at 4 ppm, while the peaks related to PAA segment (1.75–2.5 ppm), which is still soluble at this temperature, are observable in the ^{1}HNMR spectrum according to Figure (4.23, b). Thus, at 48 ^{o}C, the PVCL resonance peak intensity is significantly lowered than one at 25 ^{o}C because of the highly restricted motions of the PVCL segments as a result of the PVCL collapse. Dynamic ^{1}HNMR analyses results, therefore, confirmed that copolymer has LCST over 45 ^{o}C in accordance with turbidity measurement.

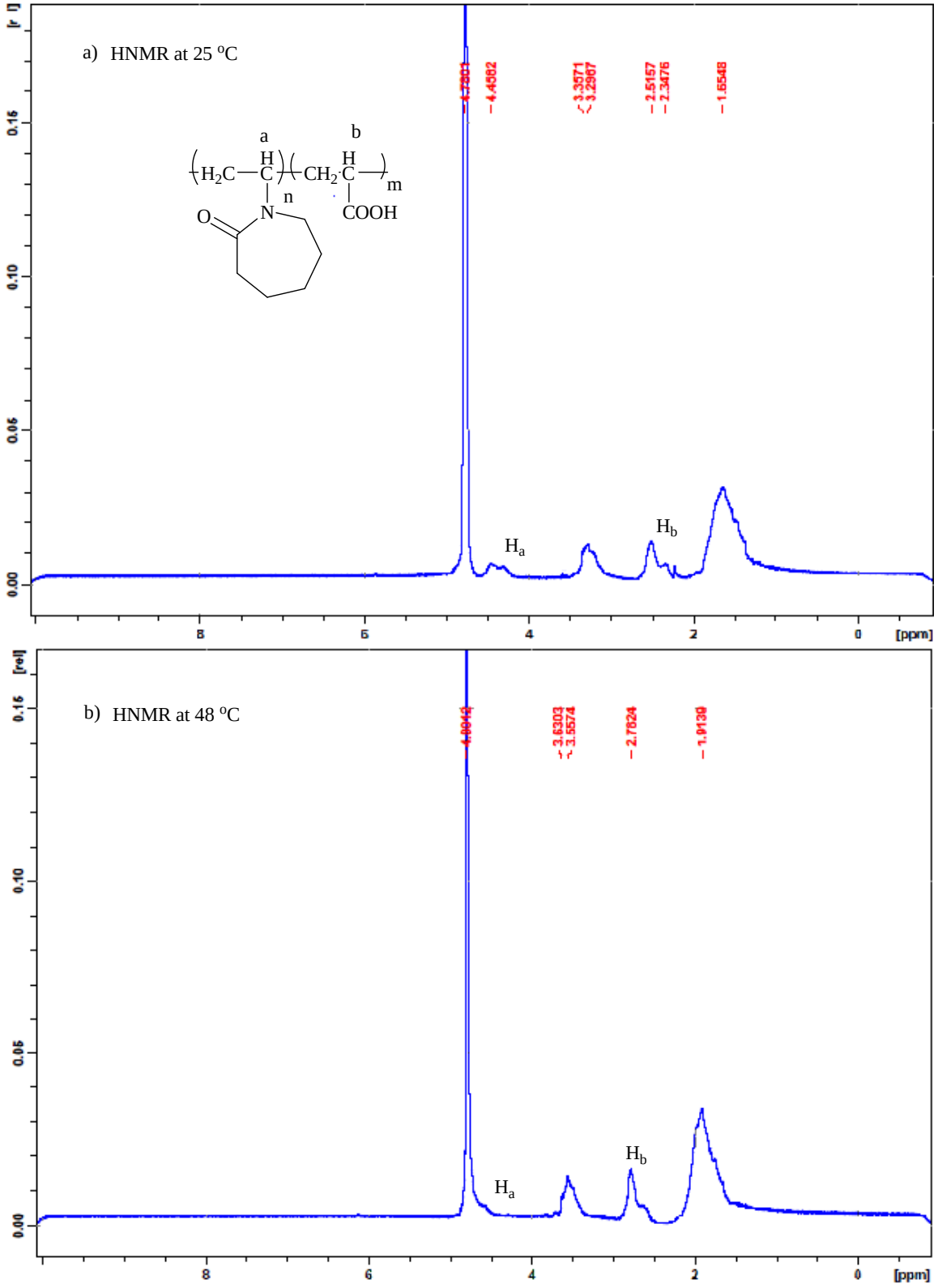

Figure 4.23 ^{1}HNMR spectra of PVCL-*b*-PAA$_2$ in D_2O (1.0 mg mL^{-1}) at 25 °C (a) and 48 °C (b)

Hydrodynamic diameter (Dh) of the PVCL-*b*-PAA_2 buffer solutions (1.0 mg mL^{-1}) at different pH is plotted against temperature according to DLS measurements as displayed in Figure 4.24. Results are summarized in table 4.6, and compared with ones obtained by turbidimetry method. Obviously, a dramatic increase in Dh within a very narrow temperature range is detected from Figure 4.24. This is attributed to the thermo-induced dehydration of the PVCL block above its LCST that caused generation of thermo-induced physically assembled micelles [58] as demonstrated in Figure 4.25.

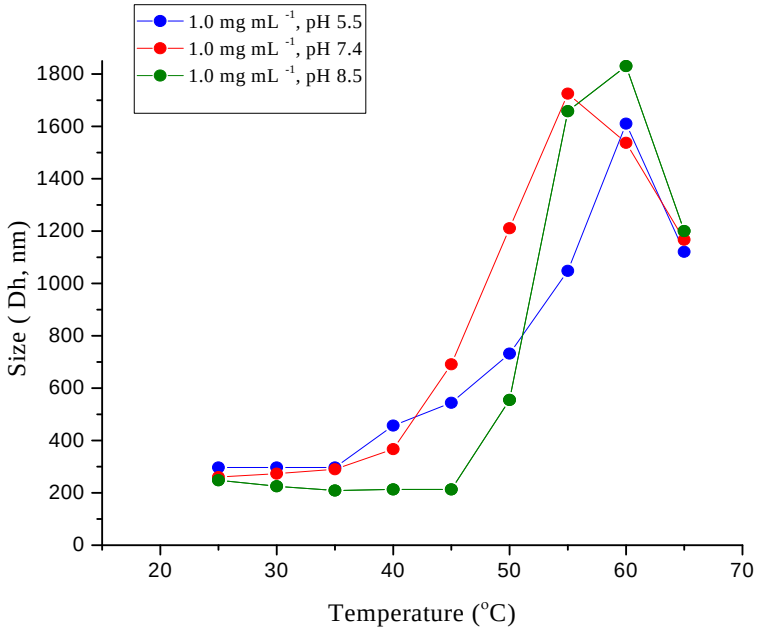

Figure 4.24 Dependence of Dh on the temperature for the PVCL-*b*-PAA_2 copolymer solutions with concentration of 1.0 mg mL^{-1} at various pH values *via* DLS analysis

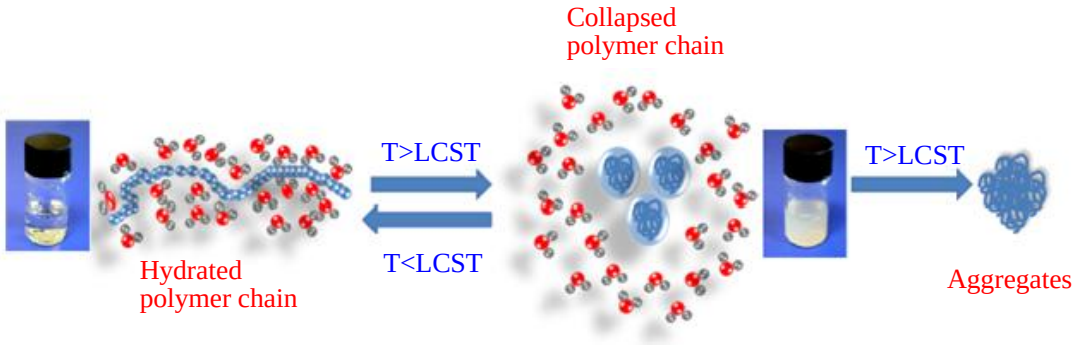

Figure 4.25 Self-Assembly of PVCL-*b*-PAA_2 diblock copolymer in solution above LCST

Table 4.6 indicates that the obtained data are in good agreement with those obtained from turbidity method and ^{1}HNMR analysis as expected. Consequently, these results clearly

indicated a pH-dependent LCST behavior of copolymer, which can be tailored to fall just above the physiological temperature by simply adjusting hydrophilicity of the acrylic acid units in the structure of copolymer.

Buffer solution of PVCL-*b*-PAA$_2$ with concentration of 1.0 mg mL^{-1}		
pH	LCST (^{o}C)- UV	LCST (^{o}C)- DLS
8.5	50	45
7.4	45	40
5.5	40	35

Table 4.6 LCST of copolymer solution in buffer phosphate 10 mM with concentration of 1.0 mg mL^{-1}

To conclude, we have demonstrated the synthesis of PVCL homopolymer and block PVCL-*b*-PVPON copolymer *via* well-controlled RAFT (co)polymerization. Polymers were characterized by ^{1}HNMR, GPC, TEM, and FTIR. The heat-induced behavior of the synthesized copolymers in solution was studied using ^{1}HNMR, turbidimetry, and DLS. All (co)polymers dissolved in water at ambient conditions below their cloud point values, and micellar morphologies were demonstrated to form from the (co)polymers at temperatures above their LCST due to the temperature-triggered association of dehydrated PVCL segments. The association temperature can be decreased by increasing (co)polymer concentration, or increasing the polymerization degree with the hydrophilic PVPON segment.

Diblock copolymers PVCL-*b*-PAA prepared according to free radical polymerization containing temperature- and pH-responsive segments at an appropriate composition self assembled in water in response to both temperature and pH changes. The cloud point temperatures of the buffered solutions of this copolymer has a maximum value at pH around 8.5, which is determined by the counterbalance of the hydrophilic charged carboxylate groups and the destabilizing effect of the cations. Moreover, The the presence of carboxyl groups derived from poly acrylic acid units of the copolymer could offer the potential to build up multifunctional nanocomposite for effective drug delivery in therapeutic application.

Chapter 4

References

1. M. Szwarc. Advances in polymer science. **1983**, *49*, 1-177.
2. HL. Hsieh.; RP. Quirk. Anionic polymerization: principles and practical applications. **1996**, 1st edn. Marcel Dekker, New York, 1-711.
3. G. Moad.; E. Rizzardo.; SH. Thang. *Acc Chem Res.* **2008**, *41*, 1133.
4. M. Szwarc. Ionic polymerization and living polymers. **1993**, 1st edn. Chapman & Hall, New York.
5. O. F. Solomon.; D. S. Vasilescu.; V. Tararescu. *J. Appl. Polym. Sci.* **1969**, *13*, 1.
6. C. Wu.; A. C. W. Lau. *Macromolecules*. **1999**, *32*, 581.
7. L. Shao.; M. Hu.; L. Chen.; L. Xu.; Y. Bi. *React Funct Polym*. **2012**, *72*, 407.
8. Y. Deng.; S. Zhang.; G. Lu.; X. Huang. *Polym. Chem.* **2013**, *4*, 1289.
9. M. Destarac. *Polym. Rev.* **2011**, *51*, 163.
10. a) V. Sciannamea.; R. Jerome.; C. Detrembleur. *Chem. Rev.* **2008**, *108*, 1104, b) J. Nicolas.; Y. Guillaneuf.; C. Lefay.; B. Charleux. *Prog. Polym. Sci*. **2013**, *38*, 63.
11. J. S. Wang.; S. G. Gaynor.; J. Matyjaszewski. *Polym. Prepr.* **1995**, *36*, 465.
12. N. Zhang.; S. R. Samanta.; B. M. Rosen.; V. Percec. *Chem. Rev.* **2014**, *114*, 5848.
13. a) J. Chiefari.; Y. Chong.; F. Ercole.; J. Krstina.; G. Moad. *Macromolecules.* **1998**, *3*, 5559, b) M. J. Flanders.; W. M. Gramlich. *Polym. Chem.* **2018**, *9*, 2328.
14. a) A. Debuigne.; R. Poli.; C. Jerome.; R. Jerome.; C. Detrembleur. *Prog. Polym. Sci.* **2009**, *34*, 211, b) M. Hurtgen.; C. Detrembleur.; C. Jerome.; A. Debuigne. *Polym. Rev.* **2011**, *51*, 188, c) L. E. Allan.; M. R. Perry.; M. P. Shaver. *Prog. Polym. Sci.* **2012**, *37*, 127.
15. Z. M. O. Rzae.; S. Dincer.; E. Piskin. *Prog. Polym. Sci.* **2007**, *32*, 534.
16. H. Wei.; S. X. Cheng.; X. Z. Zhang.; R. X. Zhuo. *Prog. Polym. Sci.* **2009**, *34*, 893.
17. M. Hurtgen.; J. Liu.; A. Debuigne.; C. Jerome.; C. Detrembleur. *J. Polym. Sci. Polym. Chem.* **2012**, *50*, 400.
18. M. Beija.; J. D. Marty.; M. Destarac. *Chem. Commun.* **2011**, *47*, 2826.
19. a) X. Y. Jiang.; Y. J. Li.; G. L. Lu.; X. Y. Huang. *Polym. Chem.* **2013**, *4*,1402, b) X. Y. Jiang.; G. L. Lu.; C. Feng.; Y. J. Li.; X. Y. Huang. *Polym.Chem.* **2013**, *4*, 3876.

20. a) P. Singh.; A. Srivastava.; R. Kumar. *J. Polym. Sci. Polym. Chem.* **2012**, *50*, 1503, b) I. Negru.; M. Teodorescu.; P. O. Stanescu.; C. Draghici.; A. Lungu.; A. Sarbu. *Mater. Plast.* **2010**, *47*, 35.
21. A. Kermagoret.; C. A. Fustin.; M. Bourguignon.; C. Detrembleur.; C. Jérôme.; A. Debuigne. *Polym. Chem.* **2013**, *4*, 2575.
22. C. Detrembleur.; M. C. De Pauw-Gillet.; S. Mornet.; E. Duguet.; C. Jerome. *Polym. Chem.* **2014**, *5*, 799.
23. D. C. Wan.; Q. Zhou.; H. T. Pu.; G. J. Yang. *J. Polym. Sci. Polym.Chem.* **2008**, *46*, 3756.
24. S. perrier.; P. Takolpuckdee. *J. Polym Sci. Part A. Polym Chem*. **2005**, *43*, 5347.
25. Y. C. Yu.; U. H. Kang.; J. H. Youk. *Colloid Polym. Sci.* **2012**, *290*, 1107.
26. a) M. L. Tebaldi.; L. A. Fiel.; A. M. Santos.; S. S. Guterres.; A. Pohlmann. *J. Macromol. Sci. Pure Appl. Chem.* **2013**, *60*, b) S. M. Ponce-Vargas.; N. A. Cortez-Lemus.; A. Licea-Claverie. *Macromol. Symp.* **2013**, *56*, *325*.
27. G. Moad.; E. Rizzardo.; S. H. Thang. *Acc. Chem. Res.* **2008**, *41*, 1133.
28. J. Chiefari.; R. Mayadunne.; C. L. Moad.; G. Moad.; M. A. Skidmore. *Macromolecules*. **2003**, 36, 2273.
29. N. A. Cortez-Lemus.; A. Licea-Claverie. *Prog. Polym. Sci*. **2016**, *53*, 1.
30. A. B. Lowe.; C. L. McCormick. *Prog Polym Sci*. **2007**, *32*, 283.
31. G. Moad.; E. Rizzardoand.; S. H. Thang. *Polym. Int*. **2011**, *60*, 9.
32. H. Willcock.; R. K. O'Reilly. *Polym. Chem.* **2010**, *1*, 149.
33. A. S. Hoffman. *Adv. Drug Deliv. Rev.* **2013**, *65*, 10.
34. B. Jeong.; S. W. Kim.; Y. H. Bae. *Adv. Drug Deliv. Rev.* **2002**, *54*, 37.
35. E. C. Abenojar.; S. Wickramasinghe.; J. Bas-Concepcion.; A. C. S. Samia. *Prog Nat Sci Mater Int.* **2016**, *26*, 440.
36. a) D. C. Wan.; Q. Zhou.; H. T. Pu.; G. J. Yang. *J. Polym. Sci. Polym. Chem.* **2008**, *46*, 3756, b) J. Spevacek.; J. Dybal.; L. Starovoytova.; A. Zhigunova. *Soft Matter.* **2012**, *8*, 6110.
37. a) F. Meeussen.; E. Nies.; H. Berghmans.; S. Verbrugghe.; F. Du Prez. *Polymer*. **2000**, *41*, 859, b) Y. Maeda.; H. Yamamoto.; I. Ikeda. *Langmuir*. **2001**, *17*, 6855.
38. H. Vihola.; A. Laukkanen.; L. Valtola.; H. Tenhu.; J. Hirvonen. *Biomaterials*. **2005**, *26*, 3055.
39. J. Ramos.; A. Imaz.; J. Forcada. *Polym. Chem*. **2012**, *3*, 852.
40. J. Li.; B. Wang.; Y. Wang. *Int. J. Pharmacol*. **2006**, *2*, 513.

41. a) P. Arsula Rose.; P. K. Praseetha.; M. Bhagat.; P. Alexander. *Technol Cancer Res Treat.* **2013**, *12*, 463, b) L. M. Sanchez.; D. A. Martin.; V. A. Alvarez.; J. S.Gonzalez. *Colloids Surf A.* **2018**, *543*, 28.
42. X. Liang.; E. Kharlampieva.; Y. Wang.; V. Kozlovskaya. *J. Polym. Sci. part A: Polym. Chem.* **2014**, *52*, 2725.
43. M. Beija.; J. D Marty.; M. Destarac. *Prog. Polym. Sci*. **2011**, *36*, 845.
44. X. Zhao.; O. Coutelier.; C. Delmas.; M. Destarac.; J. D. Marty. *Polym. Chem*. **2015**, 6, 5233.
45. D. Wan.; Q. Zhou.; H. Pu.; G. Yang. *J. Polym. Sci. Part A: Polym. Chem*. **2008**, *46*, 3756.
46. M. Destarac.; C. Brochon.; J-M. Catala.; A. Wilczewska.; S. Z. Zard. *Macromol. Chem. Phys*. **2002**, *203*, 2281.
47. J. U. Izunobi.; C. L. Higginbotham. *J. Chem. Educ*. **2011**, *88*, 1098.
48. G. Vancoillie.; D. Frank.; R. Hoogenboom. *Prog. Polym. Sci*. **2014**, *39*, 1074.
49. X. Liang.; V. Kozlovskaya.; Y. Chen.; O. Zavgorodnya.; E.Kharlampieva. *Chem. Mater*. **2012**, *24*, 3707.
50. J. E. Chung.; M. Yokoyama.; T. Aoyagi.; Y. Sakurai.; T. Okano. *J. Control. Release*. **1998**, *53*, 119.
51. E. Yu. Kozhunova.; Q. Ji.; J. Labuta.; I. R. Nasimova. *eXPRESS Polymer Letters*. **2018**, *12*, 1005.
52. H. G. Schild. *Prog. Polym. Sci*. **1992**, *17*, 163.
53. a) C. M. Lehr.; J. A. Bouwstra.; H. E. Bodde.; H. E. Junginger. *Pharm. Res*. **1992**, *9*, 70, b) H. Brondsted.; J. Kopecek. *ACS Symp. Ser*. **1992**, *480*, 285, c) R. Kishi.; T. Miura.; H. Kihara.; T. Asano.; Yosomiya. *J. Appl. Polym. Sci*. **2003**, *89*, 75, d) D. Kuckling.; A. Richter.; K. F. Arndt. *Macromol. Mater.Eng*. **2003**, *288*, 144, e) V. T. Pinkrah.; M. J. Snowden.; J. C. Mitchell.; G. R. Fern. *Langmuir*, **2003**, *19*, 585, f) S. R. Lustig.; G. J. Everlof.; G. D. Jaycox. *Macromolecules*, **2001**, *34*, 2364, g) A. Hervault.; A. E. Dunn.; M. Lim.; C. Boyer.; D. Mott.; N. T. K. Thank. *Nanoscale*. **2016**, *8*, 12152, h) Y. Zheng.; L. Wang.; L. Lu.; Q. Wang.; B. C. Benicewicz. *ACS Omega*. **2017**, *2*, 3399.
54. S. M. Ponce-Vargas.; N. A. Cortez-Lemus.; A. Licea-Claverı´. *Macromol. Symp*. **2013**, *325-326*, 56.
55. N. I. Shtanko.; W. Lequieu.; E. J. Goethals.; F. E. Du Prez. *Polym Int*. **2003**, 52, 1605.
56. YE. Kirsh, Water soluble poly-N-vinylamides, J Wiley & Sons, Chichester (**1998**).

57. V. Bulmus.; Z. Ding.; C. J. Long.; P. S. Stayton.; A.S. Hoffman. *Bioconjugate Chem.* **2000**, *11*, 78.
58. C. M. Schilli.; M. Zhang.; E. Rizzardo.; S. H. Thang.; A. H. E. Muller. *Macromolecules.* **2004**, *37*, 7861.

Chapter5

Encapsulation of Magnetic Nanoparticles by Thermoresponsive Polymers

The functionalization of magnetic nanoparticles (MNPs) surface is a useful method for tuning the overall properties of nanoparticles to fit targeted applications. The surface modification of MNPs by functional molecules/polymers has different tasks to fulfill [1]: (i) provide functional groups at the surface for further derivatization, (ii) enhance MNPs stabilization in various solvents extending their application possibilities, (iii) modify the capability to assemble the particles in specific arrays, or the ability to target desired chemical, physical, or biological environments, and (iv) reduction of their toxicity. Consequently, appropriate surface functionalization of MNPs, which makes them biocompatible and bio-specific, is a prerequisite for various nano-bio applications.

Despite the potential benefits that functionalized MNPs have rendered to nanomedicine, some applications remains still challenging; for instance, *in vivo* efficient drug delivery inside the target cell. In this context, the decoration of MNPs with smart polymer could significantly improve already existing MNPs characteristics, and help to surmount this challenge. Therefore, in our work, with the aim of improving multi-modal cancer therapy, we propose a novel approach to obtain polymer coated magnetic nanoparticles as agents for combined drug delivery and hyperthermia. The composite nanoparticles (CNP) used in this work consisted of superparamagnetic iron oxide nanoparticles coated by thermo-responsive (co)polymers including poly-N-vinylcaprolactm (PVCL), poly (N-vinylcaprolactam-*b*-vinylpyrrolidone) (PVCL-*b*-PVPON), and dual stimuli responsive poly (N-vinylcaprolactam-*b*-acrylic acid). In the present chapter we will discuss the synthesis of the two building blocks of the core-shell nanosystems, and we will present the strategy adopted for encapsulation of Fe_3O_4-68 in the stimuli-responsive (co)polymers, performed *via* post modification ‘grafting to’ and ‘grafting from’ methods. Moreover, we will show how the polymeric shell improves colloidal stability, and confer stimuli responsive behavior to the magnetic nanohybrids.

5.1. Modification of MNPs

Uncoated iron oxide MNPs are not stable in water at neutral pH or in physiological fluids, tending to agglomerate and precipitate quickly. Since nanoparticles (NPs) attract to each other due to magnetic dipolar interactions and weaker Van der Waals forces, surface modification of MNPs is often indispensable to make the NPs suspensions stable.

There is a wide variety of functionalization methods for modification of the surface of magnetic nanoparticles including [2]:

1. Anchoring of a functional group
2. Stabilization of iron oxide MNPs using polymer chains
    - Grafting ‘onto’ versus ‘from’
    - Stabilization of iron oxide MNPs using monofunctional polymer chains *via* exchange chemistry
    - Stabilization of iron oxide MNPs using functional diblock polymers
3. Micelle and liposome encapsulation

5.1.1 Anchoring of Ligand with Specific Functional Group

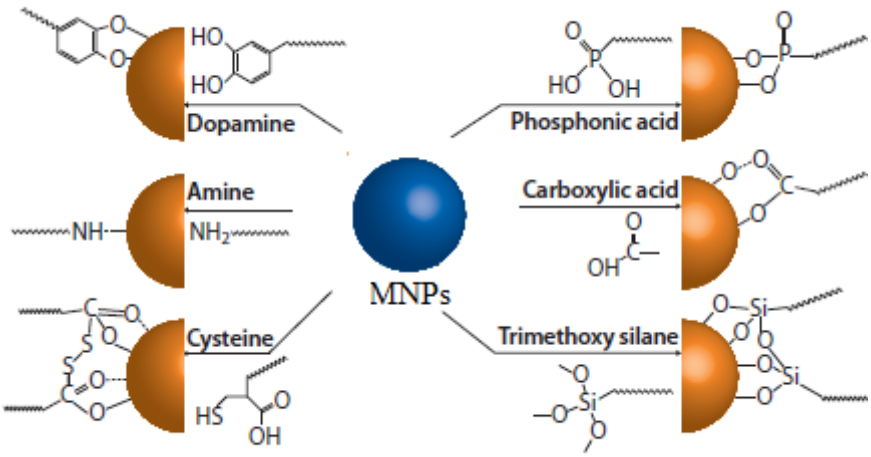

Figure 5.1 Groups that can be used to anchor polymers on iron oxide MNPs surfaces [2]

The presence of iron-derived positive charges on the surface of MNPs due to the lack of oxygen ions, which determine vacancies, provides a versatile synthetic handle, allowing attachment of different functionalities. A range of strategies can be used to stabilize metal

nanoparticles by exploiting electrostatic, hydrophobic, chelating, and covalent interactions as demonstrated in Figure 5.1.

One of the most important and widely employed functional groups is the carboxylic acid, which can coordinate to the surface of iron oxide MNPs covalently. For instance, the –COOH group of oleic acid has been employed for iron oxide MNPs surface decoration during synthesis in organic solvents. Citric acid has been used commercially for the stabilization of iron oxide MNPs such as in the MRI contrast agent VSOP C184. However, the –COOH/MNPs coordination bond is labile and can be broken easily by increasing temperature or by exchange with another carboxylic acid compound [3-7].

Phosphonic acid also shows a strong affinity for iron oxide MNPs surfaces through the formation of Fe–O–P– bonds [8]. These bonds are more stable than the carboxylic acid bond, and have shown stability for several weeks at neutral pH. Moreover, phosphonic acid has a higher grafting density than the carboxylic acid group [8].

Finally, dopamine can coordinate to the iron oxide MNPs surfaces as a result of improved orbital overlap of the five-member ring [9]. This approach has been widely used to attach a range of biologically important molecules such as peptides and amino acids to iron oxide MNPs [10]. However, problems with the stability of this bond in water and biological fluids have been reported by Carpenter *et al*. after long exposure periods [11]. Phosphonic acid and dopamine groups appear to improve iron oxide MNPs stability over a larger range of pH and temperature compared with carboxylic acid groups.

5.1.2 Stabilization of MNPs Using Polymer Chains

For many applications in medicine, a polymer coating on the iron oxide MNPs is preferred over simple functionalization with small organic compounds. A polymer coating provides colloidal stability in water through steric stabilization, and can provide surface functionality allowing the possibility of designing hybrid particles with capacity for multimodal tracking, targeting, delivery, and stimulated release of therapeutic agents such as peptides, proteins, drugs, and DNA/RNA.

5.1.3 Grafting 'to' Versus 'From'

Nanohybrids comprising a polymer and an inorganic support can be generally prepared by four main methods as schematized in Figure 5.2:

(a) "*in situ*" preparation, in which the inorganic support is synthesized from a precursor in the presence of the polymer;

(b) surface-initiated polymerization / "grafting from", in which the inorganic surface is functionalized with an initiator or a chain transfer agent (CTA) and then polymerization of the desired monomer is carried out;

(c) post-modification / "grafting to", in which preformed polymer and inorganic support are mixed together, and the polymer chains physically adsorb onto (post-modification) or covalently bind ("grafting to") the inorganic surface;

(d) "grafting through", in which the polymerization of a given monomer is carried out in the presence of the support, previously modified with polymerizable moieties.

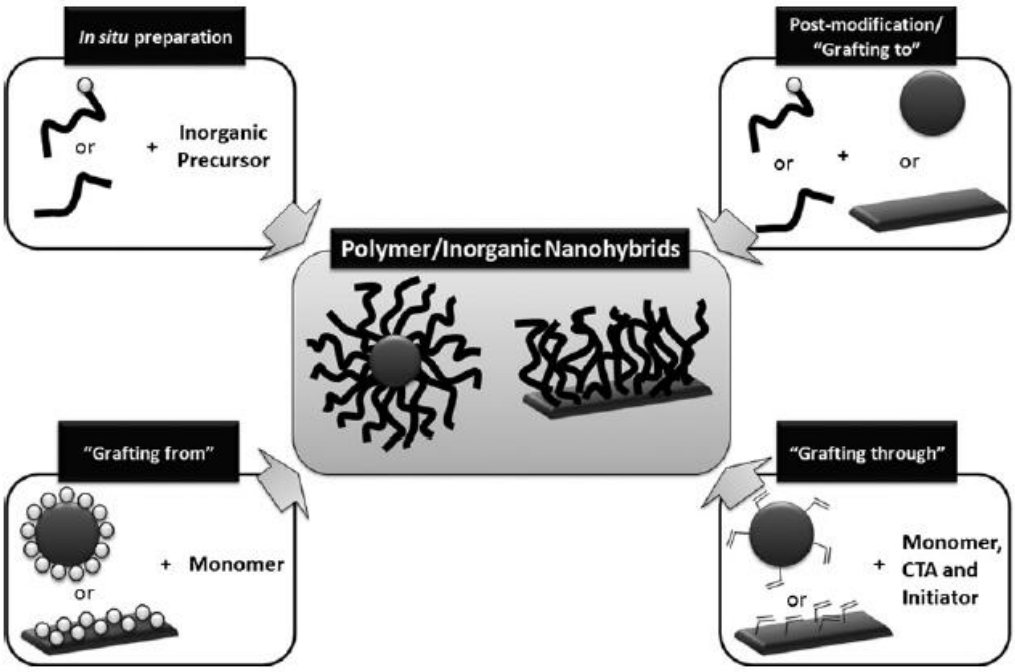

Figure 5.2 Scheme of the most common preparation methods of polymer/inorganic nanohybrids [12]

Each of these approaches has advantages and disadvantages. It is well known that grafting 'from' yields a higher grafting density than the grafting 'to' approach. However, grafting 'to' allows control of polymer architecture and functionality, and is therefore more versatile than the grafting 'from' method. In addition, grafting 'from' can present difficulties in maintaining the integrity of the hybrid nanoparticles in organic solvents. However, the use of living radical polymerization with a carefully designed protocol can facilitate the modification of iron oxide MNPs, using the grafting 'from' approach [12-17].

5.1.4 Stabilization of Iron Oxide MNPs Using Monofunctional Polymer Chains via Exchange Chemistry

The attachment of polymer chains onto iron oxide MNPs can be achieved using polymers with functionality capable of binding to the iron oxide MNPs by exchange of surface ligands. State-of the- art of these methods is to prepare inorganic nanoparticles that are stabilized by alkyl phosphines, amines, thiol, or carboxylic acids. These groups have proven to be most efficient in controlling nanocrystal growth during synthesis, and to provide stability of the final particles in solution. The exchange of these surface ligands with polymers could be an attractive route for a flexible and versatile polymer attachment [18-20].

5.1.5 Stabilization of Iron Oxide MNPs Using Functional Diblock Polymers

The attachment of polymer chains to iron oxide MNPs can also be achieved *via* multiple interactions between the polymer chains and the particle surface. This multiple attachment strategy should enhance the stability of the resultant hybrid nanoparticles, and can be achieved through the use of block or random copolymers. The insertion of several functional groups along the copolymer backbone increases the number of possible anchoring points on the iron oxide MNPs surface. However, the control of polymer architecture is a crucial factor influencing polymer aggregation. As a case in point, when statistical copolymers are used, the presence of multiple groups on the backbone can result in interactions with several particles leading to flocculation, so in the case of di- and multi-block polymers, the functional block should be kept relatively short (several units) to avoid flocculation. The introduction of several attachment points on a single chain can also reduce the packing density. Many examples exist of this multi-interaction approach, based on the use of different types of functionality, such as dopamine [21], carboxylic acid [22] and trimethyl silane [23], yielding stable nanoparticles.

5.2 Encapsulation of Magnetic Nanoparticles by Poly N-vinylcaprolactam via Post Modification Method

As a first attempt, Fe_3O_4 nanoparticles (Fe_3O_4-68) were encapsulated by poly (N-vinylcaprolactam) *via* ‘’grafting to’’ method. Indeed, we expected that carbonyl group from thermo-responsive PVCL can make coordinate covalent bond by donating electrons to the empty d-orbital of the metal (Fe) to bond strongly on the surface of MNPs. To this aim, 13.5 mg of DEG-stabilized Fe_3O_4-68 was mixed with the 4.0 mL DEG containing 10.0 mg PVCL. The resulting suspension was sonicated and stirred for two hours at room temperature. Afterward, the obtained nanocomposite was precipitated by addition of acetone and recovered by magnet decantation. Then, final nanocomposite was dispersed into 20.0 mL buffer phosphate (10 mM, pH = 7.4), and the concentration of the suspension was determined by ICP analysis. According to ICP-AES measurement, a mean concentration of magnetic nanocomposite dispersed in solution was about 0.11 wt % respect to the Fe_3O_4 nanoparticles. Details of the encapsulation procedure of Fe_3O_4 coated PVCL is given in Appendix A.7.

Morphological characteristics of magnetic nanoparticles with and without poly (N-vinylcaprolactam) coating are shown in the TEM micrographs of Figure 5.3. Figure (5.3, A), a typical TEM image of the MNPs after the coating, clearly shows that most of the nanoparticles are polycrystalline nearly spherical in shape, with an average diameter of 18.0 nm, as evaluated from a statistical analysis over 300 iron oxide nanoparticles. For comparison, Figure (5.3, C) illustrates a TEM image of MNPs before polymer coating, with the same average size of 18 nm, so the comparison between these two images suggests that the most of nanoparticles are still uncoated or, alternatively the thickness of the polymer is very thin; moreover, Figure (5.3, D) displays the size distribution of a suspension of MNPs after polymer coating, which was obtained from three independent runs (15 measurements each). The average diameter of MNPs, was found 39.0 nm (PDI ~ 0.22), much larger than that found from TEM, indicating that the MNPs are largely aggregated due to the poor adhesive strength of polymer coatings on their surface.

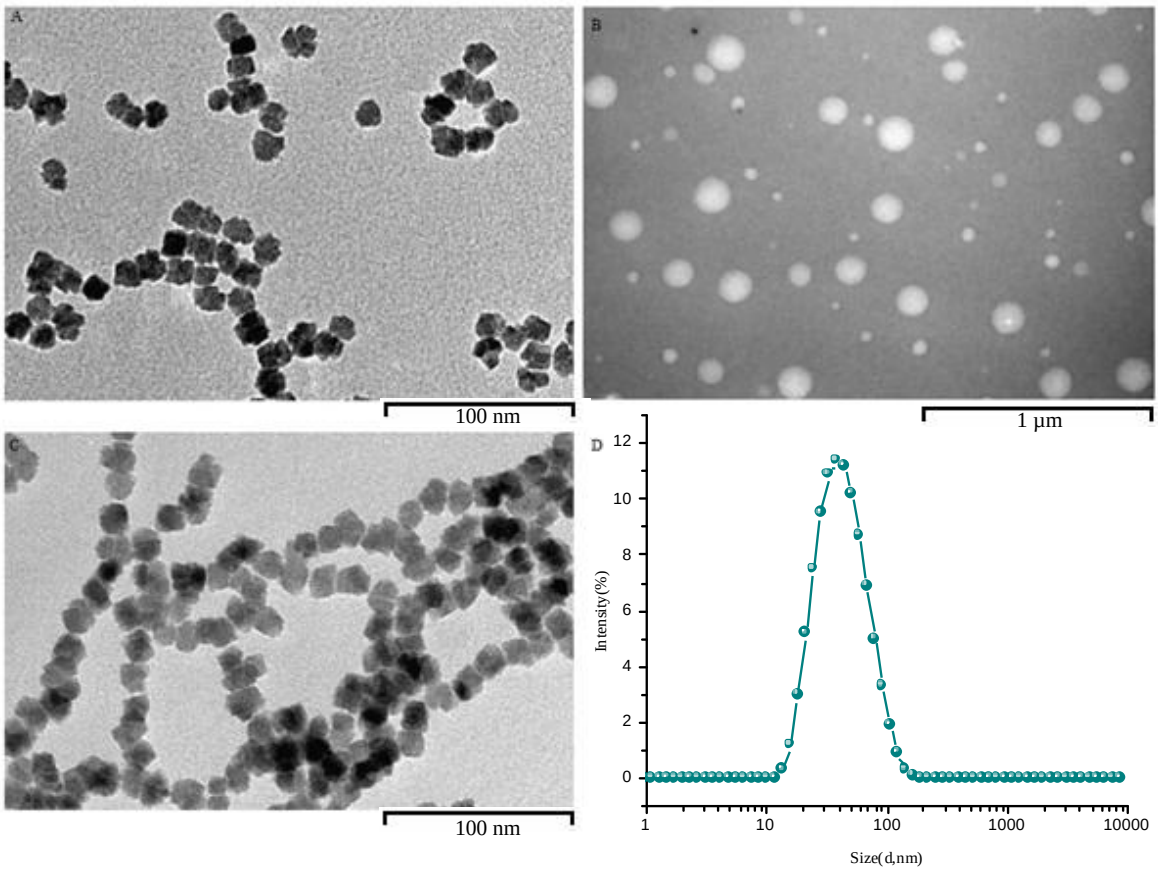

Figure 5.3 TEM images of Fe_3O_4-68 after the polymer conjugation (A), PVCL nanosphere (B), Fe_3O_4-68 before polymer conjugation (C), DLS histogram of hydrodynamic diameter of a Fe_3O_4-68@PVCL (D)

To clarify this point the weight loss of the functionalized Fe_3O_4-68 was determined by using a thermogravimetric analyzer under a nitrogen atmosphere (60 cm^3/min). The sample, which contains 30.6 mg of the thermoresponsive coated Fe_3O_4-68, was heated from room temperature to 1000 °C with the heating rate set at 5 °C/min. TGA curve for PVCL–MNPs as displayed in Figure 5.4 revealed weight losses occurred at two steps. The first step between 100 ^oC and 190 ^oC was due to the loss of residual water in the sample. The pronounced weight loss between 200 ^oC and 600 ^oC was related to the degradation of PVCL [24]. There was no significant weight change between 600 ^oC and 1000 ^oC, implying the presence of only iron oxide within the temperature range. Figure 5.4 also exhibits TGA curve of Fe_3O_4-68 NPs before polymer coating. The first significant weight loss between 40 ^oC and 193 ^oC (0.54 wt %) can be attributed to the evaporation of water molecules on the surface. The sharp mass loss observed around 200 ^oC to 550 ^oC (3.1 wt %) corresponds to the combustion of diethylen glycol (DEG) in the sample.

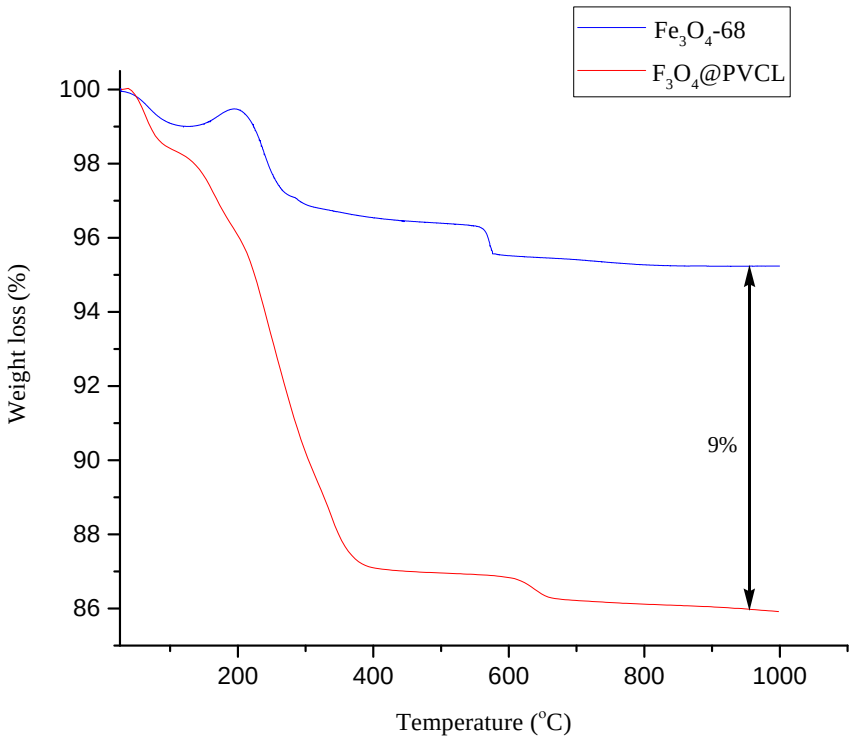

Figure 5.4 Thermogravimetric analysis of PVCL functionalized Fe_3O_4-68 (red line) and uncoated MNPs (blue line)

From the percentage of weight loss in the TGA curve, the composition of the Fe_3O_4-68 @ PVCL was estimated 91.0 wt % Fe_3O_4-68 and 9.0 wt % PVCL. These results indicated that Fe_3O_4-68 was not successfully encapsulated by PVCL.

To conclude, according to TEM and TG analyses, the smart nanocomposite containing Fe_3O_4-68 core and PVCL shell did not fulfil our goal as we expected, likely due to the weak thermoresponsive polymer adherence on their surface. To overcome this drawback, MNPs were encapsulated by thermoresponsive copolymer PVCL-*b*-PVPON by ‘’garfting to’’ approach to provide stable suspension usable for biological system.

5.3 Encapsulation of Magnetic Nanoparticles by PVCL-b-PVPON by Post Modification Method

The same procedure as that used for Fe_3O_4-68@PVCL preparation was employed to prepare Fe_3O_4-68 @PVCL-*b*-PVPON nanocomposite. The obtained product was suspended into 20.0 mL phosphate buffer (10 mM, pH = 7.4), and stored for long time without any

stability problem. Preparation procedure of this nanocomposite is explained completely in Appendix A.8.

Morphology of coated Fe_3O_4-68 was investigated by TEM as shown in Figure (5.5, A). In this case also from TEM images is not possible to distinguish encapsulation of MNPs by copolymer.

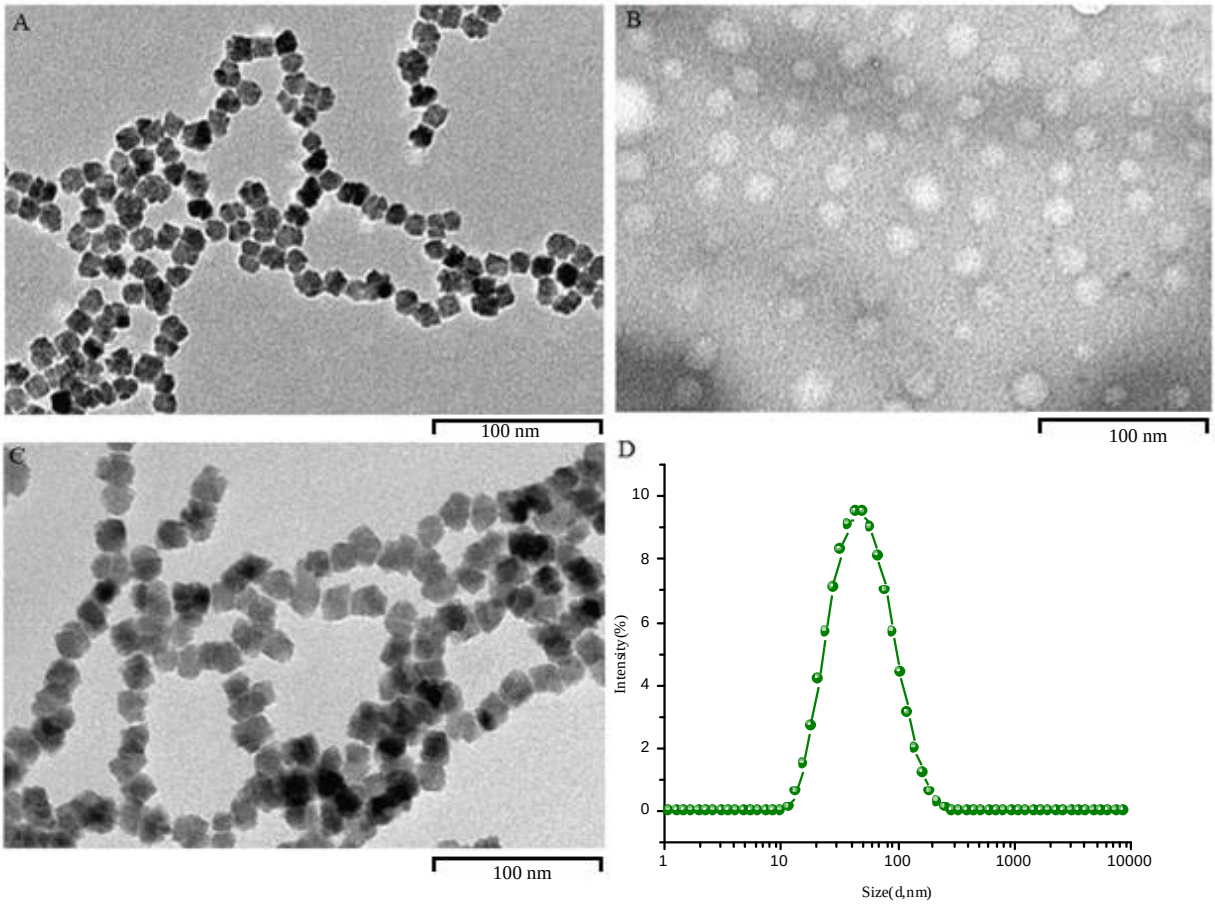

Figure 5.5 TEM views of Fe_3O_4-68 after polymer conjugation (A) the PVCL-*b*-PVPON (B), DLS histogram of hydrodynamic diameter of a Fe_3O_4-68@PVCL-*b*-PVPON suspension (C), Fe_3O_4-68 NPs before the copolymer conjugation (D)

Similarly, DLS analysis (Figure 5.5, D) was performed by six independent runs (15 measurements each) on 1.0 mL of suspension, and results indicated that the hydrodynamic radius of the coated MNPs in suspension is 45 nm with PDI ~ 0.22, which is larger than that found from TEM, which could be as a result of aggregation.

The organic content of the Fe_3O_4-68@PVCL-*b*-PVPON was determined using TGA in the temperature range from 25 ^oC to 1000 ^oC under a nitrogen atmosphere (60 cm^3/min). Figure 5.6 reveals the weight loss of the functionalized MNPs as a function of temperature

occurs in two steps. The first step between 100 ^{o}C and 200 ^{o}C is attributed to the loss of residual water in the sample, while the second mass loss observed around 215 ^{o}C to 575 ^{o}C can be ascribed to the degradation of PVCL-*b*-PVPON. Moreover, according to the Figure 5.6, in the absence of a polymer coating, the weight loss is about 4.0 wt % for the whole temperature range, corresponding to the desorption of water and combustion of DEG from the surface of Fe_3O_4-68.

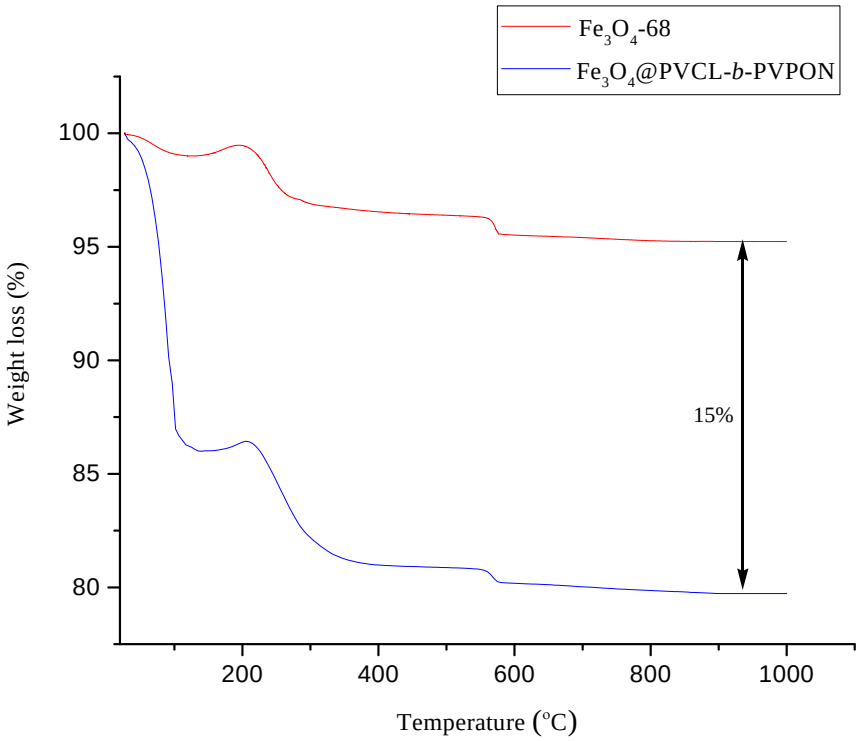

Figure 5.6 Thermogravimetric analysis of PVCL-*b*-PVPON functionalized Fe_3O_4-68 (blue line) and uncoated MNPs (red line)

Based on the percentage of weight loss in the TGA curve, the composition of the Fe_3O_4-68@ PVCL-*b*-PVPON contained 85.0 wt % MNPs and 15.0 wt % PVCL-*b*-PVPON, indicating that the PVCL-*b*-PVPON was bound to the MNPs surface with low yield.

Encapsulation of Fe_3O_4-68 with thermo-responsive PVCL-*b*-PVPON was also analyzed by FT-IR measurement, displayed in Figure 5.7. For the IR spectrum of Fe_3O_4@PVCL-*b*-PVPON, the broad band (3000–3500 cm^{-1}) centered around 3383 cm^{-1} can be originated from residual water. The aliphatic C-H stretching peaks, which located at 2937 cm^{-1} and 2865 cm^{-1} with low intensity, suggesting the small quantity of copolymer shell adhered on the MNPs surface. This observation was also confirmed by the fact that the

absorption bands at around 1661-1624 cm^{-1} correspond to characteristic carbonyl amide bonds (NHC=O) of PVCL-*b*-PVPON (Appendix A.5, Figure A.4), were not appeared in the FT-IR spectrum of polymer coated MNPs.

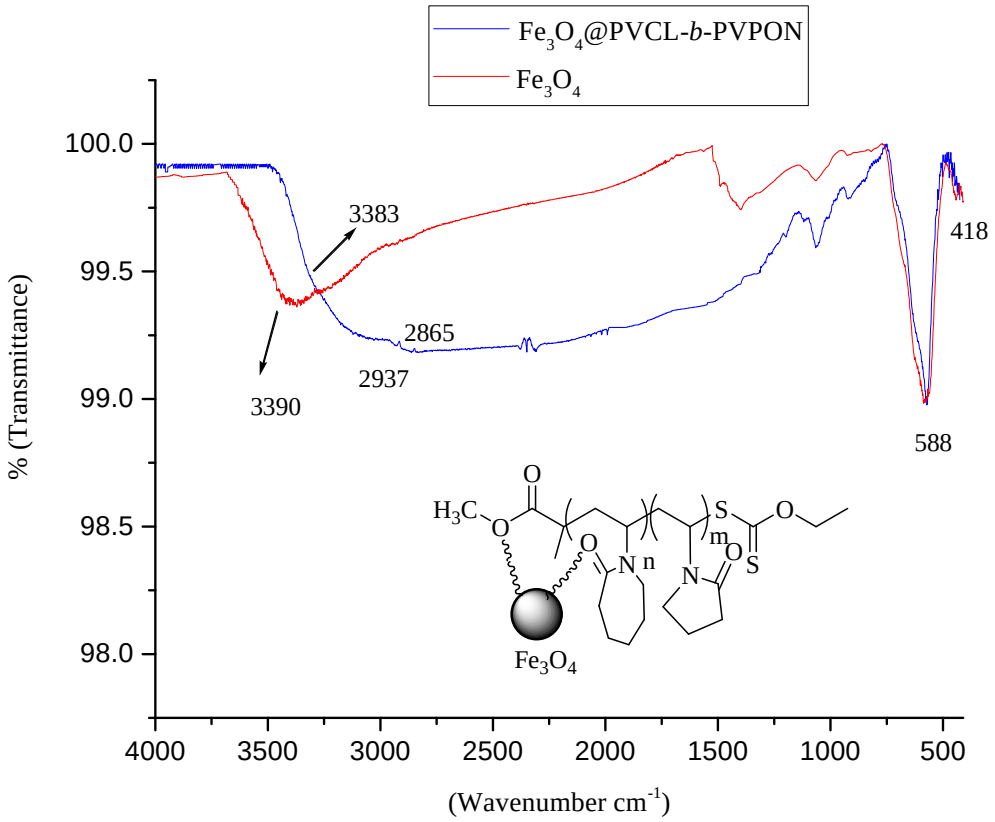

Figure 5.7 FTIR spectra of Fe_3O_4-68 coated with PVCL-*b*-PVPON (blue line) and Fe_3O_4-68 (red line)

However, two characteristic absorption bands, assigned at 588 cm^{-1} and 418 cm^{-1}, which are the characteristic peaks of the stretching vibration of Fe-O bonds from MNPs were clearly observed for both samples. Furthermore, the characteristic absorption band appeared at 3390 cm^{-1} in the spectrum of MNPs was attributed to the water.

To summarize, these data confirm that functionalization of Fe_3O_4-68 by thermo-responsive PVCL-*b*-PVPON through ‘’grafting to’’ approach did not proceed as expected. We, thus, decided to modify (co)polymer structure by grafting acrylic acid units in polymeric backbone to directly anchor the polymer on MNPs surface. In fact, as previously discussed, poly acrylic acid can easily bind to iron oxide MNPs and stabilize them, providing both electrostatic and steric repulsions against aggregation. Moreover, the large number of

carboxylate groups on the surface allows further modifications such as bioconjugation for *in vivo* application.

5.4 Functionalization of Fe_3O_4-68 by In Situ Copolymerization of PVCL-b-PAA

As alternative route, we explored *in situ* copolymerization, which is a well established technique to prepare magnetic nanocomposites. Indeed, this technique offers several advantages such as simplicity, (especially for the embedding of MNPs in cross-linked nanogel or microsphere) [25], having control on polymer chain length and molecular weight with high drug loading capacity [26].

As demonstrated in Scheme 5.1, the decoration of Fe_3O_4-68 surface by PVCL-*b*-PAA temperature sensitive copolymer was performed directly *in situ* on Fe_3O_4-68 (0.2 mol % with respect to NVCL) by free radical copolymerization between N-vinylcaprolactam (NVCL, 90.0 mol %), acrylic acid (AA, 10.0 % mol), and 2.0 mol % of AIBN (initiator) dissolved in 15.0 mL DMF. The obtained functionalized Fe_3O_4-68 NPs were dispersed in 10.0 mL distilled water.

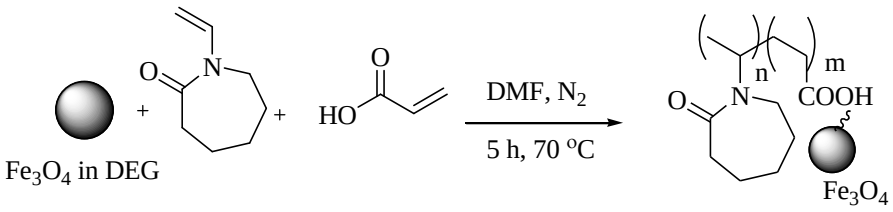

Scheme 5.1 Encapsulation of Fe_3O_4-68 by thermo-responsive copolymer PVCL-*b*-PAA

Particle size and size distribution of encapsulated Fe_3O_4-68 (0.011 wt % of Fe_3O_4 according to ICP analysis) were determined by DLS measurement on 2.0 mL of suspension as shown in Figure 5.8, and average particle size was estimated corresponding to three independent runs (15 measurements each run). DLS result indicated that particles are nearly uniform in size with PDI ~ 0.247 and with average hydrodynamic diameter of 128.0 nm. Moreover, negative surface charge of -17.0 mV was obtained consistently with the presence of carboxylate group on the surface of the nanosystems. However, for electrostatic stabilization of the MNPs, a high zeta potential above -30.0 mV is required; accordingly, under the copolymerization conditions utilized for MNPs in DMF the reaction did not give the desired colloidally stable nanocomposite, and polymer coated nanoparticles precipitated out of solution within the first few days of polymerization.

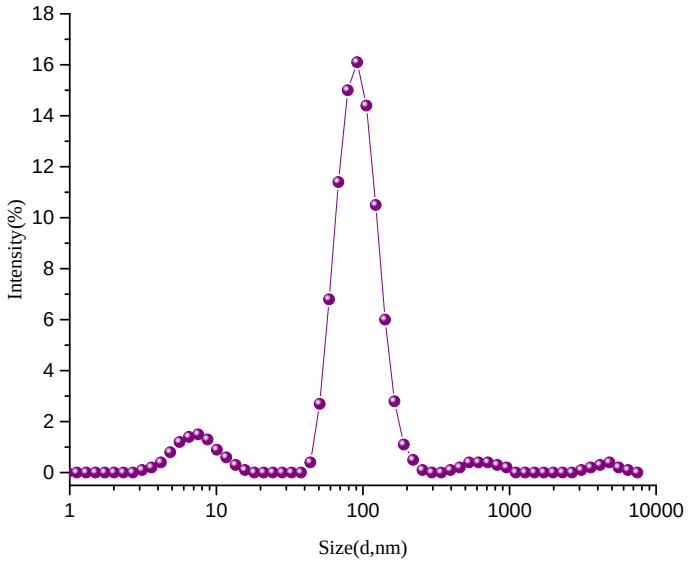

Figure 5.8 Size distribution of *in situ* encapsulated Fe_3O_4-68 by thermoresponsive PVCL-*b*-PAA

5.5 Functionalization of Fe_3O_4-68 by PVCL-b-PAA Corresponding to "Grafting to" Method

Since also *in situ* polymerization did not afford the desired product, we made another attempt using a covalent "grafting to" approach between PVCL-*b*-PAA copolymer and amine-surface functionalized Fe_3O_4-68 to stabilize nanoparticles. For this purpose, as shown in Scheme (5.2, a), aqueous suspension of Fe_3O_4-68@6-AHPA (preparation procedure is described in Appendix A.9.2) was mixed with a methanolic solution containing PVCL-*b*-PAA_2, (1-ethyl-3-(3-dimethylaminopropyl) carbodiimide hydrochloride (EDC), and N-hydroxysuccinimide (NHS) as carboxylic group activators, and the obtained functionalized Fe_3O_4-68 MNPs were dispersed in 10.0 mL buffer phosphate 10 mM, pH = 7.4. The same procedure was also repeated in ethanol using 4-(dimethylamino) pyridine (DMAP), and N,N'-Dicyclohexylcarbodiimide (DCC) as coupling reagents, to facilitate amide bond formation between acrylic acid units of copolymer and amine group on the surface of Fe_3O_4-68 (Scheme 5.2, b), and similarly the obtained MNPs were dispersed in 10.0 mL buffer phosphate 10 mM, pH = 7.4. Notwithstanding the fact that there are many publications concerning functionalization of MNPs by thermoresponsive polymer *via* amide bond formation, in our case, this approach was not suitable enough to give highly stable smart nanocomposite aqueous suspension. Consequently, we attempted to carry out surface

modification of Fe_3O_4-68 by temperature sensitive PVCL-*b*-PAA_2 *via* strong coordinate bonding (this type of interaction is central to lewis acid-base theory) between carboxylic acid units as an anchor to iron oxide surface without addition of any crosslinker as displayed in Scheme (5.2, c).

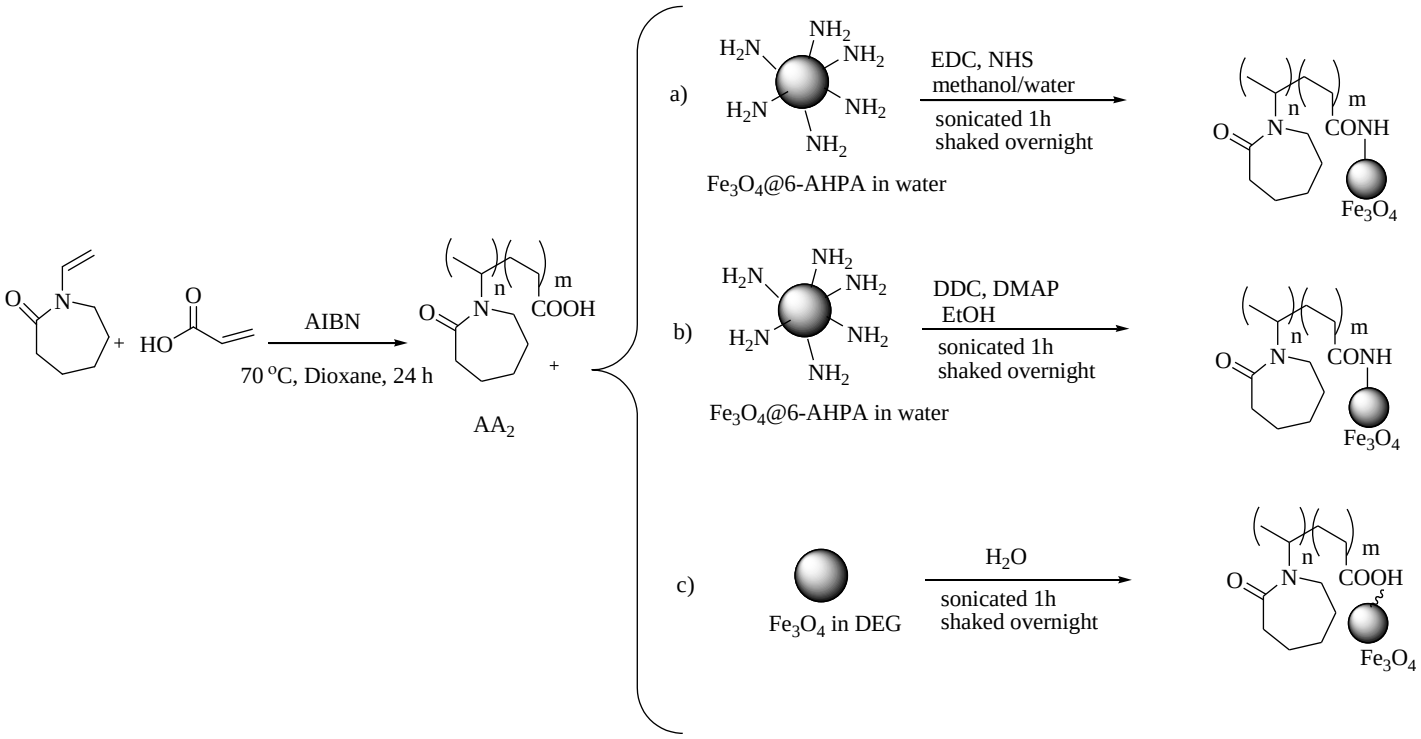

Scheme 5.2 Surface functionalization of Fe_3O_4-68 by thermoresponsive copolymer

In this way, encapsulation of Fe_3O_4-68 was performed by simply mixing aqueous copolymer solution with Fe_3O_4-68 nanoparticles under sonication for 1 h and agitation at room temperature overnight. Full experimental details of the synthesis procedure are given in Appendix A.10. The obtained nanoparticles were dialyzed by dialysis bag (MWCO ~ 14 KDa) against distilled water, and directly utilized for DLS and ICP characterization. ICP analysis indicated mean concentration of magnetic nanocomposite dispersed in 20.0 mL solution was about 0.14 wt % respect to the Fe_3O_4 nanoparticles

The average size of Fe_3O_4-68 coated PVCL-*b*-PAA_2 was found ca. 99.0 nm by DLS analysis according to 15 measurements based on four independent runs on 1.0 mL of suspension as exhibited in Figure 5.9. A uniform dispersion of nanocomposite with the polydispersity index, PDI ~ 0.194 was confirmed by DLS characterization as well.

In order to consider stability of surface modified MNPs suspension and effectiveness of surface modification method, zeta potential was measured. According to the measurement for the smart nanohybrid suspension the zeta potential value was -36.0 mV, confirming the suspension was highly stable in neutral pH, and the negative surface charge evidenced the presence of acrylic acid block grafted strongly on the iron oxide nanoparticles surface.

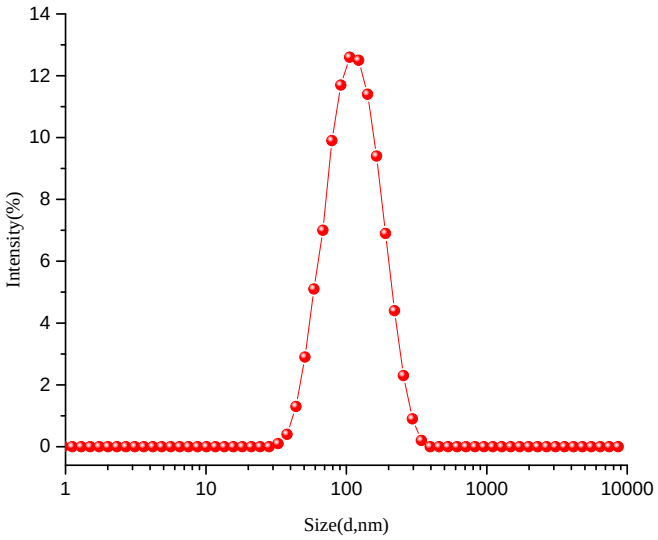

Figure 5.9 Size distribution of Fe_3O_4-68 coated PVCL-*b*-PAA_2

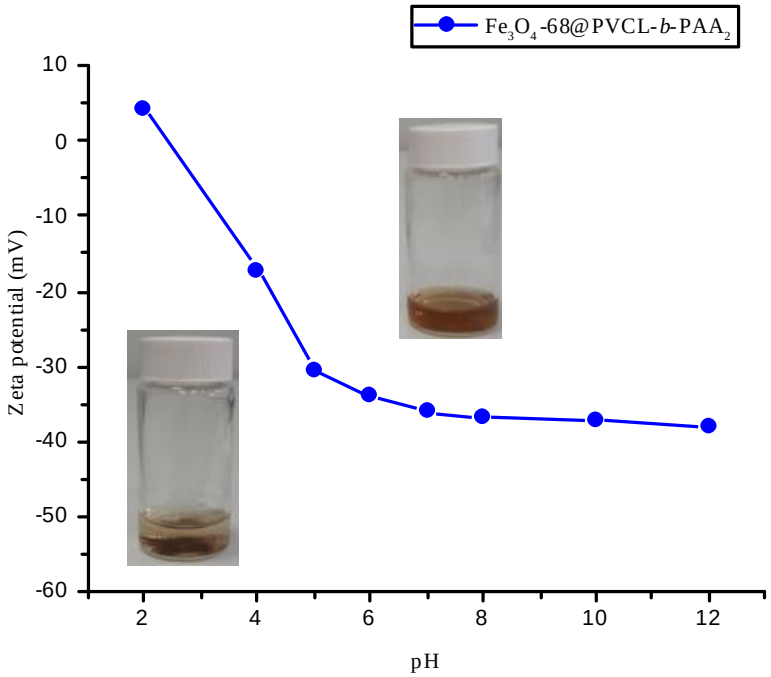

Figure 5.10 Zeta potential as a function of pH measured by dispersion the smart nanocomposite in buffer phosphate solution and then adjusting the pH with NaOH 0.1M

In order to check the pH responsive behavior of the nanosystem, the zeta potential of suspension was measured as a function of pH at room temperature, and results are reported in Figure 5.10.

Smart nanohybrids are highly stable from pH 5.5 to 12 with large negative surface charge (from -38.0 to -33.0 mV) due to the deprotonation of carboxylic acid units. As pH reduced below 5, the dispersion started losing the stability and complete precipitation occurred as a result of protonation of carboxylic groups, which caused small positive surface charge +4.0 mV; however, by addition of more NaOH solution, clear and stable dispersion can be recovered by shaking or sonication.

The morphology of Fe_3O_4/PVCL-*b*-PAA_2 nanocomposite was investigated by TEM as demonstrated in Figure 5.11.

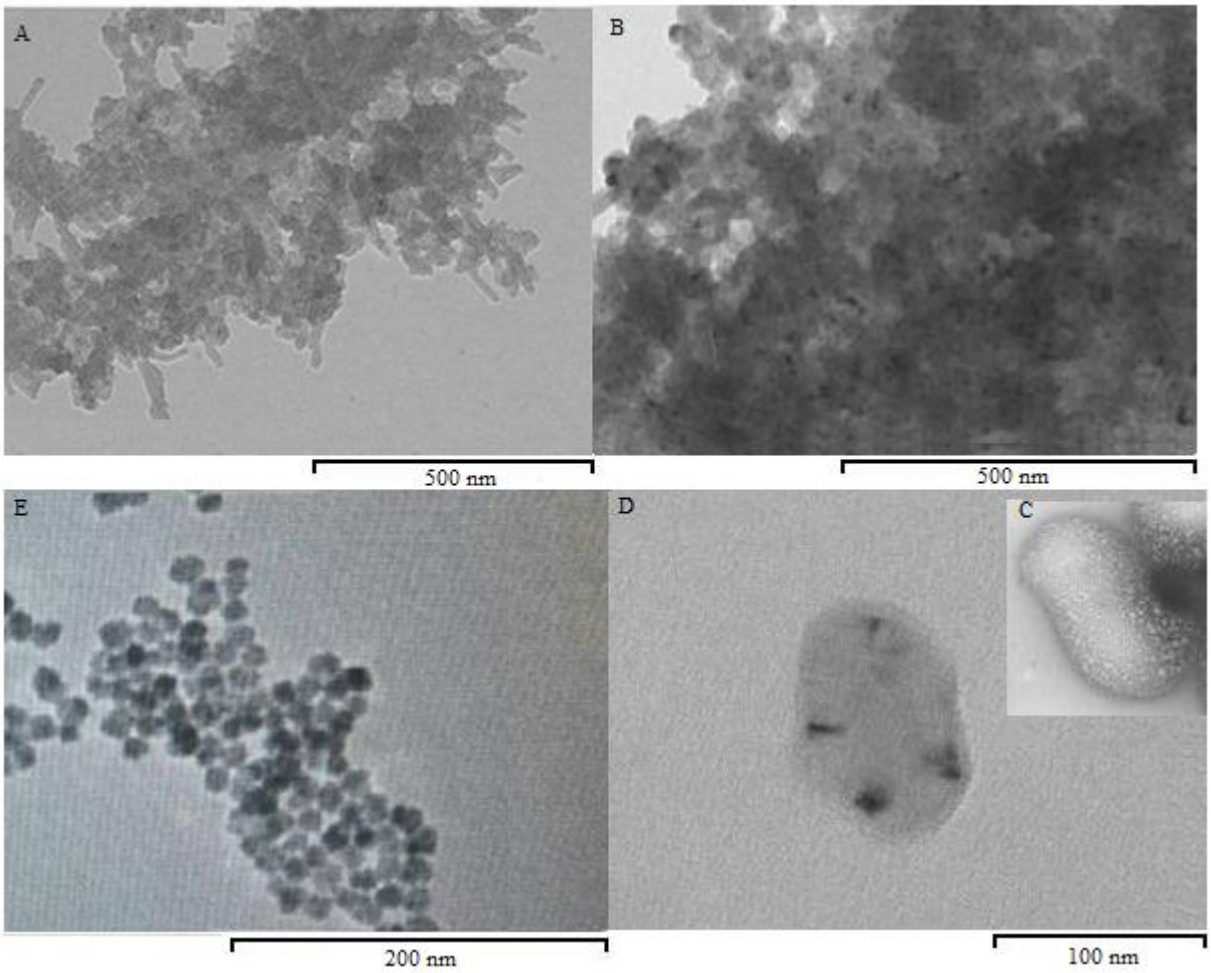

Figure 5.11 TEM images of PVCL-b-PAA_2 (A), Fe_3O_4-68 encapsulated PVCL-*b*-PAA_2 (B), polymer before MNP inclusion at higher resolution (C), MNPs@PVCL-*b*-PAA_2 at higher resolution (D), Fe_3O_4-68 before polymer coating

Figure (5.11, A) reveals the PVCL-*b*-PAA_2 as a short chain morphology with average length in the 60.0-80.0 nm range. It can be seen from the Figure (5.11, B) that MNPs are well distributed within the polymer matrix, and from the comparison with Figures (5.11, C, D) it is obvious that the composite nanoparticles retained the oval shape of the polymer in their structure. The average diameter of nanohybrid based on statistical analysis over 500 nanoparticles dispersed in water is 60.0 nm as shown in Figure (5.11, D), where a representative particles is observed. This average size value is smaller than that one found from DLS analysis. Indeed, this might result from the existence of a structured water layer adjacent to the hydrophilic surface of nanocomposite, which can enhance the hydrodynamic radius measured by DLS as compared to TEM morphogram.

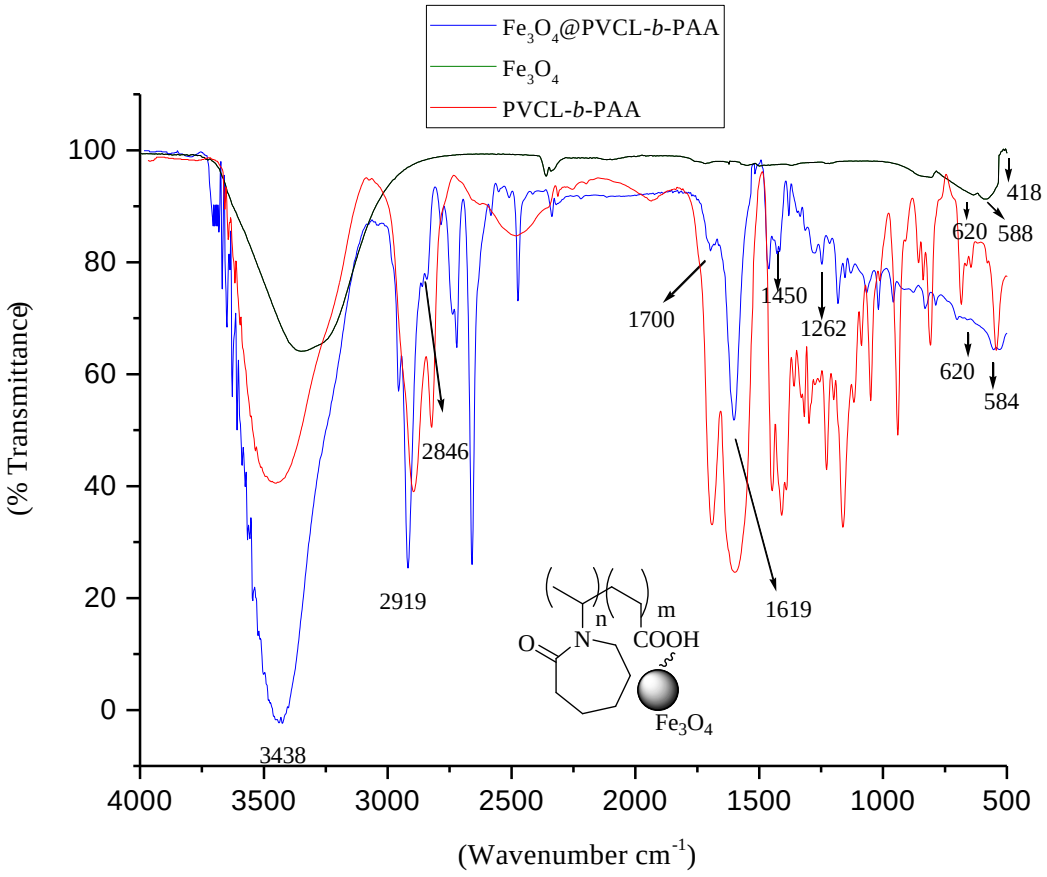

Figure 5.12 FTIR spectra of Fe_3O_4-68 coated by thermo-responsive PVCL-*b*-PAA_2 (blue line), PVCL-*b*-PAA_2 (red line), and uncoated Fe_3O_4-68 (green line)

Encapsulation of Fe_3O_4-68 with thermoresponsive PVCL-*b*-PAA_2 was confirmed by FT-IR analysis, shown in Figure 5.12. For copolymer functionalized Fe_3O_4-68 (blue line) two peaks are observed at 1700 cm^{-1} and 1619 cm^{-1}, which are characteristic of stretching vibration of HO-C=O (carboxylic) groups in acrylic acid domain and amide carbonyl group

(NHC=O) in PVCL domain on the surface of MNPs that are similarly revealed in FT-IR spectrum of PVCL-*b*-PAA (red line). In the spectrum of nanocomposite (blue line) the peak at 1450 cm^{-1} is representative of C-OH groups and that one at 1262 cm^{-1} is assigned to the C-O groups in consequence of polymer coating. The broad band centered around 3438 cm^{-1} is attributed to the absorption of water from the air. The characteristic Fe–O stretching vibration bands are also observed at 620 cm^{-1} and 584 cm^{-1} as seen clearly in FT-IR spectrum of uncoated Fe_3O_4 (green line). Moreover, two peaks at 2846 cm^{-1} and 2919 cm^{-1}, corresponding to aliphatic C-H groups of polymer shell, confirm polymer grafted on the surface of MNPs successfully.

The amount of PVCL-*b*-PAA_2 bound on the Fe_3O_4-68 surface was assessed by TG analysis. As shown in Figure 5.13, TGA curve of smart nanocomposite (red line) revealed two steps in weight loss: the first significant weight loss at 95 ^oC can be attributed to the evaporation of residual water on the surface, and then the sharp mass loss observed around 230 °C to 576 °C corresponds to the thermal decomposition of PVCL-*b*-PAA_2. Above 576 °C no significant weight change is observed, implying the presence of only iron oxide nanoparticles.

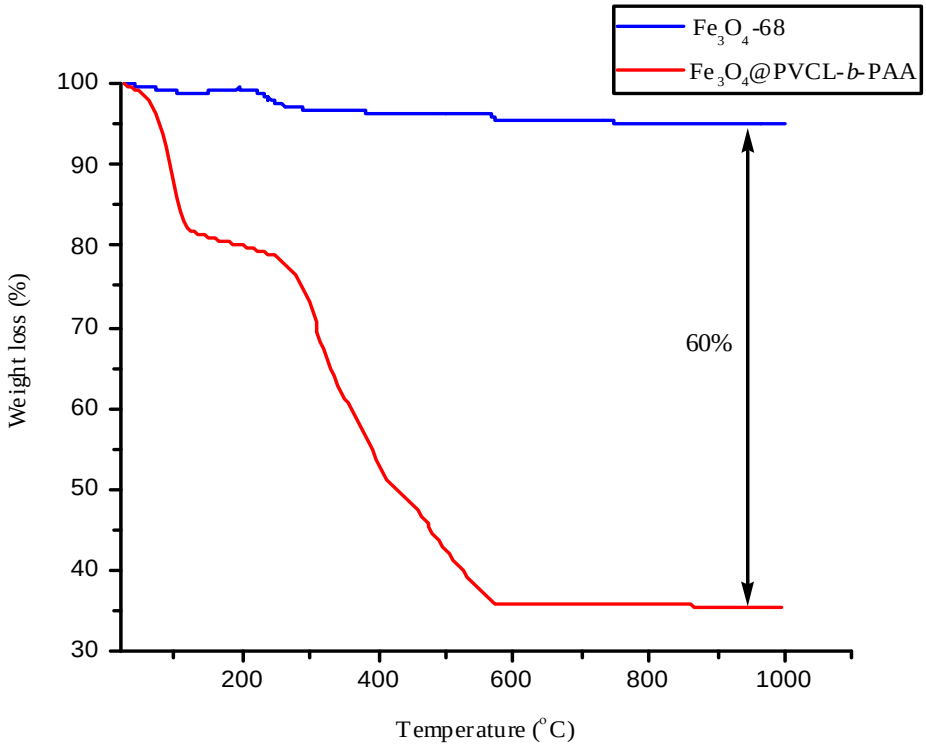

Figure 5.13 TG curve of smart nanocomposite made up of Fe_3O_4-68 core and PVCL-*b*-PAA_2 shell (red line), uncoated Fe_3O_4-68 (blue line)

Moreover, according to the TGA curve of uncoated MNPs (blue line), in the absence of a polymeric shell, the weight loss is about 4.0 wt % for the whole temperature range, corresponding to the desorption of water and combustion of DEG from the surface of Fe_3O_4-68. Therefore, the weight ratio estimated by TGA analysis (40.0 wt % MNPs and 60.0 wt % PVCL-*b*-PAA_2) proves that MNPs are effectively incorporated in the polymer matrix.

Subsequently, we determined the temperature-responsive property of the smart nanocomposite at pH 7.4 and 5.5, using DLS measurement on 1.0 mL suspension containing 6.0 mg mL^{-1} copolymer and 0.14 wt % MNPs, as discussed in chapter 4. The expected phase transition was observed by heating from 25 °C to 65 °C with a rate of 5 °C/min and equilibration time of ca. 10 min as reported in Figure 5.14.

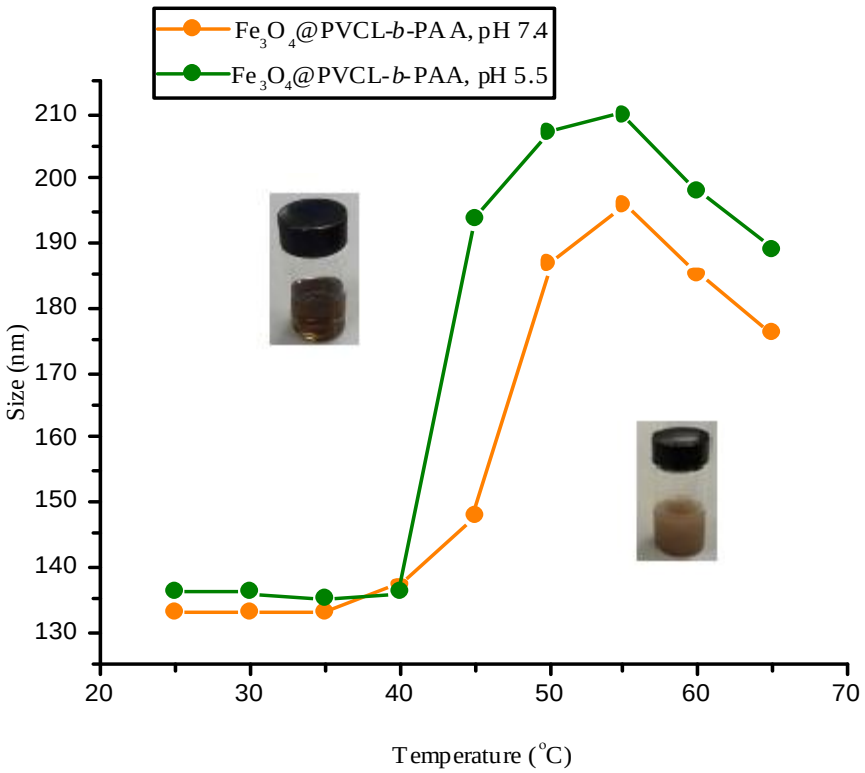

Figure 5.14 Hydrodynamic size variation of Fe_3O_4-68@copolymer as a function of temperature, evaluated by DLS

Below 35 °C ($T < LCST$) at pH 7.4, the particle size of the suspension was almost constant, indicating that the polymer adhered strongly on the MNPs surface, and prevented aggregation formation. From 35 °C to 45 °C the size of the magnetic nanohybrids gradually grew and

at $T \geq 45$ ^{o}C particle size strongly enhanced, indicating that LCST was reached. Indeed, at temperature below 45 ^{o}C, the hydrophilic copolymer chains stretched into water and separated every particle from its neighbors by steric and electrostatic force. When the temperature increased above 45 ^{o}C, the hydrophilic structure transformed into hydrophobic, and due to the loss of steric force, composite nanoparticles formed big aggregates, resulting in the increase of the particle size. We, likewise, observed the same temperature responsive behavior of Fe_3O_4-68@PVCL-*b*-PAA_2 at pH 5.5 although the LCST was shifted to lower temperature ~ 40 ^{o}C as a consequence of protonation of the carboxylate groups. The obtained results confirmed that the smart nanocomposite is dual pH and temperature-sensitive, as extensively discussed in chapter 4. It is worth pointing out that LCST of copolymer solution with concentration of 6.0 mg mL^{-1} after grafting on the surface of MNPs at neutral pH (LCST ~ 45 ^{o}C) and acidic pH (LCST ~ 40 ^{o}C) is 5 ^{o}C larger than LCST of copolymer solution without MNPs at the same pH and concentration (LCST ~ 40 ^{o}C at pH 7.4 and LCST ~ 35 ^{o}C at pH 5.5) because introduction of MNPs in polymer matrix increases LCST value significantly; indeed, introduction of magnetic nanoparticles provides additional steric hindrances inside the polymer matrix, which could hamper the aggregation of the hydrophobic polymer segments that takes place above LCST. Consequently, higher thermal energy is required to overcome this barrier, and the collapse of the copolymer occurs at higher temperature [27-29].

.

In order to have a complete characterization of the obtained nanohybrids, magnetic behavior of functionalized Fe_3O_4-68 at 10 K and 300 K was investigated. The magnetometric study was performed on dried powder of sample and the principal magnetic parameters obtained, and summarized in table 5.1 along with parameters relevant to uncoated iron oxide magnetic nanoparticles. As displayed in Figure 5.15, the saturation magnetization (Ms) and the remanence (Mr) of uncoated Fe_3O_4 and copolymer coated Fe_3O_4 at 300 K and 10 K are nearly equal for two samples. A small difference is observed in the coercivities, which can be ascribed to lower magnetic dipolar interaction between the magnetite cores in the coated samples as a consequence of the copolymer shell shielding [30,31]. Moreover, the magnetic remanence values at room temperature are ca. zero for magnetite nanoparticles before and after polymer coating, while at 10 K magnetic irreversibility occurs. Thus, thermoresponsive coated MNPs at room temperature exhibit magnetization properties similar to uncoated MNPs, showing a superparamagnetic-like behavior.

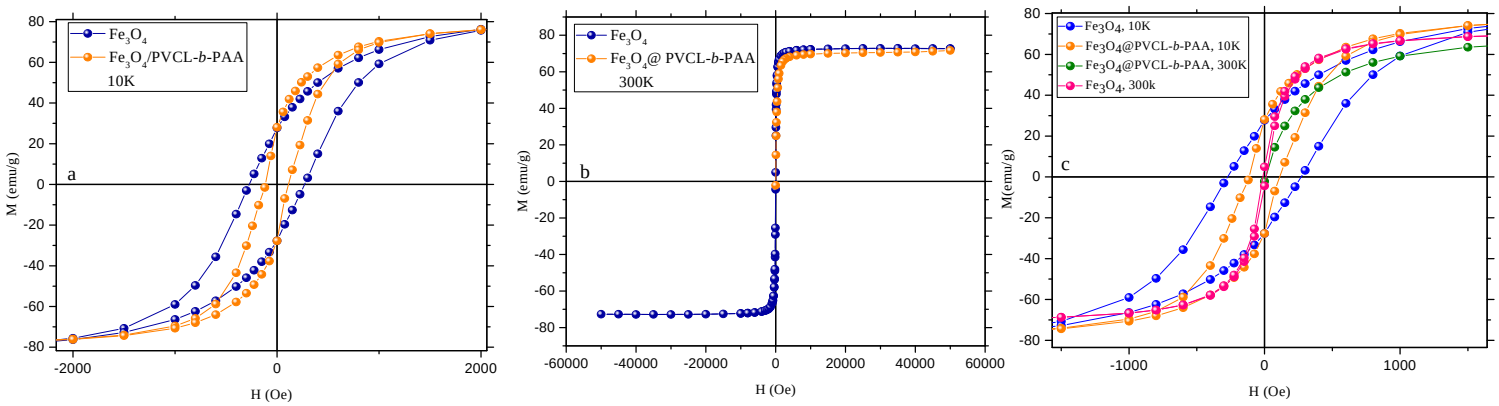

Figure 5.15 Hysteresis loops of copolymer coated and uncoated MNPs at 10 K, (a) and 300K (b), enlargement of the low field region of the four loops, showing the transition from blocked to superparamagnetic state (c)

Sample	Ms (emu g^{-1}) 300 K	Ms (emu g^{-1}) 10 K	Particle size (nm)	Mr (emu g^{-1}) 10 K	Coercivity (Oe) 10K
Fe_3O_4	76	84	18.0	28	300
Fe_3O_4-copolymer	77	80	60.0	27	150

Table 5.1 Magnetic properties of Fe_3O_4-68 after and before polymer coating. Data are normalized for the amount of inorganic material

The hyperthermic efficiency was evaluated on 1.0 mL of aqueous suspension of Fe_3O_4-68@PVCL-*b*-PAA_2 at two different concentrations of magnetite 0.4 wt % (A) and 0.14 wt % (B) under applying an AMF with frequency of 183 kHz and amplitude of 17 kA m^{-1} for 5 min. The heating generated by samples under the AMF led to an increase in the temperature of suspension, and the temperature variation as a function of time is shown in Figures 5.16.

As seen in Figure 5.16, a large temperature increase for both samples is observed, and the two suspensions reaching 60 ^{o}C (A) and 43 ^{o}C (B) after 5 min of field application. From the initial slope of the heating curves, SAR values of two samples were estimated to be 183.0 W $g_{(Fe3O4)}^{-1}$ and 253.0 W $g_{(Fe)}^{-1}$ for sample (A), and 150.0 W $g_{(Fe3O4)}^{-1}$ and 206.0 W $g_{(Fe)}^{-1}$ for sample (B). In both cases, the heating power generated by the sample is sufficient to induce *in vivo* drug release.

It should be pointed out that the magnetic field strength and frequency used in the present work are lower than those reported in many other works in literature [18–20], and is below the threshold for clinical applications. Hence, a further enhancement of heating ability can be obtained by using stronger magnetic field.

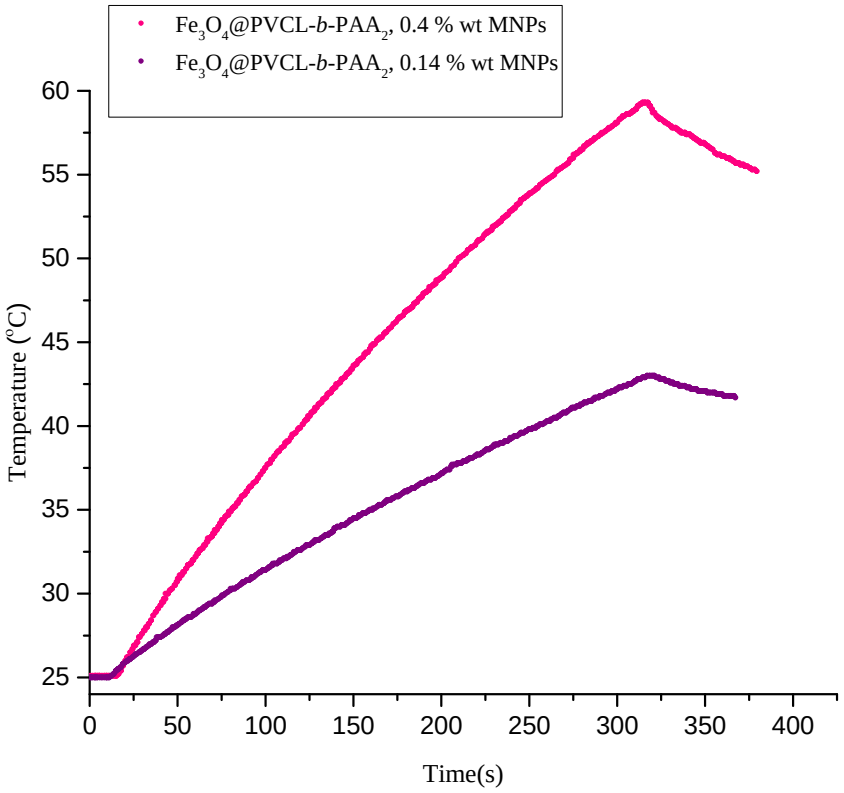

Figure 5.16 Temperature *vs* time curves of the Fe_3O_4-68 functionalized PVCL-*b*-PAA_2

In conclusion, the Fe_3O_4-68/PVCL-*b*-PAA_2 magnetic nanohybrids were successfully prepared by "grafting to" method without applying any crosslinker. The ability of this temperature and pH-responsive block copolymer to stabilize MNPs suspension in aqueous media was studied by TEM, DLS, and zeta potential measurements. FTIR and TG analyses also confirmed the polymer is effectively grafted on the surface of MNPs. The remarkable advantage of this system is that it is solely made of iron oxide MNPs and hydrophilic polymers such as poly N-vinylcaprolactam and poly acrylic acid, which are non-toxic and biodegradable, and thus can be used for biological application. Most importantly the polymer preserves pH and temperature responsive properties, resulting in a stimuli-responsive biocompatible nanohybrid, which has potential to produce high quantity of heat in response to harmless alternating magnetic field.

Chapter5

References

1. a) E. Umut. Surface modification of nanoparticles used in biomedical applications. **2013**, chapter 8, pp186, b) C. Tudisco.; M. T.Cambria.; G. G.Condorelli. Biomedical Applications of Functionalized Nanomaterials, Concepts: Development and Clinical Translation, Micro and Nano Technologies. **2018**, Pages 335-370.
2. C. Boyer.; M. R. Whittaker.; V. Bulmus.; T. P. Davis. *NPG Asia Mater.* **2010**, *2*, 23.
3. T. A. Heimer.; S. T. D. Arcangelis.; F. Farad.; J. M. Stipala.; G. J. Meyer. *Inorg. Chem.* **1996**, *35*, 5319.
4. Y. T. Tao. *J. Am. Chem. Soc.* **1993**, *115*, 4350.
5. G. Kataby.; M. Lojocarie.; R. Prozarov.; A. Gedanken. *Langmuir*. **1999**, *15*, 1703.
6. P. G. Hoertz.; R. A. Carlisl.; G. J. Meyer.; D. Wang.; E. Galoppini. *Nano Lett.* **2003**, *3*, 325.
7. J. Ge.; Y. Hu.; M. Biasini.; C. Dong.; J. Guo.; W. P. Beyermann.; Y. Yin. *Chem. Eur. J.* **2007**, *13*, 7153.
8. a) Y. Sahoo. *Langmuir*. **2001**, *17*, 7907, b) K. Gharbi.; F. Salles.; P. Mathieu.; C. Amiens.; D. Ciuculescu-Pradines. *New J. Chem.* **2017**, *41*, 11898.
9. L. Wang. *J. Am. Chem. Soc.* ***2006***, *128*, 13358.
10. R. Zhu.; W. Jiang.; Y. Pu.; K. Luo.; Y. Wu.; Z. Gu. *J. Mater. Chem*. **2011**, *21*, 5464.
11. M. D. Shultz.; J. U. Reveles.; S. N. Khanna.; E. E. Carpenter. *J. Am. Chem. Soc.* **2007**, *129*, 2482.
12. M. Beija.; J. D. Martya.; M. Destarac. *Prog. Polym. Sci*. **2011**, *36*, 845.
13. J. Tian.; Y. K. Feng.; Y. S. Xu. *Macromol. Res.* **2006**, *14*, 209.
14. L. Wang.; K. G. Neoh.; E. T. Kan.; B. Shuter.; S. C. Wang. *Adv. Funct. Mater.* **2009**, *19*, 2615.
15. X. Jiang.; Y. Li.; G. Lu.; X. Huang. *Polym. Chem*. **2013**, *4*, 1402.
16. M. Lattuada.; T. A. Hatton. *Langmuir.* **2007**, *23*, 2158.
17. H. Kakwere.; M. P. Leal.; M. E Materia.; A. Curcio.; T. Pellegrino. *ACS Appl. Mater. Interfaces*, **2015**, *7*, 10132.
18. C. Boyer. *J. Mater. Chem.* **2009**, *19*, 111.
19. R. Narain.; M. Gonzales.; A. S. Hoff man.; P. S. Stayton.; K. M. Krishnan. *Langmuir.* **2007**, *23*, 6299.

20. G. Huang. *J. Mater. Chem.* **2009**, *19*, 6367.
21. M. I. Shukoor. *Chem. Mater.* **2008**, *20*, 3567.
22. F. Zhang.; C. C. Wang. *Langmuir*. **2009**, *25*, 8255.
23. H. Lee. *J. Am. Chem. Soc.* **2006**, *128*, 7383.
24. S. Kozanoglu.; T. Zdemir.; A. Usanmaz. *J Macromol Sci Pure Appl Chem.* **2011**, *48*, 467.
25. Y. Salinas.; A. M. Castilla.; M. Resmini. *Polym. Chem.* **2018**, *9*, 2271, b) X. Qi.; L. Xiong.; J. Peng.; D. *Tang. RSC Adv*. **2017**, *7*, 19604.
26. N. Ngwuluka. *AAPS Pharm Sci Tech.* **2010**, *11*, 1603.
27. A. Pich.; S. Bhattacharya.; Y. Lu.; V. Boyko.; H. J. Adler. *Langmuir*. **2004**, *20*, 10706.
28. J. Rubio-Retama.; N. E. Zafeiropoulos.; C. Serafinelli.; R. RojasReyna.; B. Voit.; E. Lopez Cabarcos.; M. Stamm. *Langmuir*. **2007**, *23*, 10280.
29. C. Dionigi.; Y. Pin˜eiro.; A. Riminucci.; M. Ban˜obre.; J. Rivas.; V. Dediu. *Appl Phys A.* **2014**, *114*, 58.
30. S. A. Gomez-Lopera.; R. C. Plaza, A.V. Delgado. *J Colloid Interf Sci.* **2001**, *240*, 40.
31. W. Voit.; D. K. Kim.; W. Zapka.; M. Muhammed.; K. V Rao. *Mater Res Soc Symp Proc.* **2001**, *676*, Y7.8 .1–6.

Chapter 6

Drug Loading & Drug Release

Chapter 5 described the development of magnetic nanocomposites (MNCs) constituted by an iron oxide magnetic nanoparticles core and a pH- and thermo-responsive poly (vinylcaprolactam-*b*-acrylic acid) (PVCL-*b*-PAA) shell, that have potential to be used as both hyperthermic agent and drug carrier. In the following, we will outline the conjugation of the anticancer drug doxorubicin (DOX), a potent chemotherapeutic drug used clinically for the treatment of a broad spectrum of cancers, to the pH- and thermo-responsive MNCs to provide advanced drug delivery system for the controlled release of DOX.

Herein, in this chapter, the developed therapeutic nanosystem is investigated as multifunctional nanocarrier by measuring the percentage of doxorubicin released under the application of a harmless AMF (H = 17 kA m^{-1}, f = 183 kHz). Cytotoxicity of Fe_3O_4-68@PVCL-*b*-PAA_2 before and after drug loading is also evaluated.

6.1 Drug Loading

The investigation of the efficiency of the processes of loading and release of DOX loaded-Fe_3O_4-68@PVCL-*b*-PAA_2 MNCs was performed on 20.0 mL of two suspensions, containing different concentrations of MNPs and copolymer (0.14 wt % of Fe_3O_4 as well as 6.0 mg mL^{-1} of copolymer, samples A, and 0.4 wt % of Fe_3O_4 as well as 10.0 mg mL^{-1} copolymer, samples B). The approach followed for drug loading is schematically described in Figure 6.1, and explained completely in Appendix A.11.

DOX was loaded on PVCL-*b*-PAA_2 coated Fe_3O_4-68 in buffer phosphate with pH adjusted at 7.4 (samples $A_{7.4}$, $B_{7.4}$ similar to physiological pH) and 5.5 (samples $A_{5.5}$, $B_{5.5}$, corresponding to the mimicked tumour pH) simply by incubating at 25 ^oC in darkness for 72 h. After incubation, the DOX-loaded nanocomposite suspension was dialyzed against buffer phosphate 10 mM, pH = 7.4 (or 5.5) using dialysis membrane bag (MWCO ~ 1 kDa) for 24 h to remove the non-encapsulated drug. The concentration of free DOX in dialysis fluid was analyzed by UV-Vis spectroscopy at a specific wavelength 480 nm to determine the drug Encapsulation Efficiency *(EE)*, and Drug Loading Contents *(DLC)* defined as:

:

$$EE\ (\%) = \frac{mass\ of\ total\ drug - mass\ of\ unloaded\ Drug}{mass\ of\ total\ Drug}$$

$$DLC\ (\mu g\ mg^{-1}) = \frac{mass\ of\ loaded\ Drug}{mass\ of\ total\ Drug + mass\ of\ polymer + mass\ of\ MNPs}$$

The loading data obtained for the six samples are summarized in table 6.1.

Suspension in 20.0 mL buffer phosphate 10 mM	MNPs (wt %)	Polymer (mg mL^{-1})	Initial DOX (mg mL^{-1})	*EE* (%)	*DLC* (µg mg^{-1})
($A_{7.4}$): Fe_3O_4@polymer-DOX	0.14	6.0	0.225	90.0	29.0
($B_{7.4}$): Fe_3O_4@polymer-DOX	0.4	10.0	0.225	92.0	18.0
($B_{5.5}$): Fe_3O_4@polymer-DOX	0.4	10.0	0.225	53.0	10.0
($A_{5.5}$): Fe_3O_4@polymer-DOX	0.14	6.0	0.225	45.0	14.0
($C_{7.4}$):Fe_3O_4@polymer-DOX	0.4	10.0	0.375	96.0	23.0
($D_{7.4}$): Fe_3O_4@polymer-DOX	0.14	6.0	0.375	98.0	50.0

Table 6.1 Encapsulation efficiency and drug loading capacity

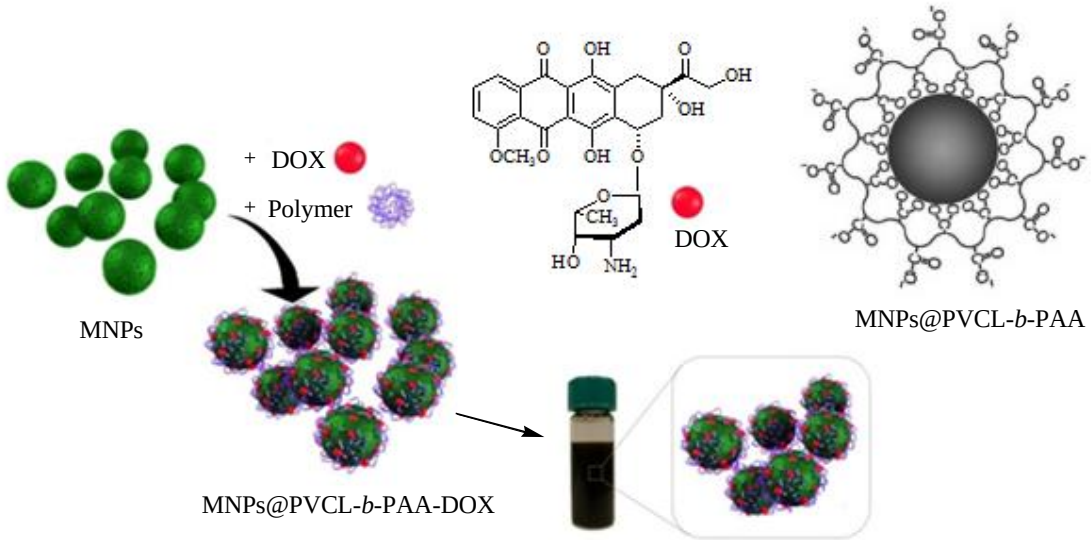

Figure 6.1Preparation of DOX loaded-Fe_3O_4-68@PVCL-*b*-PAA_2

According to the table 6.1, the results confirm the extraordinary capability of Fe_3O_4-68@PVCL-*b*-PAA_2 MNCs to load high contents of DOX at neutral pH. This ability can be ascribed to the $\pi - \pi$ stacking interactions between the aromatic rings of DOX, and

the carbonyl groups in the structure of PVCL-*b*-PAA_2 -based nanocomposite [1]. Moreover, the functionalization of Fe_3O_4-68 with PVCL-*b*-PAA_2 leaded to a high negative surface charge (zeta potential values ca. -36.0 mV), which also allows electrostatic interactions with positively charged DOX (pKa = 8.3) at pH = 7.4. On the other hand, in acidic pH % *EE* and % *DLC* of samples ($A_{5.5}$, $B_{5.5}$) decreased as a result of the protonation of poly acrylic acid in the structure of copolymer shell, resulting in repulsive electrostatic force between positive surface charge of DOX and the copolymer shell.

Importantly, the encapsulation efficiency *(EE)* of Fe_3O_4-68@PVCL-*b*-PAA_2 ($C_{7.4}$ and $D_{7.4}$) at neutral pH can be further enhanced by increasing the initial DOX concentration in the suspension. For instance, by using DOX with concentration of 0.375 mg mL^{-1} in 20.0 mL of suspension, an outstanding encapsulation efficiency of 96.0 % and 98.0 % with drug loading capacity of 23.0 and 50.0 µg mL^{-1} for samples $C_{7.4}$ and $D_{7.4}$ were obtained respectively.

6.2 Dual pH- and Temperature-Dependent In Vitro Drug Release in the Absence of AMF

The pH and temperature-responsive magnetic nanohybrids developed in this work was designed to have a LCST of ~ 45 ^oC at pH ~ 7.4 and LCST ~ 40 ^oC at pH ~ 5.5, that can be specifically utilized as smart drug delivery systems to trigger the release of drug by acidic pH values and temperature simultaneously.

The drug release behavior of 5 mL buffer suspension of sample $A_{7.4}$ was studied by dialysis technique at different pH conditions (pH ~ 7.4, 5.5 and 4.5 roughly corresponding to the physiological pH, the pH of tumour microenvironment, and that of intracellular tumour endosome/lysosome pH conditions respectively) in addition to different temperatures, i.e. 25 ^oC, 37 ^oC (below LCST), and 48 °C (above LCST), corresponding to ambient temperature, physiological temperature, and temperature that can be reached by the hyperthermic treatment (drug release process is fully described in Appendix A.12). Although 48 °C may seem slightly high temperature to simulate hyperthermia, we chose this value because the temperature at the MNPs surface can easily reach this value without necessarily producing a significant increase in the surrounding medium [2, 3].

The cumulative release of DOX was determined from the corresponding calibration curves of DOX at pH values of 4.5, 5.5, 7.4, and the percentage of drug release was assessed according to the following formula:

$$Cumulated\ released\ DOX = \left(\frac{Q_{t+}Q_{t-1}}{Q_{total}}\right) \times 100\ (\%)$$

Where Q_t and Q_{t-1} are the cumulative amounts of DOX released at time t and $t-1$, and Q_{total} is amounts of loaded DOX in the nanocomposite.

The obtained results are shown in Figure 6.2.

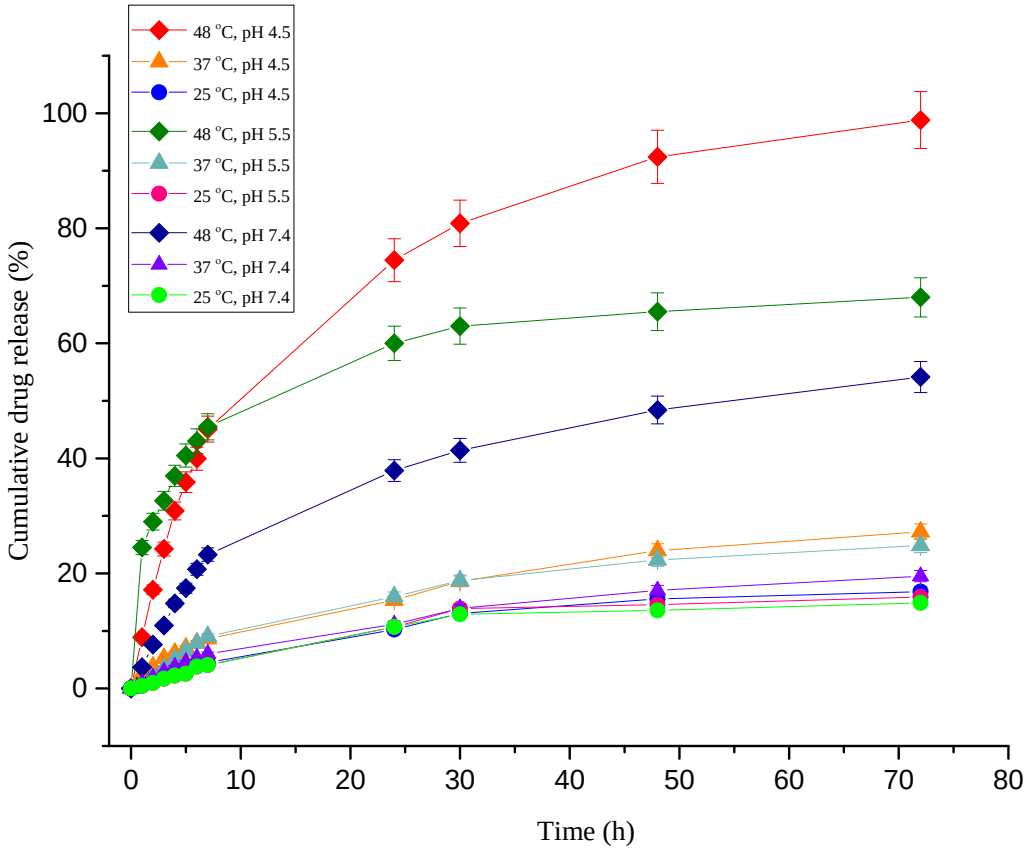

Figure 6.2 Release of doxorubicin (DOX) from drug loaded Fe_3O_4-68@PVCL-*b*-PAA_2 under different pH values (7.4, 5.5, and 4.5) and temperatures (25 °C, 37 °C, and 45 °C). Standard deviation of triplicate drug release tests (n=3)

The drug release curves of sample $A_{7.4}$ all follow the same trend: a rapid release of DOX is obtained within the first 7 h, followed by a slower rate of release in the next hours. Analysis of the curves shows that just a very low amount of DOX was released at physiological pH conditions (i.e. pH = 7.4) both at 25 °C and 37 °C (4.4 % and 7.2 % after 7 h, respectively). The drug release was also low at pH = 5.5 and pH = 4.5 i.e., 4.6 % and 7.6 % at 25 °C, 8.2 % and 9.3 % at 37 °C after 7 h. However, at pH = 7.4 the drug nanocarriers show an increase of the released DOX around 24.0 %, and remarkable release of 45.0 % at pH ~ 5.5 and 4.5 at 48 °C after 7 h. A similar behavior is observed also if a longer

period is considered: a maximum of 15.0 % (at 25 ^{o}C), 19.5 % (at 37 ^{o}C), and 54.0 % (at 48 ^{o}C) of DOX was released under physiological conditions after 72 h, when only the temperature stimulus triggered the drug release. At pH ~ 5.5, after 72 h a maximum drug release of 16.0 % and 25.0 % were achieved for 25 ^{o}C and 37 ^{o}C respectively. However, this value sharply increases up to 72.0 % at 48 °C, when the pH and thermoresponsive polymer shrinks, squeezing drug out from the nanocomposite as exhibited in Figure 6.3. Finally, at pH = 4.5 an almost complete release of the encapsulated drug (98.8 %) is observed at 48 ^{o}C after 72 h, when the DOX-MNCs were exposed to both pH and temperature stimuli, which rupture the nanocomposite. It should also be noted that at acidic pH, the primary amine group of free DOX is protonated (pKa = 8.3), therefore, increasing its solubility in aqueous medium, facilitating its expulsion out of the polymer layer.

These data, thus, demonstrate that by combining both effect of the pH and the temperature, a controlled release of the DOX can be obtained. Other important reasons behind this promising pH/temperature-responsive drug release behavior of the Fe_3O_4-68@PVCL-*b*-PAA_2 material comes from the fact that the $\pi - \pi$ stacking interaction between the carbonyl groups of nanocomposite and the aromatic moieties of DOX molecules can be easily disrupted under a mild acidic environment [4].

.

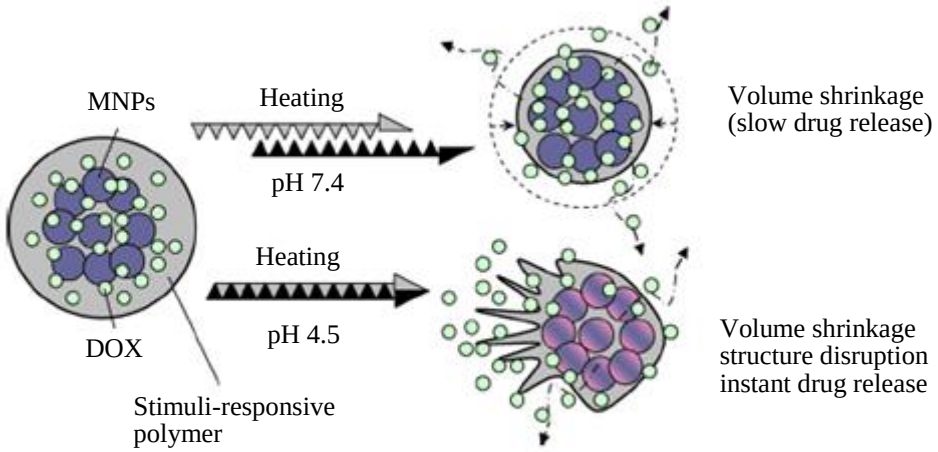

Figure 6.3 Scheme of the drug release mechanisms operating in our MNCs. Gentle release caused by shrinkage of temperature-responsive polymer under heating at neutral pH and intense release at pH 4.5-5.5 due to additional ruptures of the nanocomposite [5]

This pH-dependent controlled release phenomenon can be also ascribed to the increased protonation of the carboxylic acid unites of PVCL-*b*-PAA_2 nanocarrier surface as the pH of the aqueous solution decreases from 7.4 to 4.5 with the associated loss of negative surface

charge. This will lead to a reduction of the electrostatic attraction between PVCL-*b*-PAA_2 and DOX protonated molecules, increasing the progressive drug release.

Overall, the pH- and temperature-responsive drug release results obtained in this work, suggest the great ability of the designed PVCL-*b*-PAA-based magnetic nanocarriers to be applied as efficient drug encapsulation and delivery systems with an extremely good pH and temperature sensitivities for an intelligent and on-demand drug release on acidic tumour microenvironments with combination of hyperthermia performance.

6.3 Drug Release under the Application of an AMF

The observed pH- and temperature-dependence drug delivery profiles highlight the convenience of exploiting the magnetic properties of the magnetite cores to induce a temperature increase by external application of an AMF. Thus, in addition to an endogenous stimuli (pH) that boosts the localized drug release on the tumour site, we can externally enhance this effect by inducing a temperature increase through magnetic hyperthermia.

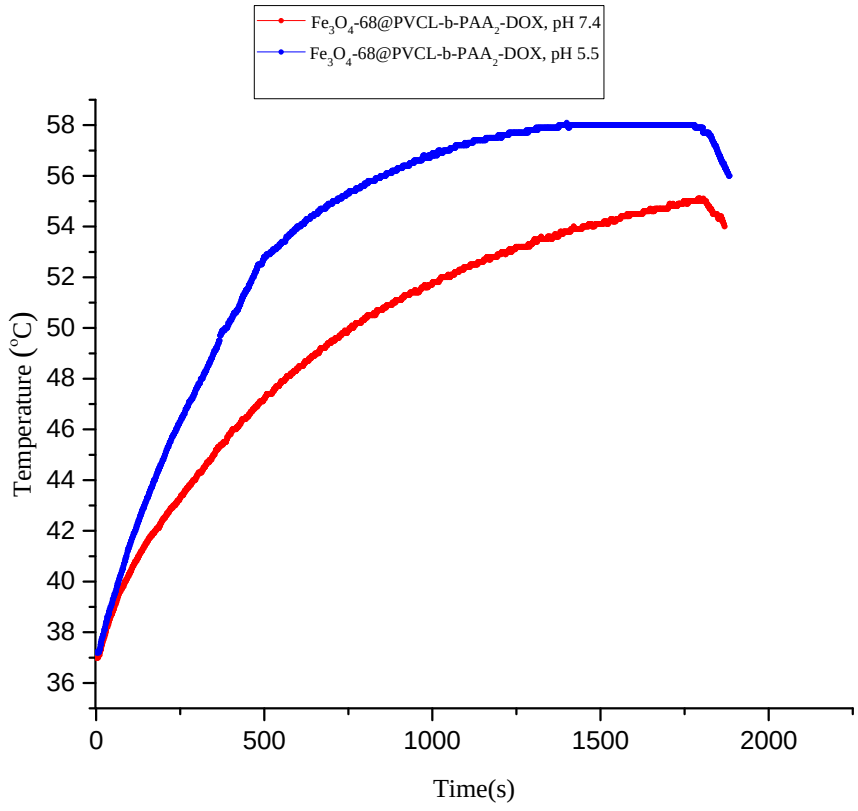

Figure 6.4 Magnetically induced thermal response curve of Fe_3O_4-68@PVCL-*b*-PAA_2-DOX (0.14 wt % of MNPs at pH ~ 7.4 (red plot) and pH ~ 5.5 (blue plot) for dual pH- and thermal-responsive drug delivery

For this purpose, 5 mL of samples $A_{7.4}$ (pH = 7.4 and LCST ~ 45 ^{o}C) or $A_{5.5}$ (pH = 5.5 and LCST ~ 40 ^{o}C), which contained 0.21 mg mL^{-1} and 0.1 mg mL^{-1} of loaded-DOX respectively, were exposed to the AMF (f = 183 kHz and H = 17 kA m^{-1}) at initial temperature (37 ^{o}C) similar to physiological temperature. As displayed in Figure 6.4, a suitable temperature for hyperthermia treatment (48 ^{o}C) was reached within 6' min for sample ($A_{7.4}$) and 11' min for sample ($A_{5.5}$), and SAR values of both samples ($A_{7.4}$ ~ 276.0 W g $_{(Fe)}^{-1}$ and $A_{5.5}$ ~ 427.0 W g $_{(Fe)}^{-1}$) were estimated based on the initial slope of the heating curve *vs* time.

Cumulative DOX release of samples ($A_{7.4}$, $A_{5.5}$) as a function of time was estimated at different time interval (30, 40, 50, and 60 min) under applying the AFM and results are plotted in Figure 6.5. In contrast, the drug release without application of AMF was also carried out on 5.0 mL of both samples ($A_{7.4}$, $A_{5.5}$) at 37 ^{o}C, and treated in the same way for comparison. Experimental details of drug release are completely given in Appendix A.13.

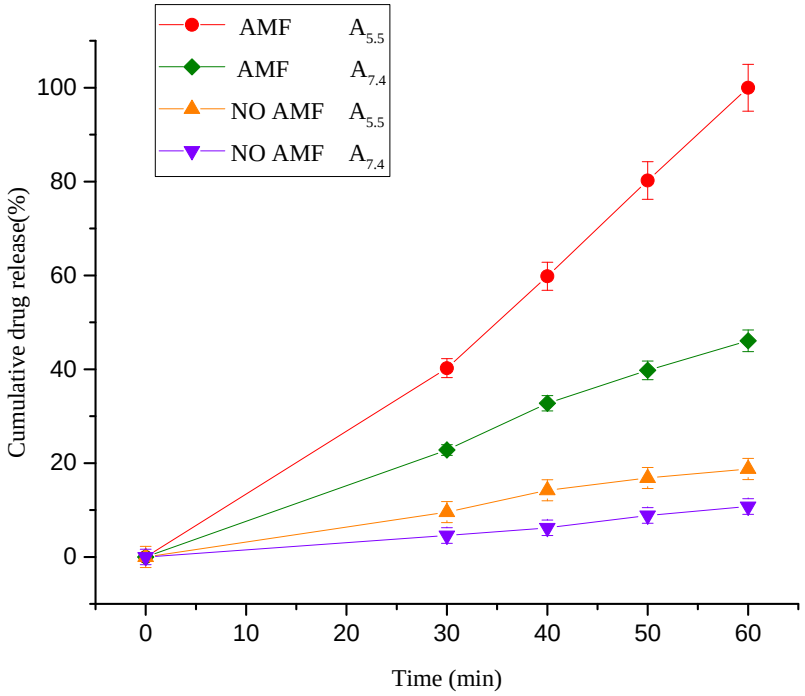

Figure 6.5 Cumulative DOX released from Fe_3O_4-68@PVCL-*b*-PAA_2-DOX NPs (0.14 wt % MNPs) for different exposure time to the AMF. Standard deviation of triplicate drug release tests (n=3)

After each drug release experiment with and without AMF, samples were centrifuged, and the supernatants analyzed by UV-Vis spectroscopy to determine the amount of DOX released. As revealed in Figure 6.5, for samples kept at 37 ^{o}C without application of the AMF, low drug release percentage was estimated after 60 min at both pH (~ 10.0 % at pH ~ 7.4 and 17.0 % at pH ~ 5.5). Conversely, significant drug release capability of the

nanosystem was observed at hyperthermia temperature for both samples ($A_{7.4}$, $A_{5.5}$) after 30 min under AMF. Indeed, 23 % of DOX at pH ~ 7.4 and 40.2 % at pH ~ 5.5 were released. After one hour, the maximal drug release percentage at pH = 7.4 was 47.0 %, while almost total percentage of DOX (~ 99.98 %) was noticeably released at pH ~ 5.5 after 60 min under applying AMF by enhancing temperature of samples up to 55 ^{o}C during heating cycle; consequently, these promising results confirm that in addition to an endogenous stimuli (pH) that could boost the localized drug release on the tumour site, this effect could be externally enhanced by inducing a temperature increase through localized magnetic hyperthermia by applying external magnetic field.

6.4 A Smart Hyperthermia with Switchable Drug Release

AMF-triggered drug release behaviors of the DOX-loaded nanocomposite particles were performed under continuous' application of the AMF. Comparison of the release patterns of DOX in Figure 6.5 and 6.2 shows that the drug release can be accelerated by application of an external magnetic field. It is speculated that the higher temperature (55 ^{o}C) obtained with the application of the AMF, is responsible for the enhancement in release rates due to increased drug diffusivity. To go one step further, we verified the possibility to have a controlled AMF-triggered drug release.

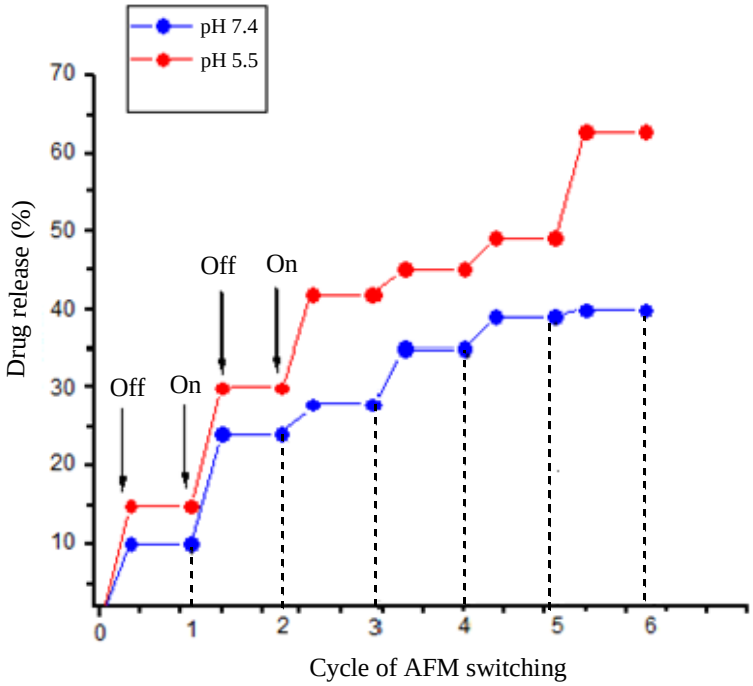

Figure 6.6 On-off switching cycle of AMF and DOX release profile corresponding to reversible swell-shrink property of Fe_3O_4-68@PVCL-*b*-PAA_2-DOX nanocomposite in response to field application

To this aim, AMF was introduced under ‘‘intermittent’’ condition (10’ steps) for overall time of 60 min, and results were compared with the ones obtained by applying the field continuously for the same amount of time. Hyperthermia switchable drug release was performed on 5.0 mL of samples $B_{7.4}$ (MNPs 0.4 wt %, LCST ~ 45 ^{o}C, SAR ~ 453.0 W $g_{(Fe)}^{-1}$) and $B_{5.5}$ (MNPs 0.4 wt %, LCST ~ 40 ^{o}C, SAR~ 427.0 W $g_{(Fe)}^{-1}$), containing 0.21 mg mL^{-1} and 0.12 mg mL^{-1} DOX, respectively. Drug release process is explained in Appendix A.14 with more details.

The field was first applied for 10 min, a time long enough for both samples $B_{7.4}$ and $B_{5.5,}$ to reach 50 ^{o}C. The AMF was then turned ‘off’ for 10 min, allowing cooling them down to 25 ^{o}C. This process was repeated 6 times. After each cycle samples were centrifuged, and supernatant was analyzed by UV-Vis spectroscopy to evaluate amount of drug release, and results are reported in Figure 6.6.

According to Figure 6.6, from first to sixth cycles of AMF application DOX is released up to ca. 40.0 % at pH = 7.4 and 63.0 % at pH = 5.5, and no release occurs when the AMF is switched off. In other words, almost more than half amount of DOX was released after 6 cycles in acidic pH, whereas less than 50.0 % of DOX was released at physiological pH during the heating ‘on’ process. The result at pH 7.4 is in good agreement with that obtained by continuous AMF application, while at pH = 5.5 the drug release is ca. 33.0 % less than one measured under continuous AMF application.

Thus, at ‘on’ state and pH = 7.4, the MNCs deformed only under influence of temperature changes, triggering the release of the drug molecules. However, in acidic pH the additional pH stimulus boosts drug release, and magnetic hyperthermia can extremely enhance the effect. On the other hand, when the magnetic field is off, the DOX release does not change at each cycle. In fact, the polymer absorbs water and re-swells, thus, strongly slowing down the drug release. We, therefore, can conclude that this composite nanoparticles are also feasible for application in ‘‘on/off’’ drug delivery systems for *in vivo* application by exploiting the triggering induced by application of the AMF.

6.5 Cytotoxicity Study

Nanoparticles used as a therapeutic agent in drug delivery system must be preferably nontoxic. Hence, the cell biocompatibility of Fe_3O_4-68@PVCL-*b*-PAA_2 MNCs were investigated by WST-1 assay in triplet at different MNPs concentrations before DOX conjugation during 24 hours of incubation on A375 human melanoma cells, and results are

demonstrated in Figure 6.7 (conducting cell viability studies with more details are described in Appendix A.15). Moreover, cytotoxicological effect of Fe_3O_4-68@PVCL-*b*-PAA_2-DOX containing 14.0 µg mL^{-1} DOX with different concentrations of MNPs was assessed by WST-1 assay with the same incubation time according to the same procedure explained in Appendix A.15, and results are reported in Figure 6.8.

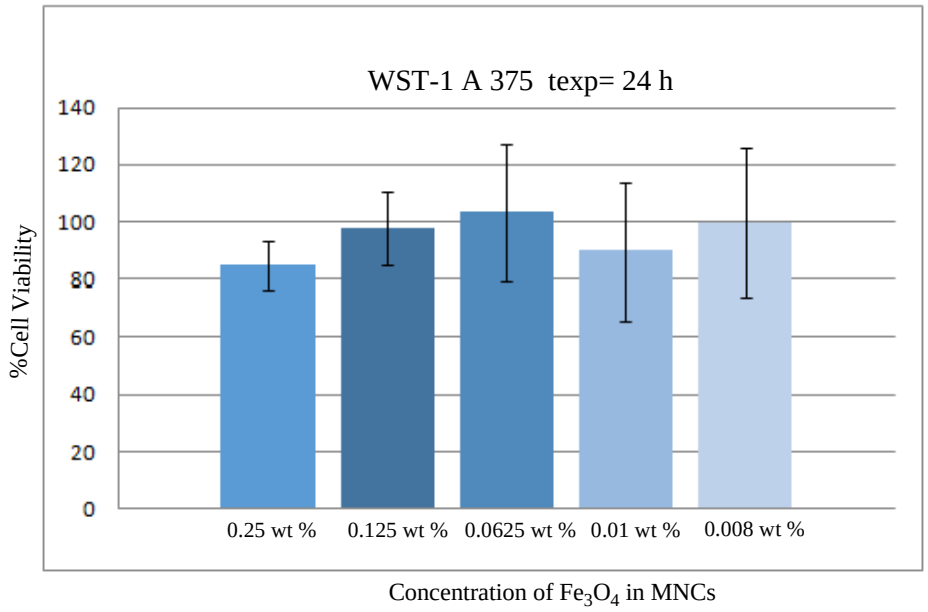

Figure 6.7 Cell viability (%) assessed by WST-1 assay after 24 h of incubation with Fe_3O_4-68@PVCL-*b*-PAA_2 before DOX loading with respect to a cell control sample

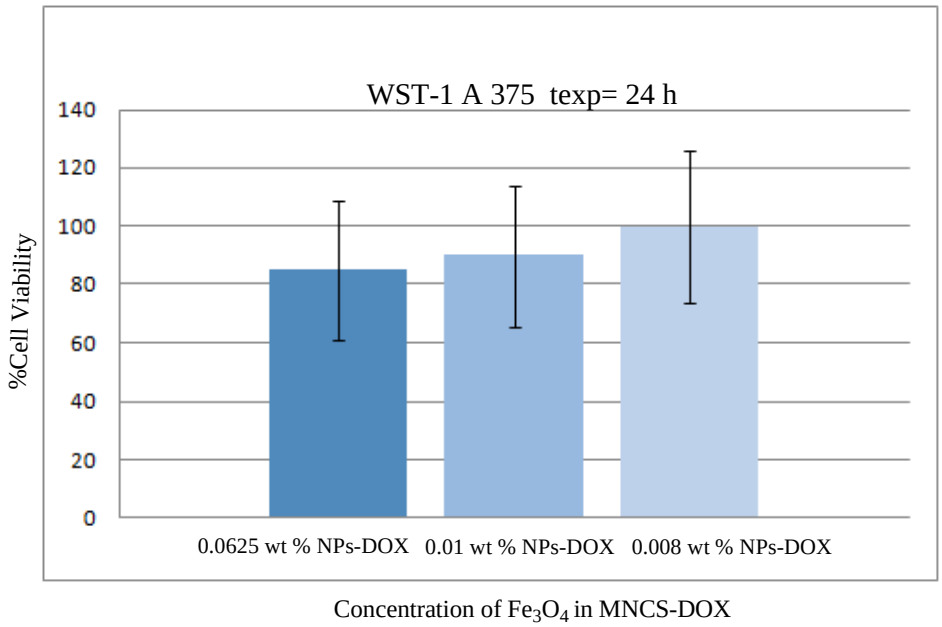

Figure 6.8 Cell viability (%) assessed by WST-1 assay after 24 h of incubation with Fe_3O_4-68@PVCL-*b*-PAA_2-DOX containing 14.0 µg mL^{-1} DOX with respect to a cell control sample

Cell viability studies revealed that there is no difference in viability percentage of A375 human melanoma cells incubated for 24 h with polymer coated nanoparticles and control for all samples considered, even after DOX conjugation. These data indicate that the MNCs are not cytotoxic, and the amount of drug released at physiological pH and body temperature is so low to have any effect on cell viability of A375 human melanoma cells, so these results verify the possibility of using these nanosystems as efficient cargo carrier for controlled drug delivery.

To conclude, in this study, MNPs grafted with copolymer PVCL-*b*-PAA, were successfully developed as multifunctional nanocarriers for therapeutic applications. This hybrid nanomaterial was found to be an efficient nanoheater at relatively low concentrations, with exceptional drug loading capacity and controlled drug release, triggered by the acidic tumour microenvironment in combination with hyperthermia performance. Significantly, the external application of an AMF (magnetic hyperthermia) was observed to further induce the drug release. The dual pH- and temperature-responsive drug delivery behavior observed in these nanosystems showed a burst release of the drug at mimicked acidic tumour environment, whereas at physiological pH and temperature, negligible amount of drug was released, confirming that the drug was efficiently retained in the nanocarrier.

Chapter 6

References

1. M. Gisbert-Garzarán.; M. Manzano.; M. Vallet-Regí. *Bioeng*. **2017**, *4*, 1.
2. M. Creixell.; A. C. Bohorquez.; M. Torres-Lugo.; C. Rinaldi. *ACS Nano*. **2011**, *5*, 7124.
3. B. Kozissnik.; A. C. Bohorquez.; J. Dobson.; C. Rinaldi. *Int. J. Hyperth*. **2013**, *29*, 706.
4. X. Yu.; Y. Zhu. *Sc. Tech. Adv. Mater*. **2016**, *17*, 229.
5. T. Y. Liu.; S. H. Hu.; D. M. Liu.; I. W. Chen. *Nano Today*. **2009**, *4*, 52.

Chapter 7

Conclusions and Perspectives

The experimental work, presented here was focused on the design of a novel smart magnetic nanocomposite, composed of iron oxide magnetic nanoparticles enclosed in a dual pH and temperature responsive poly (N-vinylcaprolactam-*b*-acrylic acid) polymer for controlled drug delivery in combination with hyperthermia performance for therapeutic application. To realize this goal, magnetic nanoparticles with suitable magnetic characteristics for efficient conversion of magnetic energy into heat were prepared, and embedded in a multi stimuli responsive polymer, optimized for drug encapsulation and controlled release under the application of an external alternating field with frequency and amplitude suitable for application in human being.

Although thermal decomposition and co-precipitation approaches are the most commonly synthetic methods, employed for MNPs preparation, here we focused on the polyol synthetic procedure since MNPs synthesized by this approach exhibit excellent heating performance for hyperthermia due to their specific morphology. By this technique flower-like shaped, monodisperse, spinel ferrite Fe_3O_4 nanoparticles in the form of stable dispersion in diethylen glycol, were prepared. X-ray diffraction and TEM analyses confirmed MNPs have a good crystallinity, with crystallite size of 14 nm and average particle diameter of 18.0 nm. Due to the optimal particle size and specific morphology, nanoparticles exhibited superparamagnetic behavior with high magnetization saturation (Ms ~ 76 emu g^{-1}), high capability of heat generation potential, and huge specific absorption rate value (SAR ~ 357.0 W $g^{-1}_{(Fe)}$) under application of an AC magnetic field with f = 183 kHz and H = 17 kA m^{-1} even at relatively low concentration of ~ 1.0 mg mL^{-1}. These properties are extremely promising in view of the clinical application of this nanomaterial as heat mediator for magnetic fluid hyperthermia.

Second, pH and temperature responsive poly (N-vinylcaprolactam-*b*-acrylic acid) (PVCL-*b*-PAA) was prepared by free-radical polymerization approach. PVCL-based copolymer was selected as a smart polymer owing to the high biocompatibility, lower toxicity, and proper thermal sensitivity that PVCL shows with respect to PNIPAM, which is widely used polymer for temperature-triggered drug release. Moreover, thanks to the

presence of PAA blocks in polymer backbone, the copolymer is sensitive to pH as well. PVCL-*b*-PAA was synthesized successfully, and buffer solution of this copolymer (0.1 wt %) at different pH (5.5 to 8.5) revealed reversible phase transition behavior at temperature between 40 ^{o}C-50 ^{o}C, above physiological temperature (~ 37 ^{o}C) and close to that which can be easily achieved by hyperthermia treatment, depending on pH of the media and concentration of polymer solution.

As a third step, surface modification of superparamagnetic iron oxide nanoparticles by stimuli responsive PVCL-*b*-PAA was performed for the first time using a ''grafting to'' approach, exploiting the PAA units in the structure of copolymer, which act as proper anchor for surface functionalization of MNPs. The final suspension was highly stable and monodispersed with negative surface charge, as indicated by zeta potential measurement, confirming strong adherence of polymer on the surface of MNPs. Then, Doxorubicin, a positive-charge anticancer drug, widely used as chemotherapeutic drug, was loaded on the magnetic nanocomposites. Thanks to the strong electrostatic interaction with the negative surface charge arising from the presence of carboxylate in the polymer, very high encapsulation efficiency (> 92.0 %) at neutral pH was obtained.

The dual pH- and temperature-responsive nature of the nanocarrier allowed for a burst release of the drug at mimicked acidic tumour environment upon application of an external alternating magnetic field, whereas at physiological pH and body temperature negligible amount of drug was released, confirming that the drug was efficiently retained in the nanocarrier. Smart nanocomposite, besides, demonstrated reversibly switchable behavior in response to self-generated heat from the incorporated MNPs upon the magnetic field application; consequently, Fe_3O_4@PVCL-*b*-PAA_2 exhibited the dynamically and reversibly tunable structures of smart nanohybrids, that have the potential to be utilized as a device for hyperthermia treatment of tumour as well as a switchable drug release platform by simple switching an AMF 'on' and 'off'. Furthermore, the developed nanocarriers showed low cytotoxicity during 24 h incubation on A375 human melanoma cells. Therefore, the presented strategy and findings can represent a new way to design and synthesize stable smart magnetic nanocomposite materials with novel structures for targeted combinatorial thermo-chemotherapy triggered by abnormal acidic cell microenvironments on tumour site, with the subsequent minimization of side effects on the healthy cells.

Appendix A

Materials and Methods

A.1 Starting Materials

All chemicals of analytical quality were purchased from Sigma-Aldrich Co. with the exception of O-ethyl xanthic acid potassium salt, purchased from Alfa Aesar Co. Water was deionized and filtered with a Milli-Q System (Merck Millipore Co., Germany). 2,2´-Azobis (2-methylpropionitrile) (AIBN) was recrystallized from methanol before use. N-vinylcaprolactam, N-vinylpyrrolidone, and acrylic acid were distilled under low pressure before copolymerization. 1,4-Dioxane was dried by sodium before use. All the other reactants and solvents were used with no further purification. Dialysis bag with molecular weight cut-off (MWCO) of 14 kDa, dialysis kit with MWCO of 1 KDa, Dulbecco's Modified Eagle Medium (DMEM), a culture medium used for A375 cells, Fetal Bovine Serum (FBS), and A375 human melanoma cell line were purchased from Sigma Aldrich Co.

A.2 Synthesis of Iron Oxide Superparamagnetic Nanoparticles (Fe_3O_4-68)

Fe_3O_4-68 NPs were prepared by polyol method. First, iron (III) acetate was prepared by mixing Fe^0 (10.024 g, 0.179 mol) and 100.0 g of CH_3COOH (1.67 mol) in the presence of H_2O_2 (11.73 mL, 0.5 mol) in 400.0 mL of DEG. Then, Fe $(CH_3COO)_3$ (46.6 g, 0.2 mol) was added to a solution of $FeCl_2$ (12.675 g, 0.1 mol) in 130.0 mL of DEG under N_2 flow. Afterward, precursors were mixed together under mechanical stirring for 10 minutes, and temperature was increased with a heating rate of 2 °C/min up to 150 °C for one hour, and then kept under refluxing at 170 °C for 19 h. At about 170 °C formation of magnetic nanoparticles started. Subsequently the dark brown dispersion was air cooled to room temperature, and stored under N_2 atmosphere to prevent any oxidation to maghemite, γ- Fe_2O_3. The dark brown dispersion contains about 1.33 wt % of Fe_3O_4 according to ICP measurement. In order to increase the particle size of Fe_3O_4-68 to provide flower-like nanoparticles, the half quantity of prepared magnetic nanoparticles in DEG, containing 1.33 wt % MNPs, was used as seeds and reaction was similarly repeated with half amount of precursors during 5 h at 170 ^oC.

A.3 Synthesis of Methyl 2-[(Ethoxycarbonothioyl) Sulfanyl] Propanoate

The RAFT CTA (Methyl 2-[(ethoxycarbonothioyl)sulfanyl]propanoate) was prepared according to the procedure as shown in Scheme A.1. First, methyl-2-bromopropionate (5.0 g, 30 mmol) was dissolved in 50.0 mL of methanol in a flask on ice bath, and then O-ethyl xanthic acid potassium salt (5.3 g, 33.0 mmol) was added to the solution and reacted for a day. Afterward, ethyl ether and hexane mixture (200.0 mL, ether/hexane 50/50) was used to extract the product from the solution. The extraction solution was washed with deionized water several times and dried with 26.0 wt % NaCl aqueous solution. After solvent evaporation, 3.0 g of CTA was obtained, and molecular structure of product was determined by ^{1}HNMR assignment. ^{1}HNMR (400 MHz, $CDCl_3$): δ= 1.41 (t, 3H), 1.57 (d, 3H), 3.75 (s, 3H), 4.40 (q, 1H), 4.61 (q, 2H).

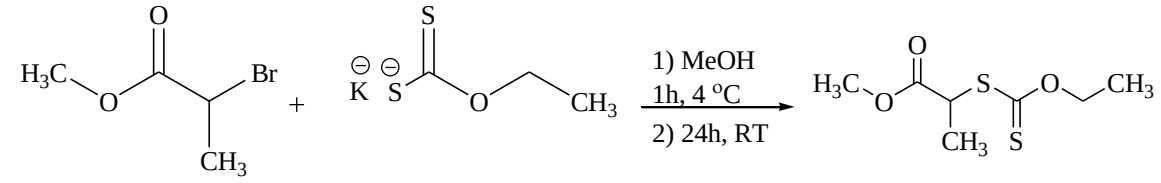

Methyl-2-Bromopropionate | Potassium Ethyl Xanthogenate | Chain Transfer Agent (CTA)

Scheme A.1 Synthesis of Chain Transfer Agent

A.4 RAFT Synthesis of PVCL

Scheme A.2 displays synthesis process of PVCL by RFT polymerization. Firstly, a Schlenk tube containing N-vinylcaprolactam (NVCL) (5.0 g, 35.92 mmol), CTA (34.4 mg, 0.1 mmol), AIBN (13.5 mg, 0.05 mmol), and dioxane (16.0 mL) was degassed by four freeze–pump–thaw cycles, kept under nitrogen flow, and heated at 60 °C under stirring for 20 h in an oil bath. The reaction mixture was then cooled down with liquid nitrogen to stop the polymerization. Finally, a sample was withdrawn and analyzed by ^{1}HNMR and FTIR to access the molecular structure of PVCL as shown in Figure A.1 and Figure A.2 respectively, while the remaining solution was precipitated in hexane. The precipitated polymer was filtered off, dried under vacuum, and purified by dialysis bag with MWCO of 1 kDa against distilled water for three days. After lyophilization, polymer was obtained as powder and kept at 4 ^{o}C.

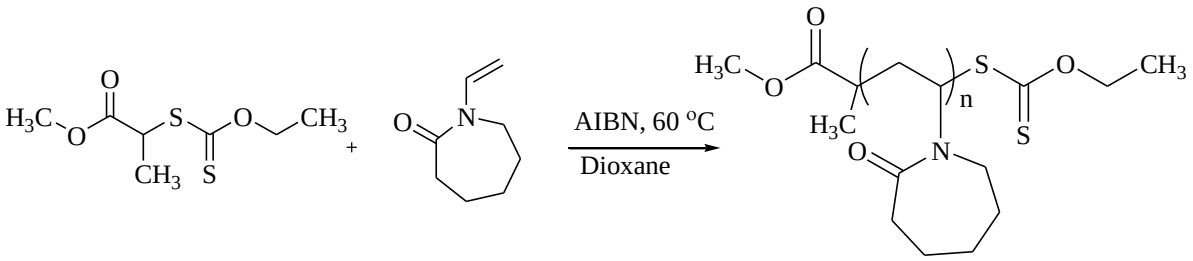

Scheme A.2 Synthesis of PVCL by RAFT polymerization

^{1}HNMR (400 MHz, $CDCl_3$): δ= 4.39 ppm (H_a,−NCH−of the *α* position), 3.18 ppm (OCH_3 –O=$COCH_3$−of CTA), 3.1 ppm (H_b,−NCH_2−), 2.4 ppm (H_c, −$COCH_2$−) and 1.76 ppm (H_e, −CH_2− of the caprolactam ring, and H_d, −CH_2− of the backbone).

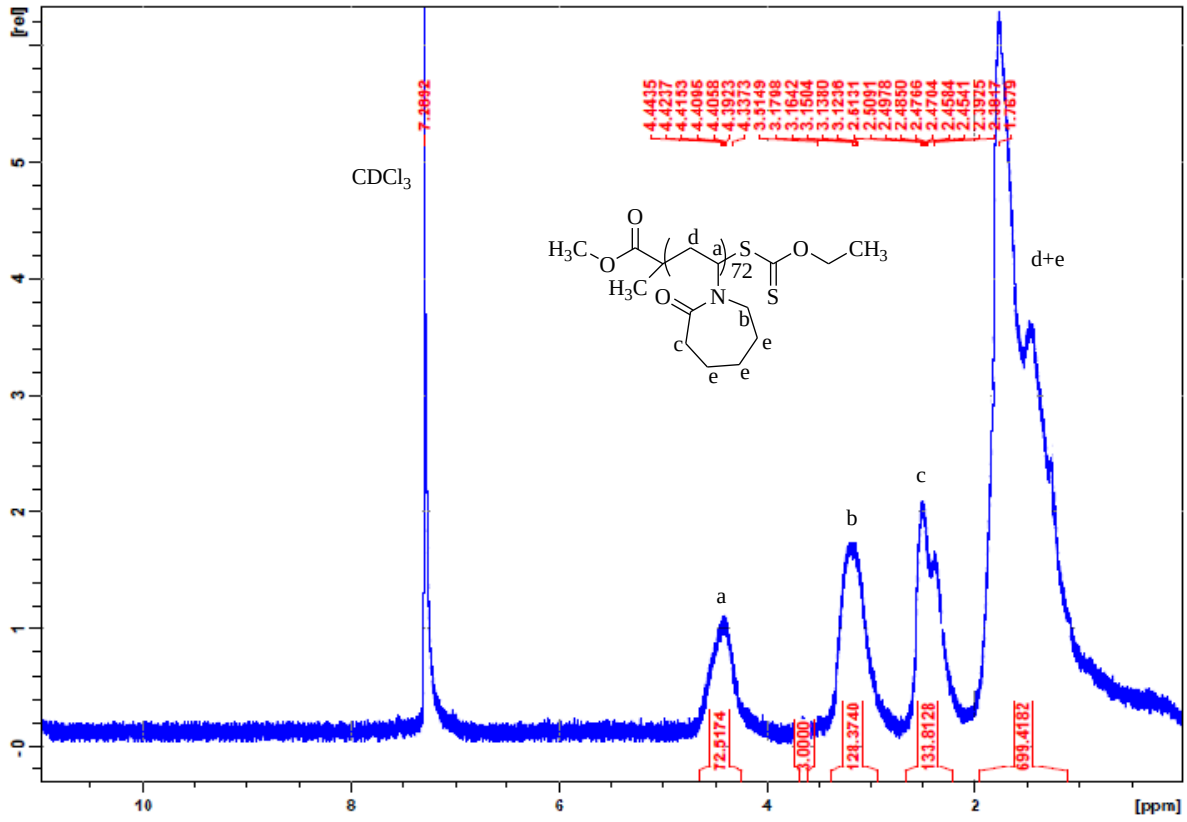

Figure A.1 ^{1}HNMR of PVCL

The IR spectrum of PVCL is depicted in Figure A.2. As it is seen from the spectrum, the polymer reveals a broad absorption in the 3507 cm^{-1} region due to O-H stretching from absorbed water molecules since PVCL absorbs moisture from the air easily. Furthermore, two stretching peaks at 2932 cm^{-1} and 2853 cm^{-1} can be representative for absorption of aliphatic C-H groups in polymer structure. Moreover, IR spectrum of copolymer shows an absorbent

peak of amide carbonyl groups (NH-C=O) in PVCL domain at 1623 cm^{-1}, while the peaks at 1479 cm^{-1} and 1200 cm^{-1} are assigned to the characteristic absorptions of its C-N and C-O groups respectively. The more characteristic bands in the spectrum of the PVCL correspond to the moiety C=S at 1081 cm^{-1} and to the stretching of C-S at 668 cm^{-1}, confirming the presence of chain transfer agent in polymeric backbone.

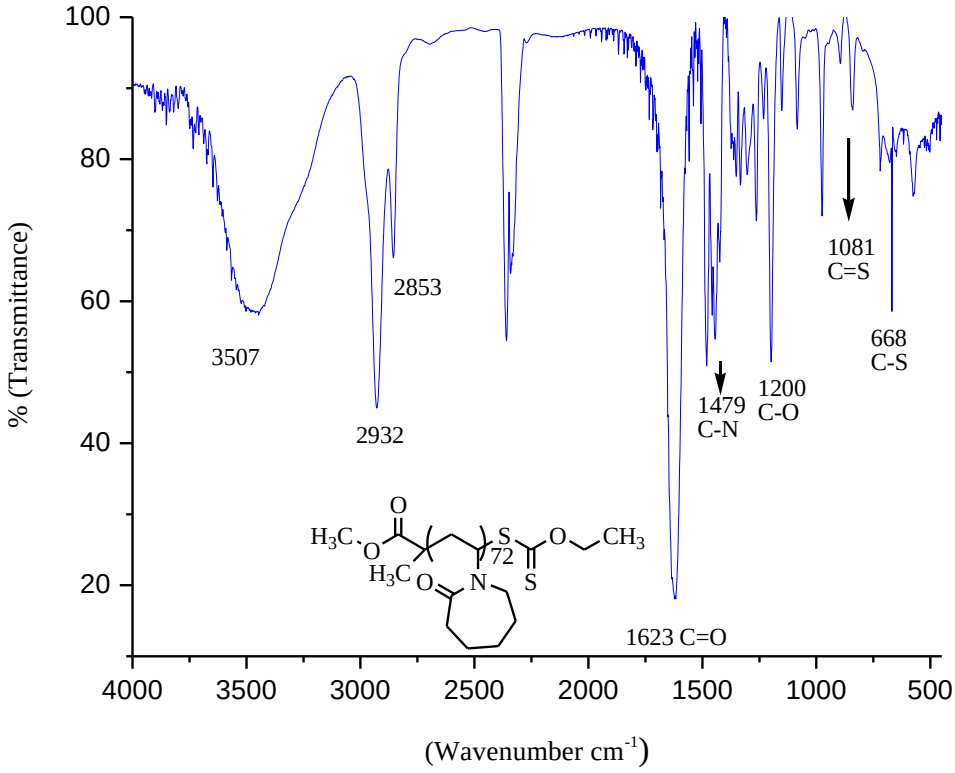

Figure A.2 FTIR spectrum of PVCL

A.5 RAFT Synthesis of PVCL-b-PVPON

As displayed in Scheme A.3, RAFT polymerization of PVCL-*b*-PVPON was performed following the same procedure used for PVCL, reported in section A.4, and started from a mixture of NVCL (8.7 g, 62.0 mmol), N-vinylpyrrolidone (NVPON) (1.3 g, 11.69 mmol), CTA (0.092 g, 0.44 mmol), AIBN (0.036 g, 0.22 mmol), and dioxane (15.0 mL). Purification of copolymer was performed by dialysis bag with MWCO ~ 1 KDa

against distilled water for three days. ^{1}HNMR and FTIR characterization were performed to evaluate the molecular formula of PVCL-*b*-PVPON as shown in Figure A.3 and A.4.

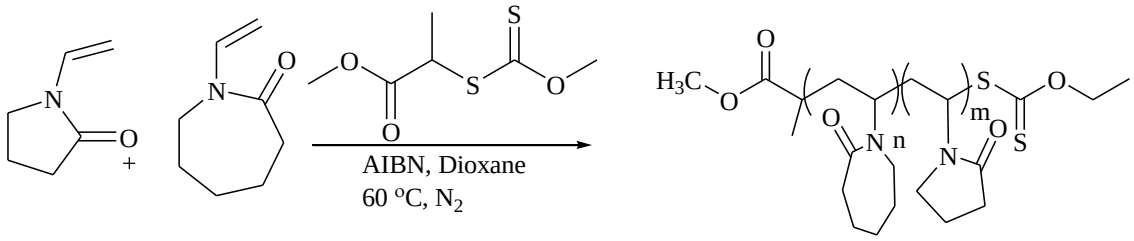

Scheme A.3 Synthesis of PVCL-*b*-PVPON by RAFT polymerization

^{1}HNMR (400 MHz, $CDCl_3$): δ= 4.38 ppm (H_a,–NCH–of the *α* position), 3.69 ppm ($1H_a'$,–NCH–of the the *α* position), 3.21 ppm ($2H_b$, –NCH_2– of the caprolactam ring and $2H_{b,}'$-$COCH_2$– of the pyrrolidone ring$_{),}$ 2.5-2.4 ppm ($2H_c$, –$COCH_2$– of the caprolactam ring and $2H_c'$, –NCH_2– of the pyrrolidone ring), 2.0 ppm ($2H_d'$, –CH_2–of the backbone), and 1.68-1.48 ppm ($2H_d$, –CH_2–of the backbone, $6H_e$,–CH_2– of the caprolactam ring, $2H_e'$,–CH_2– of the pyrrolidone ring)

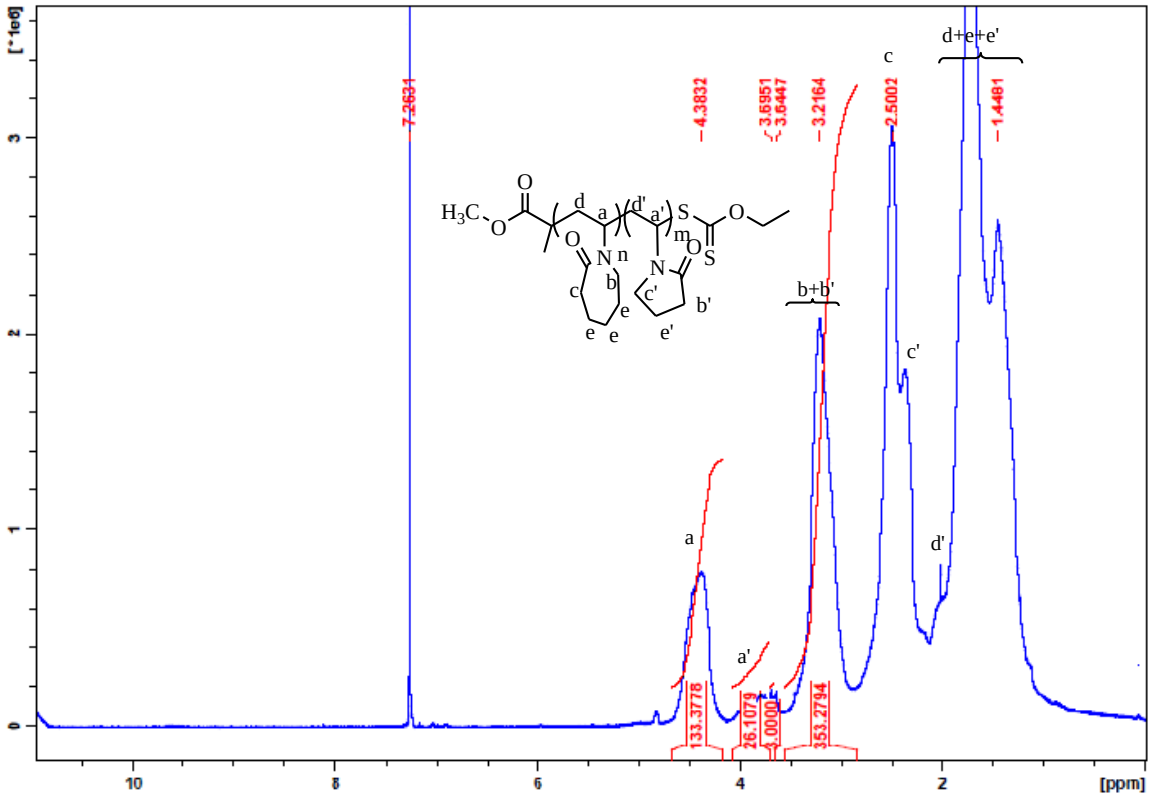

Figure A.3 ^{1}HNMR of PVCL-*b*-PVPON

Figure A.4 exhibits broad peak in the IR spectrum of the copolymer at 3500 cm^{-1}, corresponding to the O-H stretching absorption peak of water. As demonstrated in

Figure A.2, the PVCL homopolymer has a single absorption band at 1623 cm^{-1} associated with the stretching vibration of the carbonyl group in the caprolactam ring; however, the additional absorption band at 1661 cm^{-1} appears when the PVPON segment is grown in the structure of copolymer as shown in Figure A.4. According to the IR spectrum of PVCL-*b*-PVPON, the aliphatic C-H stretching peaks are assigned at 2928 cm^{-1} and 2858 cm^{-1}, and the -CH_2- peaks appear at 1436 cm^{-1}. Moreover, two peaks at 1460 cm^{-1} and 1290 cm^{-1} are attributed to the C-N and C-O groups in the structure of copolymer. In addition, two characteristic peaks corresponding to C=S and C-S of CTA are observed in 1085 cm^{-1} and 668 cm^{-1} respectively.

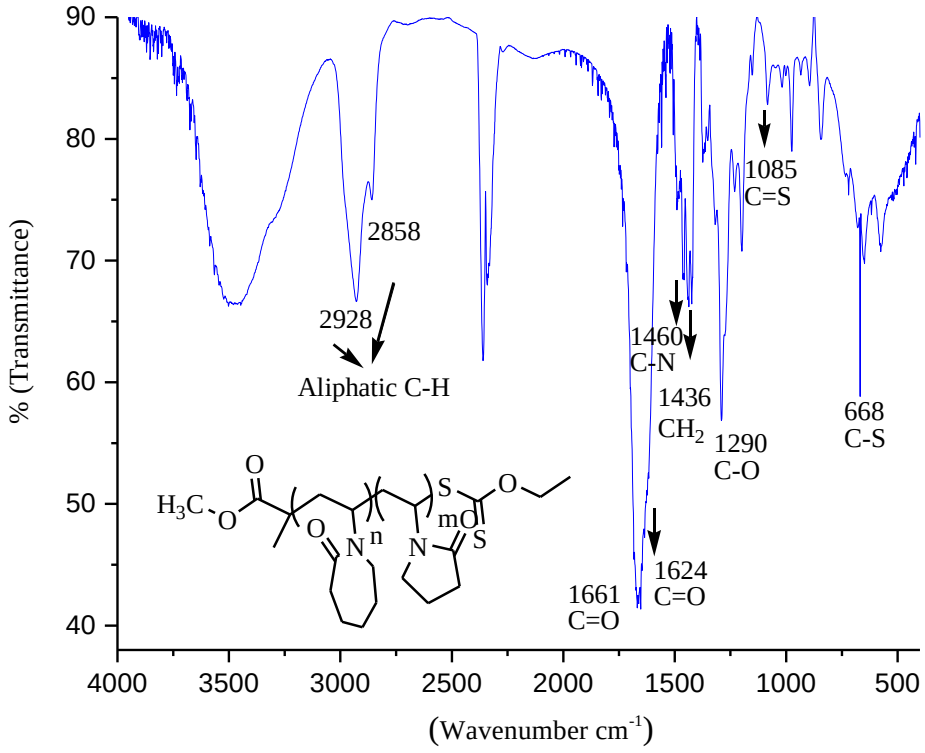

Figure A.4 FTIR spectrum of PVCL-*b*-PVPON

A.6 Synthesis of PVCL-b-PAA by Free Radical Polymerization

The PVCL-*b*-PAA copolymer was prepared by free radical copolymerization of NVCL with acrylic acid (AA) in the presence of AIBN as initiator as displayed in Scheme A.4. The procedure used 1.0 g (80.0 mol %) of NVCL, 0.123 mL (20.0 mol %) of AA, and 2.0 mol % of AIBN dissolved in 12.0 mL of solvent (DMF, polymer AA_1, dioxane, polymer

AA_2, and isopropanol, polymer AA_3). The mixture was purged with nitrogen for 30 min and let to react in an oil bath at 70 ^oC for 24 h under nitrogen flow. Afterward, the solution was cooled to room temperature, and the copolymer was precipitated in diethyl ether at low temperature. The precipitation was carried out three times to remove unreacted materials, and the product dried in vacuum at room temperature for 48 h. Further purification was performed by dialysis technique using dialysis bag with MWCO of 14 kDa against distilled water for 24 h, and then after lyophilization, polymer was stored at 4 ^oC. Formation of three copolymers was confirmed by ^{1}HNMR and FTIR characterization as revealed in Figures A.5 and A.6 respectively, and results were similar for all three samples.

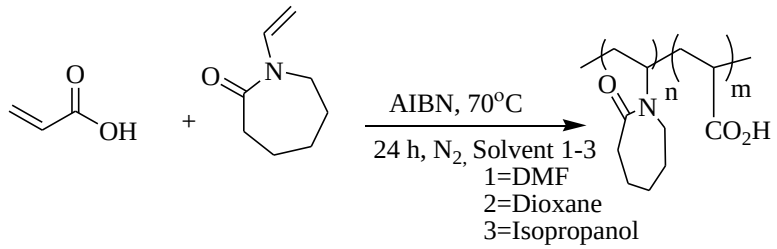

Scheme A.4 Free radical polymerization of PVCL-*b*-PAA

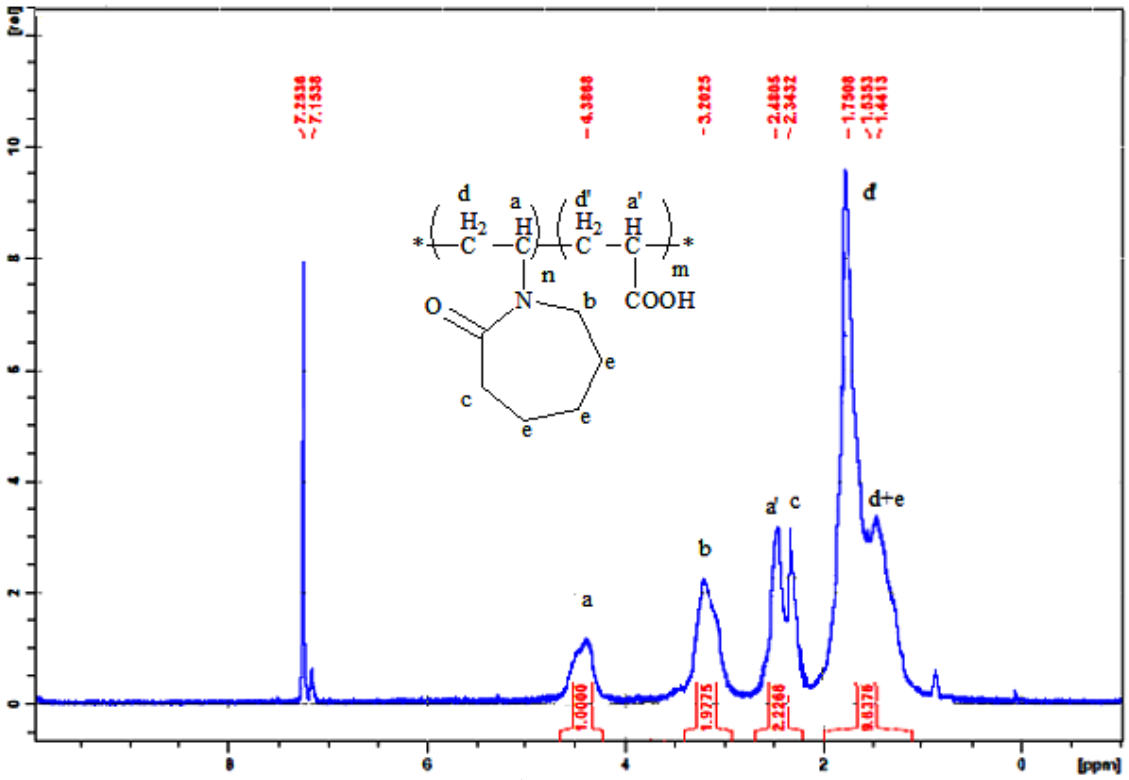

Figure A.5 ^{1}HNMR of copolymer

^{1}HNMR spectroscopy was performed using a NMR spectrometer (400 MHz) with $CDCl_3$ as the solvent. The ^{1}HNMR spectra of copolymers AA_1, AA_2, and AA_3 exhibited peaks at 4.38 ppm ($1H_a$, –NCH–of the α position), 3.20 ppm ($2H_b$,–NCH_2–), 2.48 ppm ($1H_{a'}$, –HCO_2CH– of the α position), 2.34 ppm ($2H_c$, –$COCH_2$– of the caprolactam ring), 1.78 ppm ($2H_{d'}$, –CH_2– of the backbone), 1.53 ppm ($2H_d$, -CH_2-of the backbone), 1.44 ppm ($6H_e$, –CH_2–of the caprolactam ring).

Corresponding to Figure A.6, IR spectrum of copolymer shows an absorption typical peak of amide carbonyl group (-CON-) in PVCL domain at 1637 cm^{-1}. The IR also reveals a peak at 1724 cm^{-1} caused by the stretching vibration of -COOH (carboxylic) groups in AA domain, while the peak at 1260 cm^{-1} can be assigned to the characteristic absorptions of its C-O groups. Moreover, a wide peak at 3538 cm^{-1} is attributed to the absorptions of OH groups of absorbed water from the air. The peaks at 2856 cm^{-1} and 2928 cm^{-1} reveal the presence of aliphatic C-H groups in the structure of polymers. A specific peak at 2510 cm^{-1}, besides, is assigned to the internal hydrogen bond formation between carboxylic acid groups in polymeric chain.

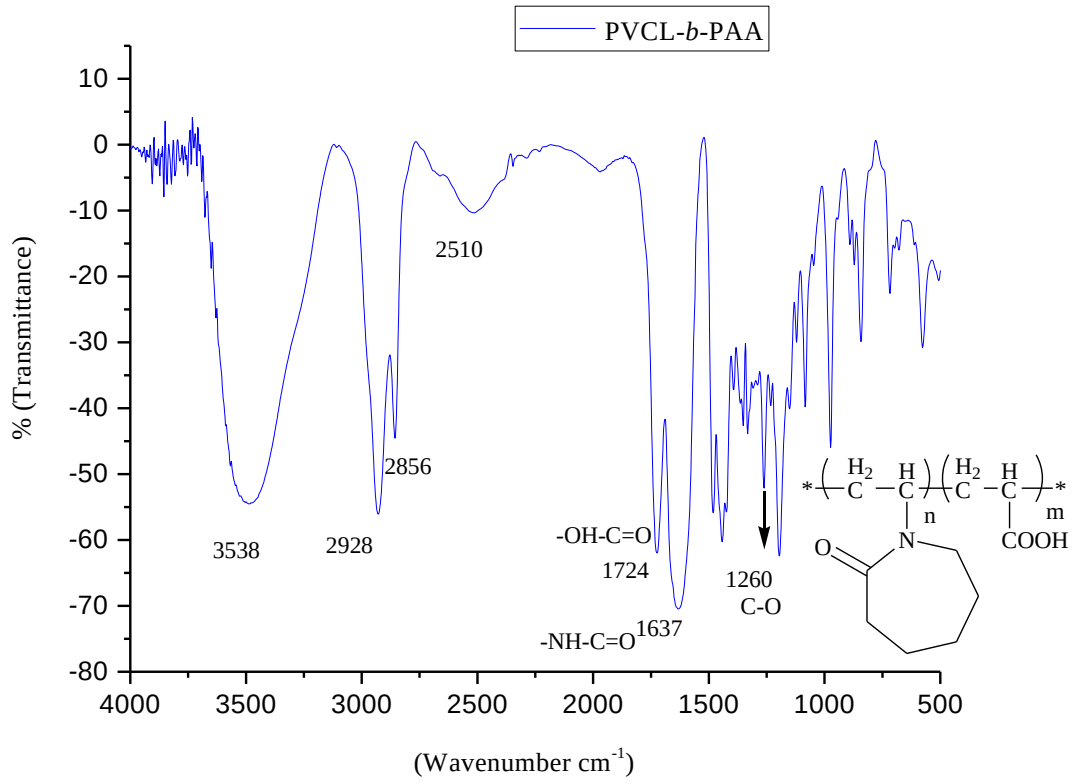

Figure A.6 FTIR spectrum of PVCL-*b*-PAA

A.7 Encapsulation of Magnetic Nanoparticles by PVCL Corresponding to Post Modification Method

DEG-stabilized nanoparticles (Fe_3O_4-68) (13.5 mg, 0.0581 mmol) were added to 4.0 mL DEG containing PVCL (10.0 mg, 0.92 µmol, M_n ~ 10857 g mol^{-1}). Once the mixture was complete, the resulting suspension was sonicated for an hour at 0 ^oC and stirred for two hours at room temperature. The obtained nanocomposite was precipitated by addition of acetone and recovered by magnet decantation. The resulting nanoparticles were washed thoroughly with ethanol/acetone three times to remove excess of polymer. Final nanocomposite was dispersed into 20.0 mL phosphate buffer (10 mM, pH = 7.4), and ICP-AES analysis indicated a mean concentration of magnetic nanocomposite dispersed in solution of 0.11 wt %.

A.8 Encapsulation of Magnetic Nanoparticles by PVCL-b-PVPON by Post Modification Method

DEG-stabilized magnetic nanoparticles (13.5 mg, 0.0581 mmol) was added to 4.0 mL DEG containing PVCL-*b*-PVPON (10.0 mg, 0.5 µmol, M_n ~ 20857 g mol^{-1}) under sonication for an hour at 0 ^oC and stirred for two hours at room temperature. Acetone was added to the suspension to precipitate the nanocomposite, which was subsequently recovered by magnet decantation. The resulting NPs were washed thoroughly with ethanol/acetone three times to remove excess of polymer and redispersed in buffer phosphate (10 mM, pH = 7.4). Concentration of magnetic nanocomposite suspended in solution was 0.1066 wt % as obtained by ICP analysis.

A.9 Coating of MNPs by Capping Ligands

A.9.1 Functionalization of MNPs by PAA

100.0 mL of acetone was added to 5.0 mL of Fe_3O_4-68 suspended in DEG (66.5 mg, 0.286 mmol Fe_3O_4). The precipitate was washed 3 times with ethanol/acetone to remove DEG completely. Afterward, 15.0 mL aqueous solution containing PAA (1.0 mg mL^{-1}) was mixed with Fe_3O_4-68 NPs and sonicated for one hour. Then, the resulting nanoparticles suspension was stirred vigorously at 25 ^oC for 2 h. Finally, MNPs were separated *via* magnetic decantation, washed with ethanol three times and redispersed in 15.0 mL distilled water.

A.9.2 Functionalization of MNPs by 6-AHPA

Surface functionalization of Fe_3O_4-68 with 6-aminohexylphosphonic acid (6-AHPA) was performed using 6-aminohexylphosphonic acid (6-AHPA) ligand that permits both a strong covalent bond between the MNPs and itself to give a free amino group on the surface of MNPs for the further functionalization. Typically, 5.0 mL of MNPs suspended in DEG (66.5 mg, 0.286 mmol) was precipitated by addition of 100.0 mL acetone before surface modification. Precipitate washed three times with ethanol/acetone to remove DEG completely. Afterward, 15.0 mL ethanol contained 6-AHPA (1.0 mg mL^{-1}) was mixed with MNPs precipitate and sonicated for one hour. Then, the resulting nanoparticles suspension was stirred vigorously at 25 ^{o}C for 2 h. Finally, MNPs were washed with ethanol three times *via* magnetic decantation and redispersed in 10.0 mL distilled water.

A.10 Encapsulation of Fe_3O_4-68 by PVCL-b-PAA_2

Firstly, 1.5 mL of Fe_3O_4-68 suspended in DEG (19.95 mg, 0.086 mmol Fe_3O_4) was precipitated by addition of 50.0 mL acetone and then nanoparticles were washed 3 times with ethanol/acetone to completely remove DEG. Secondly, PVCL-*b*-PAA_2 (0.1178 g, 0.43 µmol, M_n ~ 271890 g mol^{-1}) was dissolved in 20.0 mL Milli-Q water by addition of 15.0 µL NaOH 0.1 M up to pH ~ 9 (the solubility of copolymer at neutral pH is too low due to the internal hydrogen bonds between acrylic acid groups in polymeric backbone); afterward, pH was adjusted to 7.4 by addition of HCL 0.1 M. Fe_3O_4-68 NPs precipitate was added to the polymer solution, sonicated for one hour, and then kept under shaker at room temperature overnight. Finally, functionalized MNPs were dialyzed with dialysis bag (MWCO of 14 KDa) against Milli-Q water for 24 h. According to the ICP analysis, final suspension contains 0.14 wt % MNPs. The same procedure was used to prepare functionalized MNPs contains 0.4 wt % iron oxide nanoparticles just by properly modifying the initial quantities of Fe_3O_4-68 NPs (4.5 mL of the MNPs suspended in DEG with 1.33 wt % respect to Fe_3O_4 ~ 59.85 mg, 0.258 mol Fe_3O_4) and copolymer (0.2 g, 0.735 µmol).

A.11 Doxorubicin Loading on Fe_3O_4 Coated PVCL-b-PAA_2

PVCL-*b*-PAA_2 coated Fe_3O_4-68 NPs were dispersed in 15.0 mL buffer phosphate 10 mM, (pH = 8.5), and then pH was adjusted to 7.4 (samples $A_{7.4}$, $B_{7.4}$ and $C_{7.4}$, $D_{7.4}$) or 5.5 (samples $A_{5.5}$ and $B_{5.5}$) by addition of HCL 0.1 M to provide smart nanocomposite suspension with 0.14 wt % of MNPs and 6.0 mg mL^{-1} copolymer for sample A and 0.4 wt %

of MNPs and 10.0 mg mL^{-1} copolymer for sample B by following the same procedure, which was reported in section A.10. Afterward, 5.0 mL aqueous solution of doxorubicin (DOX) (0.9 mg mL^{-1} for samples A, B and 1.5 mg mL^{-1} for samples C, D) was added to the suspension and the mixture was incubated at 25 °C at darkness for 72 h. After incubation the DOX-loaded nanocomposite suspension was dialyzed against buffer phosphate 10 mM, pH = 7.4 or 5.5 using dialysis membrane bag (MWCO ~ 1 kDa) for 24 h to remove the non-encapsulated drug. The concentration of free DOX in dialysis fluid was analyzed by UV-Vis spectroscopy at a specific wavelength 480 nm to determine the drug encapsulation efficiency (EE), and Drug Loading (DLC) Contents. A calibration curve of DOX in buffer phosphate 10 mM, pH ~ 7.4 or pH ~ 5.5 was made as the reference.

A.12 In Vitro Drug Release Behavior in the Absence of Alternating Magnetic Field (AMF)

In order to study the pH and temperature dependence of the drug release kinetics in the absence of an AMF, 6 sets of experiments were performed. That means, the drug release was studied at 25 °C, 37 °C (physiological temperature, < LCST), and 48 °C (hyperthermia temperature, > LCST), and for each temperature, samples were held at pH = 7.4, the physiological pH, pH = 5.5, and pH = 4.5 to mimic acidic tumour pH values. Typically, 5.0 mL of Fe_3O_4-68@PVCL-*b*-PAA_2@DOX dispersed in buffer phosphate with the selected pH (7.4, 5.5 or 4.5) were inserted in a dialysis bag (MWCO ~ 14 kDa) and dialyzed against 50.0 mL of buffer phosphate with the same pH value, under mild stirring. A dialysate volume of 10 times that of the dialysis bag was chosen to ensure sink conditions for the DOX. Moreover, this volume was required for the dialysis bag to be fully immersed in the medium. Dialysis set up were either maintained to room temperature, or placed into preheated water baths at 37 °C and 48 °C. At predetermined time points (i.e. 30 min, 1, 2, 3, 4, 5, 6,7, 24, 30, 48, and 72 h), whole dialysate (50.0 mL) was taken out, and 50.0 mL of fresh buffer phosphate with the appropriate pH was added to preserve sink conditions. Afterward, the volume of 50.0 mL extracted dialysate was decreased to 5.0 mL by rotary evaporation at 25 ^{o}C, so that the absorbance of DOX released in the dialysis fluid became in the detectable range of UV-Vis spectroscopy.

A.13 Drug Release Under an Alternating Magnetic Field

5.0 mL of sample $A_{7.4}$ with an iron concentration of 0.14 wt % was placed in the magnetic coil of the instrument and then after the suspension was stabilized at the

physiological body temperature (37 °C), the AMF with f = 183 kHz and H = 17 kA m^{-1} was applied for different time interval (30, 40, 50, and 60 min). The sample, then, was taken out of the instrument after selected time interval, and centrifuged 15 min to separate the nanoparticles from supernatant. Nanoparticles were collected and redispersed in 5.0 mL fresh buffer phosphate 10 mM, pH = 7.4, and supernatant was analyzed by UV-Vis absorption spectroscopy at wavelength 480 nm for the evaluation of the amount of drug released. The amount of DOX released from sample $A_{5.5}$ under the AMF was evaluated following the same procedure.

A.14 Smart Hyperthermia with Switchable Drug Release

5.0 mL of suspension of Fe_3O_4-68@PVCL-*b*-PAA_2-DOX in buffer phosphate 10 mM, pH = 7.4 contains 0.4 wt % MNPs ($B_{7.4}$) was placed in the copper coil. The AMF with frequency of 183 kHz and intensity of 17 kA m^{-1} was turned on for 10 min, allowing the nanocomposite suspension to be heated up to 50 ^{o}C. The AMF was then turned off, and allowed cooling down to 25 ^{o}C. This process was repeated for 6 times. The released DOX during each cycle was collected by centrifugation and its absorbance at 480 nm was measured by UV-Vis spectroscopy. The cumulated released DOX was calculated using the following equation,

$$\textit{Cumulated released DOX} = \frac{D_{release\ at\ X}}{D_{total}} \times 100\ (\%)$$

where $D_{release\ at\ X}$ is the cumulative amount of released DOX at X cycle of AMF application and D_{total} is the total amount of incorporated DOX in the nanocomposite.

Switchable drug release of sample ($B_{5.5}$) was assessed by following the same procedure as sample ($B_{7.4}$).

A.15 Cytotoxicity Assay

Cell viability against DOX loaded magnetic nanoparticles was investigated by WST-1 assay on melanoma cancer cells (A375). Briefly, A375 human melanoma cells were seeded in 96-well plates in complete culture medium composed of Dulbecco's Modified Eagle's (DMEM) medium supplemented with 10.0 % fetal bovine serum (FBS), 10.0 mg mL^{-1} penicillin G sodium and 10.0 mg mL^{-1} streptomycin sulfate. Indeed, about 5000 viable cells were added to each well of a 96-well culture plate and incubated at 37 ^{o}C under 5.0 % CO_2 atmosphere overnight to allow cells to attach to wells of cell culture plates. Then, the medium from A375 cells were replaced with 100.0 µL of fresh complete culture medium, containing

Fe_3O_4-68@PVCL-*b*-PAA_2-DOX composed of 14.0 µg mL^{-1} DOX with different concentration of MNPs (0.065, 0.01, and 0.008 wt % Fe_3O_4) in triplet. Afterward, 100.0 µL of the crude toxin in addition to 10.0 µL of cell proliferation reagent WST-1 (Roche) were added to each well and incubated at 37 °C under 5.0 % CO_2 in a humidified incubator for 24 h. Negative controls (medium culture) and positive controls (medium culture and cells) were also included in every experiment. After 24 h incubation, the absorbance of samples was measured in a microplate reader (Bio-Rad) at 450 nm. The percent cytotoxicity was calculated from the following equation:

$$(A\ Experimental\ value - A\ negative\ control) / (A\ positive\ control - A\ negative\ control) \times 100$$

Where *A Experimental value* is the absorbance with the sample, *A negative control* is the absorbance with media control, and *A positive control* is the absorbance with cells control.

Cytotoxicity of Fe_3O_4-68@PVCL-*b*-PAA_2 MNCPs contains 0.25, 0.125, 0.0625, 0.01, and 0.008 wt % of Fe_3O_4 in 100.0 µL complete medium before drug loading was measured exactly by following the same procedure.

Appendix B

Instrumentations

This section describes the instruments used for the characterization of magnetic nanoparticles, thermoresponsive polymers, and smart magnetic nanocomposite investigated in this study. These involve mainly the facilities for determination of particles size, morphology, and structure of magnetic nanoparticles, thermoresponsive polymers as well as smart nanocomposite. The instruments including DLS, ICP, DSC-TG, FTIR used in this work are located at Colorobbia Consulting S.r.l, while UV spectrometer, NMR, SQUID, XRD, and TEM are located at LAMM, Chemistry Department, University of Florence. Gel permeation chromatography analysis of polymers was performed at the Department of Industrial Chemistry of University of Pisa from the research group of Prof. F. Chiellini.

B.1 GEL Permeation Chromatography

The GPC apparatus used to determine the molecular weight of PVCL and PVCL-*b*-PVPON, consisted of a Waters™ 600 Controller equipped with a Waters 410 Differential Refractometer and a Waters™ 600 Pump, managed by ChromNAV software (Jasco Europe, Lecco, Italy). A Plgel guard column and two PLgel Mixed D 5 μm columns (7.5 × 300 mm) (Agilent, CA, USA) were employed. The eluent was tetrahydrofuran CHROMASOLV® Plus (THF) and the flow rate was maintained at 1.0 mL min^{-1}. Polystyrene standards (Sigma-Aldrich) were used to obtain a calibration curve (2-1000 kDa). Prior to analysis the samples were dissolved in the eluent at a concentration of 5.0 mg mL^{-1} and filtered by using cellulose ester filters (0.2 μm).

GPC analysis of PVCL-*b*-PAA was carried out with a Waters 600 model equipped with a Waters 410 Differential Refractometer and two Ultrahydrogel TM linear 6–13 μm columns (7.8 × 300 mm) (Fluka Analytical) at room temperature. Mobile phase constituted by water (HPLC grade) was eluted at a flow rate of 1.0 mL min^{-1}. Polyethylene oxide standards (Polymer Laboratories, UK) were used to obtain a calibration curve (*Mn* range 560–879000 g mol^{-1}). Prior to analysis, the samples were dissolved in water at a concentration of 5.0 mg mL^{-1} and filtered by using cellulose ester filters (0.2 μm).

B.2 Dynamic Light Scattering

DLS measurement was performed on 1.0-2.0 mL of dispersions of MNPs, polymers, or magnetic nanocomposite in water or buffer phosphate 10 mM at different pH, in a quartz cuvette. DLS was performed using a Nano-ZS Zetasizer (ZEN 3600-Malvern) equipped with a He–Ne laser (633 nm) at an angle of 173^{o}.

B.3 Zeta Potential Measurements

Zeta potential measurements were carried out using a Nano-ZS Zetasizer (ZEN 3600-Malvern) instrument. An equilibration time of 2 min was allowed before each measurement and at least five replicate measurements were made for each sample.

B.4 Fourier Transform Infrared Spectroscopy

The FT-IR spectra of the products were recorded with a double-beam Agilent Technology Cary 640 Series FTIR spectrometer in range of 4000–500 cm^{-1} using KBr pellets.

B.5 ICP-AES

The quantitative analysis of iron content was carried out with an Atomic Emission Spectrometer coupled with an Inductively Coupled Plasma torch (ICP-AES, Varian 710-ES). To analyze iron content, powder samples were digested with 2.0 mL of HNO_3 and 2.0 mL of HCL. The calibration standard was prepared by serial dilution of a commercial standard solution of Fe 1000 mg mL^{-1}. The wavelength used for the determination of Fe is 238 nm. The operating conditions were optimized to obtain maximum signal strength.

B.6 DSC-TG

TGA analyses have been performed using a NETZSCH STA 449C Jupiter instrument. Measurements were performed on about 50.0 mg of dried magnetic nanocomposite deposited into an alumina sample-holder. The scanning temperature range was set from room temperature up to 1000°C under gradual heating (5 $^{o}C\ min^{-1}$) and measurements were carried out under N_2 flux. Results were elaborated with a Proteus Analysis (Netzsch) software.

B.7 Turbidimetric Analysis

UV-Vis spectroscopy (UV-Vis) measurements were performed at the Department of Organic Chemistry of the University of Florence (Prof. S. Cicchi) by recording the transmittance of 1.0 mL polymer aqueous solutions with a Varian Carry 4000 UV

spectrophotometer at a wavelength ranging from 200 nm to 800 nm. The measurements were carried out by monitoring change in transmittance as a function of temperature at 500 nm wavelength for PVCL, PVCL-*b*-PVPON, and 570 nm wavelength for PVCL-*b*-PAA. Before each measurement, the sample was left to equilibrate at the desired temperature for 5 min.

B.8 Nuclear Magnetic Resonace (NMR)

^{1}HNMR spectra of the copolymers were recorded on a Bruker 400 MHz NMR spectrometer. The copolymer solutions with concentrations of 1.0 mg mL^{-1} were prepared in $CDCl_3$ or D_2O, and measured at 25 ^{o}C and 50 ^{o}C.

B.9 Transmission Electron Microscopy (TEM)

The average diameter and size distribution of MNPs, polymers, and smart magnetic nanocomposite (MNCs) were determined by Transmission Electron Microscopy (TEM) images recorded using a CM12 PHILIPS transmission electron microscope operating at 100 kV using a LaF_6 source. Samples were prepared by drop drying a dilute aqueous suspension of MNPs, smart magnetic nanocomposite, or polymer solution (1.0 mg mL^{-1}) onto 200 mesh carbon-coated copper grids. The recorded micrographs were processed by means of the iTEM TEM Imaging Platform software (Olympus), and were further analysed with the FIJI open software.

B.10 XRD

Powder X-ray diffraction (XRD) measurements were carried out using a Bruker D8 Advance diffractometer equipped with Cu Kα (1.54178 Å) radiation and operating in θ−θ Bragg−Brentano geometry at 40 kV and 40 mA. Lattice parameters were evaluated on averaging over (400), (511) and (440) peaks. The determination of the mean crystallite diameter, *d*, was performed using the Scherrer equation, $d = (0.9\lambda)/(\beta \cos\theta)$, where λ is the wavelength of the incident X-ray (1.54178 Å), θ the diffraction angle, and β the full-width at half-maximum. The quantification of the phase percentage was obtained analyzing the diffraction pattern by the Rietveld method with TOPAS software.

B.11 Magnetic Characterization and SAR evaluation

Magnetic measurements were performed using a Quantum Design MPMS SQUID magnetometer operating in the 1.8–350 K temperature range and with an applied field up to 50 kOe. Measurements were performed on pressed powder of sample. All data were

corrected for the diamagnetic contribution of the sample holder, and were normalized to the amount of magnetic material as evaluated from elemental analysis. Zero Field Cooled–Field Cooled (ZFC/FC) curves were obtained by measuring the temperature dependence of the magnetization applying a probe magnetic field (50 Oe), after cooling the sample in the absence (ZFC) or in the presence (FC) of the field. A rough estimate of T_B value accuracy is given by the half interval between the temperatures of two subsequent acquisition points, *i.e.*, 2.5 K. The field dependence of the magnetic moment (M *vs.* H) was measured cycling the field between ±50 kOe at 2.5 K and 300 K. The accuracy of H_C, M_R, and M_S evaluation can be estimated as low as 3%.

The evaluation of Specific Absorption Rate (SAR) was performed through calorimetric measurements by recording temperature kinetics of samples exposed to an alternating magnetic field. The instrument is adapted from a commercial setup, composed by a 6 kW Fives Celes power supply, a water-cooled induction coil and a series of variable capacitors (420 nF to 4.8 μF) for setting the required frequency. Such resonant RLC circuit is able to produce an alternating magnetic field in the range of 50–400 kHz and with amplitude up to 19.1 kA m^{-1} (Figure B.1) The frequency and field amplitude values used in this work (183 kHz, 17.0 kA m^{-1}) were chosen in order to operate under the physiological limit, $Hv < 5 \times 10^9$ A m^{-1} s^{-1}, beyond which deleterious responses of living tissues are observed. The sample was placed in the middle of the induction coil, inside a polystyrene sample holder placed in a glass Dewar connected to a glycol thermal bath in order to isolate the sample bath from the thermal gradient of the coils and from the environment (Figure B.2). The real amplitude of the magnetic field was determined by an AMF Life Systems high frequency probe. Measurements of the sample temperature were performed by an optical fiber thermometer connected to a digital temperature recorder (Fotemp).

Figure B.1 Power supply MP6-400 6kW®, Fives Celes Inc. and FoTemp optical fiber thermometer

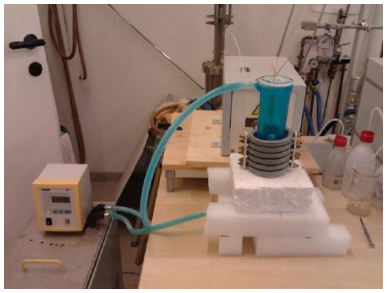

Figure B.2 Detail of the Ethylene glycol thermostated system